

**EFFECT OF THERMAL LOADING ON POST ELASTIC  
BEHAVIOUR OF AXISYMMETRIC BAR AND  
ROTATING DISK**

*Thesis submitted by*

**PRIYAMBADA NAYAK**

**Doctor of Philosophy  
(Engineering)**

**DEPARTMENT OF MECHANICAL ENGINEERING  
FACULTY COUNCIL OF ENGINEERING & TECHNOLOGY  
JADAVPUR UNIVERSITY  
KOLKATA, INDIA**

**2018**



# JADAVPUR UNIVERSITY

KOLKATA-700032, INDIA

INDEX NO. 237/13/E

## 1. Title of Thesis:

*Effect of Thermal Loading on Post Elastic Behaviour of Axisymmetric Bar and Rotating Disk*

## 2. Name, Designation & Institution of the Supervisor:

**Prof. Kashinath Saha**

Associate Professor, Department of Mechanical Engineering,  
Jadavpur University, Kolkata-700032

## 3. List of Publications (Referred Journals):

- I. **Nayak, P. and Saha, K.N.**, Analytical study on elastic limit speed of non-uniform rotating disks considering thermal effect on elasticity modulus, *Applied Mechanics and Materials*, (2014), 592-594, 1001-1005.
- II. **Nayak, P. and Saha, K.N.**, Elastic limit angular speed of solid and annular disks under thermo-mechanical loading, *International Journal of Engineering, Science and Technology*, (2016), 8 (2), 30-45.
- III. **Nayak, P. and Saha, K.N.**, Optimized design of thermo-mechanically loaded non-uniform bars by using a variational method, *Journal of Physics: Conference Series*, (2016), 738, 1-7.
- IV. **Nayak, P. and Saha, K.N.**, Analysis of statically indeterminate non-uniform bar problem in post elastic domain by an iterative variational method, *Applied Mathematical Modelling*, (2017), 51, 86-108.
- V. **Nayak, P. and Saha, K.N.**, Growth of yield front in thermo-mechanically loaded non-uniform bars using an iterative variational method, *Journal of Strain Analysis*, (2018), 53 (2), 66-79.

VI. **Nayak, P. and Saha, K.N.**, Elasto-plastic analysis of thermo-mechanically loaded functionally graded disks by an iterative variational method, Engineering Science and Technology, an International Journal, (<https://doi.org/10.1016/j.jestch.2019.04.007>).

**4. List of Patents:** Nil

**5. List of Presentations in National/International Conferences:**

- I. **Nayak, P. and Saha, K.N.**, A numerical study on the optimal design of rotating disks under thermal environment, 58<sup>th</sup> congress of Indian Society of Theoretical and Applied Mechanics, BESU Shibpur, Howrah, India, 18-21 December 2013 (Paper ID - sm-fp-6).
- II. **Nayak, P. and Saha, K.N.**, Thermal effect in the design of rotating non-uniform disks considering variations in density and elasticity modulus, 5th International Congress on Computational Mechanics and Simulation, CSIR-SERC, Chennai, India, 10-13 December 2014 (Paper ID-80).
- III. **Nayak, P. and Saha, K.N.**, Thermal stress effect on rotating disk, 6<sup>th</sup> International Conference on Theoretical, Applied, Computational and Experimental Mechanics, IIT Kharagpur, India, 29-31 December 2014 (Paper ID-466).
- IV. **Nayak, P. and Saha, K.N.**, Growth of yield front in statically indeterminate bar by using domain decomposition method, 6<sup>th</sup> International Congress on Computational Mechanics and Simulation, IIT Mumbai, India, 27<sup>th</sup> June-1<sup>st</sup> July 2016 (Paper ID-761).
- V. **Nayak, P. and Saha, K.N.**, A numerical study on effect of varying material properties on limit angular speed of non-uniform rotating FGM disks under thermomechanical environment, National Conference on Advances in Thermal Engineering, Jadavpur University, Kolkata, India, 23-24 September 2016 (Paper ID-ATE 004).
- VI. **Nayak, P. and Saha, K.N.**, Effect of yield stress variation on yield front growth of non-uniform bars subjected to thermal load, 1<sup>st</sup> International Conference on Mechanical Engineering, Jadavpur University, Kolkata, India, 4-6 January 2018 (Paper ID-98).



## CERTIFICATE FROM THE SUPERVISOR/S

*This is to certify that the thesis entitled “Effect of Thermal Loading on Post Elastic Behaviour of Axisymmetric Bar and Rotating Disk” submitted by Ms. PRIYAMBADA NAYAK who got her name registered on 01.11.2013 for the award of Ph.D. (Engineering) degree of Jadavpur University is absolutely based upon her own work under my supervision and that neither her thesis nor any part of the thesis has been submitted for any degree/ diploma or any other academic award anywhere before.*

---

**(Kashinath Saha)**

Signature of the Supervisor  
and date with Office Seal



## *Acknowledgement*

---

The work presented in this thesis would not have been possible without my close association with many people who were always there when I needed them the most. I take this opportunity to acknowledge them and extend my sincere gratitude for helping me make this Ph.D. thesis a possibility. In this first place I would like to offer my utmost gratitude to my thesis supervisor, Prof. Kashinath Saha, for his generous assistance, inspired ideas and unrelenting support from the very early stage of this research as well as giving me extraordinary experiences throughout the work. His input and patience has been invaluable in helping me to learn how to do research, and to navigate some of the more emotionally challenging aspects of this research work. I shall always remain indebted to him.

I acknowledge the Council of Scientific and Industrial Research (CSIR), Government of India for providing me with the necessary financial support to pursue research at Jadavpur University.

I sincerely acknowledge Prof. Sankar Dhar for teaching the basics of theory of plasticity that proved to be very useful to carry out this research work.

I am very much grateful to Dr. Shubhankar Bhowmick and Dr. Anirban Mitra, for extending their sincere support, valuable guidance and consistent encouragement throughout the course of the thesis work.

I would like to express my gratitude to all the members (past and present) of the Machine Element Laboratory, who have been with me throughout the completion of this thesis. I would like to acknowledge Brajesh Panigrahi and Amit Banerjee for being a friend before a labmate. Our association goes a long way since days of post graduation and they have been with me ever since then as a friend, a companion and labmate. Thank you for being with me in ups and downs of life over the last few years. My special thanks to Sushanta Ghuku for his involvement and support during the presented work. My heartfelt thanks to my fellow labmates, Santanu Duari, Milan Das, Bikash Panja, Ajay Waghmare, Prasanna Gadhari, Sanjib Kundu, Abhijit Biswas, Arkadeb Mukhopadhyay, Smrutiranjana Pradhan, Tamonash Jana, for always being there and bearing with me the good and bad times during my wonderful days of Ph.D. My special words of gratitude to my friend Hareram Lohar for his association.

I would like to convey my thanks to the Head of the Department, Laboratory-in-Charge, Machine Elements Laboratory and all academic and technical staffs of Mechanical Engineering Department, Jadavpur University.

In this respect, I would also like to grab this opportunity to express my heart-felt gratitude to my family members and friends whose support, suggestions and helping attitude helped my way out to the completion of the thesis. I thank the Almighty for giving me the strength and patience to work through all these years. I dedicate this thesis to Sadguru Paramahansa Shrimad Swami Nigamananda Saraswati Deva.

Finally, I would like to thank everybody who was important to the successful realization of this thesis, as well as expressing my apology that I could not mention personally one by one.

**Priyambada Nayak**

## *Table of Contents*

---

	<b>Page No</b>
List of Publications and Presentations from the Thesis	i
Certificate of supervisor	iii
Acknowledgement	v
Table of Contents	vii
List of Notations	xiii
List of Figures	xvii
List of Tables	xxix
Abstract	xxxix
<b>Chapter 1 INTRODUCTION</b>	<b>1-16</b>
1.1 Objectives of the study	1
1.2 Introduction to Material Models	6
1.2.1 Yield (Failure) criteria	6
1.2.2 Post elastic behaviour	7
1.2.3 Functionally graded materials	9
1.3 Thermal effect	10
1.3.1 Thermal parameters	11
1.3.2 Thermal stress	11
1.4 Method of analysis	12
1.5 Layout of the thesis	15
<b>Chapter 2 LITERATURE REVIEW</b>	<b>17-48</b>
2.1 Introduction	17
2.2 Analysis of bar problems	17
2.2.1 Elasto-plastic analysis of isotropic bars	18
2.2.2 Elasto-plastic analysis of composites and FGM bars	20
2.3 Material behavior of rotating disks	22
2.3.1 Disks made of isotropic materials	23

2.3.1.1	Analysis of rotating disks in elastic region	23
2.3.1.2	Elasto-plastic analysis of rotating disks	25
2.3.2	Disks made of anisotropic materials	29
2.3.2.1	Disks made of composites and FGMs: Elastic analysis	31
2.3.2.2	Disks made of composites and FGMs: Post-elastic analysis	35
2.4	Types of loading on rotating disks	37
2.4.1	Disks under centrifugal loading	37
2.4.2	Disks under thermal loading	38
2.4.3	Disks under thermo-mechanical loading	40
2.5	Some related area and complicating effects	42
2.5.1	Application of numerical methods	42
2.5.2	Modelling of creep behaviour	44
2.5.3	Experimental work	46
2.6	Summary	47
<b>Chapter 3</b>	<b>ELASTIC LIMIT ANGULAR SPEED OF ROTATING DISKS UNDER THERMO-MECHANICAL LOADING</b>	<b>49-78</b>
3.1	Introduction and literature review	49
3.2	Mathematical formulation	51
3.3	Results and discussion	54
3.3.1	Convergence and validation of the formulation	57
3.3.2	Effect of temperature distributions	58
3.3.3	Effect of temperature on the variation of density	67
3.3.4	Effect of temperature on yield stress	69
3.3.5	Effect of temperature on elasticity modulus	73
3.3.6	Effect of temperature on simultaneous variation of density and elasticity modulus	75
3.4	Summary	78

<b>Chapter 4</b>	<b>ANALYSIS OF STATICALLY INDETERMINATE BAR PROBLEM IN POST ELASTIC DOMAIN</b>	<b>79-115</b>
4.1	Introduction and literature review	79
4.2	Mathematical formulation	82
4.2.1	Deviatoric stress and strain intensities	82
4.2.2	Work of deformation	83
4.2.2.1	Linear elastic state (Hooke's law)	84
4.2.2.2	Yield state	84
4.2.2.3	Hardening state	84
4.2.3	Description of the bar problem	85
4.2.4	Solution of the problem	87
4.2.4.1	Elastic solution	87
4.2.4.2	Solution for post-elastic domain	89
4.2.4.2.1	Three region formulation	90
4.2.4.2.2	Four region formulation	92
4.3	Validation study	93
4.3.1	Revised formulation using iterative variational method	98
4.3.1.1	Iterative variational method (IVM) using domain decomposition method (DDM)	99
4.3.1.2	The iterative scheme for revised formulation	100
4.3.2	Analytical solution of the problem with variationally based boundary conditions	103
4.4	Results and discussion	105
4.4.1	Effect of aspect ratio and slenderness ratio on clamped-free taper bar	106
4.4.2	Post-elastic behaviour of clamped-clamped uniform taper bar	106
4.4.3	Post-elastic behaviour of clamped-clamped non-uniform taper bar	110
4.4.4	Results for clamped-clamped uniform taper bar with trilinear material model	112

4.5	Summary	115
<b>Chapter 5</b>	<b>GROWTH OF YIELD FRONT IN THERMO-MECHANICALLY LOADED ISOTROPIC AND FG BARS</b>	<b>117-164</b>
5.1	Introduction	117
5.2	Thermo-elasto-plastic analysis of isotropic non-uniform bars	118
5.2.1	Mathematical formulation	120
5.2.2	Results and discussion	123
5.2.2.1	Validation study	126
5.2.2.2	Elasto-plastic behaviour of clamped-clamped linear taper bar	127
5.2.2.3	Elasto-plastic behaviour of clamped-clamped parabolic bar	134
5.2.2.4	Results for multilinear (four segment) material model	139
5.2.2.5	Elasto-plastic behaviour considering yield stress variation with temperature	143
5.3	Thermo-elasto-plastic analysis of functionally graded non-uniform bars	147
5.3.1	Mathematical formulation	150
5.3.1.1	Solution of the problem	152
5.3.2	Results and discussion	152
5.3.2.1	Elasto-plastic behaviour of FGM taper bar	156
5.3.2.2	Effect of material parameters $V_{c0}$ and $n$	158
5.3.2.2.1	Effect of the ceramic content at the right fixed end, $V_{c0}$	159
5.3.2.2.2	Effect of the volume fraction coefficient, $n$	160
5.3.2.3	Elasto-plastic behaviour of FGM parabolic bar	160
5.3.2.4	Results for multilinear (four segment) material model for FGM taper bar	161
5.4	Summary	163



<b>Chapter 6</b>	<b>ELASTOPLASTIC ANALYSIS OF THERMO-MECHANICALLY LOADED FGM DISKS</b>	<b>165-197</b>
6.1	Introduction and literature review	165
6.2	Mathematical formulation	167
6.2.1	Material properties determination for FGM	168
6.2.2	Formulation of the thermo-mechanical problem	170
6.2.3	Total PE in post elastic state of FGM	172
6.2.4	Post-processing	175
6.3	Results and discussion	177
6.3.1	The description of parameters	177
6.3.1.1	Geometrical properties of the disk	177
6.3.1.2	Material properties of the disk	178
6.3.1.3	Effect of temperature on FGM disk	180
6.3.2	Validation study	182
6.3.3	Present results	185
6.3.3.1	Effect of geometry variation on elasto-plastic behaviour of FGM annular disk	186
6.3.3.2	Study on the yield and collapse limit temperature	189
6.3.3.3	Effect of material parameters $V_{c0}$ and $n$	190
6.3.3.3.1	Effect of the ceramic content at the outer radius, $V_{c0}$	190
6.3.3.3.2	Effect of the ceramic distribution coefficient, $n$	191
6.3.3.4	Effect of the nature of temperature distribution	192
6.3.3.5	Results for FGM disk with trilinear material model	193
6.3.3.6	Study on plastic strain	195
6.4	Summary	197
<b>Chapter 7</b>	<b>CLOSURE</b>	<b>199-203</b>
7.1	Conclusions	199
7.2	Future scope of work	202
	<b>Bibliography</b>	<b>205-227</b>



## *List of Notations*

---

$a, b$	Inner and outer radii of disk
$A$	Cross-sectional area at any axial location of bar
$A_0, A_l$	Cross-sectional area corresponding to largest and smallest diameters of bar
$A_R$	Aspect ratio of the bar
$c_i$	Vector of unknown coefficients
$d$	Diameter of circular bar at any axial location
$d_0, d_l$	Largest and smallest diameter of the bar
$e_r, e_\theta$	Elastic strain in radial and tangential directions of rotating disk
$E, E_l$	Young's modulus and tangent modulus of the material
$\{f\}$	Load vector
$F$	Concentrated axial load of bar
$F_0, F_l$	Reaction forces developed at the left and right fixed ends of bar
$F_y, F_c$	Elastic limit load and plastic collapse load of bar
$g(\Gamma)$	Modulus of plasticity
$G$	Rigidity modulus of the material
$h_0, h$	Thickness at the root and thickness at any radius of the disk
$I_l$	Area moment of inertia of the bar at fixed end in the right
$k, K$	Coefficient of volumetric compression and bulk modulus
$[K]$	Stiffness matrix
$L$	Total length of the bar
$L_e, L_p$	Length of the elastic and plastic region of bar
$L_f, L_b$	Length of domain 1 and domain 2 of bar
$L_{fe}, L_{fp}$	Length of elastic and plastic regions of domain 1 of bar
$L_{be}, L_{bp}$	Length of elastic and plastic regions of domain 2 of bar
$n, k$	Parameters controlling the thickness variation of the disk

$r, \theta, z$	Radial, tangential and axial directions
$r_y$	Radial location of yield front at the initiation of yielding of disk
$\bar{r}$	Parameter $(b - a)$
$S$	Deviatoric stress
$S_R$	Slenderness ratio of the bar
$T$	Temperature distribution along the axial direction of bar Temperature distribution along the radial direction of rotating disk
$T_0, T_l$	Temperature at the larger and smaller fixed end of the bar
$T_{1\omega}$	Yield limit temperature at a given rotational speed
$T_{2\omega}$	Collapse temperature corresponding to a given rotational speed
$T_a, T_b$	Inner and outer surface temperature of the disk
$T_c$	Plastic collapse temperature of bar
$T_y$	Elastic limit temperature of bar
$u$	Displacement along axial direction for bar Displacement along radial direction for rotating disk
$U$	Total strain energy
$U_e$	Elastic part of strain energy
$U_p$	Post-elastic part of strain energy
$V$	Potential energy of external load
$V_c, V_m$	Volume fraction of ceramic and metal constituents along axial direction of FGM bar Volume fraction of ceramic and metal constituents along radial direction of FGM disk
$x$	Axial coordinate for bar
$x_p$	Dimensional value of plastic front location of bar
$\alpha$	Coefficient of thermal expansion
$\Gamma$	Shear strain
$\delta$	Variational operator
$\varepsilon_r, \varepsilon_\theta$	Total strain in radial and tangential directions of rotating disk

$\varepsilon_x$	Strain along axial direction
$\varepsilon^*$	Thermal strain
$\lambda_c$	Non-dimensional collapse load of bar
$\nu, \nu_p$	Poisson's ratio in elastic and post-elastic state
$\xi$	Normalized axial coordinate for bar
	Normalized co-ordinate in radial direction for rotating disk, $(r - a)/\bar{r}$
$\xi_1, \xi_2$	Normalized coordinate in domain 1 and domain 2 of bar
$\xi_1^e, \xi_1^p$	Normalized coordinate in elastic and plastic region of domain 1 of bar
$\xi_2^e, \xi_2^p$	Normalized coordinate in elastic and plastic region of domain 2 of bar
$\xi^e, \xi^p$	Normalized coordinate in elastic and plastic region of bar
	Normalized radial coordinate in elastic and plastic region of rotating disk
$\Pi$	Total potential energy
$\rho$	Density of the material
$\sigma_x$	Stress along axial direction
$\sigma_y$	Yield stress of the material
$\sigma_r, \sigma_\theta$	Stress along radial and tangential direction of rotating disk
$\sigma_{ult}$	Ultimate stress of the material
$\sigma_{vm}$	von Mises stress
$\phi_i$	Set of functions used for approximation of displacement field $u$
$\phi_i^e, \phi_i^p$	Set of functions defining approximate displacement field $u$ in elastic and post-elastic regions
$\phi_{i1}, \phi_{i2}$	Portions of the functions $\phi_i$ in domain 1 and domain 2 of bar
$\phi_{i1}^e, \phi_{i1}^p$	Portions of the functions $\phi_{i1}$ in elastic and plastic regions of domain 1 of bar
$\phi_{i2}^e, \phi_{i2}^p$	Portions of the functions $\phi_{i2}$ in elastic and plastic regions of domain 2 of bar
$\phi_o$	Start function of orthogonal set of functions
$\psi$	Proportionality constant between stress and strain deviatorics upto yield limit state

$\psi(\Gamma)$	Function of intensity of shear in post yield hardening state
$\omega$	Dimensional angular speed of the disk
$\omega_{IT}$	Elastic limit speed at a given temperature
$\omega_{2T}$	Plastic limit speed corresponding to a given temperature
$\omega_y$	Dimensional value of limit angular speed
$\bar{\omega}_y$	Normalized limit angular speed, $\omega_y b \sqrt{\rho/\sigma_y}$
$\omega_y b$	Limit angular tip speed

## *List of Figures*

---

	<b>Page No</b>
<b>Figure 1.1.</b> Applications of axisymmetric bars and rotating disks	2
<b>Figure 1.2.</b> Linear elastic and linear strain hardening elasto-plastic behaviour	8
<b>Figure 3.1.</b> Rotating disk under various temperature distribution profiles for (a) specified outer surface temperature ( $T_b$ ) and (b) specified inner surface temperature ( $T_a$ )	56
<b>Figure 3.2.</b> Plot of convergence of normalized limit angular speed with coordinate functions	57
<b>Figure 3.3.</b> Comparison of displacement ( $u$ ), radial ( $\sigma_r$ ) and tangential stresses ( $\sigma_t$ ) for: (a) solid taper disk, (b) annular taper disk, (c) annular taper disk subjected to temperature gradient, (d) annular taper disk with density variation and (e) annular taper disk subjected to both density and temperature gradient	59
<b>Figure 3.4.</b> Plots for normalized limit angular speed ( $\bar{\omega}_y$ ) with outer surface temperature ( $T_b$ ) having different temperature distributions: (a) uniform, (b) linear, (c) exponential and (d) parabolic	60
<b>Figure 3.5.</b> Plots for normalized limit angular speed ( $\bar{\omega}_y$ ) with inner surface temperature ( $T_a$ ) having different temperature distributions: (a) uniform, (b) linear, (c) exponential and (d) parabolic	61
<b>Figure 3.6.</b> Distribution of radial ( $\sigma_r$ ), tangential ( $\sigma_t$ ) and von-Mises stress ( $\sigma_{vm}$ ) field corresponding to yield limit state in an annular disk subjected to (a) pure centrifugal loading due to rotation only, (b) combined loading with higher inner surface	62

temperature ( $T_a$ ) and (c) combined loading with higher outer surface temperature ( $T_b$ )

- Figure 3.7.** Effect of outer surface temperature distributions ( $T_b$ ) on normalized limit angular speed ( $\bar{\omega}_y$ ) for different disk geometries: (a) uniform, (b) taper, (c) exponential and (d) parabolic 64
- Figure 3.8.** Effect of inner surface temperature distributions ( $T_a$ ) on normalized limit angular speed ( $\bar{\omega}_y$ ) for different disk geometries: (a) uniform, (b) taper, (c) exponential and (d) parabolic 65
- Figure 3.9.** Variation of disk material properties  $\rho$ ,  $\sigma_y$  and  $E$  with temperature: (a) density ( $\rho$ ), (b) yield Stress ( $\sigma_y$ ) and (c) Elasticity modulus ( $E$ ) for structural steel with grade S350GD+Z at different specified temperatures 66
- Figure 3.10.** Effect of density variation on limit angular tip speed for different temperature distributions of outer surface  $T_b$ : (a) uniform, (b) linear, (c) exponential and (d) parabolic temperature 67
- Figure 3.11.** Effect of density variation on limit angular tip speed for different temperature distributions of inner surface  $T_a$ : (a) uniform, (b) linear, (c) exponential and (d) parabolic temperature 68
- Figure 3.12.** Yield Stress variation in the disk for (a) linear temperature distribution and (b) parabolic temperature distribution 69
- Figure 3.13.** Variation of von Mises stress ( $\sigma_{vm}$ ) for parabolic temperature distribution profile for uniform disk at (a)  $\omega = 0$  rad/s and (b)  $\omega = 1000$  rad/s, at four different outer surface temperatures ( $T_b$ ) 70



<b>Figure 3.14.</b>	Variation of von Mises stress ( $\sigma_{vm}$ ) for parabolic temperature distribution profile for (a) uniform disk and (b) parabolic disk, at four different angular speeds	70
<b>Figure 3.15.</b>	Solid lines indicate the distribution of radial ( $\sigma_r$ ), tangential ( $\sigma_t$ ) and von-Mises stress ( $\sigma_{vm}$ ) field corresponding to yield limit state in an annular disk subjected to combined loading with higher outer surface temperature. Dotted lines indicate the variation of yield stress with temperature as reported in Figure 3.9(b).	71
<b>Figure 3.16.</b>	Plots of limit peripheral speed with outer surface temperature ( $T_b$ ) having different temperature distributions: (a) uniform, (b) linear, (c) exponential and (d) parabolic temperature	72
<b>Figure 3.17.</b>	Variation of elasticity modulus along the radius of the disk having different temperature distributions (a) linear and (b) parabolic temperature	73
<b>Figure 3.18.</b>	Plots of normalized limit angular speed with outer surface temperature ( $T_b$ ) having different temperature distributions: (a) uniform, (b) linear, (c) exponential and (d) parabolic temperature	74
<b>Figure 3.19.</b>	Simultaneous variation of density and elasticity modulus ( $E$ ) with temperature	75
<b>Figure 3.20.</b>	Plots of limit peripheral speed with outer surface temperature ( $T_b$ ) having different temperature distributions: (a) uniform, (b) linear, (c) exponential and (d) parabolic temperature	76
<b>Figure 3.21.</b>	3D and contour plots of von Mises stress showing its variation with rotational speed (rad/sec) and $T_b$ ( $^{\circ}\text{C}$ ) for various disk geometries: (a) uniform, (b) taper, (c) exponential and (d) parabolic	77
<b>Figure 4.1.</b>	(a) Taper bar geometry and (b) The loaded bar with domain 1	86

	and domain 2. Solid and dotted lines indicate bar with uniform and non-uniform taperness respectively	
<b>Figure 4.2.</b>	Representation of nomenclatures: (a) Three region and (b) Four region	91
<b>Figure 4.3.</b>	(a) Linear elastic and linear strain hardening elasto-plastic behavior and (b) deviatoric stress-shear strain diagram, for linear strain hardening material	94
<b>Figure 4.4.</b>	(a) Linear elastic and bilinear strain hardening elasto-plastic behavior and (b) deviatoric stress-shear strain diagram for bilinear strain hardening material	94
<b>Figure 4.5.</b>	Validation plots for a uniform taper bar ( $A_R = 0.1$ ) with different values for $S_R$ for (a#) normalized load vs. normalized plastic front location and (b#) normalized stress vs. normalized length with (#1) bilinear and (#2) trilinear material behaviour	96
<b>Figure 4.6.</b>	Validation plots for a non-uniform taper bar ( $A_R = 0.1$ ) with different values for $S_R$ for (a#) normalized load vs. normalized plastic front location and (b#) normalized stress vs. normalized length with (#1) bilinear and (#2) trilinear material behaviour	97
<b>Figure 4.7.</b>	Plot of stress fields for a clamped-clamped taper bar as obtained in (a) Abaqus CAE and (b) Present study	98
<b>Figure 4.8.</b>	Taper bar with reaction forces at fixed ends	99
<b>Figure 4.9.</b>	Flow chart for the solution algorithm	102
<b>Figure 4.10.</b>	Validation plot for a clamped-clamped taper bar with Abaqus CAE using (a) DDM with IVM and (b) DDM alone	103
<b>Figure 4.11.</b>	Plot of displacement fields for a clamped-clamped uniform and non-uniform taper bar as obtained in analytical method and present study for (a) $L_f = 0.4$ and (b) $L_f = 0.6$	106
<b>Figure 4.12.</b>	3D and contour plots of non-dimensional collapse load ( $\lambda_c$ ) showing it's variation with $A_R$ and $S_R$ for (a) uniform taper	107

	and (b) non-uniform taper	
<b>Figure 4.13.</b>	3D and contour plots of non-dimensional collapse load $\lambda_{c1}$ and $\lambda_{c2}$ showing it's variation with $A_R$ and $S_R$ for load application point (a1, a2) $\xi_f = 0.3$ (b1, b2) $\xi_f = 0.4$ (c1, c2) $\xi_f = 0.5$ (d1, d2) $\xi_f = 0.6$ and (e1, e2) $\xi_f = 0.7$	109
<b>Figure 4.14.</b>	Waterfall plot of stress variation with load for a uniform taper bar with $A_R = 0.025$ and $S_R = 100$ for different load application point (a) $\xi_f = 0.4$ (b) $\xi_f = 0.5$ (c) $\xi_f = 0.6$ (d) $\xi_f = 0.7$	110
<b>Figure 4.15.</b>	Plot of plastic front location variation with load for a uniform taper bar for load application point (a) $\xi_f = 0.4$ (b) $\xi_f = 0.5$ (c) $\xi_f = 0.6$ (d) $\xi_f = 0.7$	111
<b>Figure 4.16.</b>	3D and contour plots of non-dimensional collapse load $\lambda_{c1}$ and $\lambda_{c2}$ showing it's variation with $A_R$ and $S_R$ for load application point (a, b)	112
<b>Figure 4.17.</b>	Waterfall plot of stress variation with load for a non-uniform taper bar with $A_R = 0.025$ and $S_R = 100$ for load application point (a) $\xi_f = 0.4$ (b) $\xi_f = 0.5$ (c) $\xi_f = 0.6$ (d) $\xi_f = 0.7$	113
<b>Figure 4.18.</b>	Plot of plastic front location variation with load for a taper bar with linear variation in area for load application point (a) $\xi_f = 0.4$ (b) $\xi_f = 0.5$ (c) $\xi_f = 0.6$ (d) $\xi_f = 0.7$	114
<b>Figure 4.19.</b>	3D and contour plots of non-dimensional collapse load $\lambda_{c1}$ and $\lambda_{c2}$ showing it's variation with $A_R$ and $S_R$ for load application point (a, b) for trilinear model	115
<b>Figure 5.1.</b>	(a) Schematic diagram of geometry of taper bar and (b) four typical geometries for $L=1.2$ m	117
<b>Figure 5.2.</b>	(a) Stress-strain plot for mild steel (MS) at 20 °C showing linear elastic and linear strain hardening elasto-plastic behavior	124

and (b) deviatoric stress-shear strain diagram, for linear strain hardening material

<b>Figure 5.3.</b>	Variations in temperature (a) increasing and (b) decreasing	125
<b>Figure 5.4.</b>	Plot of elasto-plastic strain for clamped taper bar ( $A_R = 0.025$ and $S_R = 100$ ) corresponding to plastic collapse temperature $T_c$ : (a) linear and (b) parabolic temperature distribution	125
<b>Figure 5.5.</b>	Validation plot of stress field for clamped taper bar	126
<b>Figure 5.6.</b>	3D and contour plots of elastic limit temperature ( $T_y$ ) and plastic collapse temperature ( $T_c$ ) with its variation with $A_R$ and $S_R$ for clamped taper bars under (a1,a2) uniform, (b1,b2) linearly decreasing and (c1,c2) parabolically decreasing temperatures	127
<b>Figure 5.7.</b>	3D plot of volume showing its variation with $A_R$ and $S_R$ for (a) taper and (b) parabolic bars	128
<b>Figure 5.8.</b>	3D and contour plots of elastic limit temperature and plastic collapse temperature per unit volume with its variation with $A_R$ and $S_R$ for taper bars under (a1,a2) uniform, (b1,b2) linearly decreasing and (c1,c2) parabolically decreasing temperatures	129
<b>Figure 5.9.</b>	3D and contour plots of limit load factor ( $T_c/T_y$ ) showing its variation with $A_R$ and $S_R$ for a taper bar of $L=1.2$ m for (a) uniform, (b) linear and (c) parabolic temperature variations	130
<b>Figure 5.10.</b>	Plot of limit load factor ( $T_c/T_y$ ) variation with $A_R$ for different $S_R$ for a taper bar of $L=1.2$ m for (a) uniform, (b) linear and (c) parabolic temperature variations	131
<b>Figure 5.11.</b>	Waterfall plot and projections of stress fields at different temperatures for a taper bar of $A_R = 0.1$ and $S_R = 20$ , under (a) uniform, (b) linearly decreasing and (c) parabolically decreasing temperatures	132

<b>Figure 5.12.</b>	Plot of plastic front location variation with temperature for a taper bar of $A_R = 0.1$ and $S_R = 20$ , under (a) uniform, (b) linearly decreasing and (c) parabolically decreasing temperatures	133
<b>Figure 5.13.</b>	3D and contour plots of elastic limit temperature ( $T_y$ ) and plastic collapse temperature ( $T_c$ ) with its variation with $A_R$ and $S_R$ for parabolic bars under (a1,a2) uniform, (b1,b2) linearly decreasing and (c1,c2) parabolically decreasing temperatures	134
<b>Figure 5.14.</b>	3D and contour plots of elastic limit temperature and plastic collapse temperature per unit volume with its variation with $A_R$ and $S_R$ for parabolic bars under (a1,a2) uniform, (b1,b2) linearly decreasing and (c1,c2) parabolically decreasing temperatures	135
<b>Figure 5.15.</b>	3D and contour plots of limit load factor ( $T_c/T_y$ ) showing its variation with $A_R$ and $S_R$ for a parabolic bar under (a1,a2) uniform, (b1,b2) linear and (c1,c2) parabolic temperature variations	136
<b>Figure 5.16.</b>	Plot of limit load factor ( $T_c/T_y$ ) variation with $A_R$ for different $S_R$ for a parabolic bar of $L=1.2$ m for (a) uniform, (b) linear and (c) parabolic temperature variations	137
<b>Figure 5.17.</b>	Waterfall plot and projections of stress fields at different temperatures for a parabolic bar of $A_R = 0.1$ and $S_R = 20$ , under (a) uniform, (b) linearly decreasing and (c) parabolically decreasing temperatures	138
<b>Figure 5.18.</b>	Plot of plastic front location variation with temperature for a parabolic bar of $A_R = 0.1$ and $S_R = 20$ , under (a) uniform, (b) linearly decreasing and (c) parabolically decreasing temperatures	139
<b>Figure 5.19.</b>	Linear elastic and trilinear elasto-plastic behaviour (multilinear	140

with four segment material model)

- Figure 5.20.** 3D and contour plots of elastic limit temperature ( $T_y$ ) and plastic collapse temperature ( $T_c$ ) with its variation with  $A_R$  and  $S_R$  for clamped taper bar with multilinear material model under (a1,a2) uniform, (b1,b2) linearly decreasing and (c1,c2) parabolically decreasing temperatures 141
- Figure 5.21.** Waterfall plot and projections of stress fields at different temperatures for a taper bar of  $A_R = 0.1$  and  $S_R = 20$  for multilinear material model under (a) uniform, (b) linearly decreasing and (c) parabolically decreasing temperatures 142
- Figure 5.22.** Plot of variation in plastic front location variation with temperature for taper bar with multilinear material model under (a) uniform, (b) linearly decreasing and (c) parabolically decreasing temperatures 143
- Figure 5.23.** (a) Yield stress variation with temperature of mild steel, after Martinez (2016) and (b) Stress-strain plot for yield stress variation showing bilinear material behaviour 144
- Figure 5.24.** 3D and contour plots of elastic limit temperature ( $T_y$ ) and plastic collapse temperature ( $T_c$ ) with its variation with  $A_R$  and  $S_R$  for taper bars considering yield stress variation with temperature under (a1,a2) uniform, (b1,b2) linearly decreasing and (c1,c2) parabolically decreasing temperatures 145
- Figure 5.25.** Waterfall plot and projections of stress fields at different temperatures for a taper bar with yield stress variation of  $A_R = 0.1$  and  $S_R = 20$ , under (a) uniform, (b) linearly decreasing and (c) parabolically decreasing temperatures 146
- Figure 5.26.** Plot of variation in plastic front location variation with temperature for taper bar considering yield stress variation under (a) uniform, (b) linearly decreasing and (c) parabolically 147

	decreasing temperatures	
<b>Figure 5.27.</b>	Schematic bilinear stress-strain curve for the FGM	151
<b>Figure 5.28.</b>	Plots for ceramic volume fraction $V_c$ for six materials, FGM AI, FGM BI, FGM AII, FGM BII, FGM AIII and FGM BIII	153
<b>Figure 5.29.</b>	Normalized yield stress and elasticity modulus variation with temperature of mild steel, after Martinez (2016)	155
<b>Figure 5.30.</b>	Waterfall plot of stress fields at different temperatures for FGM taper bar of $A_R = 0.1$ and $S_R = 20$ , under (a) uniform, (b) linearly decreasing and (c) parabolically decreasing temperatures	156
<b>Figure 5.31.</b>	Plot of propagation of yield front location with increase in temperature for FGM taper bar of $A_R = 0.1$ and $S_R = 20$ , under (a) uniform, (b) linearly decreasing and (c) parabolically decreasing temperatures	157
<b>Figure 5.32.</b>	Plot of propagation of yield front location with increase in temperature for different $V_{c0}$ values for FGM taper bar under (a) uniform, (b) linearly decreasing and (c) parabolically decreasing temperatures	158
<b>Figure 5.33.</b>	Plot of propagation of yield front location with increase in temperature for different $n$ values for FGM taper bar under (a) uniform, (b) linearly decreasing and (c) parabolically decreasing temperatures	159
<b>Figure 5.34.</b>	Plot of propagation of yield front location with increase in temperature for FGM taper and parabolic bar under (a) uniform, (b) linearly decreasing and (c) parabolically decreasing temperatures	161
<b>Figure 5.35.</b>	Waterfall plot of stress fields at different temperatures for FGM taper bar of $A_R = 0.1$ and $S_R = 20$ , for multilinear material model under (a) uniform, (b) linearly decreasing and (c) parabolically decreasing temperatures	162

<b>Figure 5.36.</b>	Plot of propagation of yield front location with increase in temperature for FGM taper bar of $A_R = 0.1$ and $S_R = 20$ , for both the material models under (a) uniform, (b) linearly decreasing and (c) parabolically decreasing temperatures	163
<b>Figure 6.1.</b>	Plots for ceramic volume fraction $V_c$ for six materials, FGM AI, FGM BI, FGM AII, FGM BII, FGM AIII and FGM BIII	178
<b>Figure 6.2.</b>	Stress-strain plots at locations (a) $r=0.2\text{m}$ , (b) $r=0.3\text{ m}$ and (c) $r= 0.5\text{ m}$ for FGM AI	179
<b>Figure 6.3.</b>	Variation in material properties of the disk: (a) elasticity modulus, (b) tangent modulus and (c) yield stress	181
<b>Figure 6.4.</b>	Plot for temperature variation	181
<b>Figure 6.5.</b>	Normalized yield stress and elasticity modulus variation with temperature for mild steel (Seif et al. (2016))	182
<b>Figure 6.6.</b>	(a) Plastic limit speed ( $\omega_2$ ) versus ceramic distribution coefficient ( $n$ ) for two different ceramic volume fraction ( $V_{c0}$ ) values, (b) the disk geometry	183
<b>Figure 6.7.</b>	Validation of (a) radial and tangential stresses and (b) von-Mises stress	184
<b>Figure 6.8.</b>	Validation of total radial and tangential strains	184
<b>Figure 6.9.</b>	Waterfall plots of variation of von-Mises stress with rotational speed under linear temperature field for (a) uniform, (b) taper, (c) exponential and (d) parabolic disk geometries	186
<b>Figure 6.10.</b>	Plot of propagation of yield front with increase in rotational speed for (a) uniform, (b) taper, (c) exponential and (d) parabolic disk geometries, under linear temperature field	187
<b>Figure 6.11.</b>	Plot of propagation of yield front with increase in rotational speed with and without thermal loading for (a) uniform, (b) taper, (c) exponential and (d) parabolic disk geometries	188
<b>Figure 6.12.</b>	Plot of propagation of yield front with temperature for (a) uniform, (b) taper, (c) exponential and (d) parabolic disk	189



	geometries	
<b>Figure 6.13.</b>	Effect of material parameter $V_{c0}$ on propagation of yield front with increase in rotational speed for (a) uniform, (b) taper, (c) exponential and (d) parabolic disk geometries, while the disk is under linear temperature distribution	191
<b>Figure 6.14.</b>	Effect of material parameter $n$ on propagation of yield front with increase in rotational speed for (a) uniform, (b) taper, (c) exponential and (d) parabolic disk geometries, while the disk is under linear temperature distribution	192
<b>Figure 6.15.</b>	Waterfall plots of variation of von-Mises stress with rotational speed for uniform disk under (a) uniform, (b) linear, (c) exponential and (d) parabolic temperature distributions	193
<b>Figure 6.16.</b>	Yield front propagation with increase in rotational speed for uniform disk under (a) uniform, (b) linear, (c) exponential and (d) parabolic temperature distributions	194
<b>Figure 6.17.</b>	Waterfall plots of variation of von-Mises stress with rotational speed for trilinear material model for (a) uniform, (b) taper, (c) exponential and (d) parabolic disk geometries, while the disk is under linear temperature distribution	195
<b>Figure 6.18.</b>	Plot of propagation of yield front with increase in rotational speed for (a) uniform, (b) taper, (c) exponential and (d) parabolic disk geometries, for trilinear material model	196
<b>Figure 6.19.</b>	Plots of (a) radial and (b) tangential plastic strain at fully plastic speed for different geometries under linear temperature distribution for bilinear model	196
<b>Figure 6.20.</b>	Plots of (a) radial and (b) tangential plastic strain at fully plastic speed for different geometries under linear temperature distribution for trilinear model	197



## *List of Tables*

---

	<b>Page No</b>
<b>Table 3.1</b>	Disk geometry 55
<b>Table 4.1</b>	Validation of results on $F = 300800$ N for a clamped-clamped taper bar 103
<b>Table 4.2</b>	Graphical representation of clamped-clamped uniform taper bar 107
<b>Table 4.3</b>	Elastic and plastic limit loads for domain 1 and domain 2 of taper bar for two different geometries with bilinear material model (case A and B of Table 4.1) 108
<b>Table 4.4</b>	Elastic and plastic limit loads for domain 1 and domain 2 of taper bar for two different geometries with trilinear material model 114
<b>Table 5.1</b>	Validation of compressive stress for clamped linear taper bar 126
<b>Table 5.2</b>	Material properties of the FGM bar 153
<b>Table 5.3</b>	Material properties of the bar at different normalized coordinates for FGM AI 154
<b>Table 6.1</b>	Material properties of the FGM disk 178
<b>Table 6.2</b>	Material properties of the disk at different normalized coordinates for FGM AI 180
<b>Table 6.3</b>	Validation of stresses for FG ( $V_{c0} = 1$ and $n = 2$ ) disk subjected to thermo-mechanical loading 185



The present thesis investigates the elasto-plastic behaviour of axisymmetric bars and rotating disks subjected to mechanical and thermal loads. In case of bars, the loading is uniaxial and the problem is essentially one-dimensional. A one dimensional problem is attributed by the presence of one-dimensional fields, e.g., stress, strain, displacement, etc. In case of rotating disks, the loading is in-plane and the presence of radial and tangential stress field makes the problem two-dimensional. In this class also the basic problem is defined in terms of radial displacement field. Hence, the mathematical analysis of axisymmetric bar and disk problems are quite similar. In the present thesis problem, the material of construction is assumed to be of two types, (a) isotropic and homogeneous and (b) isotropic and functionally graded. The elastic analysis of bar and rotating disk is solved upto limit (yield) state using total minimum potential energy principle. The limit elastic study is then extended to post-elastic domain to investigate the effect of material non-linearity of the performance of the structures. The post-elastic investigation of axisymmetric bar and rotating disk is addressed using an extension and application of minimum potential energy principle in Hencky's total deformation theory of plasticity. In this case, the strain energy is computed from hydrostatic and deviatoric stress-strain components. The von-Mises yield criterion and its associated flow rule assuming linear strain hardening (bilinear) material behaviour is adopted for the present work. The study on the extension of the linear strain hardening model for multiple straight line segments is also carried out. The entire formulation for all the simulation studies of the present thesis work is displacement based and the unknown displacement field is approximated by finite linear combination of admissible orthogonal coordinate functions and unknown coefficients. The set of functions come from a suitably selected start function and the higher order orthogonal functions are generated numerically by using Gram Schmidt orthogonalization scheme. The solution algorithm is actualized with the assistance of MATLAB<sup>®</sup> computational simulation software.

The elasto-plastic analysis of statically indeterminate non-uniform bars subjected to concentrated axial load has been performed using an iterative variational method. The elasto-plastic behaviour of thermo-mechanically loaded non-uniform bars is also studied. The results obtained for these one dimensional problems are in good agreement with the available results and with the results generated by a known finite element package, Abaqus. Some of the results

presented for these problems showing the effect of geometry parameters like aspect ratio, slenderness ratio and the type of taperness.

In the present thesis, the effect of disk geometries and temperature distribution on the thermo elastic stresses and deformation states has been carried out. The effect of temperature on various material properties is also studied. Limit angular speed of the disks is calculated under thermo-mechanical loading and reported in dimensional form as limit peripheral speed and dimensionless form as normalized limit angular speed. The elasto-plastic analysis of FGM disk under thermo-mechanical loading is also addressed in the present work. The material of the FG disk is considered to be metal-ceramic composite with a continuous variation of volume fraction of metal and ceramic along the radial direction. The results obtained from the present numerical method have been compared with benchmark results and good agreement is observed establishing the validity of the proposed methodology. Some of the results presented for these problems are new of their kind and may serve as benchmarks for further study. It is believed that the outcome of the present simulation embodied in the thesis will be helpful for both industrial design development and academic point of view.

## **INTRODUCTION**

### **1.1 Objectives of the study**

Axisymmetric objects belong to the class of solids of revolutions which are loaded symmetrically. Both the objects (bar and rotating disk) are axisymmetric. In case of bars, because the length is much greater than its other two dimensions and the loading is uniaxial, the problem is essentially one-dimensional, attributed by the presence of one-dimensional stress field while the loading is in-plane in case of rotating disks. Presence of radial and tangential stress field makes rotating disk, a two-dimensional problem. In this class, the basic problem is defined in terms of radial displacement field. These objects find vast applications in various engineering applications such as in steam and gas turbine rotors, turbo generators, turbojet engines, centrifugal compressors, components like gears, flywheels, etc. and various other branches of mechanical, civil and aeronautical engineering. A few of the important fields of application of the commercially used axisymmetric objects used in industries, machineries, automobiles and aeronautical structures are shown in Figures 1.1(a-d).

Analysis and design of these axisymmetric structures is therefore of continuing interest to the scientific and engineering communities. Accurate and conservative assessments of maximum load carried away by the structure, as well as the equilibrium path in both elastic and inelastic range are therefore of paramount importance in understanding the integrity of the structure. Determination of the equilibrium path in the elastic and inelastic range usually involves a complex analysis. Although elasticity and plasticity theories have found vast applications in engineering problems over the last few decades, there still exist certain cases where a rigorous solution cannot be obtained and approximate methods have to be applied. Or for that matter even if analytical solutions are obtained by applying classical theories of elasticity and plasticity, approximate methods are observed to provide equally efficient solutions with the added power of tackling those problems for many additional complicating effects. The objective of this thesis work is to determine the displacement field and stress distribution of axisymmetric structures in elasto-plastic domain using variational method. The usefulness of the method has been successfully adopted in solving various practical complexities associated with bar and rotating disk applications.



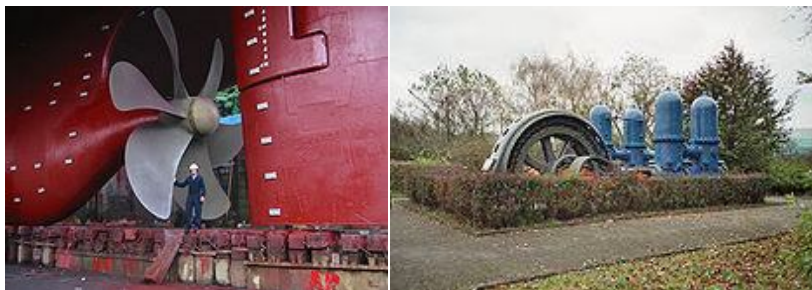
a. Rotating disks used as hydraulic and pneumatic impellers



b. Rotating disks used as transmission elements in various machineries



c. Axial members: cables of Mackinaw bridge, struts in aircraft engine mounts and hydraulic cylinders in a dump truck



d. Ship propeller and electrically driven pump

**Figure 1.1.** Applications of axisymmetric bars and rotating disks.



The present thesis employs an energy based variational approach for the analysis of the problems. The governing set of equations is obtained by the application of suitable variational principles to the energy functionals, derived conforming to the system under consideration. The entire formulation for all the simulation studies is displacement based and the unknown displacement field is approximated by finite linear combination of admissible orthogonal coordinate functions and unknown coefficients. The set of functions come from a suitably selected start function and the higher order orthogonal functions are generated numerically by using Gram Schmidt scheme.

Elasto-plastic analysis has important applications in physics and engineering design. It is important to consider the elasto-plastic behaviour of solid slender bars for the assessment of ultimate load carrying capacity. For a designer apart from elastic limit load of bars at which yielding initiates, another important parameter is the plastic collapse load of bars at which the entire bar has undergone yielding. The yield front propagation of statically indeterminate non-uniform bars has been carried out in the present thesis.

The extension and application of minimum potential energy principle in Hencky's deformation theory of plasticity based on von-Mises yield criterion and for linear strain hardening behaviour is adopted for mathematical formulation. Both determinate and indeterminate problems have been considered. For determinate problems domain decomposition method has been established and to overcome its insufficiency for indeterminate problems, an iterative variational method has been proposed successfully. The effect of geometry parameters like aspect ratio, slenderness ratio and the type of taperness on the post-elastic performance of the bar is also investigated.

Some particular applications of clamped-clamped bars involves thermal loading due to thermal expansion of the bars. Thermo-mechanically loaded bars are used extensively in industry as an extended surface or a fin that find numerous applications in compact heat exchangers, specialized installations of single and double pipe heat exchangers, etc. It is a well-known fact that the temperature gradient is higher at the base and gradually decreases towards the fin tip and this can be achieved with functional grading of material to take the advantage of excellent thermal performance of ceramics with the toughness of metals. This gave way to the idea of gradient-based varying of microstructure from one material to another material. This transition is usually based on power series. Investigation of the elasto-plastic behaviour of clamped-clamped

non-uniform bars under thermo-mechanical loading has been carried out by using numerical technique based on variational principle following von-Mises yield criterion and deformation theory of plasticity. This analysis is undertaken for both the material models: bilinear and multilinear. The temperatures corresponding to onset of yielding and total collapse are considered as markers of yield limit and collapse loads. The effect of geometry parameters, material parameters and nature of thermal load on limit temperature and stress distribution is investigated.

Estimation of stress and deformation of disk at high rotational speeds have been a subject of longstanding attention to many a researcher. The most important design parameter of a rotating disk is its operating range of angular speed. It is important to estimate the angular speed and the stress distribution of a rotating disk in fully plastic state in order to achieve an optimal structural design. The limiting speed being earmarked by initiation of yielding in the disk is termed as elastic limit speed. If the rotational speed of the disk is increased beyond limit angular, yield region expands from its initiation location and at a particular speed the entire disk comes into plastic regime. This particular speed is termed as plastic limit speed or collapse speed.

The stress and deformation state of rotating disks under thermo-mechanical loading is investigated both in the elastic and elasto-plastic range of the disk material. For elastic analysis of rotating disks, the governing equation for the system is obtained by applying the minimum potential energy principle. The effect of temperature field on material properties is studied. The influence of disk geometry and temperature field variation on the performance of rotating disks is considered in the present work and the effect on elastic limit angular speed is investigated.

Rotating disk when subjected to thermal load results in a disk of variable material properties. Mechanical design of disks involves the evaluation of centrifugal and thermal stresses and they need to be designed for approximate uniform stress distributions. Optimization of the design of a rotating disk and assessment of failure risk requires understanding its behaviour in the post-elastic domain. In this context, it is reported in various numerical and analytical works to predict the deformation, stress and strain fields and failure of a uniform rotating disk under different loading conditions. The stress field in a uniform rotating disk under elastic or elasto-plastic loading condition is not uniform and maximum resultant stresses occurs near the axis of rotation. The non-uniform stress distribution is a key barrier in designing the optimized disk with enhanced performance (e.g., uniform stress distribution, minimum weight design, maximum

stored energy, etc.). This phenomenon gave birth to the idea of varying the thickness of the rotating disk along its radius to make the stress distribution near-uniform. In the present work the effect of geometry variation on disk performance is considered for four types of geometry variation, namely, uniform, taper, exponential and parabolic.

Functionally graded structures are those in which the volume fractions of two or more materials are varied continuously as a function of position along certain dimension(s) of the structure (Reddy (2000) and Suresh and Mortensen (1998)) to achieve a required function. These materials are mainly constructed to operate under high temperature conditions. In recent years, the use of FGM increases due to their functional gradation for optimal design. In a turbine rotor, there is always a possibility that the heat from the external surface transmits to the shaft and from it to the bearings causing adverse effects on its functioning and efficiency. To deal with this situation and prevent heat from being transferred to the shaft and bearings, the disk can be made of FGM with ceramic rich at the outer surface and metal-rich at the inner surface. While the heat resistant property of the ceramic at the outer surface prevents heat from being transferred, the metal at the inner surface helps carry the stress for the transmission of torque from the disk to the shaft. However, for some specific applications such as in aerospace engineering where the component's weight and durability in high temperature environment are so crucial, the components need to be fabricated using special material such as a functionally graded material (FGM). FGMs are usually made of a mixture of ceramic and metals. The ceramic constituent of the material provides the high temperature resistance due to its low thermal conductivity. The ductile metal constituent, on the other hand, prevents fracture caused by stress due to high temperature gradient in a very short period of time. The elasto-plastic analysis of FGM disk under thermo-mechanical loading is addressed in the present work. The material of the FG disk is considered to be metal-ceramic composite with a continuous variation of volume fraction of metal and ceramic along the radial direction. The effect of geometry variations, temperature distributions and variation of material properties on limit speeds of rotating FG disk is investigated. The study on limit temperatures for different disk geometries under different temperature field distributions has also been carried out.

## 1.2 Introduction to material models

In earlier years, mechanical designs were based on linear models to easier the analysis and computational cost. In fact the linear assumptions are only valid in certain conditions for example, small strains, small displacements, small rotations, small changes in temperature, and so on. Such linear analysis provides an acceptable approximation of real-life characteristics for most problems design engineers encounter. Nevertheless, occasionally more challenging problems arise, problems that call for a nonlinear approach. The need for non-linear analysis has increased in recent years due to the need for use of optimized structures, use of new materials, addressing safety related issues of structures, etc. This has been possible due to the advent of powerful desktop computers and availability of improved non-linear solution algorithms and is required to make realistic predictions regarding the non-linear behaviour of mechanical systems. Material nonlinearities occur in solid mechanics due to nonlinear relationship between stress and strain. Material nonlinearity includes the non-linear behaviour of a material based on current deformation, deformation history, temperature, etc. Generally two types of non-linear material behaviours are encountered in mechanical structures namely rate independent and rate dependent. Rate independent refer to the case of material nonlinearity which is assumed to be time independent whereas rate dependent is the case of time dependent material nonlinearity. Post-elastic analysis of structural elements can have any one of the material nonlinearities or both of them depending upon the nature of the problem. Elasto-plastic analysis is an important area of research for solving various practical complexities associated with the structural elements applications.

### 1.2.1 Yield (Failure) criteria

A yield criterion describes a material failure in the phenomenon of plasticity. The adoption of proper yield criteria in the structural design is very important as the estimated load-bearing ability of structures is significantly affected by the choice of different yield criteria. Experimental uniaxial tension tests determine the mechanical properties of structural materials. Thus, when considering structures subjected to load, the allowable stress on which the design is based is taken as some fraction of the yield or ultimate stress obtained from these simple tension tests. Various theories of failure have been established to determine the allowable design stresses

for multi-axial stress condition. Failure refers to either yielding (ductile failure) or fracture (brittle failure) of the material. The failure can be in brittle or ductile manner or both depend on the conditions such as temperature, state of stress, loading rate, etc. However, for most practical situations, a material may be classified as either brittle or ductile. In case of ductile materials, yielding occurs first, whereas for brittle materials ultimate stress is considered as the basis of failure theories. There are two established yield criteria for ductile materials at present are Tresca's and von-Mises yield criteria. The present study is based on von-Mises yield criteria according to which total strain energy in a body can be resolved into two parts: one associated with the change in volume and the other with the distortion or change in shape. The strain energy of distortion is attributable to the yielding. The general condition of yielding based on the distortion energy theory is given by  $(\sigma_1 - \sigma_2)^2 + (\sigma_2 - \sigma_3)^2 + (\sigma_3 - \sigma_1)^2 = 2\sigma_y^2$ , where  $\sigma_1, \sigma_2, \sigma_3$  are the principal stresses. This theory explains that the phenomenon of yielding of materials is independent of hydrostatic pressure.

The solution of elastic-plastic problems using Tresca's yield criterion needs separate treatment in each region due to different forms of the yield criterion in different parts of the plastic zone. In particular, in the case when a plastic region expands over a plastically predeformed region the task becomes quite cumbersome. On the other hand, a single formulation has to be carried out for the whole plastic region in the case of the von Mises yield criterion. Due to the nonlinearity involved in the use of von Mises yield criterion, the analysis is essentially numerical.

### 1.2.2 Post-elastic behaviour

Plasticity is a class of material nonlinearity which is characterized by an irreversible straining which is not time dependent and which can only be sustained once a certain level of stress has been reached (Owen and Hinton (1980)). Plastic deformation is essentially irreversible on unloading and is incompressible in nature. The onset of plastic deformation (or yielding) is governed by a yield criterion and post-yield deformation generally occurs at a greatly reduced material stiffness.

If uniaxial behaviour of a material is considered, the exhibition of non-linear elastic or plastic behaviour can be determined by the non-linear relationship of stress-strain only, it is

determined by unloading part of the curve. The elastic material follows the same path in loading and unloading while the plastic materials shows path dependent on unloading and the solution relies upon the loading history of the plasticity problem. The formulation of elasto-plastic deformation model covers the following fundamental points:

- An explicit description between stress and strain must be formulated to describe material behaviour under elastic conditions, i.e., before the onset of plastic deformation.
- A yield criterion to define specific stress combinations that will initiate the non-elastic response to define initial yield surface.
- After initiation of yielding, two general categories that relate the plastic stress and strain: flow theory of plasticity and deformation theory of plasticity.
- A hardening rule that predicts the change in the yield surface with the progression of plastic deformation. A stress-strain relationship must be developed for post-yield behaviour, i.e. when the deformation is made up of both elastic and plastic components.

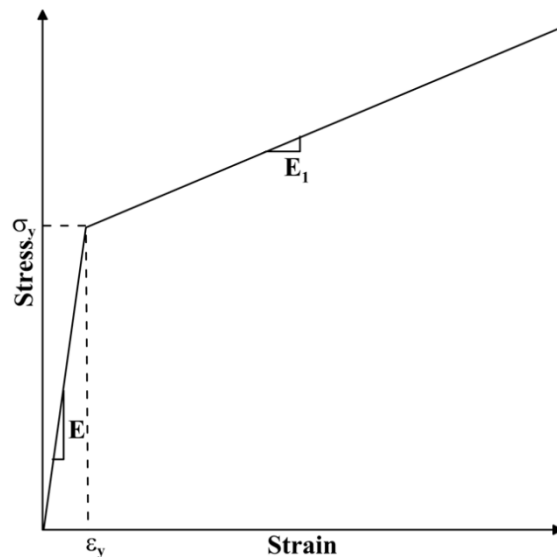


**Figure 1.2.** Linear elastic and linear strain hardening elasto-plastic behaviour.

An important phenomenon governing the plastic behaviour of a material is the strain-hardening or work-hardening. The phenomenon occurs after initial yielding when the stress level

at which further plastic deformation arises may be dependent on the current degree of plastic straining. It is necessary to idealize the stress-strain behaviour of materials in order to obtain solution of a deformation problem. There are various types of elasto-plastic models such as elastic-perfectly plastic, elastic-linearly work-hardening, elastic-non-linear hardening, Ramberg-Osgood, etc. The present thesis considers linear elastic and linear strain hardening elasto-plastic material behaviour as shown in Figure 1.2, where the gradient in the elastic region with elasticity modulus  $E$  and the gradient in the plastic region with tangent modulus  $E_t$ .  $\sigma_y$  and  $\varepsilon_y$  are the yield stress and yield strain of the material respectively. The study on the extension of the linear strain hardening model for multiple straight line segments is also carried out. The more line segments that exist, the better the measured stress-strain behaviour can be modelled.

### 1.2.3 Functionally graded materials

The idea of FGMs, i.e., functionally graded material was at first presented by Japanese researchers in the mid-1980s (Yamanouchi et al. (1990)), as high temperature resistant materials for various engineering applications such as fusion reactors and chemical plants, aircraft components, space vehicles and various other branches of mechanical, electrical and civil engineering. The mixture of metal and ceramic in FGM with desirable volume fractions gives continuous variation of mechanical and physical properties in the desired direction. Due to excellent characteristics of ceramics to resist severe environmental effect, such as high temperature, wear, and corrosion in combination with the toughness of metals acquire FGM structures which can withstand extensive mechanical loadings under high temperature conditions.

The continuous change in the microstructure of functionally graded materials (FGMs) distinguish them from the fiber-reinforced laminated composite materials, which have a mismatch of mechanical properties across an interface due to two discrete materials bonded together. As a result, the constituents of the fiber-matrix composites are prone to debonding at extremely high thermal loading. Further, cracks are likely to initiate at the interfaces and grow into weaker material sections. Additional problems include the presence of residual stresses due to the difference in coefficients of thermal expansion of the fiber and matrix in the composite materials.

Many theoretical research works on FGMs for engineering structures have been significantly increased in the last few decades which found uses in electrical devices, energy transformation, biomedical engineering, optics, etc. (Suresh and Mortensen (1998)). (Suresh and Mortensen (1998)) also provided some introduction about the fundamentals of FGMs. For other applications, FGMs can be used for a variety of potential applications in transport systems, energy conversion systems, cutting tools, machine parts, semiconductors, optics, biosystems, etc. Different potential applications require different key issues. For example, in aerospace and nuclear energy applications, the key issue is reliability rather than cost. Hence, FGMs used in these applications could be produced from a high quality of material constituents in order to have the combinations of incompatible functions such as refractoriness with toughness or chemical inertness with toughness. On the other hand, for applications of cutting and engine components, the main issue is to use FGMs to satisfy the cost/performance ratio reliability. The requirements of FGMs for these applications are wear, heat, and corrosive resistances as well as high strength of the materials. From a mechanics viewpoint, the main advantages of material property grading appear to be improved toughness, wear and corrosion resistance, and reduced residual and thermal stresses.

### **1.3 Thermal effect**

Thermal effects due to change in temperature are very important for predicting stresses and strains in a structure. Most of the mechanical structures are subjected to temperature variation. Temperature variation causes expansion or contraction of the structural material. The change in temperature makes material to expand and if this expansion is restrained, stresses are induced which affect expected performance of structure. In restrained condition, very large force is generated and its ignorance can lead to unsafe design. When structure is subjected to high temperature, it results in reduction in stiffness and strength which significantly affects the structural performance. Moreover, exposure of structures to high temperature is an extreme condition leads to change in material properties and consequently change in overall behaviour.



### **1.3.1 Thermal parameters**

Thermal properties are characteristics of materials defining the substance and its relation to temperature. To understand the change of materials performance under high temperature conditions, material properties such as thermal expansion, density and thermal conductivity needs to be evaluated. The effect of temperature on the material properties of steel is an important factor taken into account for the assessment of performance resistance of steel at high temperatures. In the case of steel, in particular, the yield strength and modulus of elasticity are strongly influenced by temperature increase.

To overcome some of the problems of durability and steel corrosion, advances in recent years led to the development of fiber-reinforced composite materials. Composites offer several advantages such as improved strength, stiffness, impact resistance, thermal conductivity and corrosion resistance. These composite materials are ideal and cost effective for structural applications where high strength to weight and stiffness to weight ratios are needed such as in aircraft and spacecraft structures. However, these composites can sustain low temperatures which introduce large residual stresses because of the mismatch of the thermal expansion coefficients between the fiber and the matrix. Micro cracks are likely to develop at the interfaces leads to debonding of composites subjected to high thermal loading. These problems are avoided by the development of functionally graded materials where the volume fraction of constituents is gradually varied across an interface as discussed in the previous section. Thus a new material concept of FGMs emerged and led to the development of superior heat resistant materials. Such materials withstand severe thermo mechanical loadings. FGMs are considered as a potential structural material for future high-speed aircraft and power generation industries.

### **1.3.2 Thermal stress**

The evaluation of thermal stresses in structures subjected to thermal loading is an important part of structural analysis. Structures such as heat exchangers, jet engine turbine blades, supersonic aircraft and missiles, or space structures should be designed to withstand thermal loading. The thermal loading can have a large number of effects on structures ranging from induced thermal strain to accelerated viscoelasticity and plasticity. Thermal stresses are induced by three main sources: (i) non-uniform temperature distributions that create non-uniform strains within a structure, (ii) external constraints that prevent the free deformation of a structure,

and (iii) differences in coefficients of thermal expansion that appear in heterogeneous structures. Two important aspects of thermal deformations must be emphasized. First, thermal strains are purely extensional: temperature changes induce no shear strains. Second, thermal strains do not generate any internal stresses, in contrast with mechanical strains that are related to internal stresses through the material constitutive law. Consequently, an unconfined material sample subjected to a uniform temperature change simply expands, but no internal stresses are developed.

Most situations in real structures under temperature field variation have a complex mix of mechanical strains due to applied loading and mechanical strains due to restrained thermal expansion. The behaviour of structures when subjected to thermal effects is governed by the fundamental relationship  $\varepsilon_{\text{total}} = \varepsilon_{\text{thermal}} + \varepsilon_{\text{mechanical}}$ . The deformed shape of the structure is governed by the total strains through compatibility conditions. The state of stress (elastic or plastic) of the structure depends only on the mechanical strains. When the thermal strains are free to develop in an unrestricted manner and there are no external loads, axial expansion results from  $\varepsilon_{\text{total}} = \varepsilon_{\text{thermal}}$ , whereas when the thermal strains are fully restrained without external loads, thermal stresses result from  $\varepsilon_{\text{thermal}} + \varepsilon_{\text{mechanical}} = 0$ .

## 1.4 Method of analysis

In the present work, approximate solution for stress and deformation of axisymmetric problems is obtained through variational principles and the governing equations are obtained by applying suitable variational principles to the corresponding energy functional of the system. Once the governing equations are obtained, approximate solution method is employed to get the solution of the problem. The present formulation is based on displacement fields of the system and so appropriate stress-strain and strain displacement relationships are employed to reduce the energy functional in terms of displacement fields of the system.

Most widely used variational method in structural mechanics using which the governing equations of the system are obtained from the energy functional is the method of virtual work. It states that a body is in equilibrium if the internal virtual work equals the external virtual work for every kinematically admissible displacement field. The principle of minimum total potential energy is another specific form of principle of virtual work. It states that for conservative

systems, of all the kinematically admissible displacement fields, those corresponding to equilibrium extremize the total potential energy and if the extremum condition is minimum, the equilibrium state is stable. Kinematically admissible displacements are those that satisfy the single-valued nature of displacements (compatibility) and the boundary conditions. The total potential energy ( $\Pi$ ) of a body is defined as the sum of total strain energy ( $U$ ) and the work potential ( $V$ ), i.e.  $\Pi = U + V$ . According to minimum total potential energy principle, the equilibrium condition of the system is obtained by letting  $\delta(\Pi) = 0$ , where  $\delta$  is the variational operator.

Various approximate methods are used in axisymmetric problems to obtain the approximate solution of the governing equations obtained through the application of variational principles to suitably formed energy functional as discussed above. Most widely used among them are the Rayleigh-Ritz method and the Galerkin method. In approximate method, the unknown field ( $u$ ) is approximated by finite linear combinations of admissible coordinate functions ( $\phi_i$ ) and unknown coefficients ( $c_i$ ) as  $u(\xi) \cong \sum c_i \phi_i$ . The approximated field is substituted in the governing equations and the variational operation at this stage gives rise to simultaneous algebraic equations. These sets of equations are expressed in matrix form as  $[K]\{c\} = \{f\}$ , where the vector  $\{c\}$  represents the unknown coefficients  $c_i$ . The terms associated with the unknown coefficients form the stiffness matrix  $[K]$  of the system and the right hand side forms the load vector  $\{f\}$ . The stiffness matrix may be linear or nonlinear depending on the problem. Solution of this algebraic set of equations gives the values of the coefficients which in turn give the unknown field.

Galerkin method is a weighted residual method in which the approximate displacement field is assumed as mentioned in the previous paragraph. When this assumed solution is substituted in the governing equation, an error is induced called the residual ( $\varepsilon$ ). This method minimizes this residual by using the coordinate functions as the weight functions. If the set of functions  $\phi_i$  comes from an orthogonal set, the solution becomes simpler and to this end, Gram Schmidt orthogonalization scheme is used. The higher order functions are generated through a numerical implementation of the Gram Schmidt orthogonalization scheme. To cater to the need of the numerical scheme, all the functions are defined numerically at some suitably selected

gauss points. For the present thesis, the weight function is chosen as unity and the interval is from 0 to 1.

The post-elastic behaviour of the axisymmetric problems is investigated on the basis of von-Mises yield criterion, its associated flow rule assuming linear strain behaviour. The post-elastic formulation is based on Hencky's Total Deformation Theory of Plasticity. A yield criterion is a hypothesis concerning the limit of elasticity under any possible combination of stresses. Generally mechanical properties are obtained by simple tension test, where the specimen is axially loaded in tension. The relationship between the strength of a mechanical component subjected to a complex state of stress and the mechanical properties of the simple tension test is obtained by theories of failure which in turn set the yield criterion. In the present thesis, von-Mises yield criterion is used which states that failure of mechanical component subjected to multi-axial stresses occurs when the strain energy of distortion per unit volume in the component becomes equal to the strain energy of distortion per unit volume in a standard tension test specimen when yielding starts.

The flow rule specifies the increment of plastic strain once the material has yielded. The total strain increment  $d\varepsilon$  is given as follows,  $d\varepsilon = d\varepsilon_{ij}^e + d\varepsilon_{ij}^p$ . Here the elastic part is obtained using Hooke's law while the plastic part of strain increment is given by  $d\varepsilon_{ij}^p = d\lambda \sigma'_{ij}$ . This equation is based on flow theory of plasticity (Kachanov (1971)), where the flow rule describes the increment of plastic strain when yielding occurs and at each load step the strain increments are calculated. However there exists another theory known as Hencky's total deformation theory of plasticity (Kachanov (1971)), which expresses the total and plastic strain components as  $\varepsilon = \varepsilon_{ij}^e + \varepsilon_{ij}^p$  and  $\varepsilon_{ij}^p = d\lambda \sigma'_{ij}$ . According to total deformation theory of plasticity, the final state of stress at a given loading is independent of the stress-strain path during the loading. Hence the components of total plastic strain are proportional to the corresponding deviatoric stress components. In situations where loading is continuous, Hencky's equations lead to results in good agreement with the observations. Furthermore, due to the advantages of mathematical convenience, Hencky's relations are used in applications where strains are small.

Under plastic deformation, the plastic strain increment may be written as  $d\varepsilon_{ij}^p = d\lambda \frac{\partial(G)}{\partial\sigma_{ij}}$ ,

where 'G' is the plastic potential. If the plastic potential is substituted by yield function then the

plastic strain increment is proportional to the gradient of the yield surface and is, therefore, normal to the yield surface. This is usually referred to as the normality condition. A flow rule obeying the normality condition is referred to as an associated flow rule. In the present work, ‘ $G$ ’ is replaced by von-Mises yield criterion and hence the investigation is said to be carried out under von-Mises yield criterion and its associated flow rule.

## **1.5 Layout of the thesis**

In the present work, the effect of thermal loading on post-elastic behaviour of axisymmetric objects has been studied. Bars and disks of various types of axisymmetric geometry are considered. The material of construction is assumed to be of two types, (a) isotropic and homogeneous and (b) isotropic and functionally graded. Effect of thermal loading is first observed in elastic domain of the material and then the effect is studied in post-elastic domain as well. A brief layout of the thesis is given below.

Chapter one introduces the subject matter of the proposed work through a brief discussion of thesis objectives. In this chapter, a concise discussion on various applications of axisymmetric bars and rotating disks is provided and an understanding of the mathematics and numerical techniques involved in the analysis is introduced.

In chapter two, an exhaustive literature survey in the proposed area of research is carried out and presented which lead to the identification of the present scope of work. The literature review focuses mostly on the topics that are useful and relevant to this research. However, many other complicated effects and associated problems are also reviewed and presented.

The limit elastic analysis of rotating disks is presented in chapter three. The objective of this analysis is to determine the stress and deformation states in a rotating disk under thermo-mechanical loading. The analysis is accomplished for different disk geometries as well as temperature distribution profiles. Results on limit elastic behaviour of solid and annular disks of varying geometry under centrifugal, thermal and thermo-mechanical loadings are validated and reported. The effect of disk geometry and temperature field variation on the performance of rotating disks is considered and normalized value of limit angular speed is furnished. The effects of temperature field on material properties are also reported.

Chapter four introduces the mathematical formulation to investigate the growth of elastic-plastic front of a statically indeterminate non-uniform bar in post-elastic regime. In this chapter,

the extension and application of minimum potential energy principle in Hencky's deformation theory of plasticity based on von-Mises yield criterion and for linear strain hardening behaviour. An iterative variational method using domain decomposition method is introduced to overcome the insufficiency of domain decomposition method for indeterminate problems. The effect of geometry parameters like aspect ratio, slenderness ratio and the type of taperness on the post-elastic performance of the bar is investigated and the relevant results are obtained in dimensionless form.

The fifth chapter deals with the investigation of growth of yield front of a thermo-mechanically loaded non-uniform bar with clamped ends in post-elastic domain. Uniform, linear and parabolic types of temperature distribution over the length of the bar are considered. The yield limit temperature and plastic collapse temperature are studied. The temperatures and limit load factors for different bar geometries and temperature distributions are reported. The results are presented showing the effect of geometry parameters and the nature of thermal load on the thermo-elasto-plastic deformation of clamped bar.

Chapter six presents the elasto-plastic analysis of functionally graded disks under thermo-mechanical loading using variational principle. The material of the FG disk is considered to be metal-ceramic composite with a continuous variation of volume fraction of metal and ceramic along the radial direction. The effect of geometry variation, variation of material properties and variations in temperature distribution field are reported. Results are presented for the initiation of yield front and its growth with increase in rotational speed and temperature.

Chapter seven draws the conclusions of the present thesis work and provides the future work related to this research for future development and investigation.

Finally, the list of research works and books cited in the thesis are provided.

## **LITERATURE REVIEW**

### **2.1 Introduction**

Different researchers have carried out various theoretical and experimental studies to investigate the elasto-plastic analysis of structural elements. The accounts of literatures are presented only for axisymmetric structural elements namely, bars and rotating disks. The materials of construction of the axisymmetric objects are found to be of various types and they are focused in a separate section. A section is also dedicated for elastic and post elastic behaviour of a particular material type. The type of loading, considered in the present research work, mainly comes from two different sources: thermal loading and centrifugal loading. However in literature review, various types of loading are also addressed in a separate section. Static analysis of bars and rotating disks provides many fronts in which research is carried out unidirectionally. Host of other research work exists taking the combinations of these complicating effects as well, the other related peripheral literatures are also considered for completeness. A host of research work aimed at the dynamic behavior of bars and rotating disks, but such literatures are not included in the scope of this review. The following sections briefly describe various literatures available related to research work on bars and rotating disks which are relevant and useful for further investigation of this research.

### **2.2 Analysis of bar problems**

Slender bars are often encountered in various structures which are used mainly to take up axial load. Bars may be subjected to tensile or compressive loadings of various forms such as externally applied surface forces, body force due to gravity, impact loadings etc. The simple analytical solution of the problem available in textbook are valid for uniform cross-section bar but the non-linearity associated with the study of stresses in elastic-plastic regimes is complicated. However, due to the advancement and efficiency of computational machines during the last two decades, the study of non-linearity associated with the study of stresses in elasto-plastic regimes becomes easier.

### 2.2.1 Elasto-plastic analysis of isotropic bars

Theoretical investigation of elastic-plastic behaviour of solid slender bars of various types of geometry as well as loading is a relevant area of work for the designers (Kachanov (1971); Hill (1950); Chakrabarty (1987); Johnson and Mellor (1962)). The load deflection behaviour of a uniform bar under body force loading in the post-elastic region is found in the textbook of Owen and Hinton (1980) as an example problem. Reddy (2005) had dealt with the same problem in greater detail, based on finite element method. Kim et al. (2006) performed fully plastic analyses for notched bars and plates through finite element limit analysis, based on nonhardening plasticity behaviour to determine the plastic limit loads and stress fields. Gang et al. (2003) carried out integrity assessment of defective pipelines by using an iterative algorithm for the kinematic limit analysis of rigid perfectly plastic bodies. The effects of various shapes and sizes of part on the plastic collapse of pipelines under internal pressure, bending moment and axial force had been investigated.

Yankelevsky (1999) analyzed the elasto-plastic behaviour of a shallow two bar truss under tension or compression loading, as well as for reversal loading, to correlate the external work to the central displacement and follow the elasto-plastic stresses and strains in the bars along the loading history. Auciello (2001) used both Rayleigh-Ritz and Lagrangian approach to consider the upper and lower bounds for free vibration frequencies of axially-loaded slender beams. Non-linear dynamics of a pin-ended elasto-plastic beam with both kinematic and isotropic hardening had been discussed by Savi and Pacheco (2001) using an iterative numerical procedure and the results indicated the practical problems in predicting the response of the beam. Genna and Symonds (1998) studied the effects of slenderness ratio and damping on dynamic plastic instabilities for certain fixed-pin supported beams, deformed plastically by a transverse pressure.

Abdalla et al. (2007) presented a simplified technique to determine the shakedown limit load of a structure using finite element method and it was applied and verified by using two bench mark shakedown problems. Problem of two-bar structure subjected to constant axial force and cyclic thermal loading, and the three cylinders subjected to constant internal pressure and cyclic high temperature variation had been solved analytically. In a subsequent work, Abdalla et al. (2011) further developed a simplified technique to handle cyclic biaxial loading resulting in multi-axial states of stress within the large square plate with a small central hole problem. In this



study, two material models were adopted: an elastic-linear strain hardening material model and an elastic-perfectly-plastic (EPP) material model. The dynamic behavior of non-uniform taper bars in post-elastic regime has been addressed by Das et al. (2009a, b) where loading was controlled statically to take the bar to its post-elastic state so as to predict its dynamic behavior in the presence of plastic deformation. Kolodziej and Gorzelanczyk (2012) analyzed both elastic and elasto-plastic torsion of prismatic bars by means of the Picard iteration. The analysis was based on Saint-Venant displacement assumption and Hencky's deformation theory of plasticity. Mukhtar and Al-Gahtani (2016) used a well-known meshless method, radial basis functions to solve the torsion of a prismatic bar having a rectangular/square cross-section. Biondi and Caddemi (2007) provided closed form solutions for multiple singularities in the flexural stiffness of clamped-clamped beam by making use of distributions such as unit step and Dirac's delta functions. The authors proposed an integration procedure that leads to closed form solutions, dependent on boundary conditions only and independent of continuity conditions along the beam span. Ghuku and Saha (2016) introduced a semi-analytical solution method using domain decomposition technique for elastic solution of statically indeterminate bar problem.

Dwivedi et al. (2002) reported springback analysis of thin rectangular bars with non-linear work hardening using finite difference method. Tayyar (2016) presented a curvature based kinematic displacement theory (KDT) for elasto-plastic finite strain solution of cantilever beams under a uniform moment distribution. In KDT, deflection is generated without assuming geometry and using differential equations of the deflection curve. Lal et al. (2017) carried out the springback analysis of hollow rectangular bars with linear work-hardening materials using deformation theory of plasticity. In this study, the elastic-plastic boundary was determined by using deformation theory of plasticity. Canales and Mantari (2017) studied the vibrational analysis of taper bars under uniform axial loading in post-elastic regime by considering shear deformation and rotary inertia. In this work, the Timoshenko beam theory and the dynamic version of the principle of virtual work are used to derive the eigenvalue problem. Vaz-Romero et al. (2016) conducted dynamic tensile tests and presented results on dynamic neck evolution in steel bars of varying diameters ranging from 1.5 mm to 4 mm. The authors also investigated this behaviour by using two different kinds of numerical calculations: (i) axisymmetric finite element simulations and (ii) one dimensional finite difference computations.

### 2.2.2 Elasto-plastic analysis of composites and FGM bars

Many materials are known to exhibit different behaviour when subjected to compressive and tensile loading. The continuous effort of engineers to design efficient materials which must be as light and economic as possible yet strong enough to withstand the most demanding functional requirements arising during their service life gave birth to a new class of materials; the functionally graded material (FGM). In material science the FGM is a non-homogeneous composite which performs as a single-phase material, by unifying the best properties of its constituent phase materials. FGMs are deemed to have an advantageous behavior over laminated composites due to the continuous variation of their material properties yet in all three dimensions which alleviate delamination, de-bonding and matrix cracking initiation issues. Functionally graded materials were developed for making engineering components which are subjected to mechanical loads under high temperature environment.

An approximate solution for homogeneous anisotropic bars was introduced in Martynovich and Martynovich (1984), reducing the problem to the solution of a Fredholm integral equation of the second kind with a regular kernel. Realistic engineering problems are solved by numerical techniques. The finite difference methods was used for both non-homogeneous and compound prismatic bars with simply and multiply connected boundaries by Ely and Zienkiewicz (1960). Katsikadelis and Sapountzakis (1985) presented boundary element method for the solution of torsion problem of composite cylindrical bars. The authors formulated the problem in terms of terms of torsion function by solving Neumann-type boundary value problem. Horgan and Chan (1999) investigated the effects of material inhomogeneity on the torsion response of linearly elastic isotropic bars. In this analysis, optimal upper and lower bounds for the torsional rigidity for non-homogeneous bars of arbitrary cross-section were established. Horgan (2007) investigated the torsion problem for inhomogeneous anisotropic bars. The results were presented on warping of cross-sections in torsion and torsional rigidities. Katsikadelis and Tsiatas (2016) formulated the torsion problem for non-homogeneous anisotropic bars in terms of the warping function and also developed a boundary-only solution to solve the resulting partial differential equation with variable coefficients under Neumann type boundary condition. Ecsedi (2013) presented some analytical solutions for Saint-Venant torsion of non-homogeneous anisotropic bars with solid and hollow cross-sections. In this study, the shear flexibility moduli were considered to be smooth functions of Prandtl's stress function of

corresponding homogeneous problem. Sapountzakis and Tsipiras (2009) presented the Boundary Element Method (BEM) to the elastic-plastic problem of composite cylindrical bars with arbitrary cross-section subjected to uniform torsional loading, taking into account the effect of geometric nonlinearity.

The earliest FGMs were introduced by Japanese scientists in the mid-1980s as ultra-high temperature resistant materials for aerospace applications (Yamanouchi et al. (1990)). Miyamoto et al. (1999) discussed the methods of FGM fabrication and general information about FGMs including microstructure analysis of the graded materials. Suresh and Mortensen (1998) provided an introduction to the fundamentals of FGMs. Noda (1991) presented an extensive review that covers a wide range of topics from thermoelastic to thermoinelastic problems. The author discussed the importance of temperature dependent properties on stresses and suggested that those properties of the material should be taken into account in order to perform more accurate analysis. Cho and Oden (2000) studied the thermal stress characteristics of functionally graded materials using finite element method. Different thermal stress characteristics for different material variations and sizes of FGM were observed. Shabana et al. (2000) analyzed the elasto-plastic thermal stresses in functionally graded materials by sing microscopic combination law. The finite element model of the formulation is developed by considering elasto-plasticity theory. Pitakthapanaphong and Busso (2002) described the thermo-elastic and thermo-elasto-plastic behaviour of FGM through analytical and semi-analytical solutions. The homogenization of the local elastoplastic FGM behaviour in terms of the properties of its individual phases was performed using a self-consistent approach and power-law strain hardening behaviour was assumed for the FGM metallic phase. Eraslan and Akis (2005) obtained the plane strain analytical solutions for functionally graded elastic and elastic-plastic pressurized tube problems. The plastic modelling was based on Tresca's yield criterion, its associated flow rule and ideally plastic material behaviour.

Alibeigloo (2010) studied FG beams integrated with piezoelectric actuator and sensor subjected to an applied electric field and thermo-mechanical load using analytical solution. In this study, the FGM properties were assumed to vary exponentially in the thickness direction and the poisson's ratio was held constant. Wattanasakulpong et al. (2011) employed an improved third order shear deformation theory to investigate thermal buckling load of FGM beam under uniform temperature rise. Ma and Lee (2012) obtained closed form solution for the non-linear

static responses of FGM beams subjected to a uniform in-plane thermal loading. The governing equations for the axial and transverse deformations of FGM beams were based on the non-linear first order shear deformation theory. Bayat and Toussi (2015) solved the elastoplastic torsion problem of hollow FGM circular shafts. The torsional shaft is considered as a thick-walled axisymmetric inhomogeneous cylindrical object, while the FG material is composed of ceramic and metallic parts with power function distribution only across the radial direction. Xin et al. (2016) investigated the elasto-plastic response of FG thick-walled tube subjected to internal pressure by using the relation of the volume average stresses of constituents and the macroscopic stress of composite material. Garg and Pant (2017) simulated thermal fracture in functionally graded materials by implementing element-free Galerkin method (EFGM). Zhang and Liew (2016) presented postbuckling analysis of axially compressed functionally graded carbon nanotube resting on Pasternak foundations by utilizing an element-free approach. Shen et al. (2017) investigated the non-linear vibration behaviour of functionally graded graphene-reinforced composite laminated cylindrical shells in thermal environments. Tsiatas and Babouskos (2017) employed a new integral equation solution to the elasto-plastic torsion problem of functionally graded bars of arbitrary cross-section, by using deformation theory of plasticity. Huang et al. (2014) presented a semi-analytic solution to analyze the buckling behaviour of elasto-plastic functionally graded cylindrical shells under torsional loading by assuming multilinear hardening model for materials. Niknam et al. (2014) investigated the non-linear bending of tapered functionally graded beams by implementing analytical and numerical approaches subjected to thermal and mechanical loading. Paul and Das (2016) presented non-linear post-buckling load of FGM Timoshenko beam under non-uniform temperature rise across the thickness of the beam at steady-state condition.

### **2.3 Material behaviour of rotating disks**

From the material viewpoint, further sub-classification is done on basis of yielding, either elastic or post elastic. Within elastic region, the material behaviour is classified into two major groups, isotropic and anisotropic. On the other hand, post-elastic stress analysis is further categorized into two groups depending on the failure criterion, viz. Tresca's or Von Mises criterion.

### **2.3.1 Disks made of isotropic materials**

Research work involving disks made of isotropic material have been carried out extensively. As such literatures can be further classified depending on the state of stresses, i.e., elastic or elastic-plastic. It is found that a major portion of the work relating to elastic-plastic stress studies has been carried out during the last two decades. One can easily comprehend the existence of nonlinearity associated with study of stresses in elastic-plastic regimes and realize the contribution of advanced and efficient computational machines during the last two decades in the analysis.

#### **2.3.1.1 Analysis of rotating disks in elastic region**

Investigations pertaining to the behavior of rotating disks within elastic zone can be traced back to Thompson (1946) wherein he provided a numerical approach to the turbine disk by considering point to point variation in thickness and other physical parameters, except Poisson's ratio. Manson (1947) presented a finite difference solution of the equilibrium and compatibility equations for elastic stresses in a symmetrical disk, which was capable of incorporating the variation in Poisson's ratio and other complexities such as shrink fits. Manson (1950) presented a simplified method for determining the disk profile to incorporate arbitrary elastic stress distribution arising out of centrifugal loading or combination of centrifugal and thermal loading. For similar loading combination and variation in physical properties at various parts of disks at different operating temperatures, Leopold (1948) calculated elastic stresses in disks with variable thickness using semi-graphical method. Theoretical studies pertaining to elastic and elastic-plastic stress analysis of rotating disk made of isotropic material were almost absent for the next two decades except the literature reported in textbooks by Calladine (1969), Timoshenko and Goodier (1970) and Srinath (2003). Sherbourne and Murthy (1974) applied dynamic relaxation technique effectively to carry out the analysis of elastic stresses for isotropic material, possessing non-linear stress-strain relationship (Ramberg-Osgood stress-strain relations). They commented on the simplicity and accuracy of the proposed method when applied to non-linear material behaviour coupled with variable geometry in rotating disks. Analysis of elastic stress state in rotating disks up to the point of yielding with the objective to determine limit angular speed has also been carried out recently. Apatay and Eraslan (2003)

presented analytical solution for elastic deformation of rotating solid and annular disk with parabolically varying thickness with free, radially constrained and pressurized boundary conditions. They reported lowered induced stresses in parabolic disks as compared to constant thickness disks and observed the effect of various geometry parameters on elastic limit angular velocities using Von Mises criterion.

Vivio and Vullo (2007) investigated the elastic stress states of rotating converging conical solid and annular disks having radial density variation subjected to thermal load based on two independent integrals of the hypergeometric differential equation describing the displacement field disks. In a subsequent work, Vullo and Vivio (2008) investigated nonlinearly variable thickness rotating solid and annular disks having radial density variation subjected to thermal load. Two powerful analytical methods, namely homotopy perturbation method (HPM) and Adomian's decomposition method (ADM) have been introduced to obtain distributions of stresses and displacements in rotating annular elastic disks with uniform and variable thicknesses and densities by Hojjati and Jafari (2008). They reported approximate solutions in the form of an infinite power series for nonlinear equations, without linearization, perturbation or discretization, by using ADM. Bayat et al. (2008) presented elastic solutions for variable thickness rotating disks made of functionally graded material having power-law variations in geometry and material properties and reported the effects of the material grading index and the geometry of the disk on the stresses and displacements. Bhowmick et al. (2008) performed an energy functional based numerical analysis to obtain limit angular speed for externally loaded rotating disks of non-uniform thickness. Chen and Fang (2011) studied the non-axisymmetric warping of a clamped-free heavy disk. The von Karman's plate model was adopted to derive the equations of motion and for the experimental study, a floppy disk was used to demonstrate the non-axisymmetric deformations when the disk is either stationary or rotating. Nejad et al. (2014) determined the stresses and displacements in a rotating cylindrical shell with variable thickness under uniform pressure by using a semi-analytical solution. In this analysis, the thick cylinder was divided into disk from layers with their thickness corresponding to the thickness of the cylinder. The governing equations of the disk layers were obtained based on first-order shear deformation theory due to the existence of shear stress in the thick cylindrical shell. Danesh and Asghari (2014) investigated the mechanical behaviour of micro-rotating disks by using strain

gradient theory. The governing equations and boundary conditions were derived with the use of variational method.

### **2.3.1.2 Elasto-plastic analysis of rotating disks**

Laszlo (1948) has first reported theoretical analysis of rotating disks in plastic regime or in region of permanent deformation, where he discussed plastic deformation of rotating rings and disks and reported that under certain conditions depending upon the stress-strain curve of the material the equilibrium of rotating rings and disks may attain instability. Millenson and Manson (1948) extended the elastic finite difference solution proposed by Manson (1947) to analyze the stress distribution in rotating disk under conditions of plastic flow and creep. Lee Wu (1950) presented an exact solution of rotating disk based on deformation theory of plasticity with axial symmetry in strain hardening range and subsequently in Lee Wu (1951) reported a partly linearized solution of plastic deformation of rotating disk considering finite strain. Manson (1951) also presented solutions for disks of work hardening materials based on von-Mises theory and deformation theory of plasticity. Mellor and Percy (1963) extended the same work for larger strain by implementing Hencky's deformation theory.

Study of non-linear behavior found resurgence in 1980s when Gamer (1983) reported that the stress distribution in a rotating solid disk obtained by several researchers and also given in many textbooks on plasticity, is not meaningful since the corresponding displacement field is incompatible with the necessary continuity requirements at the elastic-plastic interface. Later, considering the fact that the plastic core of the disk consists of two parts with different forms of yield condition, Gamer (1984a, 1984b, 1985) obtained a consistent analytical solution for the elastic-plastic response of a rotating uniform thickness solid disk using Tresca's yield condition and its associated flow rule. Gamer (1984c, 1984d) also obtained analytical solutions for the first time for elastic and elastic-plastic deformation caused by pressurized disk edges and explained the effect of increasing pressure on formation and propagation of plastic region. Guven (1994) investigated linearly hardening rotating solid disk with variable thickness for fully plastic state. The thickness was considered to vary hyperbolically along the radius. Exponential variation of thickness was first discussed by Guven (1995a) although he was not able to present a solution satisfying all boundary and continuity conditions. Guven (1995b) also investigated rotating disks with power function thickness profile. In Guven (1998), stresses in a rotating hyperbolic disk

with rigid inclusion were studied analytically and were found to be affected by thickness parameter. Guven (1997) also investigated the deformations of constant thickness rotating annular disks with rigid inclusion in the fully plastic state. In all these reported works Guven assumed Tresca's criterion and its associated flow rule along with linear strain hardening material behaviour. Guven et al. (1999) extended Gamer's (1983, 1984c, 1984d) work for rotating annular disks with two different boundary conditions. The problems were first treated for fixed inner and outer boundary conditions and secondly for free inner and fixed outer boundary conditions. Closed form solutions were obtained for both the cases, based on Tresca's yield criterion, its associated flow rule and linear strain hardening behaviour.

Applicability of Tresca's criterion, associated flow rule and linear strain hardening behaviour presented simple and easy analytical solution and hence found mention in numerous investigations carried out by Eraslan (2003), Eraslan and Orcan (2002a, 2002b), Orcan and Eraslan (2002) and other researchers. Eraslan and Orcan (2002a) extended Gamer's work to a solid convex disk with exponentially varying thickness and unlike Guven (1995a) obtained an analytical solution. Numerical results were reported for different values of geometry parameters. A similar work was carried out for power function thickness variation by Orcan and Eraslan (2002). In both of the work, the similarity in elastic plastic deformation behaviour of the convex profiles with that of uniform thickness disks was reported. However, Eraslan and Orcan (2002b) studied the elastic-plastic deformation behaviour of variable thickness solid disks having concave profiles and reported its difference from that of uniform thickness disk. Eraslan (2002a) studied inelastic stresses and displacements in rotating solid disks of exponentially varying thickness using Tresca's and von Mises yield criteria. Eraslan (2003) studied elasto-plastic deformations of disks with different parameter values of parabolic thickness functions, representing a wide range of non uniform cross-sectional profiles. He obtained closed form solutions in terms of hypergeometric functions, by performing displacement based formulation.

In recent past, elasto-plastic analysis of stress and deformation states in rotating solid and annular shafts using Tresca's yield criterion and its associated flow rule for ideally-plastic and linearly hardening materials has been performed extensively. Gamer and Lance (1983) reported an analytical solution for a linearly hardening rotating annular shaft with fixed ends. Mack (1991a, 1991b) performed a similar analysis on a rotating annular shaft and solid shaft respectively exhibiting ideally plastic behaviour with free ends and obtained the closed form



solution. In a later work, Gamer et al. (1997) studied the stresses in an elastic-plastic rotating solid shaft of ideally-plastic material behaviour with fixed ends. Recently, Eraslan (2003) extended the work of Mack (1991b) and Gamer et al. (1997) on solid shafts made of linearly hardening materials. Elastic-plastic deformation analysis of rotating solid and annular shafts exhibiting ideally-plastic behaviour with fixed as well as with free ends using Von Mises yield criterion deformation theory of elasticity and Swift-type hardening law was carried out by Eraslan (2004). The nonlinearities associated with Von Mises yield criterion were handled numerically by applying nonlinear shooting method using Newton-Raphson iterations with numerically approximated tangents.

Due to non linearity involved with the application of Von Mises criterion, the analysis demands for a numerical solution. But the advantage in using Von Mises criterion is that unlike Tresca's Criterion, here a single formulation takes care of the whole plastic region. Rees (1999) studied elastic plastic deformation of rotating solid and annular disks of uniform thickness made of elastic-perfectly plastic material and compared the solutions obtained from the two different failure criterion. Numerical procedure for solving the governing differential equation while adopting Von Mises criterion constituted of a combination of Runge-Kutta and predictor-corrector method. Radial and hoop stress distribution obtained using both the criterion showed small differences for annular disks but noticeable differences in radial stress distribution was observed for solid disks. Eraslan (2002a) extended the work of Rees (1999) to variable thickness solid disks made of elastic linearly hardening materials and studied inelastic stress state of solid disks with exponential thickness variation using both Tresca's and Von Mises criterion. Plastic limit angular speeds were established using both the criteria for different values of geometric parameter. In a recent paper Eraslan (2005) presented an analytical solution for rotating disks with elliptical thickness variation and made of linearly hardening material using Tresca's criterion and its associated flow rule. In the same paper a computational model is developed to obtain solutions using Von Mises criterion, deformation theory of plasticity and Swift-type hardening law. Non linear shooting method using Newton-Raphson iterations with its numerical derivatives is used to solve non linearity associated with Von Mises criterion. Eraslan and Argeso (2002) calculated the elastic and plastic limit angular speed for rotating disks of variable thickness in power function form. They presented analytical solutions to determine elastic limit speeds for annular disks with and without rigid inclusion and also presented numerical solution

for solid disks to determine elastic limit speeds. For calculation of plastic limit speeds, Von Mises criterion and its flow rule is applied, both linear and nonlinear hardening material behaviours are treated numerically. Eraslan (2002b) extended Guven's work (1997, 1998) to include Von Mises criterion, nonlinear isotropic hardening, any functional form of thickness variability and small and large values of hardening parameter. The thickness variation in this work is described by power and exponential functions. Ma et al. (2001) studied the stresses and deformations of rotating constant and linearly varying thickness solid and annular disks, considering unified yield criterion proposed by Yu (1983). This criterion, with suitable adjustment of weighing coefficients may be reduced to one of Tresca's, Von Mises or Yu criterion. However, the constant radial and hoop stresses at the centre of the disk reported in this paper fail to satisfy the equation of equilibrium.

Some other literatures related to elastic-plastic stress analysis using numerical computations are also available. Sterner et al. (1994) presented a new numerical scheme based on Taylor's expansion combined with iterative root finding method where the governing equilibrium equation and the constitutive relations were expressed in terms of radial stress. You et al. (1997) and You and Zhang (1999) presented numerical schemes based on perturbation method and power series solution method to investigate elastic-plastic deformations of rotating disks with uniform thickness. Based on Von Mises yield criterion combined with polynomial yield stress equivalent strain relation the stresses and displacements were computed. The results were compared favorably with those obtained using finite element solutions and analytical solutions using Tresca's criterion. This work was further extended by You et al. (2000) using Runge-Kutta numerical procedure, to compute elastic-plastic stresses in rotating annular disks of variable thickness and variable density. Alexandrova and Alexendrov (2004) aimed at demonstrating the effect of yield criterion on the size of the plastic zone. A semi analytical solution for an elastic perfectly plastic annular rotating disk and its associated flow rule was presented and comparison with solutions based on Tresca's criterion is drawn. In another work, Alexandrova et al. (2004) developed a semi analytical method based on Von Mises yield criterion and its associated flow rule to determine displacement field and strain distribution in a thin annular rotating disk of constant thickness. The influences of rotational speed and thickness variation on the plastic solution of hyperbolic annular disks in terms of von-Mises yield criterion and its associated flow rule has been reported in a work by Alexandrova and Villa Real (2006).

Bhowmick et al. (2010) investigated the growth of elastic-plastic front in rotating solid disks of non-uniform thickness having exponential and parabolic geometry variation. The problem is solved through an extension of a variational method in elasto-plastic regime. The formulation is based on von-Mises yield criterion and linear strain hardening material behaviour and the solution of the governing equation is obtained using Galerkin's principle. Alexandrova (2012) obtained continuous stress-displacement solution to thin rotating solid disk for elastic-perfectly plastic material based on equation of motion, Hooke's law, yield criterion, and conditions of continuity of stresses and/or displacement at the elastic/plastic boundary. The author reported that both the displacement field derived from the flow rule associated with Mises yield criterion and the stress distributions are continuous at the elastic/plastic boundary in contrast with the discontinuous solution based on Tresca yield criterion and its associated flow rule. Toussi and Farimani (2012) investigated the elasto-plastic deformation of rotating disks beyond its limit speed. In this study, the concepts of failure and limit speed of disks were studied by using two types of material properties including the elastic perfectly plastic and Ramberg Osgood models. Pirumov et al. (2013) presented a semi-analytical solution for the elasto-plastic stress and strain distribution in a thin annular disk subjected to pressure over its inner radius. Fanelli et al. (2015) evaluated the elastic-plastic stiffness behaviour and plastic front in spot welded joints. The spot weld joint was modelled with circular finite plate of variable thickness and with central rigid nugget. Alexandrov et al. (2018) used Drucker-Prager yield criterion and its associated flow rule to find the elastic-plastic stress and strain distributions within the rotating annular disks. Jeong and Chung (2016) provided the elasto-plastic stress distribution of rotating annular hyperbolic disks by using Drucker-Prager yield criterion. Lomakin et al. (2016) used von-Mises yield criterion to determine the elastic-plastic stress and strain distributions in rotating annular disks made of perfectly plastic material.

### **2.3.2 Disks made of anisotropic materials**

Based on type of material, the review of literature available on rotating disks made of material with general anisotropy is addressed first. Tang (1969) presented closed form solutions for rotating anisotropic disks having uniform geometry by considering elasticity theory of an anisotropic body and assuming the material to be cylindrically anisotropic with principal axis of anisotropy coinciding with principal axis of the disk. In the work, the author studied stress

distribution of a solid disk, disk mounted on a rigid shaft, and disk with a central hole. Murthy and Sherbourne (1970) studied elastic stress distribution for rotating anisotropic disks of variable thickness considering similar assumptions as considered by Tang (1969). Thickness of the disk was assumed to vary hyperbolically along the radial direction. They presented complete analytical solution of stress distribution for annular disk and disk mounted on a rigid shaft. Sherbourne and Murthy (1974) applied the technique of dynamic relaxation for analyzing disks of variable profile made of anisotropic material. They carried out the analysis for uniform solid disk, and annular disk of variable profile, the variation in thickness being a hyperbolic function of radius. The results were compared with those obtained using exact analysis in Murthy and Sherbourne (1970) and were found to be in good agreement. In the work by Reddy and Srinath (1974), closed form solutions for stresses and displacement in an anisotropic rotating circular disk of variable thickness and variable density are reported. The distribution of elastic stresses and displacements are reported and plotted for annular disks with free boundary condition and disks mounted on rigid shaft. Results indicate lower values of stresses and displacement for a disk with radially increasing density. Ari-Gur and Stavsky (1981) presented a closed form solution for rotating polar orthotropic circular disks for a particular singularity defined by orthotropy parameter that arose in classical solution provided by Glushkov (1939) when elastic stiffness coefficient in tangential direction was considered to be nine times the elastic stiffness coefficient in radial direction. In their work, they also concluded that different optimization criteria are needed for different boundary conditions in order to optimize the orthotropy parameter.

Tutuncu (1995) determined stresses set up due to centrifugal forces in specially orthotropic circular plates by modeling it as a disk attached to a shaft with free and fixed outer boundaries individually. He concluded that higher stiffness ratio or orthotropy parameter results in reduced radial stress build up in both cases and reduced tangential stresses in case of free outer boundary. But in case of fixed outer boundary, higher stiffness ratio resulted in larger tangential stresses at the outer boundary thus contributing to stability against local buckling. Horgan and Baxter (1996) studied the effect of curvilinear anisotropy on the stress response of anisotropic rotating disks. Both radial and circumferential anisotropy was considered and stress response was studied under both cases. Stress singularities were reported to arise due to focusing of anisotropy at the origin. Jain et al. (1999) studied polar orthotropic rotating disk of constant

thickness and proposed that by suitably varying orthotropy parameter anisotropic elastic constants can be tailored radially to obtain equal radial and tangential stresses. The results were found to closely agree with those obtained using FEM. Zhou and Ogawa (2002) considered a special type of Cartesian orthotropic material known as cubic anisotropic material to study the stress states of a rotating disk. They presented a rather simple approach by assuming a displacement field and formulated a closed form solution. However, the approach was found to be applicable in case of solid disks only.

All the literatures mentioned in this section, dealt with elastic analysis of disks made of anisotropic material. The work on elasto-plastic analysis is presented by Durban and Birman (1983) who used a finite strain approach for the axisymmetric problem of rotating annular disk. Material behaviour was modelled based on a anisotropic flow theory proposed by Hill. Alexandrova and Alexendrov (2004a) who explained the effect of plastic anisotropy on development of plastic zone in a rotating disk by applying Hill's quadratic orthotropic yield criterion and provided a semi analytical solution to study the stress state. Alexandrova and Villa Real (2006) studied the effect of material anisotropy on the stress–strain state in a plastically anisotropic, thin rotating disk of constant thickness and density using semi-analytical method. The material of the disk is assumed to be plastically anisotropic obeying the Hill's quadratic yield criterion. In a subsequent work by Alexandrova and Villa Real (2007) presented elasto-plastic stress distributions and limit angular velocities of rotating annular disks with hyperbolic geometry variation in terms of the von-Mises yield criterion and its associated flow rule. Callioglu et al. (2006) studied the elastic-plastic stress analysis of a curvilinearly orthotropic annular disk for strain hardening material behaviour. Eraslan et al. (2014) studied the stress and deformation states in partially plastic, orthotropic, variable thickness and non-isothermal annular disks under external pressure. Hill's quadratic yield condition and a Swift type nonlinear hardening law were used to describe the governing differential equation. Jeong and Pirumov (2017) used Hill's orthotropic yield criterion to find out the elasto-plastic stress and strain distributions in anisotropic rotating annular disks.

### **2.3.2.1 Disks made of composites and FGMs: Elastic analysis**

Composites are gradually being used as structural materials in many aerospace and automobile applications. Functionally graded composite materials are characterized by a

spatially variable microstructure. For the purpose of analysis, functionally graded materials are modeled as inhomogeneous materials with continuously varying properties. The inability of conventional materials to survive under extreme working conditions has evolved such materials. Rotating disks made of functionally graded materials are highly useful in applications where the disk is exposed to elevated temperature field. Apart from enduring severe thermal loading they also present an advantage of being light in weight. Functionally graded composite materials (FGMs) have been the subject of intense researches and attracted considerable attention in recent years. FGMs are being used as interfacial zone to improve the bonding strength of layered composites, to reduce the residual and thermal stresses in bonded dissimilar materials and as wear resistant layers in machine and engine components. One of the advantages of FGMs over laminates is that, due to continuous material property variation, there is no stress build-up at sharp material boundaries thus eliminating potential structural integrity issues such as delamination. Farshad (1974) first carried out an investigation on stress and deformation states of thin rotating solid disks made of bi-linear elastic materials. The results were compared with linear elastic solutions and possible application of the method of analysis in predicting the behaviour of fiber-reinforced composites was reported. Parmaksizoglu and Guven (1988) carried out an analysis of rotating annular disk having bi-linear elastic material behaviour and obtained solution of stress and displacement for restrained inner and outer boundary conditions. Fukui et al. (1993) extended their previous work by considering a thick-walled FG tube under uniform thermal loading. They investigated the effect of graded components on residual stresses. Tanigawa (1995) studied the applications of FGMs in many engineering sectors especially for working in high temperature environments where thermal effects due to temperature change must be taken into account. FGM circular cylinder and hollow sphere were considered by Obata and Noda (1994) to carry out the analysis of thermal stresses. Adali et al. (1998) carried out design optimization analysis of composite disks under multiple loads. Explicit solutions for free-free, fixed free and free-fixed boundary conditions were obtained and optimal fiber orientations and ply angle combinations were reported.

Reddy et al. (1999) studied axisymmetric bending and stretching of functionally graded solid and annular circular plates using the first-order shear deformation Mindlin plate theory. The solutions for deflections, force and moment resultants of the first-order theory are presented in terms of the corresponding quantities of isotropic plates based on the classical Kirchhoff plate

theory. Horgan and Chan (1999) investigated the effects of material inhomogeneity on the stress response of linearly elastic isotropic solid circular disks and presented exact solutions for the case when Young's modulus has power law dependence on radial coordinate. It is also shown that suitable tailoring of material inhomogeneity may generate identical radial and hoop stresses throughout the disk. The potential benefits of using fiber reinforced functionally graded material for rotating solid and annular disks were highlighted by Durodola and Attia (2000). Arnold et al. (2001) developed an analytical model capable of performing an elastic stress analysis for layered, annular/solid, anisotropic/isotropic disk systems, subjected to pressure surface tractions, body forces (in the form of temperature-changes and rotation fields) and interfacial misfits. The key design variables are identified and their associated influence defined. The proper performance based on the specific stored energy, in the presence of multiaxiality and material anisotropy has been addressed for disks with annular or solid geometry. Interestingly annular anisotropic disk was reported to be stronger than solid anisotropic disk where as the reverse is reported in case of solid isotropic disks.

Reddy (2000) presented a theoretical formulation, Navier's solutions of rectangular plates, and finite element models based on the third-order shear deformation plate theory for the analysis of through thickness functionally graded plates. Numerical results of the linear third-order theory and non-linear first-order theory are presented to show the effect of the material distribution on the deflections and stresses. Nemirovskii and Yankovskii (2002) proposed an iterative method for solving problems dealing with rational profiling of thermoelastic three-layered reinforced rotating disks of gas turbines. The conditions of equal-stressed reinforcement of the mid-layer and the condition of equal-strength binder of the reinforced layer or external isotropic layers are used as criteria for rational designing. Tahani et al. (2005) proposed a semi-analytical method for deformation and three dimensional stress fields in rotating annular disks made of cylindrically orthotropic nested rings using layerwise theory and the Hamilton principle. Numerical results are obtained in a clamped free and a free-free rotating disk made of two nested circumferentially wound rings. Bekta et al. (2005) analyzed elastic-plastic stresses of a thin aluminium-metal-matrix composite disk under internal pressure. Assuming Tsai-Hill yield criterion and satisfying the elastic-plastic stress-strain relations and boundary conditions for small plastic deformations, an analytical solution is reported.

Kordkheili and Naghdabadi (2007) proposed a semi-analytical thermo-elasticity solution for hollow and solid rotating axisymmetric disks made of functionally graded materials with power law distribution for the thermo-mechanical. Bayat et al. (2008) presented elastic solutions for axisymmetric rotating disks made of functionally graded material with variable thickness. They assumed the material properties and disk thickness profile to be represented by two power law distributions. In the case of hollow disk, based on the form of the power-law distribution for the mechanical properties of the constituent components and the thickness profile function, both analytical and semi-analytical solutions are given under free-free and fixed-free boundary conditions. For the solid disk, only semi-analytical solution is presented. Zenkour (2009) presented accurate elastic solution and reported numerical results for displacement and stresses at the interfaces of the composite structure disks composed of three-layer sandwich solid disks with faces made of different isotropic materials and core made of FGM. The axisymmetric displacements and stresses in functionally graded hollow cylinders, disks and spheres subjected to uniform internal pressure, using plane elasticity theory and 'Complementary Functions' method, has been proposed by Tutuncu and Temel (2009). Peng and Li (2012) investigated the elastic problem of rotating FGM orthotropic disks. The authors presented a method for transforming the problem into solving a Fredholm integral equation. Leu and Chien (2015) presented thermoelastic behaviour of FGM disks with variable thickness involving axisymmetric thermal loads including non-uniform heat source, heat flux, and temperature boundary conditions. Shahzamanian et al. (2013) presented finite element contact analysis of functionally graded brake disk subjected to centrifugal body force, bending loads, thermal loads and frictional heat. The material properties of the brake disk were assumed to be represented by a power law distribution along the thickness where the free surface was full-metal and contact surface full-ceramic. Ghafoori and Asghari (2012) proposed a three-dimensional elasticity solution for FGM cylinders with variable thickness profile. The authors investigated the variation of different parameters like stress and strain components as well as the radial displacement along the thickness for different profile functions. Kothari and Mukhopadhaya (2013) investigated the thermo-mechanical interactions inside a FGM hollow disk based on thermo-elasticity theories. The material properties were assumed to follow a volume-fraction based rule with a power law. The inner and outer surfaces of the disk were subjected to different thermal and mechanical boundary conditions. Kadkhodayan and Golmakani (2014) studied the non-linear analysis of FG



solid and hollow disks with uniform and variable thicknesses subjected to bending load. The authors used first order shear deformation theory and the large deflections von-Karman equations for the non-linear formulations and assumed Mori-Tanka distribution of material properties along the radial direction. First-order shear deformation theory (FSDT) was employed by Nejad et al. (2015) to carry out analysis on FG rotating thick hollow cylinder with variable thickness and clamped ends. The authors imposed boundary conditions and continuity conditions between the layers, radial displacement and stresses to obtain solution of the governing equation. Dai and Dai (2016) employed a semi-analytical approach for the displacements and stress fields in a rotating FGM hollow disk with variable thickness and angular speed. In this study, the material properties were assumed to vary along the radial coordinate and related to the volume fraction of each material. The modulus of elasticity and the coefficient of thermal expansion were temperature-dependent. Khorsand and Tang (2018) employed co-evolutionary particle swarm optimization (CPSO) approach coupled with a differential quadrature (DQ) to optimize the weight of functionally graded disk of varied thickness under thermoelastic loading conditions.

### **2.3.2.2 Disks made of composites and FGMs: Post-elastic analysis**

The phenomenon of the elastic-plastic is appeared because of the structural material exhibited to load exceeding the required critical load to produce initial yielding condition in the material. This phenomenon plays an important role in diverse applications including pressure vessels, flywheels, driving shafts, shafts in turbines and generators, and solid propellant grain. The problems of elastic-plastic for thick-walled cylinders have been solved by most investigators based cylinders subjected to mechanical loadings such as internal and external pressures with either thermal loading or angular velocity. Due to the advantages of FGMs over conventional composites and solid materials, these materials have been broadly studied for potentials applications of structural elements. The analysis of the elasto-plastic deformation in FGMs is another progressive field of research. Hojjati and Jafari (2009) reported analytical solutions for the elastic-plastic stress distribution in rotating annular disks with uniform and variable thicknesses and densities under plane stress assumption, Tresca's yield criterion, its associated flow rule and linear strain hardening behaviour using homotopy perturbation method. Hojjati and Hassani (2008) reported numerical method using variable material properties (VMP) theory for stress-strain analysis of rotating discs with non-uniform thickness and density. In this study, a

numerical solution based on Runge-Kutta's method for solving the governing differential equation in elastic and plastic regimes was presented. Nie and Batra (2010) analyzed axisymmetric deformations of a rotating disk made of a rubberlike material with its thickness, mass density, thermal expansion coefficient and shear modulus varying in the radial direction. The problem was analyzed by using an Airy stress function and the non-homogeneous ordinary differential equation with variable coefficients for stress function was solved by the differential quadrature method. Jahromi et al. (2012) provided an analytical method for evaluating the elasto-plastic stresses in a functionally graded rotating disk with varying elastic and plastic properties in the radial direction. The effect of different metal-ceramic grading patterns as well as the relative elastic moduli and densities of the ceramic and metallic constituents on the developed stresses were studied. Hassani et al. (2012) presented semi-exact method of Liao's homotopy analysis method (HAM) and finite element method (FEM) to obtain the stress and strain components of functionally graded elastic-strain hardening rotating disks with non-uniform thickness and material properties subjected to thermo-elasto-plastic loading. Farimani and Toussi (2013) studied the effect of volume fraction distribution on the plastic radius and limit speed in FG disks subjected to centrifugal and isothermal loadings. The variable material property theory was used for the determination of stress and deformation fields. Nejad et al. (2014) employed an exact closed-form solution for analysis of elasto-plastic rotating functionally graded disks in which Tresca's yield criterion is adopted. For various values of inhomogeneity constant, the effect of increasing the angular speed on the propagation of the plastic zone is investigated. Callioglu et al. (2015) studied the elasto-plastic stress of functionally graded rotating disks by using analytical and numerical methods. The yielding behaviour of the disk material is supposed to be non-work hardening using von-Mises yield condition. In another study, Demir et al. (2017) analyzed the elasto-plastic stresses of functionally graded hyperbolic disks subjected to uniform temperature. Nayebi et al. (2015) studied the influence of continuum damage mechanics on FG rotating disk subjected to cyclic temperature gradient loading through non-linear kinematic hardening rule. The formulation was developed on the basis of von-Mises yield criterion and the material properties were assumed to be independent of temperature. Mahdavi et al. (2016) presented thermo-mechanical analysis of elasto-plastic FG disk with variable thickness by using variable material property theory. The authors investigated the effect of the boundary conditions, temperature gradient, and thickness profile on the stress behavior of disk by the VMP method.

Kalali et al. (2016) used analytical method to provide a solution for elasto-plastic stress distribution in axisymmetric problems (rotating disk, cylindrical and spherical vessel) based on von-Mises yield criterion by assuming an isotropic material model.

## **2.4 Types of loading on rotating disk**

A host of research work aimed at the investigation of effect of various types of loading on rotating disk behaviour. Some of them are centrifugal, thermal and a combination of both, i.e., thermo-mechanical loading. For efficient design and material usage, the determination of stresses in disks subject to loading conditions is important in many industrial applications.

### **2.4.1 Disks under centrifugal loading**

Rotating disks work mostly at high angular velocity. High speed results in large centrifugal forces in disks and induces large stresses and deformations. Estimation of elastic and especially plastic limit angular velocities in the design of disks rotating at high speeds is an important subject due to a large number of applications in mechanical engineering. For this reason, the theoretical investigation of stresses and displacement in such structures has been receiving considerable attention and the topic was discussed in many standard textbooks by Calladine (1969), Timoshenko and Goodier (1970) and Srinath (2003). Tutuncu (1995) determined the stresses and deformations resulting from centrifugal forces in rotating specially orthotropic circular plates. The classical laminated plate theory is employed in the analysis and the results are presented in a manner which illustrates the effect of anisotropy. Ma et al. (2001) used a unified yield criterion to derive the stress distributions and the plastic limit angular velocities of rotating solid disk and annular disc with variable thickness. Hojjati and Jafari (2008) used homotopy perturbation method (HPM) and Adomian's decomposition method (ADM) to solve the rotating annular disks with uniform and variable thicknesses and densities. The material is assumed to follow an elastic-strain hardening behaviour and the angular velocity has been selected to limit the maximum stress below the yield limit of the material. Bhowmick et al. (2008) performed an energy functional based numerical analysis to obtain limit angular speed for externally loaded rotating disks of non-uniform thickness. Maziere et al. (2009) investigated the burst speed of elastoviscoplastic rotating disks both from experimental and computational

point of view. Two twin disks (B-disk and S-disk) made of the same nickel based super alloy were tested and finite element simulations of the B-disk were performed by using either arc length control method to overcome the limit point or dynamic simulations. Jafari (2011) obtained semi-analytical solutions for the elastic stress distribution in rotating annular disks with uniform and variable thicknesses and densities. The author used Karush-Kuhn-Tucker (KKT) optimality conditions to achieve minimum weight design for optimum disk profile. Mohan and Maiti (2013) studied the structural optimization of an axial flow compressor rotating disk. The authors used a constraint nonlinear optimization procedure based on genetic algorithms. Khalili and Peddieson (2014) evaluated the stress and deformation of elasto-plastic rotating disks of both constant and variable thicknesses by using finite difference method combined with an iterative incremental method. Nejad and Fathei (2015) studied the exact elasto-plastic deformations and stresses of rotating thick-walled FG cylindrical pressure vessels. The plastic stresses and deformations were obtained using Tresca's yield condition and its flow rule under the assumption of perfectly plastic material behavior. Zheng et al. (2016) studied the stress field in FG rotating disks with non-uniform thicknesses variable angular velocity by using finite difference method for the case of fixed-free boundary conditions.

#### **2.4.2 Disks under thermal loading**

Thermal loading is induced in a rotating disk due to existence of variable temperature field in the disk. This results in a variation in various material properties, as these are temperature dependent. Typical applications of such types of rotating disks are gas turbine disks and the problem has been treated by several researchers such as Thompson (1946), Leopold (1948), Manson (1947, 1950, 1951), Millenson and Manson (1948), Mendelson (1968), Yeh and Han (1994), Jahed et al. (2005), Farshi et al. (2004), Jahed and Sherkati (2000), Jahed and Shirazi (2001), etc. The method of analysis followed by Thompson (1946), Leopold (1948), Manson (1947, 1950, 1951), Millenson and Manson (1948), Jahed et al. (2004) and Farshi et al. (2004). These literatures have already been mentioned in previous sections. Mendelson (1968) proposed an iterative scheme based on Lamé's solution to obtain thermoplastic solution of inhomogeneous disks.

Jahed and Sherkati (2000) applied the variable material properties (VMP) method and obtained stresses for an inhomogeneous rotating disk with variable-thickness under steady

temperature field assuming the material properties as field variables. Jahed and Shirazi (2001) analyzed both loading and unloading behaviours and reported loading and residual stresses along with associated strains and displacements. Another form of axisymmetric thermal loading in disks due to exposure to circular heat source has also been studied. Gamer (1967) first investigated radial stresses in a perfectly plastic disk subjected to a circular heat source and reported temperature and stress distribution. Gamer and Mack (1985) assumed Tresca's yield criterion and its associated flow rule to study the stress distribution in a circular disk exposed to a circular heat source. Gamer and Mack (1987a, 1987b) extended the previous study and explained elastic-plastic deformation at edges of the disk and studied the transient stress distribution. In another study, Ghosh Dastidar and Ghosh (1972) presented a numerical solution based on  $J_2$  deformation theory to determine the stresses and strains in plastic range in an annular disk due to steady-state thermal gradient. Sayman (2004) and Callioglu (2004) conducted analytical investigation and presented closed form solutions on thermal stresses in an orthotropic aluminium metal–matrix composite and a glass-fiber/epoxy orthotropic disk respectively. Radial temperature variation is assumed to be parabolic in both studies and variations of tangential and radial stresses with temperature are reported. Sayman (2004) reported a close agreement between analytical and finite element solutions. An experimental study has been carried out by Sayman et al. (2005) to investigate thermal elastic-plastic stresses on a steel fiber-reinforced thermoplastic composite disc under uniform thermal distribution. Assuming non work hardening material behaviour, a numerical solution is also provided for plastic stress distribution. Sen and Sayer (2006) investigated elasto-plastic thermal stresses in a thermoplastic composite disc that is reinforced by steel fibers, curvilinearly. Finite element method (FEM) was used to calculate the thermal stress distribution in the model of composite disc. The solution was performed by ANSYS software code. Radial and tangential stresses were calculated under a uniform temperature distribution which was selected from 60 °C to 120 °C.

Callioglu (2007) investigated the stresses on rotating rectilinearly or polar orthotropic discs subjected to various temperature distributions. Vivio and Vullo (2007) studied stresses and strains in variable-thickness annular and solid rotating elastic disks subjected to thermal loads and having a variable density along the radius. Callioglu (2008) studied the stress analysis of the rotating hollow discs made of functionally graded materials under internal and external pressures. Nejad and Rahimi (2009) used the infinitesimal theory of elasticity to obtain closed

form solutions for one-dimensional steady-state thermal stresses in a rotating functionally graded (FGM) pressurized thick-walled hollow circular cylinder under generalized plane strain and plane stress assumptions, respectively. The direct method is used to solve the heat conduction and Navier equations. Peng and Li (2010) addressed the thermo-elastic problem of a rotating functionally graded hollow circular disk with varying material properties to analytically investigate steady thermal stresses. The associated boundary value problem is reduced to a Fredholm integral equation. Afsar and Go (2010) presented finite element analysis of thermo-elastic field in a thin functionally graded rotating disk subjected to a thermal load. The disk is assumed to have exponential variation of material properties and a solution is presented using finite element method. Calderale et al. (2012) carried out theoretical analysis of hyperbolic disks subjected to thermal load by expressing the temperature distribution along the radius by a polynomial relation. Ghadimi et al. (2013) determined the temperature field in the wheel-mounted brake disk. The brake disc and fluid zone were simulated as a 3D model with a thermal coupling boundary condition. Taamneh (2017) investigated thermal steady and transient analysis of turbine disk integrated with heat pipes. The steady and transient temperature variations in the presence and absence of heat pipes were investigated for various parameters such as the thermal conductivity of the disk, the convective heat transfer coefficient for the air and heat pipes, the dimension of the disk, and the number of heat pipes.

### **2.4.3 Disks under thermo-mechanical loading**

Research work involving disks under thermo-mechanical loading have been carried out extensively. Rotating disks have many applications in aerospace industry such as gas turbines and gears. These disks normally work under thermo-mechanical loads. Eslami et al. (2002) analyzed one-dimensional steady state thermal stresses in a hollow thick cylinder made of functionally graded material. The authors assumed the temperature distribution to be a function of radius, with general thermal and mechanical boundary conditions along the inside and outside surfaces. Liew et al. (2003) developed an analytical model for the thermo-mechanical behaviour of FG hollow circular cylinders subjected to the action of an arbitrary steady state or transient temperature field. Shao (2005) presented the solutions of temperature, displacements, and thermal/mechanical stresses in a functionally graded circular hollow cylinder by using a multi-layered approach based on the theory of laminated composites. The cylinder was subjected to

axisymmetric thermal and mechanical loads. Ma and Shao (2008) studied thermo-mechanical analysis of functionally graded hollow circular cylinders subjected to mechanical loads and linearly increasing boundary temperature. Thermo-mechanical stresses were obtained by employing Laplace transform techniques and series solving method for ordinary differential equation. Bayat et al. (2009) reported thermo-elastic solutions for rotating functionally graded disk with variable thickness under a steady temperature field and related material grading index and the geometry of the disk to thermo-elastic solutions. Kursuna et al. (2011) studied the elastic stress analysis of annular discs made of functionally graded materials subjected to both uniform pressures on the inner surface and a linearly decreasing temperature distribution. Callioglu et al. (2011) studied the stress analysis of functionally graded rotating annular disks subjected to internal pressure and various temperature distributions in radial direction. The solution was obtained by using infinitesimal deformation theory of elasticity and power law functions for graded parameters. Callioglu (2011) presented an analytical thermoelasticity solution for a disc made of functionally graded materials. Infinitesimal deformation theory of elasticity and power law distribution for functional gradation were used in the solution procedure. Hojjati et al. (2012) carried out the theoretical and numerical analysis of rotating disks with non-uniform thickness and material properties subjected to thermo-mechanical loadings by variable material properties (VMP), Runge-Kutta's (RK) and finite element (FE) methods using Von-Mises theory as failure criterion. Alexendrov et al. (2012) proposed two solutions to design a thin annular disc of variable thickness subject to thermo-mechanical loading and controlled the initiation of plastic yielding by Mises yield criterion. In a paper, Alexendrov and Lyamina (2012) considered the plastic limit state of a thin hollow axisymmetric disk subjected to thermo-mechanical loading with a uniform pressure distribution on the inner contour and a temperature increasing during deformation. Sharma and Yadav (2013) used finite difference method to investigate thermo-elastic-plastic stresses of a rotating FG stainless steel composite cylinder under internal and external pressure. In this study, non-linear strain hardening law and von-Mises yield criterion were considered. Mahmoudi et al. (2015) investigated the effects of using FG materials in the wheel mounted brake disk on its thermo-mechanical behaviour by using finite element model. The uncoupled thermo-mechanical analysis was performed for the disk made of FG Al-A359/SiC<sub>p</sub>, aluminum and ductile cast iron materials. Mazarei and Nejad (2016) obtained the exact thermo-elasto-plastic stresses and deformations of FG spheres. The authors assumed

perfectly plastic material behaviour and von-Mises yield criterion for the analysis. Zarandi et al. (2016) presented finite element analysis of circular disks subjected to uniform temperature loading based on von-Mises yield criterion. Temperature-dependent mechanical properties were considered for the matrix material only. Kamal et al. (2017) carried out 3D finite element method of the thermo-elasto-plastic stress analysis in thick walled cylinders subjected to a radial thermal gradient. The strain hardening behaviour of the material of the cylinder taken into account based on Tresca's yield criterion and its associated flow rule.

## **2.5 Some related area and complicating effects**

Apart from stress and deformation analysis of rotating disks in elasto-plastic domain, together with several complicated effects mentioned so far, some other features related to rotating disk behaviour are also investigated. Research work related to application of numerical methods, modelling of creep behaviour and experimental works are focused in the following sections.

### **2.5.1 Application of numerical methods**

Generally, analysis of actual engineering problems involves solution of nonlinear differential equations or linear differential equations with variable coefficients. Except for a limited number, these problems cannot be solved explicitly and normally fails to yield to exact solutions. There are two approaches to solve rotating disks problems, namely, analytical and numerical methods. For analytical solutions of rotating disks of uniform thickness, a closed-form solution is available in many standard textbooks Calladine (1969), Timoshenko and Goodier (1970), Rees (1999). However, such exact solutions do not exist for non-uniform thickness disks. Among the numerous articles reporting the results of research conducted on the subject, the most recent ones relevant to this investigation are reviewed below.

As pointed out by Hojjati and Hassani (2008), the closed-form solution of rotating discs are only available for the very basic problems of uniform material and geometrical properties and simple boundary conditions. Nevertheless there are powerful numerical methods such as FEM, BEM and FDM which are applicable in more complicated geometries and material properties. Sterner et al. (1994) pointed out these numerical analyses usually require extensive computer



resources, are tedious to perform due to extensive meshing requirements and are expensive, making them unsuitable for preliminary design type analysis. As many rotating components in use have complex cross-sectional geometries, they cannot be dealt with using the existing analytical methods. Numerical methods, such as the finite element method by many researchers Bhavikatti and Ramakrishnan (1980), Shanbhag (1984), Babu et al. (2008), Aurora et al. (2010), Elhefny and Guozhu (2013), Mohan and Maiti (2013) and the boundary element method by Raveendra and Banerjee (1991) can be applied to cope with these rotating components. You et al. (1997) and You and Zhang (1999) presented numerical schemes based on perturbation method and power series solution method to investigate elastic-plastic deformations of rotating disks with uniform thickness. Based on Von Mises yield criterion combined with polynomial yield stress equivalent strain relation the stresses and displacements were computed. The results were compared favorably with those obtained using finite element solutions and analytical solutions using Tresca's criterion.

Hojjati and Jafari (2007) employed variational iteration method (VIM) to obtain the elastic analysis of non-uniform thickness and density rotating disks subjected to only centrifugal loadings. Hojjati and Hassani (2008) used an elastic-linear hardening material for elastic-plastic analysis of rotating disks. They employed variable material properties and numerical methods of Runge-Kutta and finite element method to analyze the behavior of rotating disks in elastic and plastic regimes. Hojjati and Jafari (2008) studied the elastic analyses of non uniform thickness and density rotating disk under only centrifugal body loadings. They used two semi-exact methods, namely the homotopy perturbation and Adomian's decomposition. Turkyilmazoglu (2010) used homotopy analysis method for rotating disk flow problem and derived the solution of steady, laminar, incompressible, viscous fluid of the boundary layer flow due to a rotating disk in the presence of a uniform suction or injection. Hassani et al. (2011) obtained the analytical solutions of functionally graded (FGM) rotating disks subjected to thermo-elastic loadings by means of He's variational iteration (VIM), Adomian's decomposition (ADM) and Liao's homotopy analysis methods (HAM). They finally compared their analytical results with those of numerical Runge-Kutta's method. They showed that there are so good agreements between different applied methods which is demonstrate the ability of VIM, ADM and HAM to handle the FGM thermo-elastic rotating disks. Haslinger et al. (2016) introduced an enhanced

incremental procedure used for the numerical evaluation and reliable estimation of limit load in deformation plasticity based on compliance.

### **2.5.2 Modelling of creep behaviour**

Rotating disks are the most critical part of rotors, turbines, flywheel etc. In most of these applications, the disk has to operate under elevated temperature and is simultaneously subjected to high stresses caused by disk rotation at high speed. As a result of severe mechanical and thermal loadings, the disk undergoes creep deformations, which may severely affect its performance. In the following paragraphs a brief account of some of the relevant research works available in literature is provided.

Wahl et al. (1954) conducted the creep test in a rotating disc made of steel and simulated the results theoretically using von Mises and Tresca yield criteria describing creep behavior by power law relation and noticed that the creep deformation based on Mises criterion yielded slightly lower values compared to the experimental values. However, the theoretical results based on maximum shear theory, was found to be in a better agreement with the test values. The 1960s and 1970s lead to numerous other serious efforts in analyzing the rotor, and introducing different designs for the flywheel, with the onset of composite material development giving added impetus. A detailed review of the rotating disk problem up through the late 1960s is given by Seireg (1970). Creep analysis of orthotropic disks was carried out by Arya and Bhatnagar (1979), when they investigated the stress and strain distribution using Hill yield criterion. Ma (1959) derived some formulae based on the maximum shear theory associated with the Mises flow rule for calculating creep deformations and stress distributions in rotating solid disks of variable thickness and uniform temperature, and used the exponential function creep law at steady state conditions. Further Ma (1960) derived some formulae based on the theory of the Tresca criterion and its associated flow rule using the exponential function creep law at steady state conditions for creep strains and stress analysis in rotating solid disks of variable thickness and uniform temperature. Ma (1961) presented the stress analysis of rotating solid disks having variable thickness and variable temperature. The analysis was based on the theory of Tresca criterion and its associated flow rule, and used the exponential function creep law for steady state conditions.

Use of composites, although has allowed working at elevated temperatures, and reduced component weight, but application of aluminium and aluminium based alloys is challenged by its enhanced creep behaviour. Singh and Ray (2001) studied steady state creep response described by Norton's law in a particle reinforced isotropic functionally graded rotating disk. The particle distribution was assumed to vary linearly along the radius and increased tangential stresses but lower creep parameters at the region near the inner radius due to increased particle density the disk under investigation is made of composite containing silicon carbide in a matrix of 6061 aluminium alloy. Singh and Ray (2002) investigated the effect of anisotropy on steady state creep rate using Hill yield criterion in an aluminium silicon carbide composite rotating disk by comparing the tangential and radial stresses and consequent creep rates in the disk. Gupta et al. (2004a) investigated the steady state creep response in a rotating disk made of isotropic composites containing silicon carbide in an aluminium matrix using Sherby's constitutive creep model. Radial and tangential strain rates were reported to reduce with reducing particle size, increasing particle content and decreasing operating temperature. Gupta et al. (2004b) extended their previous work to rotating composite disks operating under radial thermal gradient. Linear particle distribution was assumed and significantly lower steady state strain rates as compared to isotropic disks with uniform particle distribution were reported. Gupta et al. (2005) modeled the creep behaviour of rotating disk made of aluminium-silicon carbide composite in presence of radial thermal as well as composition gradient. Creep response was studied following Sherby's creep law and results were compared with those obtained following Norton's creep law. Reduced steady state creep rates due to simultaneous presence of thermal and composition gradients were also reported by them. In a paper, Loghman et al. (2011) investigated the time-dependent creep stress redistribution analysis of rotating disk made of Al-SiC composite using Mendelson's method of successive elastic solution. Material creep behavior was described by Sherby's constitutive model using Pandey's experimental results on Al-SiC composite. Displacement was obtained using equations of equilibrium, stress strain, and strain displacement, a differential equation, containing creep strains. Mangal et al. (2013) investigated the steady-state creep in a cylinder made up of functionally graded material rotating at uniform angular speed. The thermal gradient in the rotating cylinder of FGM was calculated using finite element method. The study revealed that the presence of particle gradient & thermal gradient significantly affected the radial, axial and tangential and effective stresses in the cylinder. Dharmpal et al. (2015)

developed mathematical model to investigate steady state creep in a functionally graded rotating disc having variable thickness. The  $\text{SiC}_p$  content was assumed to decrease from the inner to outer radius of the disc. The creep behavior of the disc material was described by threshold stress based law with a stress exponent of 5. Khanna et al. (2015) investigated secondary creep in a rotating Al- $\text{SiC}_p$  disc having different thickness profiles and reinforcement ( $\text{SiC}_p$ ) gradients. The creep behavior was described by threshold-stress based law and yield following Tresca criterion. Rattan et al. (2016) investigated the effect of thermal residual stress on steady-state creep behavior of thermally graded isotropic disc rotating at elevated temperature. The creep analysis was carried out using isotropic Hoffman yield criterion. Bose and Rattan (2017) made an attempt to model steady-state creep for thermally graded rotating disc made of linearly varying functionally graded material. The analysis indicated that stress in disk operating under thermal gradient slightly increases in comparison to disk operating at constant temperature. The steady state creep behaviour of parabolically varying functionally graded disk subjected to thermal gradient was studied by Bose and Rattan (2018) in a subsequent work.

### 2.5.3 Experimental work

Several researchers have carried out experimental work with an objective to verify or establish the validity of a theoretical simulation study. Due to the increase in developed numerical algorithms and computational capabilities of computers in recent years, the mechanical behaviour of various structural elements has been investigated by simulation studies. However the significance of experimental has not diminished, which are now used to investigate the effect of different parameters on rotating disk behaviour. The parameters included are numerous and some of them are strength and ductility (Holms and Jenkins (1948)), strength and ductility in presence of material and fabrication defects (Holms et al. (1951)), temperature gradient (Wilterdink et al. (1952)), etc. The experimental investigations provided excellent practical insights into the behaviour of rotating disks.

The credit for initiating an experimental analysis probably goes to Robinson (1944) when he tested solid and annular disks of both constant thickness and conical profile. He evolved a semi-empirical criterion according to which bursting of disk is supposed to occur only when the average tangential stress was at par with the tensile strength of the material. Skidmore (1951) further extended the criterion by conducting a series of experiments and confirmed the results

proposed by Robinson (1944). Waldren et al. (1965) conducted experiments on bursting of rotating disks made of vacuum melted steel and on comparing the theoretical and experimental results concluded that the large plastic strains that occurred were in proportion with the strain predicted using plasticity theory. Further burst test experiments in vacuum were carried out by Percy et al. (1974) on disks made of vacuum melted disks and the permanent strain distributions along with instability and fracture conditions were observed. The experimental results were compared with theoretical ones and good correlation was obtained for ratio of radii exceeding 10. It was also observed that for annular disks of uniform thickness, at instability, the bore bifurcates into an oval shape due to formation of two necks at the bore. In a recent work, Maziere et al. (2009) investigated the bursting of turbo-engine disk both experimentally and computationally in case of over speed for twin disks made of the nickel based super-alloy.

## **2.6 Summary**

A detailed literature survey in the proposed area of research has been carried out and presented in the preceding sections which lead to the identification of the present scope of work. Literature is abundant with studies on static analysis of rotating disks in elastic regime subjected to different loading conditions. With regards to material nonlinearity, static analysis in post-elastic regime under thermo-mechanical loading is dealt with in quite a few of the works reviewed.

Review of existing literature reveals that studies of elasto-plastic analysis of statically determinate bars have been carried out by various analytical and numerical methods. However, research work on post-elastic analysis of statically indeterminate bars is scarce and research work addressing complete post-elastic analyses of non-uniform bars by using domain decomposition technique based on a direct variational method is not reported in the literatures. It is also noted that emphasis on stress and deformation problem of uniform geometry bar subjected to thermal loading is mainly addressed in elastic domain only and literatures clarifying elasto-plastic behaviour of clamped non-uniform bars under thermo-mechanical loading are rare.

There exist in published literature, a plethora of studies on investigation of elastic and thermo-elastic analysis of rotating disks. Based on the literature review as presented above, it is evident that many researchers have concentrated their attention on investigating behaviour of engineering structures made of FGMs for over the last decade. Due to several advantages of

## *Chapter 2*

FGMs in terms of high strength and toughness as well as thermal and corrosive resistances, the materials have attracted interest from researchers continuously to further investigate more significant features. The power law distribution has been used widely to define effective material properties of FGMs. Very few reports dealing with elasto-plastic stress analysis of FG disks under thermo-mechanical loading were found in literature. Moreover, there is no dedicated work on plastic limit speed and plastic limit temperature under thermo-mechanical loading. Most of them presented only the results for elastic and thermo-elastic stress analysis of FG disks.

## **ELASTIC LIMIT ANGULAR SPEED OF ROTATING DISKS UNDER THERMO-MECHANICAL LOADING**

### **3.1 Introduction and literature review**

Rotating disks are important components in various mechanical applications such as circular saws, disk brakes, hard disks, steam and gas turbine rotors, flywheels, gears, centrifugal compressors, internal combustion engines and in aerospace industries. Mechanical design of disks involves the evaluation of centrifugal and thermal stresses and they need to be designed for approximate uniform stress distributions. The basic idea behind carrying out a limit elastic analysis is to study stress and deformation behaviour of structural elements up to limit state of elasticity beyond which an infinitesimal increment of load causes the onset of yielding. The corresponding load at which yielding is initiated is termed as limit elastic load. For rotating disks, the most important design parameter of a rotating disk is its operating range of angular speed. The operating speed at which onset of yield is observed in a rotating disk is called limit elastic speed. The dimensionless angular speed corresponding to the onset of yielding is defined as normalized limit angular speed and has been considered as one of the most important design parameters.

The analyses of stresses and strains of these rotating elements have been investigated by many authors and researchers. The closed form analytical solution only deals with homogeneous disk with uniform thickness and constant material properties. However, the analytical solution of disks with variable thicknesses, variable material properties, etc., is usually difficult to find. Various types of theoretical, semi-analytical or numerical methods are used to solve complicated problems involving different thickness profiles, variation in mechanical and physical properties and boundary conditions, etc. The behavior of rotating disks under high temperature had been investigated by Thompson (1946) wherein he gave a numerical approach to the turbine disk problem by taking into account point to point variation in disk thickness and in all other physical properties except Poisson's ratio. In structural design procedure, it is inevitable that the estimation of the stress distribution and the angular velocity of a rotating disk in a fully plastic state is important and found momentum in 1980s where several researchers employed the Tresca yield criterion. Gamer (1983) pointed out that the displacement field calculated according to

Tresca's criterion and its associated flow rule at the elasto-plastic interface of a rotating disk, was discontinuous and a negative plastic strain caused by a tensile stress. To solve this problem, Gamer (1984, 1985) suggested an additional linear strain hardening for a rotating disk of constant thickness of elastic plastic material with a state of plane stress. Rees (1999) applied von Mises criteria and its associated flow rule to avoid the insufficiency of Tresca solution in the elasto-plastic stress distribution of rotating disk by using a numerical iteration method. Tresca's yield condition has been found to predict slightly lower limit angular velocities than that of von Mises. The idea was extended by Eraslan (2003) in presenting an analytical solution for elastic-plastic deformation of rotating variable thickness annular disks with free, pressurized and radially constrained boundary conditions.

Analysis of elastic stress state in rotating disks up to the point of yielding with the objective to determine limit angular speed has also been carried out. Vivio and Vullo (2007) and Vullo and Vivio (2008) studied the stresses and strains in variable thickness annular and solid rotating elastic disks subjected to thermal loads and having a variable density along the radius. Hojjati and Jafari (2008) reported approximate solutions of similar problems in the form of an infinite power series for nonlinear equations, by using Adomian's decomposition method (ADM). Bhowmick et al. (2008) performed an energy functional based numerical analysis to obtain limit angular speed for externally loaded rotating disks of non-uniform thickness. Chen and Fang (2011) studied the non-axisymmetric warping of a clamped-free heavy disk. The von Karman's plate model was adopted to derive the equations of motion and for the experimental study, a floppy disk was used to demonstrate the non-axisymmetric deformations when the disk is either stationary or rotating. Nejad et al. (2014) determined the stresses and displacements in a rotating cylindrical shell with variable thickness under uniform pressure by using a semi-analytical solution. In this analysis, the thick cylinder was divided into disk from layers with their thickness corresponding to the thickness of the cylinder. The governing equations of the disk layers were obtained based on first-order shear deformation theory due to the existence of shear stress in the thick cylindrical shell. Danesh and Asghari (2014) investigated the mechanical behaviour of micro-rotating disks by using strain gradient theory. The governing equations and boundary conditions were derived with the use of variational method.

In the present chapter, the influence of thermo-mechanical loading on stresses and deformation states in a rotating disk with varying thicknesses is investigated. For this purpose, a



numerical method based on variational principle has been proposed to formulate the problem and to obtain an approximate solution of the unknown displacement field from the governing equation. MATLAB<sup>®</sup> computational simulation software is used to implement the solution algorithm. The analysis is carried out for various disk geometries and temperature distribution profiles. Limit angular speed of the disks is calculated under thermo-mechanical loading and reported in dimensional form as limit peripheral speed and dimensionless form as normalized limit angular speed. The effect of temperature on yield stress and subsequently on the limit peripheral speed is also studied for any given temperature distribution and results are furnished in dimensional form. The effects of temperature field on other material properties are also studied. The results of some reduced problems are validated with those available in literature and very good agreement is observed. The new results, furnished graphically as design monograms, might prove helpful for the practicing engineers.

### **3.2 Mathematical formulation**

In the development of the mathematical model, it is assumed that the disk material is homogeneous, isotropic and linear elastic. For the problem under consideration, a response analysis of thermo-elastic stresses is investigated within the framework of small deformation. The disk is thin, symmetric with respect to the mid-plane and plane stress ( $\sigma_z = 0$ ) assumption is justified.

Radial displacements will occur in a rotating disk, due to the both centrifugal load and thermal load. Besides the magnitude of loading, the radial displacement field is also governed by the boundary conditions of the disk. The solution for the displacement field is obtained from the minimum total potential energy principle,  $\delta(U + V) = 0$ , where  $U$  is the strain energy stored in the disk and  $V$  is the potential energy arises both from centrifugal force and thermal load. It is already stated that the material of the disk is isotropic, so the thermal strain at any location of the disk is same in all the directions. If  $\alpha$  is thermal expansion coefficient and  $T(r)$  is the change in temperature at any radius  $r$ , then the thermal strain is given by  $\varepsilon^* = \alpha T(r)$ .

The total strain is obtained by adding the elastic strain and the thermal strain. Thus, the components of the total strain are given by  $\varepsilon_r = e_r + \varepsilon^*$  and  $\varepsilon_\theta = e_\theta + \varepsilon^*$ , where  $\varepsilon_r$  and  $\varepsilon_\theta$  denote the radial and circumferential components, respectively, with respect to the total strain

and  $e_r$  and  $e_\theta$  are the radial and circumferential components of the elastic strain. The elastic strain components are related to stresses by Hooke's law and thus the expression of total strain components become,  $\varepsilon_r = (\sigma_r - \nu\sigma_\theta)/E + \alpha T(r)$  and  $\varepsilon_\theta = (\sigma_\theta - \nu\sigma_r)/E + \alpha T(r)$ , where  $E$  and  $\nu$  are elastic modulus and Poisson's ratio. For axisymmetric problems with small strains, the relations between strains and radial displacement are given by  $\varepsilon_r = du/dr$  and  $\varepsilon_\theta = u/r$ . The total strain energy that comes from the stress and strain field of the disk, and expressed as

$$\Pi = \frac{1}{2} \int_{Vol} (\sigma\varepsilon) dv = \frac{1}{2} \int_{Vol} (\sigma_r \varepsilon_r + \sigma_\theta \varepsilon_\theta) dv. \quad (3.1)$$

Substituting the relations between stress-strain and strain-displacement, Eq. (3.1) becomes,

$$\Pi = \frac{\pi E}{(1-\nu^2)} \int_a^b \left\{ \frac{u^2}{r} + 2\nu u \frac{du}{dr} + r \left( \frac{du}{dr} \right)^2 - (1+\nu)\alpha T r \left( \frac{u}{r} + \frac{du}{dr} \right) \right\} h dr. \quad (3.2)$$

Here the total energy  $\Pi$  is decomposed into two parts. One part is the strain energy  $U$  and the other part is the potential energy  $V$ . The first part of potential energy  $V_{\text{centrifugal}}$  comes from centrifugal force field, while the second part  $V_{\text{thermal}}$ , comes from the thermal load. The expressions for  $U$ ,  $V_{\text{centrifugal}}$  and  $V_{\text{thermal}}$  are given below.

$$U = \frac{\pi E}{(1-\nu^2)} \int_a^b \left\{ \frac{u^2}{r} + 2\nu u \frac{du}{dr} + r \left( \frac{du}{dr} \right)^2 \right\} h dr \quad (3.3)$$

$$V_{\text{centrifugal}} = -2\pi\rho\omega^2 \int_a^b ur^2 h dr \quad (3.4)$$

$$V_{\text{thermal}} = -\frac{2\pi E}{(1-\nu^2)} (1+\nu)\alpha \int_a^b r \left( \frac{u}{r} + \frac{du}{dr} \right) T h dr \quad (3.5)$$

So, the expression for potential energy  $V$  under combined loading becomes,

$$V = -2\pi\rho\omega^2 \int_a^b ur^2 h dr - \frac{2\pi E}{(1-\nu^2)} (1+\nu)\alpha \int_a^b r \left( \frac{u}{r} + \frac{du}{dr} \right) T h dr. \quad (3.6)$$

On substitution of Eqs. (3.1) and (3.6) in the energy principle  $\delta(U+V)=0$ , the governing equilibrium equation is obtained as,

$$\delta \left[ \frac{\pi E}{(1-\nu^2)} \int_a^b \left\{ \frac{u^2}{r} + 2\nu u \frac{du}{dr} + r \left( \frac{du}{dr} \right)^2 \right\} h dr - 2\pi \rho \omega^2 \int_a^b u r^2 h dr - \frac{2\pi E(1+\nu)\alpha}{(1-\nu^2)} \int_a^b r \left( \frac{u}{r} + \frac{du}{dr} \right) T h dr \right] = 0. \quad (3.7)$$

Eq. (3.7) is expressed in normalized co-ordinate,  $\xi = (r-a)/(b-a)$  and using the notation  $\bar{r} = b-a$ , it takes the following form,

$$\delta \left[ \frac{E\bar{r}}{(1-\nu^2)} \int_0^1 \left\{ \frac{u^2}{(\bar{r}\xi+a)} + \frac{2\nu u}{\bar{r}} \left( \frac{du}{d\xi} \right) + \frac{(\bar{r}\xi+a)}{\bar{r}^2} \left( \frac{du}{d\xi} \right)^2 \right\} h d\xi - 2\rho\omega^2 \bar{r} \int_0^1 (\bar{r}\xi+a)^2 u h d\xi - \frac{2E(1+\nu)\alpha\bar{r}}{(1-\nu^2)} \int_0^1 (\bar{r}\xi+a) \left( \frac{u}{(\bar{r}\xi+a)} + \frac{du}{\bar{r}d\xi} \right) T h d\xi \right] = 0. \quad (3.8)$$

The boundary conditions of the displacement function  $u(\xi)$  for a solid disk are  $u|_{(0)} = 0$  and  $\sigma_r|_{(b)} = 0$ , whereas for an annular disk, these conditions are  $\sigma_r|_{(a)} = 0$  and  $\sigma_r|_{(b)} = 0$ . The necessary displacement function used to generate the higher order orthogonal functions that satisfies above boundary conditions are given below, for solid and annular disks.

$$\phi_o(r) = \frac{\rho\omega^2 r(3+\nu)}{8E} \left[ b^2(1-\nu) - \left\{ \frac{(1-\nu^2)r^2}{(3+\nu)} \right\} \right] + \frac{\alpha}{r} \left[ (1+\nu) \int_a^r T(r) r dr + \frac{(1-\nu^2)r^2}{b^2} \int_a^b T(r) r dr \right] \quad (3.9a)$$

$$\phi_o(r) = \frac{\rho\omega^2 r(3+\nu)}{8E} \left[ (b^2 + a^2)(1-\nu) - \left\{ \frac{(1-\nu^2)r^2}{(3+\nu)} \right\} + b^2 a^2 \frac{(1+\nu)}{r^2} \right] + \frac{\alpha}{r} \left[ (1+\nu) \int_a^r T(r) r dr + \frac{(1-\nu^2)r^2 + (1+\nu)a^2}{b^2 - a^2} \int_a^b T(r) r dr \right] \quad (3.9b)$$

For computational purpose, the set of orthogonal functions are used to approximate the displacement function  $u(\xi)$  as follows,

$$u(\xi) \cong \sum c_i \phi_i, i = 1, 2, \dots, n. \quad (3.10)$$

Function  $\phi_o(r)$  is normalized and the governing equation in matrix form is obtained by substituting Eq. (3.10) in Eq. (3.8).

$$\delta \left[ \frac{E\bar{r}}{(1-\nu^2)} \int_0^1 \left\{ \frac{(\sum c_i \phi_i)^2}{(\bar{r}\xi + a)} + \frac{2\nu}{\bar{r}} \left[ (\sum c_i \phi_i) \frac{d(\sum c_j \phi_j)}{d\xi} \right] + \frac{(\bar{r}\xi + a)}{\bar{r}^2} \left( \frac{d(\sum c_i \phi_i)}{d\xi} \right)^2 \right\} hd\xi \right. \\ \left. - 2\rho\omega^2 \bar{r} \int_0^1 \left\{ (\bar{r}\xi + a)^2 (\sum c_j \phi_j) \right\} hd\xi - \frac{2E\alpha\bar{r}}{(1-\nu)} \int_0^1 \left\{ (\sum c_j \phi_j) + \frac{(\bar{r}\xi + a)}{\bar{r}} \frac{d(\sum c_j \phi_j)}{d\xi} \right\} Thd\xi \right] = 0. \quad (3.11)$$

Replacing operator ‘ $\delta$ ’ in Eq. (3.11) by  $\partial/\partial c_j, j=1,2,\dots,n$  the governing yields according to Galerkin’s error minimization principle as,

$$\frac{E\bar{r}}{(1-\nu^2)} \sum_{i=1}^n \sum_{j=1}^n c_i \int_0^1 \left\{ \frac{\phi_i \phi_j}{(\bar{r}\xi + a)} + \frac{\nu}{\bar{r}} (\phi_i' \phi_j + \phi_i \phi_j') + \frac{(\bar{r}\xi + a)}{\bar{r}^2} \phi_i' \phi_j' \right\} hd\xi \\ = \rho\omega^2 \bar{r} \sum_{j=10}^n \int_0^1 \left\{ (\bar{r}\xi + a)^2 \phi_j \right\} hd\xi + \frac{E\alpha}{(1-\nu)} \sum_{j=10}^n \int_0^1 \left\{ \phi_j \bar{r} + (\bar{r}\xi + a) \phi_j' \right\} Thd\xi, \quad (3.12)$$

where ( )' indicates differentiation with respect to normalized coordinate  $\xi$ . Eq. (3.12) can be expressed as  $[K]\{c\} = \{f\}$ , which yields the solution vector  $\{c_i\}$  through a single step matrix inversion process. The problem considered in the present paper is von-Mises yield criterion under plane stress can be written in the form

$$\sigma_{vm}^2 = \sigma_r^2 - \sigma_r \sigma_\theta + \sigma_\theta^2 \geq \sigma_y^2. \quad (3.13)$$

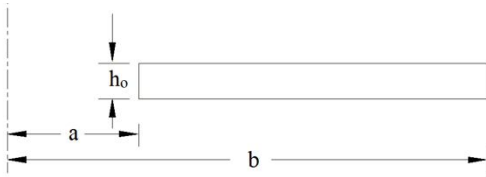
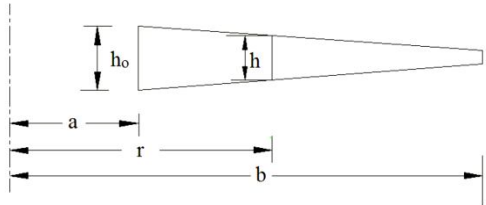
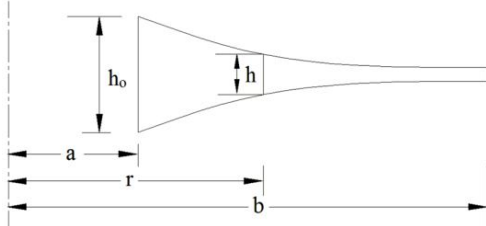
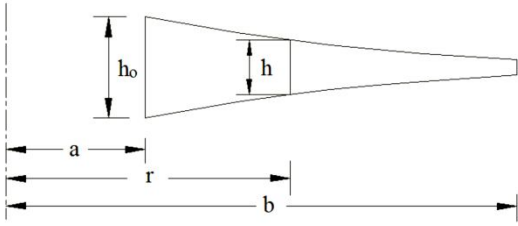
From the solution vector of Eq. (3.12), the resulting displacement field is post-processed to determine the von-Mises stress corresponding to the thermal and centrifugal loading. The loading is initiated at low values and increments are provided until the condition of yielding is reached.

### 3.3 Results and discussion

The effect of temperature on the limit angular speed for any given temperature distribution and boundary conditions are established in the present study. The analysis is carried out for four different profiles of disk, uniform, taper, exponential and parabolically varying thickness. The expression for an exponentially varying disk given by  $h(\xi) = h_o \exp[-n(\xi)^k]$ , whereas for a parabolically varying disk the expression becomes,  $h(\xi) = h_o [1 - n(\xi)^k]$ , where  $h_o$  indicates disk thickness at the inner radius of the disk. With the form of disk profile function for

parabolic thickness variation, a uniform thickness disk is obtained by setting  $n = 0$  and a linearly varying thickness (taper) is obtained by setting  $k = 1$ . The profiles considered in this study are derived by using constant volume criteria, which would help to characterize the performance of the disk. The thickness of the uniform disk is taken as 5% of its outer radius and corresponding to this volume, other disk profiles are calculated. It is further assumed that for disks of varying thickness, the tip thickness is 1% of outer radius. This particular assumption is indeed necessary to determine the geometry parameters  $n$  and  $k$ , as shown in Table 3.1.

**Table 3.1:** Disk geometry

<p style="text-align: center;">Uniform <math>\{h_o = 0.03\text{m}\}</math></p> 	<p style="text-align: center;">Taper <math>\left\{ \begin{array}{l} h_o = 0.075\text{ m} \\ k = 1 \\ n = 0.92 \end{array} \right\}</math></p> 
<p style="text-align: center;">Exponential <math>\left\{ \begin{array}{l} h_o = 0.12\text{ m} \\ k = 1.19 \\ n = 2.99 \end{array} \right\}</math></p> 	<p style="text-align: center;">Parabolic <math>\left\{ \begin{array}{l} h_o = 0.09\text{ m} \\ k = 0.43 \\ n = 0.95 \end{array} \right\}</math></p> 

The dimensionless angular speed,  $\omega_y b \sqrt{\rho/\sigma_y}$  corresponding to the onset of yielding is defined as normalized limit angular speed ( $\bar{\omega}_y$ ) and considered as the design parameter for disks under uniform temperature environment. The analysis is also carried out for various varying temperature profiles following uniform, linear, exponential and parabolic temperature distribution, as expressed in Eq. (3.14) and shown in Figure 3.1(a) and (b). It may be noted that

the mathematical relations for the four types of temperature distributions are not identical with that of the thickness distribution relations.

In the definition of dimensionless angular speed  $\omega_y b \sqrt{\rho/\sigma_y}$ , it is assumed that the disk material properties  $E$ ,  $\rho$ ,  $\sigma_y$ ,  $\alpha$  and  $\nu$  remain constant in the variable thermal field  $T(r)$ . The preliminary part of the study is carried out based on this assumption but in the later part, when the disk material properties are assumed to be function of thermal field  $T(r)$ , dimensional value of limit angular tip speed,  $\omega_y b$  in (m/s) is used as the design parameter. The numerical analysis of the present study is carried out by considering system parameter values as,  $E = 210$  GPa,  $\nu = 0.3$ ,  $\rho = 7800$  Kg/m<sup>3</sup>,  $\alpha = 11.5 \times 10^{-6}$  °C<sup>-1</sup> and initial yield stress  $\sigma_y = 350$  MPa.

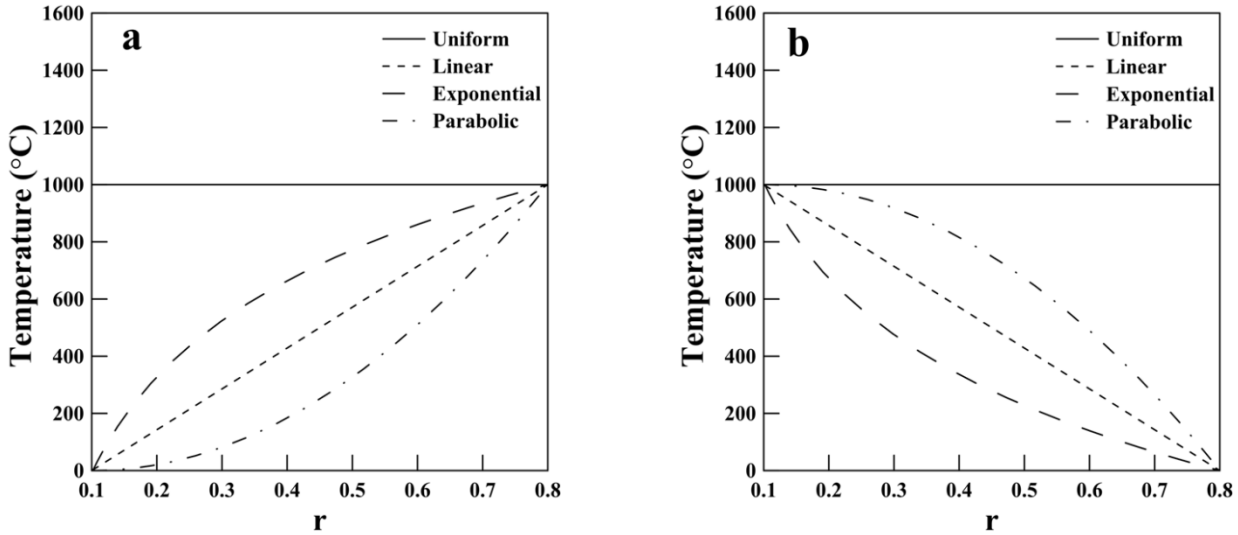


**Figure 3.1.** Rotating disk under various temperature distribution profiles for (a) specified outer surface temperature ( $T_b$ ) and (b) specified inner surface temperature ( $T_a$ ).

$$\text{Uniform: } T(\xi) = T_a \text{ or } T_b \quad (3.14a)$$

$$\text{Linear: } T(\xi) = T_a + (T_b - T_a)\xi \quad (3.14b)$$

$$\text{Exponential: } T(\xi) = \frac{(T_b - T_a) \ln(b/\xi)}{\ln(b/a)} + T_b \quad (3.14c)$$

$$\text{Parabolic: } T(\xi) = T_a + (T_b - T_a)\xi^2 \quad (3.14d)$$

The temperature field pattern is a function of temperature boundary conditions also. Two different, increasing and decreasing, temperature boundary conditions are assumed i)  $T_a = 0\text{ }^\circ\text{C}$ ,  $T_b = 1000\text{ }^\circ\text{C}$  and ii)  $T_a = 1000\text{ }^\circ\text{C}$ ,  $T_b = 0\text{ }^\circ\text{C}$ , where  $T_a$  and  $T_b$  are the inner and outer surface temperature of the isotropic disk at  $r = a$  and  $r = b$  respectively. The temperature distribution profiles, shown in Figure 3.1(a) and (b), correspond to these two boundary conditions.

### 3.3.1 Convergence and validation of the formulation

First a convergence study for the adequate number of functions is carried out on normalized limit angular speed for a uniform disk and is reported in Figure 3.2. It is observed that the normalized limit angular speed minimizes with the number of functions and the figure shows that a good convergence is achieved with nine functions and hence the subsequent computation for various parameter variations is carried out with 11 coordinate functions. The computational time as shown in the figure is also a governing criterion for selection of the number of functions. All the functions are denoted numerically by using 24 Gauss points.

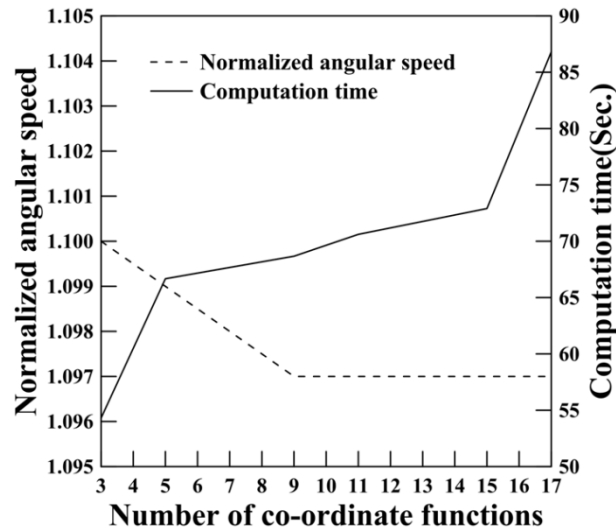


**Figure 3.2.** Plot of convergence of normalized limit angular speed with co-ordinate functions.

The validation of the present numerical scheme is made with the results of Vivio and Vullo (2007) and is presented in Figures 3.3(a)-(f). The numerical values of the system parameters used in the validation study of steel turbine rotors are  $E=204\text{ GPa}$ ,  $\nu=0.3$ ,

$\rho = 7800 \text{ Kg/m}^3$ ,  $\alpha = 12 \times 10^{-6} \text{ }^\circ\text{C}^{-1}$ . Figure 3.3(a) shows the comparison for displacement field and radial and tangential stresses for steel solid conical disk of constant density under constant rotational speed,  $\omega = 314 \text{ rad/s}$ . The outer radius,  $b = 0.8 \text{ m}$  and thickness are  $h_a = 0.1 \text{ m}$  and  $h_b = 0.02 \text{ m}$  respectively. Figure 3.3(b) shows the comparison for steel annular conical disk of constant density with  $a = 0.1 \text{ m}$ ,  $b = 0.8 \text{ m}$ ,  $h_a = 0.09 \text{ m}$  and  $h_b = 0.02 \text{ m}$ . The disk is rotating at angular velocity,  $\omega = 314 \text{ rad/s}$  and not loaded either at outer or at inner surfaces. Figure 3.3(c) shows the comparison for annular conical disk under thermal loading only, featuring the same disk geometry as in the case of Figure 3.3(b), not loaded either at inner surface or at outer surface and subjected to a temperature gradient along its radius according to polynomial  $T(r) = T_o + K_1 r + K_2 r^2 + K_3 r^3$  where  $T_o = 20 \text{ }^\circ\text{C}$ ,  $K_1 = 10^{-2} \text{ }^\circ\text{C/mm}$ ,  $K_2 = 10^{-4} \text{ }^\circ\text{C/mm}^2$  and  $K_3 = 10^{-7} \text{ }^\circ\text{C/mm}^3$ . Figure 3.3(d) shows the comparison for annular conical disk not subjected to thermal load, but rotating at angular velocity,  $\omega = 314 \text{ rad/s}$  and having variable density along its radius according to density distribution  $\rho(r) = \rho_o + \rho_1 r + \rho_2 r^2 + \rho_3 r^3$  where  $\rho_o = 7800 \text{ Kg/m}^3$ ,  $\rho_1 = 10 \text{ Kg/m}^3$ ,  $\rho_2 = 100 \text{ Kg/m}^3$ , and  $\rho_3 = 1000 \text{ Kg/m}^3$ . The rotating annular disk featuring the same disk geometry as in the case of Figure 3.3(b). Figure 3.3(e) shows the comparison for displacement field and radial and tangential stresses for rotating annular conical disk of variable density under thermal load with angular velocity,  $\omega = 314 \text{ rad/s}$ .  $T = T(r)$  and  $\rho = \rho(r)$  variation is same as in previous cases. In all the cases a fairly good agreement is obtained.

### 3.3.2 Effect of temperature distributions

The effect of temperature distributions ( $T_b$ ) on the normalized limit angular speed ( $\bar{\omega}_y$ ) is presented in Figures 3.4(a)-(d) for annular disks and in each figure, variation is shown for four different disk geometries.



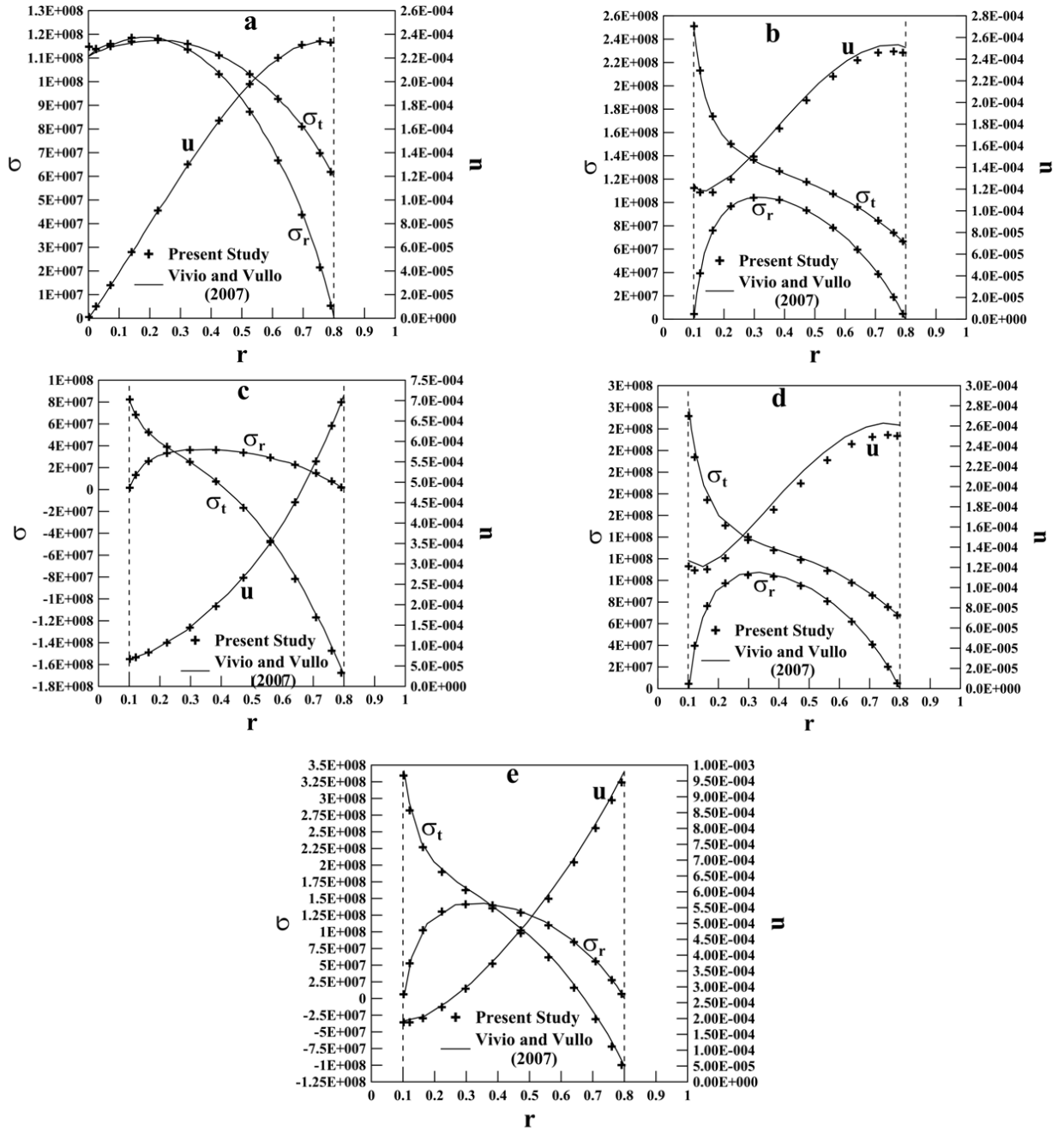


**Figure 3.3.** Comparison of displacement ( $u$ ), radial ( $\sigma_r$ ) and tangential stresses ( $\sigma_t$ ) for: (a) solid taper disk, (b) annular taper disk, (c) annular taper disk subjected to temperature gradient, (d) annular taper disk with density variation and (e) annular taper disk subjected to both density and temperature gradient.

The inner surface temperature  $T_a$  is set to 0 °C and the ratio of the outer radius to the inner radius ( $b/a$ ) is taken as 8. It is assumed that material properties  $E$ ,  $\alpha$ ,  $\rho$  and  $\nu$  remain constant in the variable thermal field of the disk. It is observed that with increase in outer surface temperature  $T_b$ , the normalized limit angular speed decreases for all type of disk geometries.

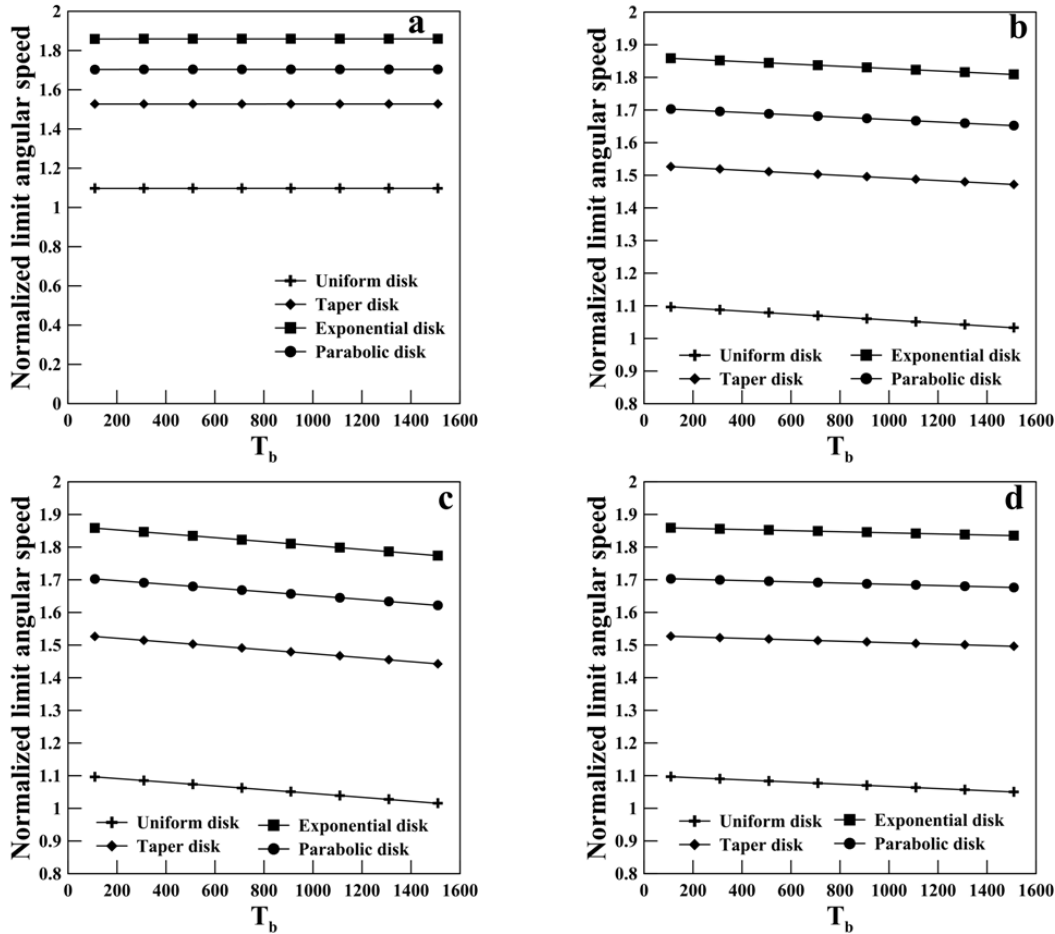


**Figure 3.4.** Plots for normalized limit angular speed ( $\bar{\omega}_y$ ) with outer surface temperature ( $T_b$ ) having different temperature distributions: (a) uniform, (b) linear, (c) exponential and (d) parabolic.

However, for uniform temperature distribution the normalized limit angular speed remains constant. Amongst the different geometries, normalized limit angular speed is maximum for exponential disk geometry. Again, in case of exponential temperature distribution, the decrease of normalized limit angular speed is prominent for different disk geometries. It is

observed in the analytical study that among all the physical parameters, co-efficient of thermal expansion  $\alpha$  has the predominant effect on the variation in  $\bar{\omega}_y$ .

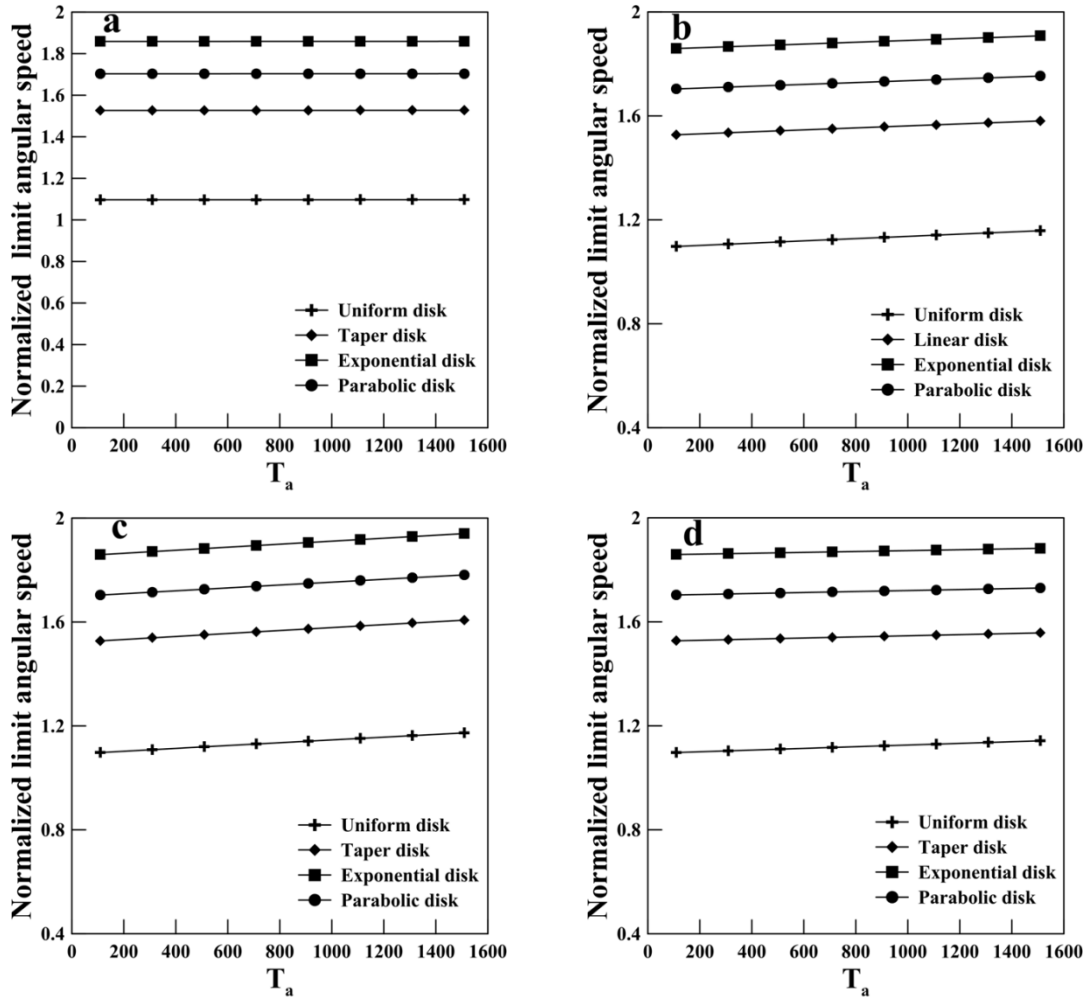


**Figure 3.5.** Plots for normalized limit angular speed ( $\bar{\omega}_y$ ) with inner surface temperature ( $T_a$ ) having different temperature distributions: (a) uniform, (b) linear, (c) exponential and (d) parabolic.

A similar study on the normalized limit angular speed variation with temperature is indicated in Figures 3.5(a)-(d), for the prescribed disk geometries and temperature distributions. Here, the inner surface temperature  $T_a$  is varied but the outer surface temperature  $T_b$  is kept fixed at 0 °C. In Figures 3.4 and 3.5, the change in material properties ( $E$ ,  $\alpha$ ,  $\rho$  and  $\nu$ ) are not considered and as obvious from Eq. (3.12) that the effect comes from thermal loading only. This thermal effect is not significant due to outer free boundary conditions.

In Figure 3.5(a), the normalized limit angular speed is constant for uniform temperature distribution as that of the previous case while in Figures 3.5(b)-(d), the normalized limit angular speed increases with increase in inner surface temperature  $T_a$  for different disk geometries for all types of temperature distributions. These figures show that the normalized limit angular speed is maximum for exponential disk geometry. The results also indicate that for exponential temperature distribution; the increase of normalized limit angular speed is prominent for different disk geometries.

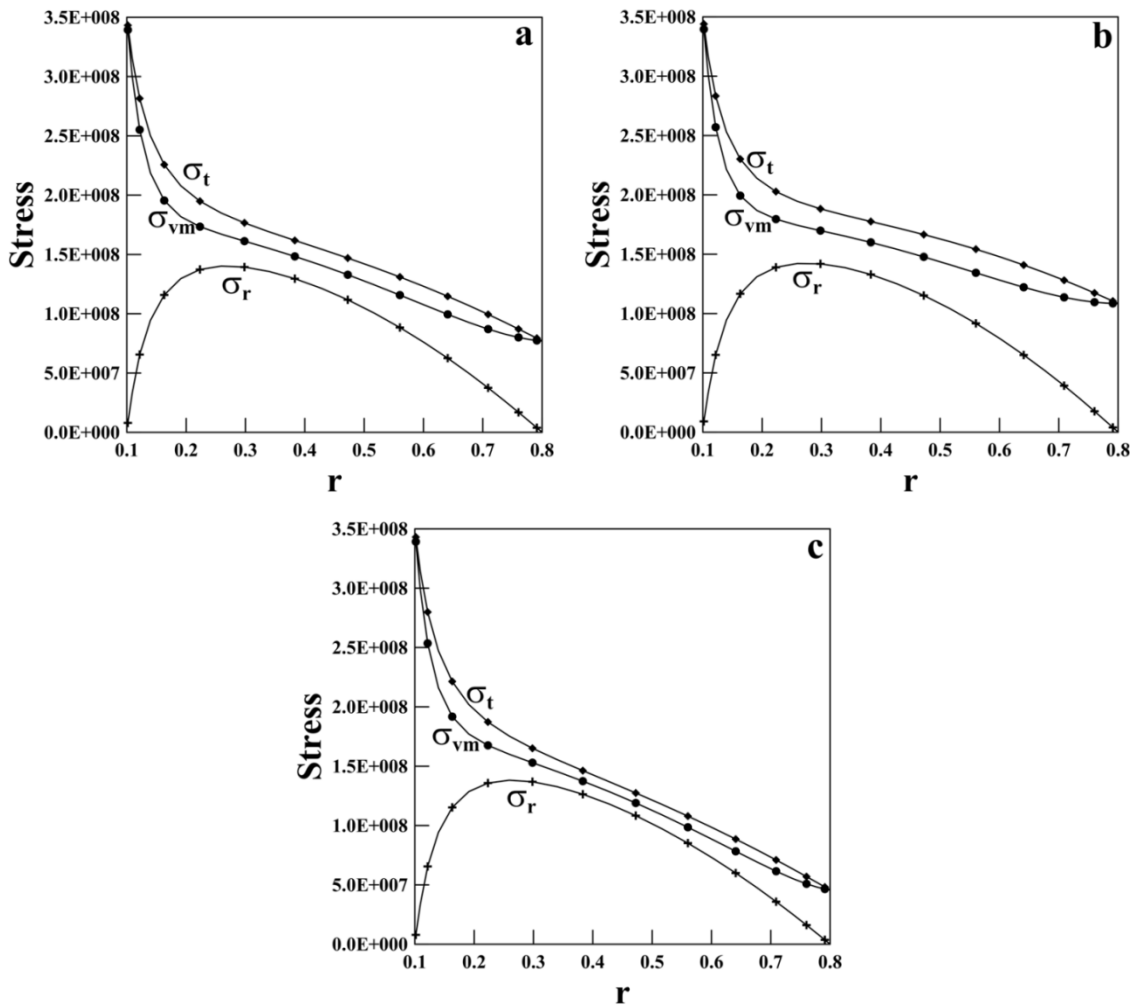


**Figure 3.6.** Distribution of radial ( $\sigma_r$ ), tangential ( $\sigma_t$ ) and von-Mises stress ( $\sigma_{vm}$ ) field corresponding to yield limit state in an annular disk subjected to (a) pure centrifugal loading due to rotation only, (b) combined loading with higher inner surface temperature ( $T_a$ ) and (c) combined loading with higher outer surface temperature ( $T_b$ ).

To explore the phenomenon in greater detail radial ( $\sigma_r$ ), tangential ( $\sigma_t$ ) and von-Mises stress ( $\sigma_{vm}$ ) fields of an annular disk ( $b/a=8$ ) is plotted in Figures 3.6(a)-(c) corresponding to the yield limit state, attained by centrifugal and the two types of thermal loading. Figure 3.6(a) indicates the stress states corresponding to limit angular speed, and Figures 3.6(b, c) considers temperature field effect corresponding to higher value of inner and outer surface temperatures, respectively. The radial stress ( $\sigma_r$ ) field is almost similar in all the cases but there is a variation in tangential stress ( $\sigma_t$ ). The reduction in tangential stress field towards the outer radius is most prominent in Figure 3.6(c), which correspond to the case of higher outer surface temperature ( $T_b$ ), whereas in Figure 3.6(b) the decrement is minimum. The tangential stress field coming from pure centrifugal loading, as shown in Figure 3.6(a), appears to be in an intermediate state. Hence the nature of variation in ( $\bar{\omega}_y$ ), as observed in Figures 3.4 and 3.5 is quite justified for combined centrifugal and thermal loading.

The effect of disk geometries on behavior of thermally loaded disks is also investigated for the normalized limit angular speed variation with temperature and shown again in Figures 3.7(a)-(d). The individual figures are for particular disk geometry and in each figure the inner surface temperature  $T_a$  is set to 0 °C and outer surface temperature  $T_b$  is varied up to 1500 °C. For all temperature distributions the normalized limit angular speed ( $\bar{\omega}_y$ ) initiate from the same initial value and decreases with increase in the surface temperature of the other boundary. However, for uniform temperature distribution, the curve remains constant. It is also seen that the decrease of normalized limit angular speed is more for exponential temperature distribution, in all the cases of different thickness profiles. Again, when the four figures are compared, it is observed that the initial value of normalized limit angular speed ( $\bar{\omega}_y$ ) is maximum for exponential disk geometry and minimum for uniform disk geometry.

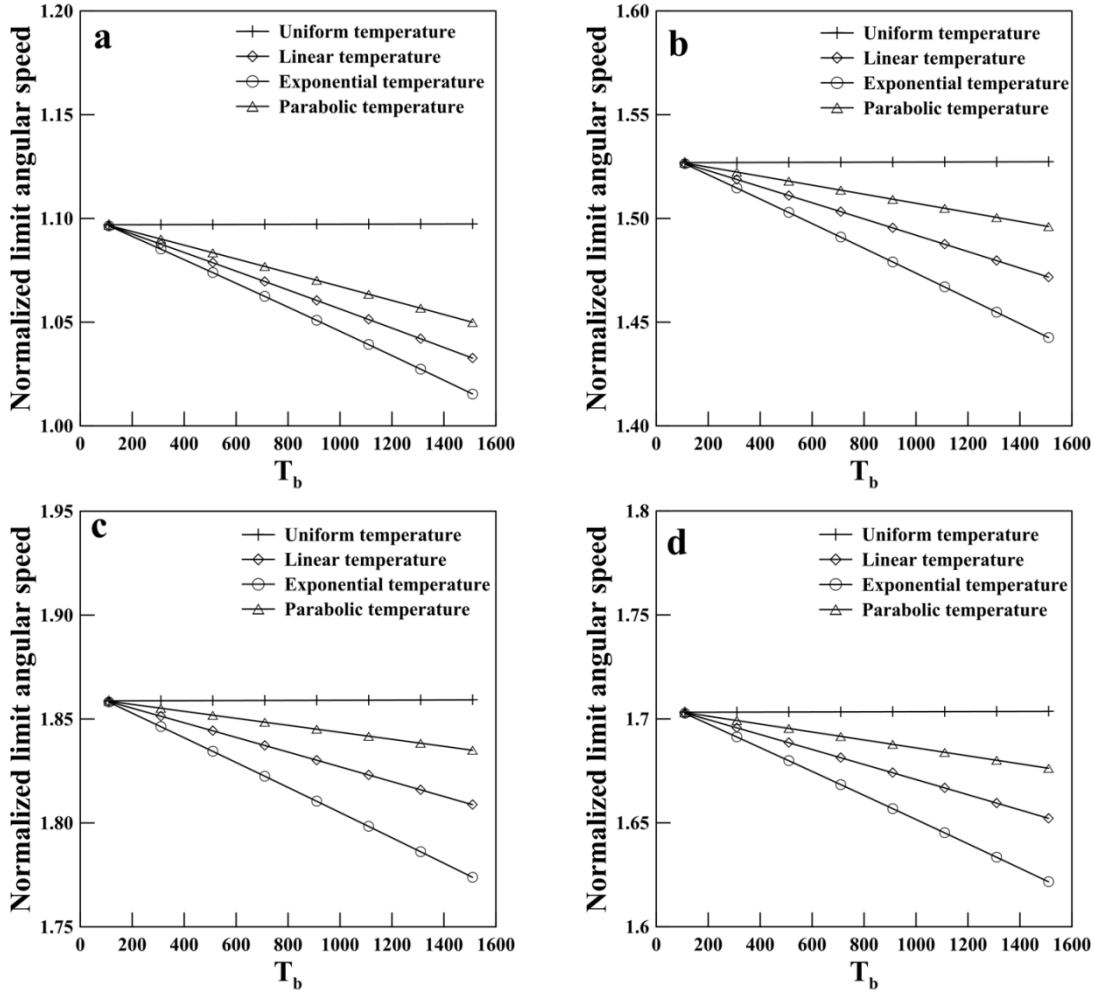


**Figure 3.7.** Effect of outer surface temperature distributions ( $T_b$ ) on normalized limit angular speed ( $\bar{\omega}_y$ ) for different disk geometries: (a) uniform, (b) taper, (c) exponential and (d) parabolic.

In Figures 3.8(a)-(d), the variations in normalized limit angular speed with increasing inner surface temperature  $T_a$  are also presented for the prescribed disk geometries and temperature distributions. Now, the outer surface temperature  $T_b$  is set to 0 °C while the inner surface temperature  $T_a$  is varied up to 1500 °C. In these figures also, the initial value of normalized limit angular speed is same for all temperature distributions and it increases with increase in the inner surface temperature, except for uniform temperature distribution. Figures 3.7 and 3.8 shows the combined effect of centrifugal and thermal load on the normalized limit angular speed ( $\bar{\omega}_y$ ) comes from linear superposition in elastic range. The combined effect is

justified by the plot for von-Mises stress ( $\sigma_{vm}$ ) in Figures 3.6(b, c). The reduction in von-Mises stress field towards the outer radius is most prominent in Figure 3.6(c), which correspond to the case of higher outer surface temperature ( $T_b$ ), whereas in Figure 3.6(b) the decrement is minimum. Hence the nature of variation in ( $\bar{\omega}_y$ ), as observed in Figures 3.7 and 3.8 is quite justified for combined centrifugal and thermal loading.

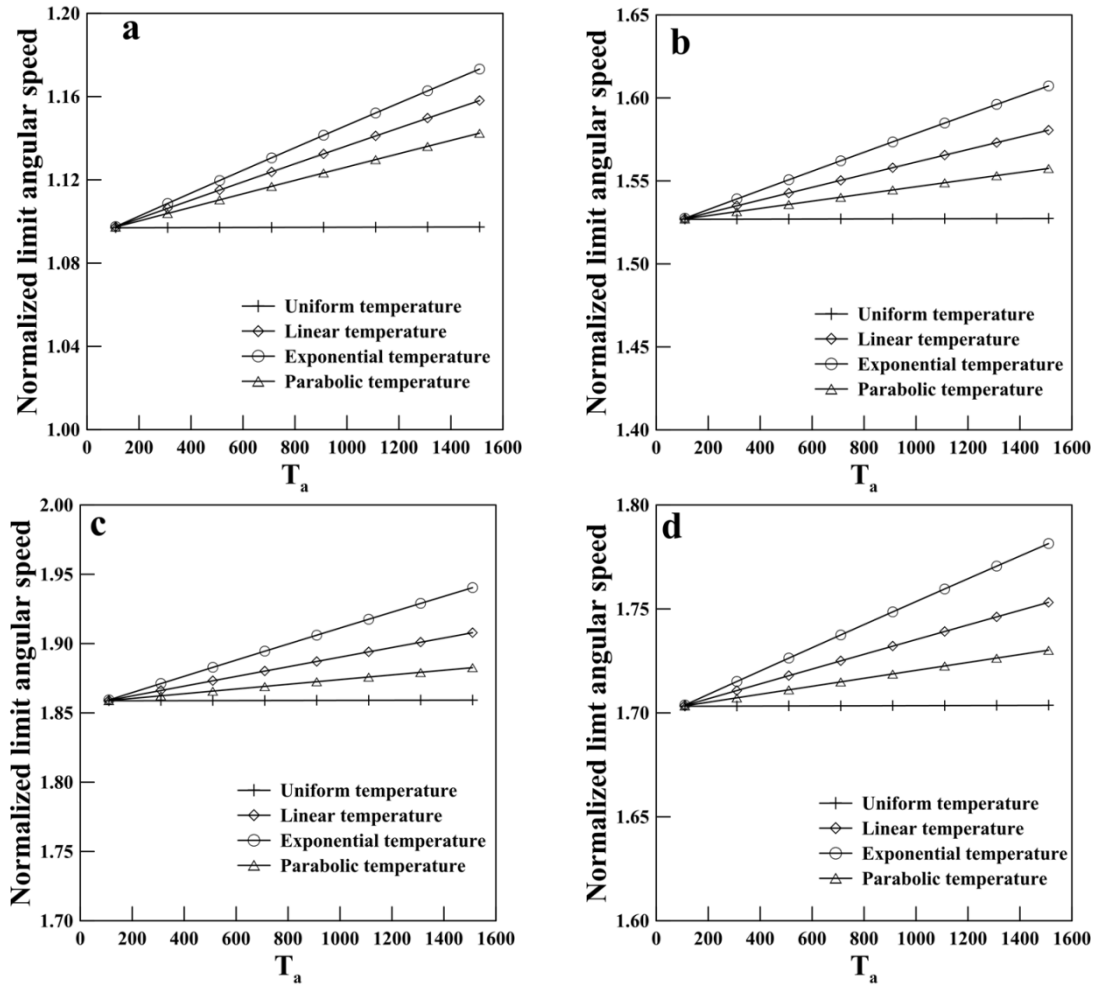


**Figure 3.8.** Effect of inner surface temperature distributions ( $T_a$ ) on normalized limit angular speed ( $\bar{\omega}_y$ ) for different disk geometries: (a) uniform, (b) taper, (c) exponential and (d) parabolic.

In the next part of the study it is assumed that the disk material properties  $\rho$ ,  $\sigma_y$  and  $E$  are functions of thermal field  $T(r)$ , and hence limit angular tip speed,  $\omega_y b$  in (m/s) is used as

the design parameter. The variations in properties are shown in Figure 3.9 for structural steel with grade S350GD+Z, following Outinen and Makelainen (2002).

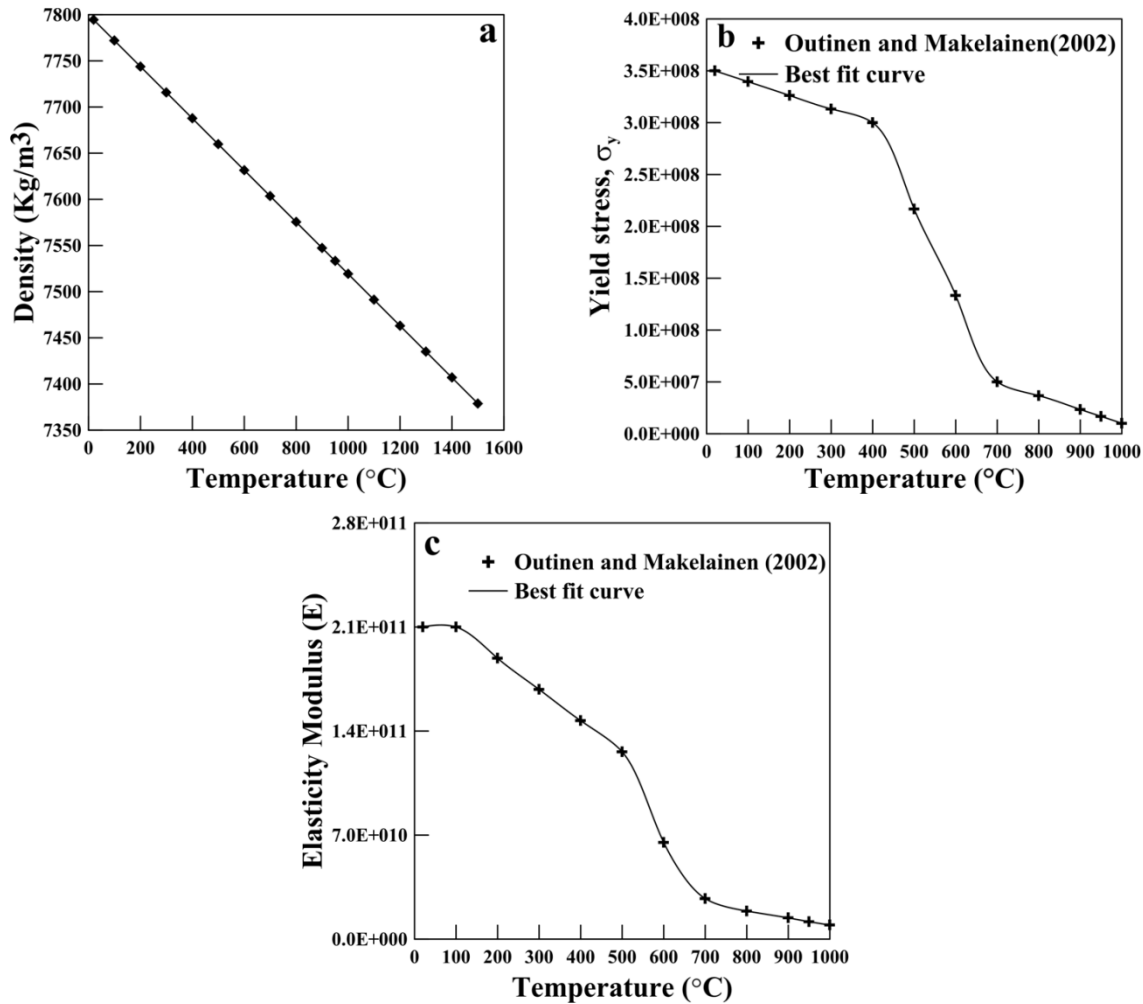


**Figure 3.9.** Variation of disk material properties  $\rho$ ,  $\sigma_y$  and  $E$  with temperature: (a) density ( $\rho$ ), (b) yield Stress ( $\sigma_y$ ) and (c) Elasticity modulus ( $E$ ) for structural steel with grade S350GD+Z at different specified temperatures.

The effect of density variation with temperature is obtained by using the relation  $\rho(r) = \rho_o [1 - \{3\alpha T(r)\}]$ , graphical representation of which is shown in Figure 3.9(a). The figure corresponds to  $\alpha = 11.5 \times 10^{-6} \text{ } ^\circ\text{C}^{-1}$ , but for other values of thermal expansion coefficient, the effect would be different. Variation in yield stress ( $\sigma_y$ ) and elasticity modulus ( $E$ ) with



temperature field is obtained by using best fit curves on the tabulated values of Outinen and Makelainen (2002).

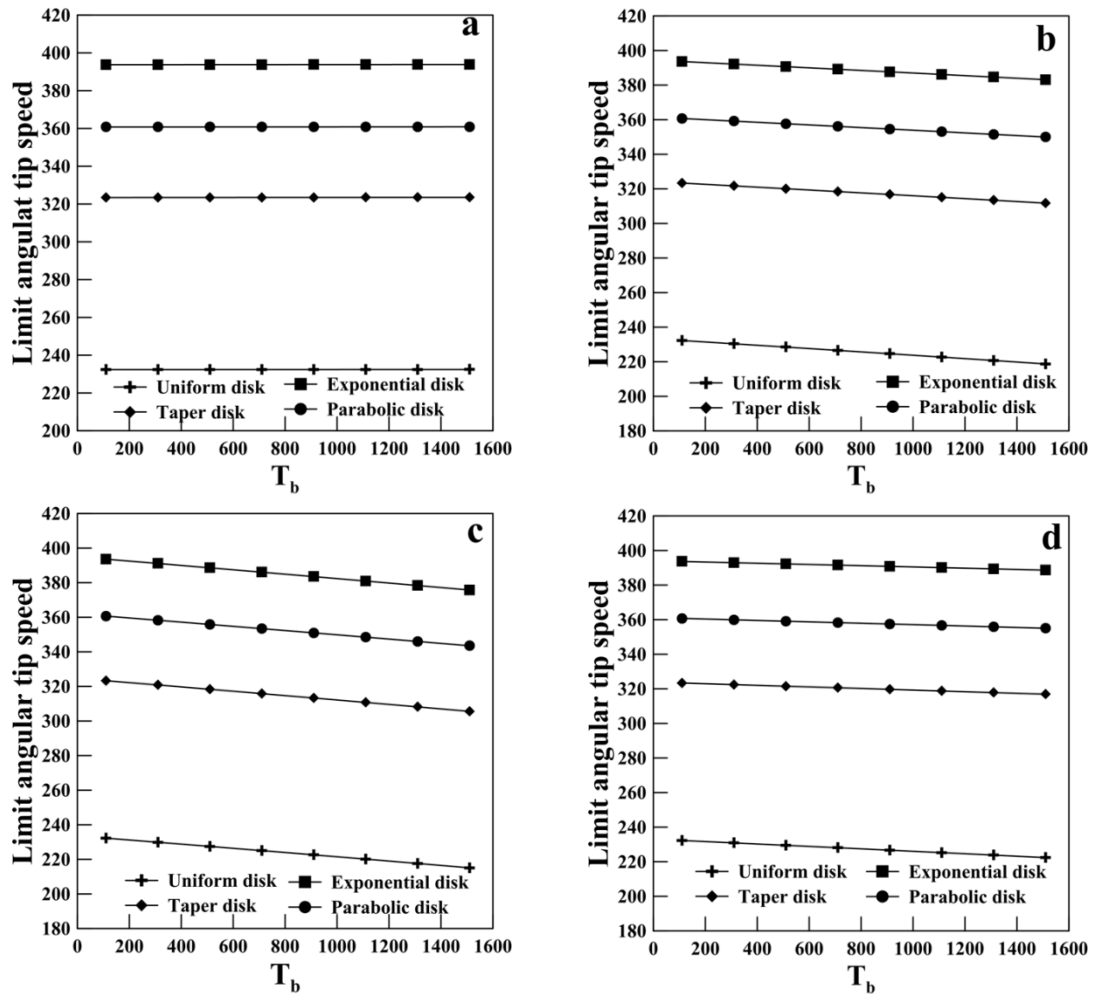


**Figure 3.10.** Effect of density variation on limit angular tip speed for different temperature distributions of outer surface  $T_b$  : (a) uniform, (b) linear, (c) exponential and (d) parabolic temperature.

### 3.3.3 Effect of temperature on the variation of density

Figures 3.10(a)-(d) show the effect of various disk geometries and temperature distributions on the limit angular tip speed ( $\omega_y b$ ), taking the temperature effect of density variation in to consideration. The inner surface temperature  $T_a$  is set to 0 °C and outer surface temperature  $T_b$  is varied up to 1600 °C.

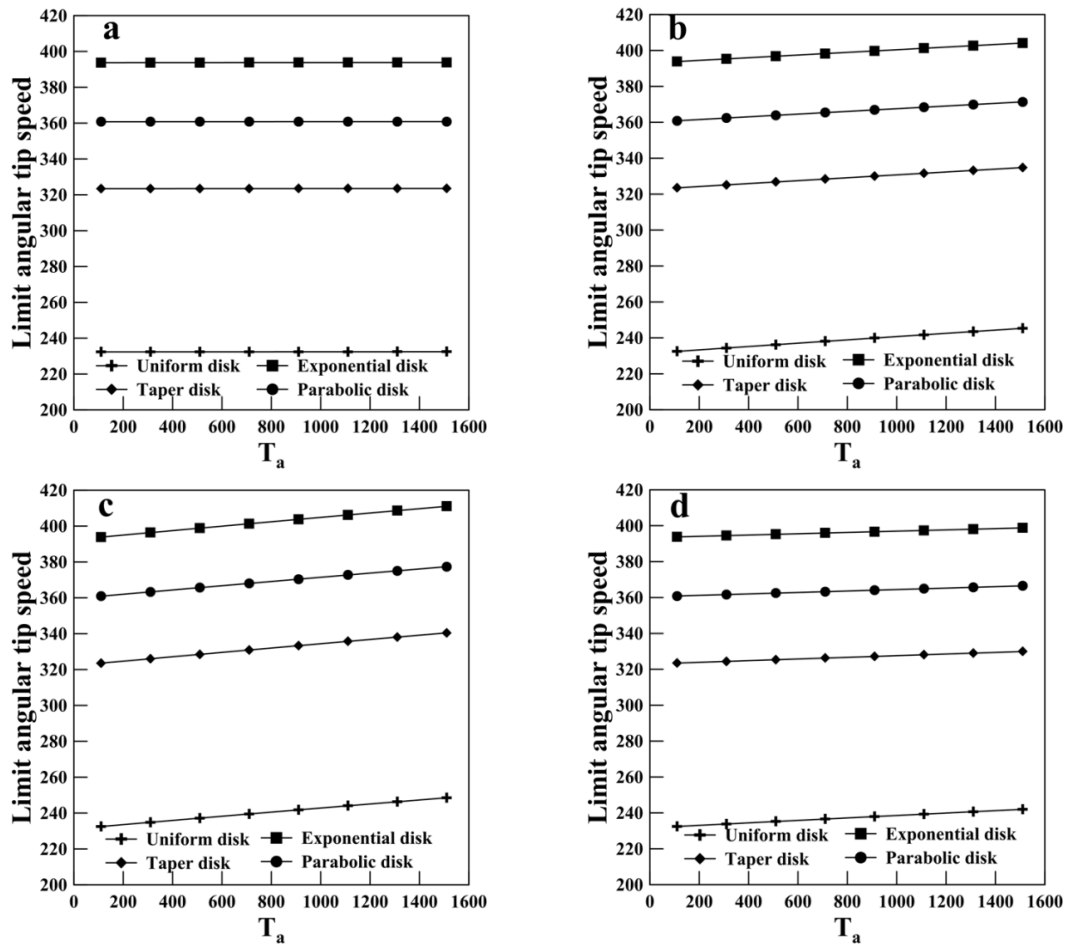


**Figure 3.11.** Effect of density variation on limit angular tip speed for different temperature distributions of inner surface  $T_a$ : (a) uniform, (b) linear, (c) exponential and (d) parabolic temperature.

As can be seen, with increase in  $T_b$ , the limit angular tip speed decreases for all the temperature distributions. But in case of uniform temperature distribution, the curve remains constant. The temperature effect on density is apparently not much pronounced in Figures 3.10(a)-(d), but for higher disk values of thermal expansion coefficient, the effect is found to be more.

The effect of density variation with temperature for the prescribed disk geometries and temperature distribution are also depicted in Figures 3.11(a)-(d). In this case, the outer surface temperature  $T_b$  is set to 0 °C and the limit angular tip speed variation with increasing inner surface temperature  $T_a$  is plotted. The variation of density is governed by the same relation of the previous case, as shown in Figure 3.9(a). As the inner surface temperature increases the limit

angular tip speed increases except for uniform temperature distribution just like in the previous case.

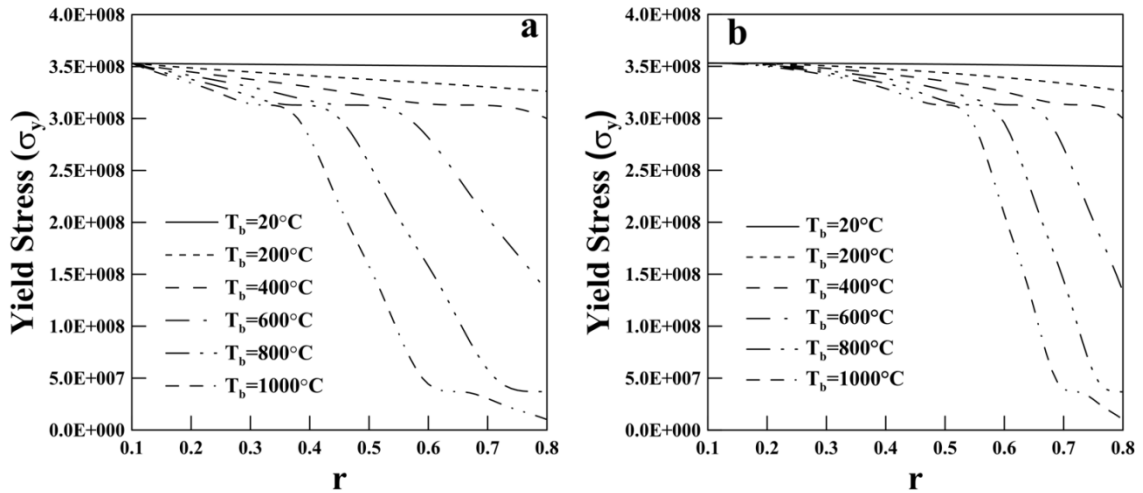


**Figure 3.12.** Yield Stress variation in the disk for (a) linear temperature distribution and (b) parabolic temperature distribution.

### 3.3.4 Effect of temperature on yield stress

The effect of temperature on yield stress is studied considering other material property values  $E$ ,  $\alpha$ ,  $\rho$  and  $\nu$  as constant. The analysis is carried out for four different temperature distribution profiles and disk profiles. For each of the non-uniform temperature distribution profiles as presented graphically in Figure 3.1(a), the temperature boundary condition is assumed as  $T_a = 0^\circ\text{C}$  and  $T_b = 1000^\circ\text{C}$ . The variation of yield stress with temperature is already reported in Figure 3.9(b). Figures 3.12(a) and (b) shows the variation of yield stress with the disk radius using  $T_b$  as a parameter for a disk with linear and parabolic temperature distributions. The figures are derived from the temperature variation with radius and yield stress variation with temperature, i.e., from the combination of Figure 3.1(a) and Figure 3.9(b). It can be seen that in both the cases the yield stress decreases as radius of the disk increases and outer surface temperatures increases.

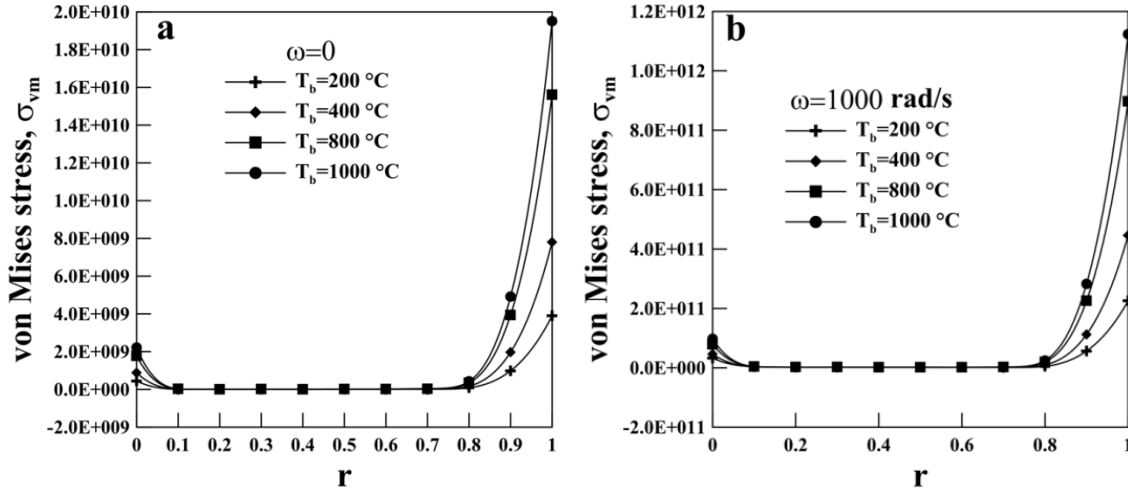


**Figure 3.13.** Variation of von Mises stress ( $\sigma_{vm}$ ) for parabolic temperature distribution profile for uniform disk at (a)  $\omega = 0$  rad/s and (b)  $\omega = 1000$  rad/s, at four different outer surface temperatures ( $T_b$ ).

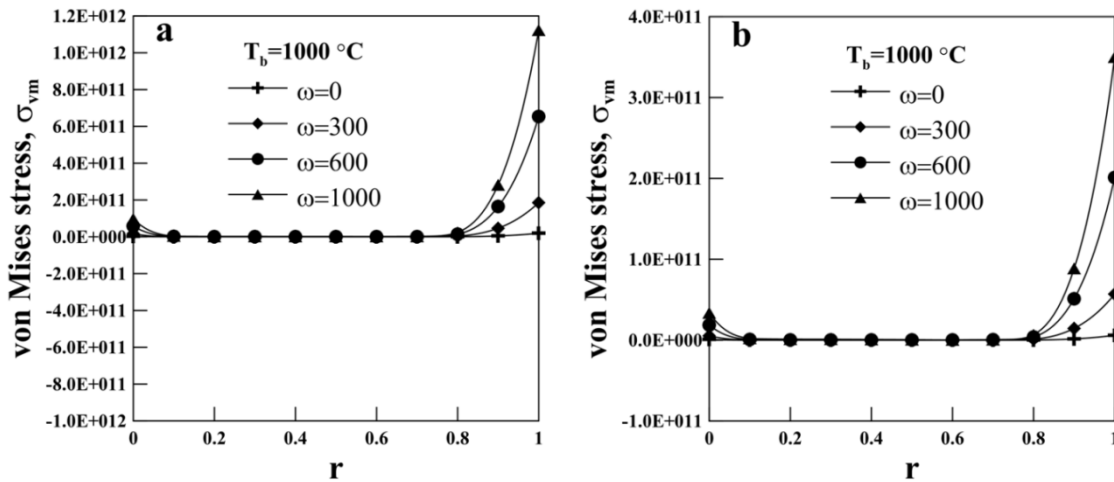


**Figure 3.14.** Variation of von Mises stress ( $\sigma_{vm}$ ) for parabolic temperature distribution profile for (a) uniform disk and (b) parabolic disk, at four different angular speeds.

The effect of temperature variation on von Mises stress is studied first and the stress distribution with radius is plotted in Figures 3.13(a) and (b) for uniform disk with parabolic temperature distribution profile. The study is carried out for two different angular speeds  $\omega = 0$  rad/s and  $\omega = 1000$  rad/s respectively. It is observed that von Mises stress ( $\sigma_{vm}$ ) first decreases towards the inner radius of the disk and then remains constant for all the specified

outer surface temperatures and again there is an increase in von Mises stress ( $\sigma_{vm}$ ) towards the outer radius of the disk. It is also observed that the induced von Mises stress profile increase with outer surface temperature values. For the two different cases of static and rotating disk, the von Mises stress is higher for the rotating one, being apparent in Figure 3.13(b).

In the next study, the variation of von Mises stress for different values of angular speeds is considered and shown in Figures 3.14(a) and (b). In this case, temperature distribution is assumed to be parabolic and the two figures present results for uniform and parabolic thickness disks. It is observed that von Mises stress ( $\sigma_{vm}$ ) increases with increase in angular speeds but the increase is significantly lower in parabolic disk geometry as compared to uniform disk geometry.

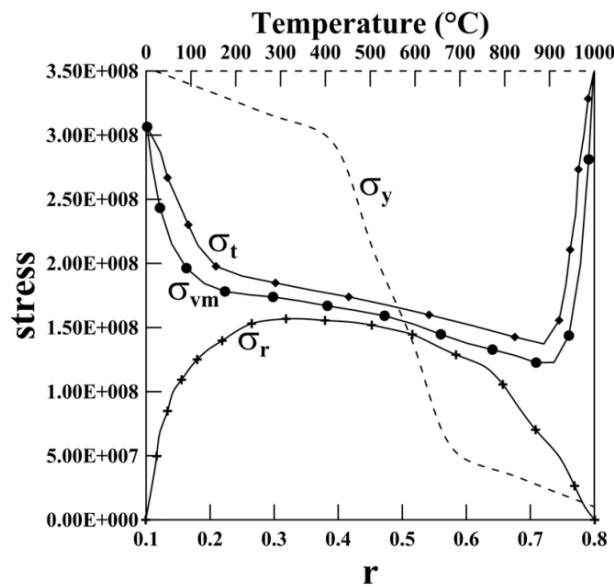


**Figure 3.15.** Solid lines indicate the distribution of radial ( $\sigma_r$ ), tangential ( $\sigma_t$ ) and von-Mises stress ( $\sigma_{vm}$ ) field corresponding to yield limit state in an annular disk subjected to combined loading with higher outer surface temperature. Dotted lines indicate the variation of yield stress with temperature as reported in Figure 3.9(b).

To explore the phenomenon as observed in Figures 3.13 and 3.14, the radial ( $\sigma_r$ ) and tangential ( $\sigma_t$ ) and von-Mises stress ( $\sigma_{vm}$ ) fields of an annular disk ( $b/a=8$ ) is plotted in Figures 3.15 corresponding to the yield limit state, attained by combined effect of centrifugal and thermal loading. From the Figure 3.15, it is observed that the von-Mises stress reaches the uniaxial yield stress value at the outer edge thereby initiates yielding at the outer edge and propagates towards

the root of the disk. As a consequence, the growth of post-elastic region with increase in thermo-mechanical loading is unidirectional until it attains a fully plastic state and in such a situation, the domain of the disk beyond yield limit is divided into two regions (inner elastic-outer plastic). Further load increment divides the disk into three regions (inner plastic-intermediate elastic-outer plastic). Additional load increments cause the disk to attain a fully plastic state. This phenomenon is well explained in chapter 6 of the thesis.

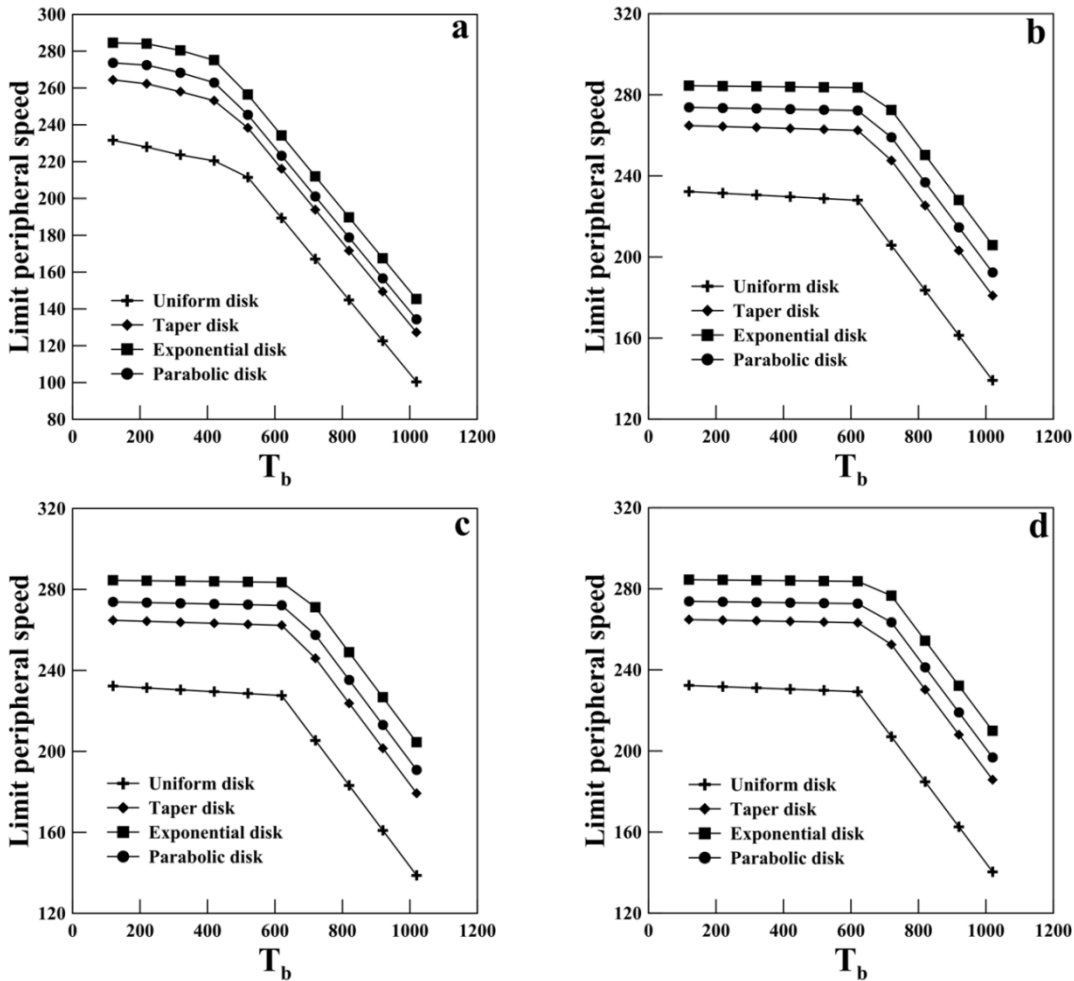


**Figure 3.16.** Plots of limit peripheral speed with outer surface temperature ( $T_b$ ) having different temperature distributions: (a) uniform, (b) linear, (c) exponential and (d) parabolic temperature.

A comparison of the induced stress profile of von Mises stress ( $\sigma_{vm}$ ) due to thermo-mechanical loading with the allowable yield stress profile (as shown in Figure 3.12) would establish the limit angular speed for any given temperature distribution and boundary conditions.

This angular speed is not amenable for normalization by the parameter  $\omega_y b \sqrt{\rho/\sigma_y}$ , as  $\sigma_y$  is a field variable here. Hence this speed is called as limit peripheral speed and is presented in dimensional form. Figures 3.16(a)-(d) show the variation of limit peripheral speed with  $T_b$  for different disk geometries and temperature distributions. From these figures it is illustrated that, there is a fall of limit peripheral speed with increase in outer surface temperature and this reduction is more prominent after 400 °C. The observation is supported by the fact that beyond this temperature the yield stress also falls rapidly with temperature, as shown in Figure 3.12.

### 3.3.5 Effect of temperature on elasticity modulus

The effect of temperature on elasticity modulus is studied considering the numerical values of the system parameter as  $\sigma_y = 350$  MPa,  $\nu = 0.3$ ,  $\rho = 7800$  Kg/m<sup>3</sup> and  $\alpha = 11.5 \times 10^{-6}$  °C<sup>-1</sup>. For each of the non-uniform temperature distribution profile as presented graphically in Figure 3.1(a), the temperature boundary condition is assumed as  $T_a = 0$  °C,  $T_b = 1000$  °C. The variation of elasticity modulus with temperature is obtained from the experimental values reported by Outinen and Makelainen (2002) and presented earlier in Figure 3.9(c).

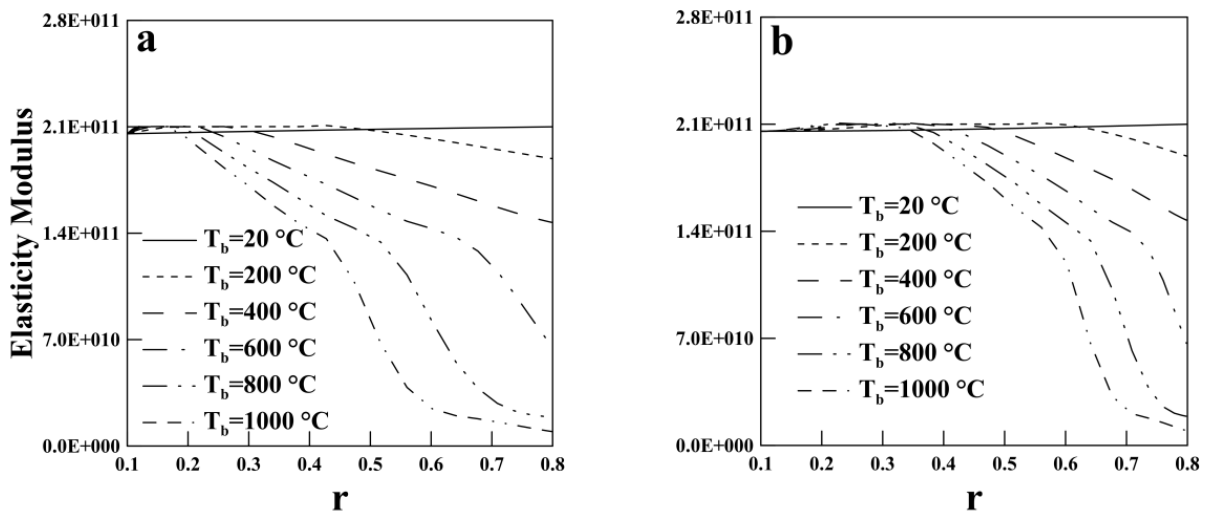


**Figure 3.17.** Variation of elasticity modulus along the radius of the disk having different temperature distributions (a) linear and (b) parabolic temperature.

The variation of elasticity modulus with radius is presented in Figures 3.17(a) and (b) for a disk with linear and parabolic temperature distributions at different specified outer surface temperatures. It is seen that in both the cases the elasticity modulus decreases with radius and this trend becomes more predominant with increase in the values of outer surface temperatures.

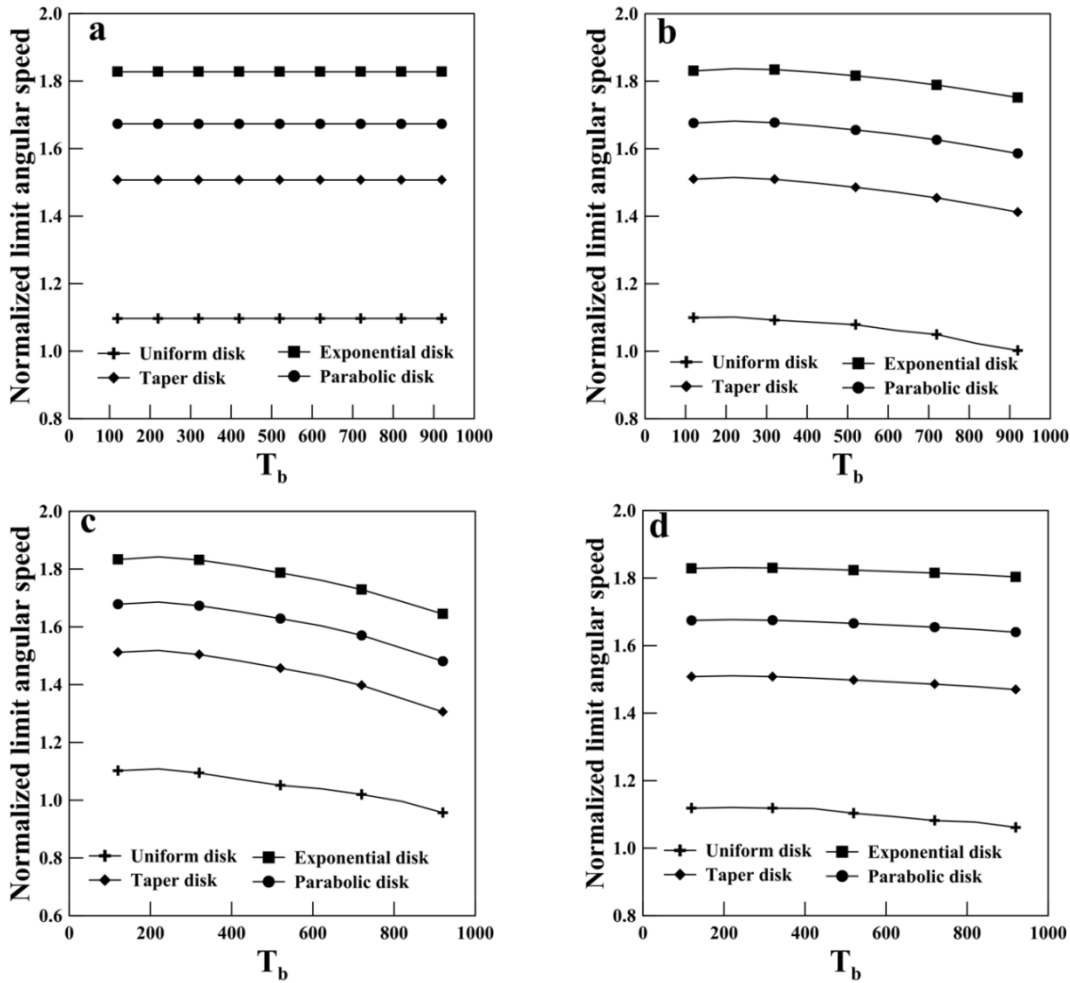


**Figure 3.18.** Plots of normalized limit angular speed with outer surface temperature ( $T_b$ ) having different temperature distributions: (a) uniform, (b) linear, (c) exponential and (d) parabolic temperature.

Figures 3.18(a)-(d) indicates the variations of normalized limit angular speed ( $\omega_y b \sqrt{\rho/\sigma_y}$ ), with outer surface temperature  $T_b$  for different disk geometries and in each figure the effect is shown for four different temperature distributions. These figures indicate fall of normalized limit angular speed with increasing outer surface temperatures except for uniform



temperature distribution, where it remains constant. The reduction is more prominent in exponential temperature distribution. It may be noted that  $\bar{\omega}_y$  has been used as design parameter because density and yield stress is assumed to be constant in this analysis.

### 3.3.6 Effect of temperature on simultaneous variation of density and elasticity modulus

The effect of temperature on both density and elasticity modulus is considered in this section with the same variation of density and elasticity modulus with temperature, as considered previously. The simultaneous variation of density and elasticity modulus with temperature is presented in Figure 3.19 once again, being the simultaneous plots of Figures 3.9(a) and 3.9(c) upto 1000 °C.

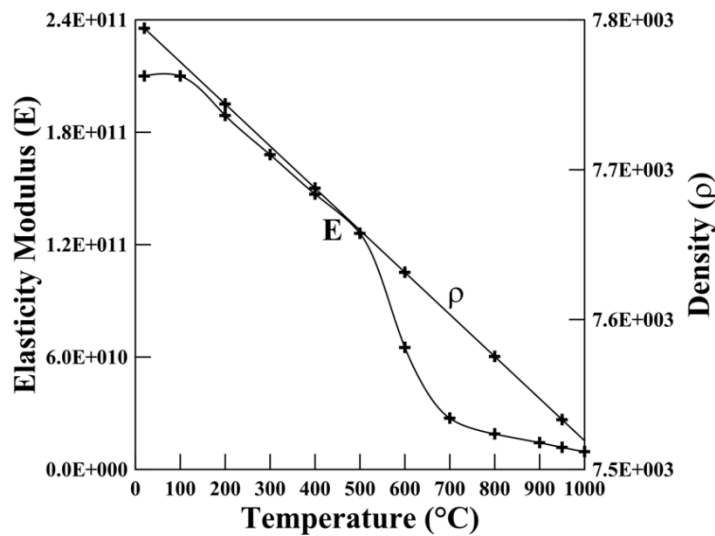


**Figure 3.19.** Simultaneous variation of density and elasticity modulus ( $E$ ) with temperature.

The effect of temperature on both density and elasticity modulus with temperature for the prescribed disk geometries and temperature distribution are depicted in Figures 3.20(a)-(d). In this case, the temperature boundary condition is assumed as  $T_a = 0$  °C, and outer surface temperature  $T_b$  is varied up to 1000 °C. The variation of limit peripheral speed  $\omega_y b$  with increasing outer surface temperature  $T_b$  is plotted, for each of the four temperature distribution profiles. The effects of four different disk geometries are presented in each of these figures.

There is a decrease in limit peripheral speed when outer surface temperature increases but exception exists for uniform temperature distribution. The decrease of limit peripheral speed is more for exponential temperature distribution, in line with the observations of previous cases, but the effect is slightly more prominent due to the combined effect of temperature on both density and elasticity modulus.

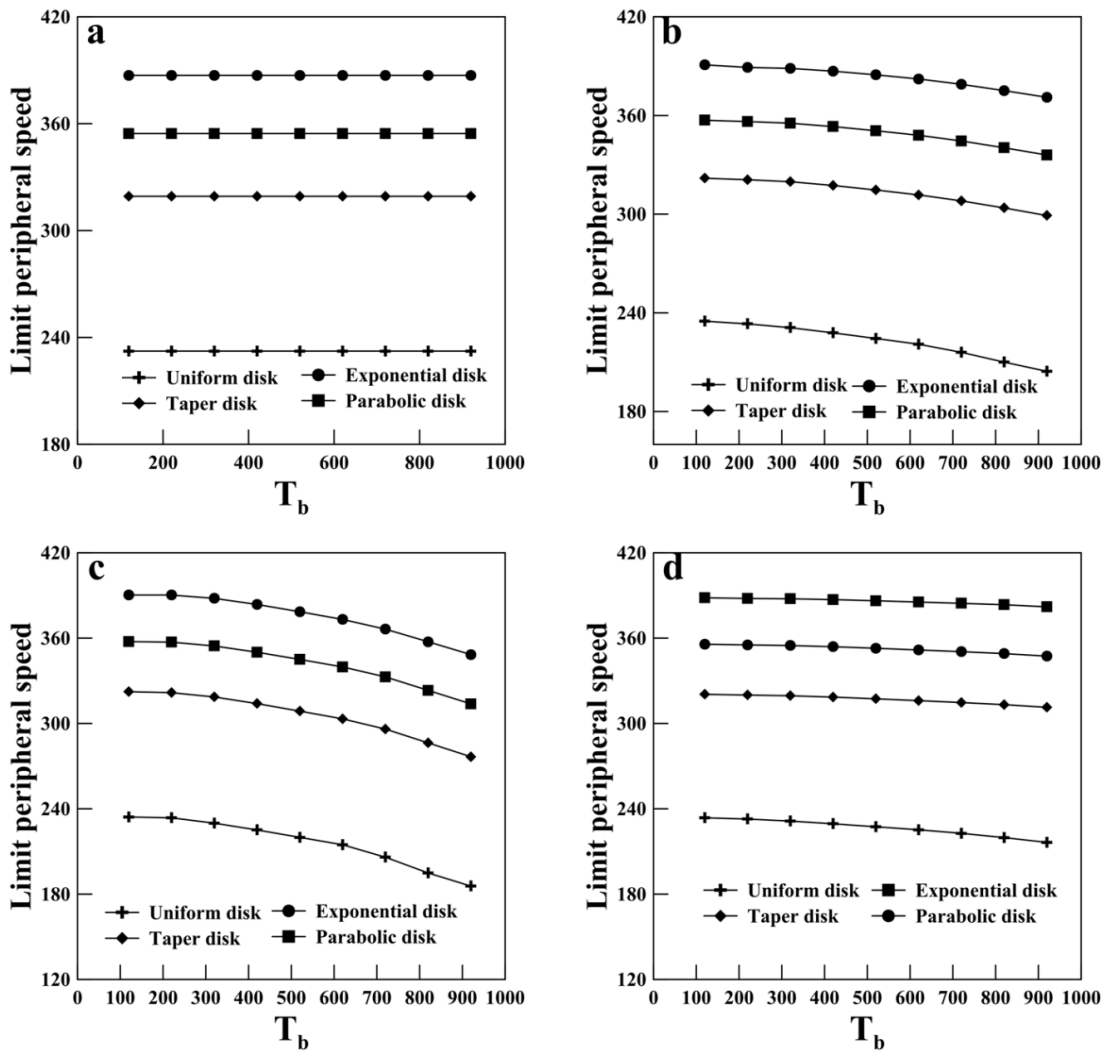


**Figure 3.20.** Plots of limit peripheral speed with outer surface temperature ( $T_b$ ) having different temperature distributions: (a) uniform, (b) linear, (c) exponential and (d) parabolic temperature.

Finally, 3D and contour plots of von Mises stress showing its simultaneous variation with rotational speed and temperature for four different disk geometries is presented in Figures 3.21(a)-(d). In these figures, temperature field is assumed to have linear variation, with the

temperature boundary conditions:  $T_a = 0$  °C and  $T_b =$  prescribed. However, the physical parameters of the disk material are assumed to be constant, in these plots. It is observed that with increase in  $T_b$  as well as rotational speed, von Mises stress increases.

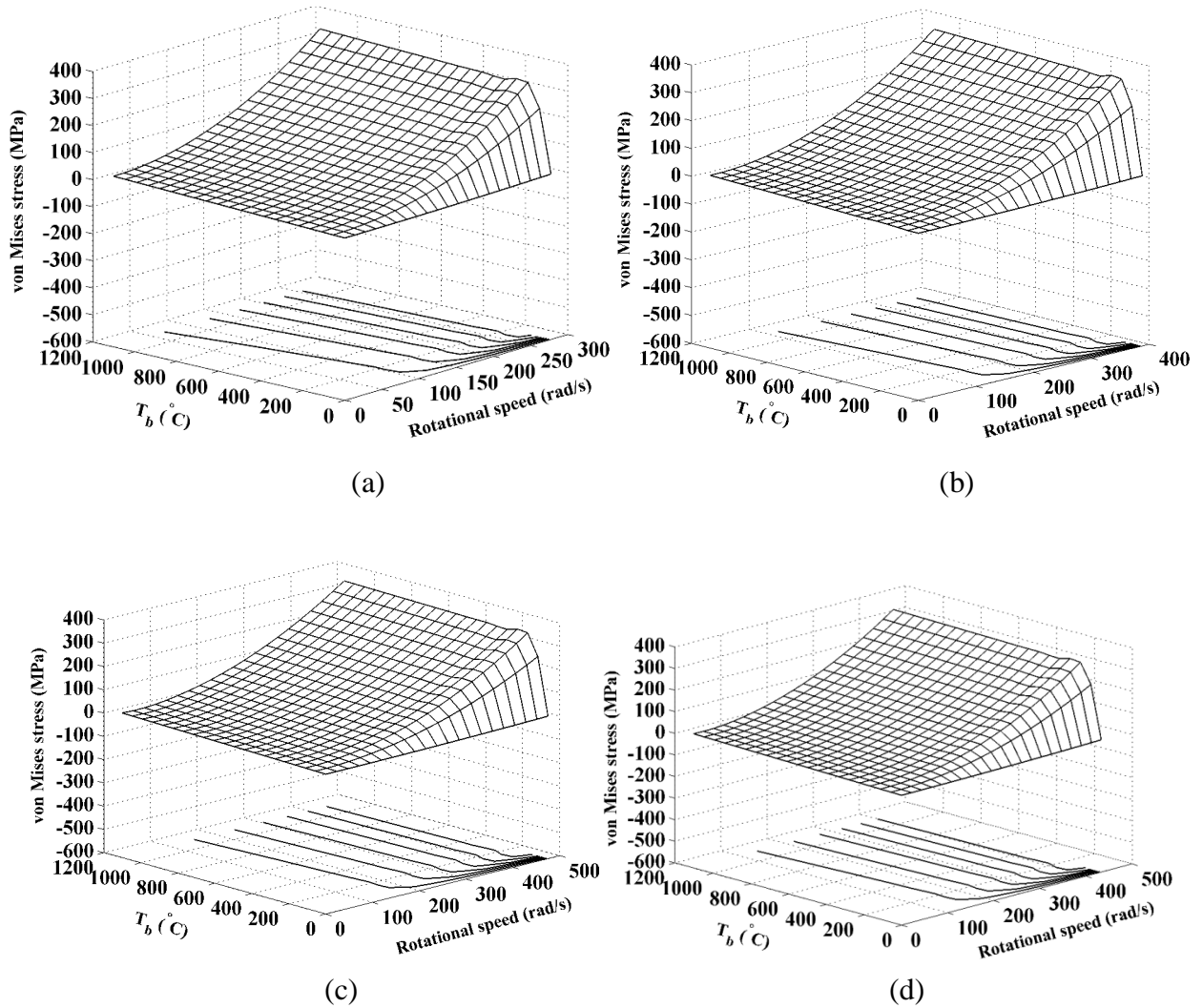


**Figure 3.21.** 3D and contour plots of von Mises stress showing its variation with rotational speed (rad/sec) and  $T_b$  (°C) for various disk geometries: (a) uniform, (b) taper, (c) exponential and (d) parabolic.

### 3.4 Summary

The chapter presents the rotating disk behavior for combined thermal load and rotational inertia effects by using an approximate solution. The approximate solution of the unknown displacement field from the governing equation is obtained by assuming a series approximation following Galerkin's principle. The proposed method has been validated successfully with existing literatures and very good agreement is reported. The effect of disk geometry and temperature field variation on the performance of rotating disks is considered and normalized value of limit angular speed is furnished. The effect of temperature on yield stress is also studied and the limit peripheral speed for any given temperature distribution and boundary conditions is established under thermo-mechanical loading in dimensional form. Also the effect of temperature field on the material properties such as density, elasticity modulus and combination of both density and elasticity modulus is considered in the present chapter and the numerical results are furnished. A future study in this direction would give more insight into the design of rotating disks with various industrial applications. These results are furnished graphically as design monograms which might prove helpful for the practicing engineers.

# **ANALYSIS OF STATICALLY INDETERMINATE BAR PROBLEM IN POST ELASTIC DOMAIN**

## **4.1 Introduction and literature review**

Axially loaded solid slender bar is a widely used machine element found in almost every application of structural engineering. In the arena of mechanical, civil and aeronautical engineering also, such an element is often used to model machine components, elements of a building, aeronautical structures, etc. During a heavy external loading, the material of an axially loaded bar element goes into its non-linear range of behavior when the yield limit load is exceeded. The simple analytical solution of the problem available in textbook are valid for uniform cross-section bar but the non-linearity associated with the study of stresses in elastic-plastic regimes is complicated. The problem becomes further complicated when the nature of loading on the bar renders it statically indeterminate. Solution of statically indeterminate problems for different structural elements is well known for linear elastic material behaviour (Timoshenko (1930)) and the elasto-plastic behaviour of solid slender bars of various types of geometry as well as loading is a relevant area of work for the designers (Hill (1950)).

The load deflection behaviour of a uniform bar under body force loading in the post-elastic region is found in the textbook of Owen and Hinton (1980) as an example problem. Reddy (2005) had dealt with the same problem in greater detail, based on finite element method. Kim et al. (2006) performed fully plastic analyses for notched bars and plates through finite element limit analysis, based on nonhardening plasticity behaviour. Gang et al. (2003) carried out integrity assessment of defective pipelines by using an iterative algorithm for the kinematic limit analysis of rigid perfectly plastic bodies. The effects of various shapes and sizes of part on the plastic collapse of pipelines under internal pressure, bending moment and axial force had been investigated.

Yankelevsky (1999) analyzed the elasto-plastic behaviour of a shallow two bar truss under tension or compression loading, as well as for reversal loading, to correlate the external work to the central displacement and follow the elasto-plastic stresses and strains in the bars along the loading history. Auciello (2001) used both Rayleigh-Ritz and Lagrangian approach to consider the upper and lower bounds for free vibration frequencies of axially-loaded slender

beams. Non-linear dynamics of a pin-ended elasto-plastic beam with both kinematic and isotropic hardening had been discussed by Savi and Pacheco (2001). Genna and Symonds (1988) studied the effects of slenderness ratio and damping on dynamic plastic instabilities for certain fixed-pin supported beams, deformed plastically by a transverse pressure.

Abdalla et al. (2007) presented a simplified technique to determine the shakedown limit load of a structure using finite element method and it was applied and verified by using two bench mark shakedown problems. Problem of two-bar structure subjected to constant axial force and cyclic thermal loading, and the three cylinders subjected to constant internal pressure and cyclic high temperature variation had been solved analytically. In a subsequent work, Abdalla et al. (2011) further developed a simplified technique to handle cyclic biaxial loading resulting in multi-axial states of stress within the large square plate with a small central hole problem.

The dynamic behavior of non-uniform taper bars in post-elastic regime has been addressed by Das et al. (2009a, b) where loading was controlled statically to take the bar to its post-elastic state so as to predict its dynamic behavior in the presence of plastic deformation. Kolodziej and Gorzelanczyk (2012) analyzed both elastic and elasto-plastic torsion of prismatic bars by means of the Picard iteration. The analysis was based on Saint-Venant displacement assumption and Hencky's deformation theory of plasticity. Mukhtar and Al-Gahtani (2016) used a well-known meshless method, radial basis functions to solve the torsion of a prismatic bar having a rectangular/square cross-section. Biondi and Caddemi (2007) provided closed form solutions for multiple singularities in the flexural stiffness of clamped-clamped beam by making use of distributions such as unit step and Dirac's delta functions. The authors proposed an integration procedure that leads to closed form solutions, dependent on boundary conditions only and independent of continuity conditions along the beam span. Ghuku and Saha (2016) introduced a semi-analytical solution method using domain decomposition technique for elastic solution of statically indeterminate bar problem. Tayyar (2016) presented a curvature based kinematic displacement theory (KDT) for elasto-plastic finite strain solution of cantilever beams under a uniform moment distribution. In KDT, deflection is generated without assuming geometry and using differential equations of the deflection curve. Lal et al. (2017) carried out the springback analysis of hollow rectangular bars with linear work-hardening materials using deformation theory of plasticity. In this study, the elastic-plastic boundary was determined by using deformation theory of plasticity. Canales and Mantari (2017) studied the vibrational

analysis of taper bars under uniform axial loading in post-elastic regime by considering shear deformation and rotary inertia. In this work, the Timoshenko beam theory and the dynamic version of the principle of virtual work are used to derive the eigenvalue problem.

It is evident from the above discussion that extensive studies of elasto-plastic analysis of statically determinate bars have been carried out by various analytical and numerical methods. However, research work addressing complete post-elastic analyses of non-uniform bars by using domain decomposition technique based on a direct variational method is not reported in the literatures. Research work on post-elastic analysis of statically indeterminate bars is scarce and hence in the present chapter, a numerical method based on variational principle for elasto-plastic analysis of such taper bars has been proposed. The solutions of statically indeterminate bar problems are critical in general, because they are not amenable to a ready analytical solution. A clamped axially loaded bar problem becomes indeterminate when the load is concentric, and it results in a singularity point in the domain. In the present bar problem more such singularity points arise when the bar is in post-elastic state, at higher magnitude of concentrated load and the other points come from the yield front location. The computational domain is divided into sub-domains based on the location of singularity points. The formulation is based on von-Mises yield criterion and for linear strain hardening type material behaviour. The governing equation is derived through an extension of a variational method in elasto-plastic regime and solution is obtained by using Galerkin's approximation principle. The approximate solution further needs an iterative method to locate the growth in the yield front. The solution algorithm is implemented with the help of MATLAB<sup>®</sup> computational simulation software and validation of the formulation is carried out successfully for some reduced problems. The present mathematical model is also successfully validated with analytical results and the results of finite element analysis software Abaqus CAE. The effect of geometry parameters like aspect ratio, slenderness ratio and the type of taperness on the post-elastic performance of the bar is investigated and the relevant results are obtained in dimensionless form. The term bar used in this thesis is in generic sense and hence the formulation is applicable for all one dimensional elements, e.g., rods, pipes, truss members, etc.

## 4.2 Mathematical formulation

The present problem employs an energy based variational approach to get the appropriate governing equations for the non-uniform bars in elasto-plastic state. The formulation is displacement based and the unknown displacement field is approximated by finite linear combination of admissible orthogonal functions. Present analysis is carried out for isotropic, homogeneous and bilinear material model, but the proposed method is generalized enough to include any other non-linear material behaviour, as well. However formulation of the present problem is valid for monotonic loading only and possible load reversal from plastic region is not included into consideration.

According to total deformation theory of plasticity (Kachanov (1971)), the final state of stress at a given loading is independent of the stress-strain path during the loading. Hence, the components of total plastic strain at the end of each load-step are proportional to the corresponding deviatoric stress components. It should be noted that the expressions for the plastic strains are exact for proportional loading and in such situations Hencky's equations (1924) lead to results, in good agreement with the observations. However, several authors (Chen (1986); Jahed and Dubey (1997); Budiansky (1959)) pointed out the applicability of total deformation theory for a range of loading paths other than proportional loading without violating the general requirements for physical soundness of a plasticity theory.

### 4.2.1 Deviatoric stress and strain intensities

The stress tensor in terms of principal stresses has the form  $T_\sigma = \sigma T_1 + D_\sigma$ , where,  $\sigma = (\sigma_1 + \sigma_2 + \sigma_3)/3$  is the mean or hydrostatic pressure,  $T_1$  is unit matrix and  $D_\sigma$  is stress deviatoric tensor that characterizes the tangential (shear) or deviatoric stress. The second invariant of stress deviatoric, being a non-negative quantity is used to define deviatoric or shear stress intensity as follows:

$$S = +\sqrt{I_2(D_\sigma)} = \frac{1}{\sqrt{6}} \sqrt{(\sigma_1 - \sigma_2)^2 + (\sigma_2 - \sigma_3)^2 + (\sigma_3 - \sigma_1)^2}. \quad (4.1)$$



Similarly the strain tensor  $T_\varepsilon$  can be conveniently represented as  $T_\varepsilon = \frac{\varepsilon}{3}T_1 + D_\varepsilon$ , where  $\varepsilon = \varepsilon_1 + \varepsilon_2 + \varepsilon_3$  is the relative change in volume and  $\varepsilon T_1$  is a tensor corresponding to volume dilation. The second invariant ( $I_2(D_\varepsilon)$ ) of strain deviatoric is a non-negative quantity which defines deviatoric or shear strain intensity as follows:

$$\Gamma = +2\sqrt{I_2(D_\varepsilon)} = \sqrt{\frac{2}{3}\sqrt{(\varepsilon_1 - \varepsilon_2)^2 + (\varepsilon_2 - \varepsilon_3)^2 + (\varepsilon_3 - \varepsilon_1)^2}}. \quad (4.2)$$

It is already stated that material of the bar is isotropic, homogeneous and linear-elastic followed by linear strain hardening. Further, the analysis is carried out based on the assumptions that the volumetric change is an elastic deformation, proportional to the mean pressure,  $\varepsilon = 3k\sigma$  where  $k = (1 - 2\nu)/E$ . As the stress and strain deviatorics are proportional,  $D_\varepsilon = \psi D_\sigma$  where,  $\psi$  is a scalar quantity. It is evident that the stress and strain deviatoric are coaxial and their principal values are respectively proportional. In form of components of the strain and stress deviatorics,

$$e_{ij} = \psi s_{ij}. \quad (4.3)$$

Using Eq. (4.3), the shear strain intensity  $\Gamma$ , can be expressed in terms of deviatoric (shear) stress intensity,  $S$  as

$$\Gamma = 2\psi S. \quad (4.4)$$

With the help of total deformation theory of plasticity, the total strain can be expressed as

$$\varepsilon_{ij} = k\sigma\delta_{ij} + \psi s_{ij}. \quad (4.5)$$

Eq. (4.5) is known as Hencky's relations, which can easily be transformed to solve for stresses as follows:

$$\sigma_{ij} = \frac{\varepsilon}{3k}\delta_{ij} + \frac{1}{\psi}e_{ij}. \quad (4.6)$$

### 4.2.2 Work of deformation

Computation of strain energy stored in a loaded bar is usually done from its principal stress and strain fields. However, beyond elastic regime it is convenient to express the stress and strain fields through their hydrostatic and deviatoric components. Hence, to maintain a uniform

formulation although in the present study, strain energy is computed from hydrostatic and deviatoric components, starting from the very beginning of loading. So, with the aid of Eq. (4.5), the increment to the work of deformation can be expressed as:

$$dU' = \sigma_{ij} d\varepsilon_{ij} = d(A' + \psi S^2) + S^2 d\psi, \quad (4.7)$$

where  $A'$  denotes the elastic energy of volumetric compression ( $A' = 3k\sigma^2/2 = \varepsilon^2/6k$ ) and eliminating the function  $\psi$  from Eq. (4.7), we find  $dU' = \sigma d\varepsilon + S d\Gamma$ . Here the first term is the elastic energy of volumetric compression and the second is the increment in the work of shape deformation. The expressions of  $dU'$  differ in elastic, exact yield and post-elastic states and they are given below for ready reference.

#### 4.2.2.1 Linear elastic state (Hooke's law)

In linear elastic state ( $\psi = 1/2G$ ), the increment in work of deformation is the total differential of the elastic potential and is given by

$$U' = \frac{1}{2} K \varepsilon^2 + \frac{1}{2} G \Gamma^2. \quad (4.8)$$

Here  $K = E/(3(1 - 2\nu))$  is the bulk modulus,  $G = E/(2(1 + \nu))$  is the modulus of rigidity and  $\nu$  is Poisson's ratio.

#### 4.2.2.2 Yield state

Assuming von-Mises yield criterion, at yield, the deviatoric stress intensity attains the value of shear stress at yield  $S = \tau_s$  and hence from Eq. (4.4),  $\psi = \Gamma/2\tau_s$ . The potential of work of deformation is given by

$$U' = \frac{1}{2} K \varepsilon^2 + \tau_s \Gamma. \quad (4.9)$$

#### 4.2.2.3 Hardening state

In the post yield hardening state  $\psi$  becomes a function of the intensity of shear and, if the shear strain intensity is taken as a measure of the hardening, then we obtain a relation of the form

$S = g(\Gamma)\Gamma$ , where  $g(\Gamma)$  is some positive function, characteristic for a given material. By virtue of Eq. (4.4), we obtain  $\psi = 1/(2g(\Gamma))$ . The increment in work of deformation is expressed as

$$U' = \frac{1}{2}K\varepsilon^2 + \int g(\Gamma)\Gamma d\Gamma. \quad (4.10)$$

The second term characterizes the work of the change of shape of an element of the body. In hardening state, the expression in Eq. (4.10) is solved using method of successive approximations (Kachanov (1971)).

### 4.2.3 Description of the bar problem

The present analysis is carried out for taper bars of solid circular cross-section as shown in Figure 4.1(a) where the solid line indicates linear variation in diameter and the dotted line indicates linear variation in cross-sectional area. The diameter of the bar ( $\phi d$ ) at any axial location  $x$  is given by,  $d = d_0 - \xi(d_0 - d_1)$ , where  $d_0$  is the largest diameter at  $x = 0$  and  $d_1$  is the smallest diameter at the other end of the bar ( $x = L$ ). Location  $x$  is expressed in terms of the normalized axial coordinate  $\xi(= x/L)$ , where  $L$  is the total length of the bar. For a bar with linear variation in area similar definition is given by,  $A = A_0 - \xi(A_0 - A_1)$ , where  $A_0$  and  $A_1$  represents the areas corresponding to the diameters  $d_0$  and  $d_1$  respectively. Hence, in this case the variation in diameter is non-linear, being given by the relation  $d = \sqrt{[d_0^2 - \xi(d_0^2 - d_1^2)]}$ . Furthermore, the geometry of the bar is defined by the slenderness ratio (ratio of length to radius of gyration corresponding to the minimum radius of the bar) and aspect ratio (ratio of difference in radii of two ends to length). The slenderness ratio is a measure of lateral stability and its mathematical expression is given by  $S_R = L/k(r_1)$ , where  $k(r_1)$  is the radius of gyration of the bar, corresponding to the minimum cross-section, i.e.,  $k(r_1) = \sqrt{I_1/A_1}$ . The aspect ratio is the measure of overall taper of bar and is expressed as  $A_R = (r_0 - r_1)/L$ . The nature of variation in taperness with length is the third geometry parameter and is given mathematically by diameter gradient.

When the bar is subjected to an internal concentrated axial load  $F$ , the whole domain is decomposed into two sub-domains about the point of application of the load, as shown in Figure

4.1(b). The lengths of the two domains (marked as 1 and 2) are denoted by  $L_f$  and  $L_b (= (L - L_f))$ . The normalized axial coordinates in domain 1 and domain 2 are given by  $\xi_1 = x/L_f$  and  $\xi_2 = (x - L_f)/(L - L_f)$  respectively. For the purpose of computation, the lengths of domain 1 and 2 are denoted by using normalized length parameters  $\xi_f = L_f/L$  and  $\xi_b = (L - L_f)/L$ . Although a clamped-clamped bar is shown in Figure 4.1(a, b) in line with the present analysis, but a clamped-free bar is also considered for the validation study. For clamped ended bars internal force  $F$  will produce reactions  $F_0$  and  $F_1$  at the respective boundaries which are not shown in Figure 4.1(b) but discussed in detail later in section 4.3.1.

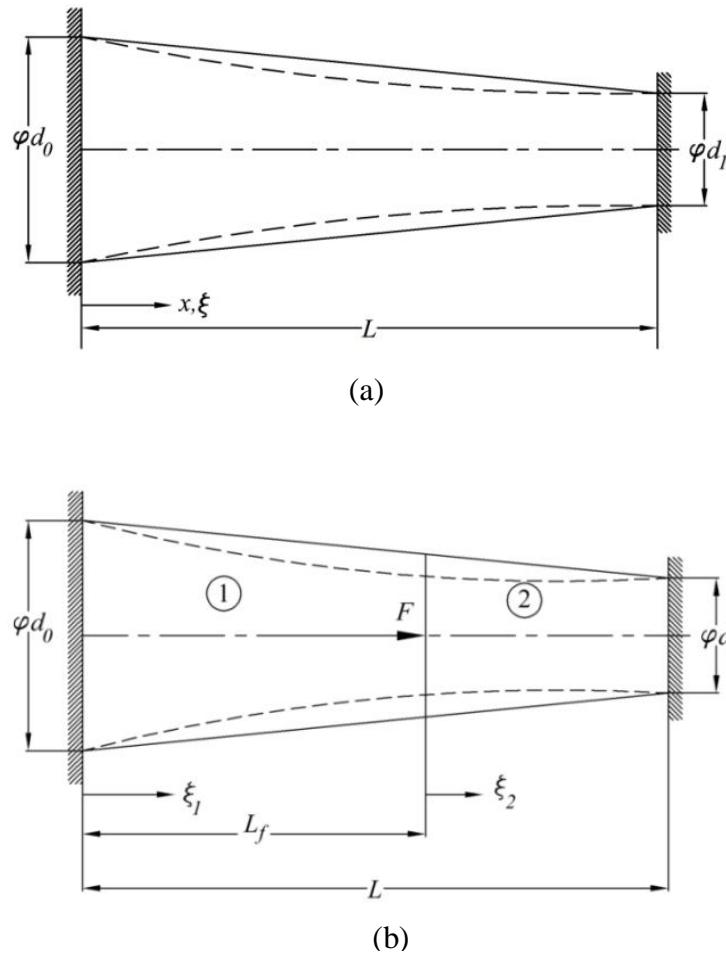


**Figure 4.1.** (a) Taper bar geometry and (b) The loaded bar with domain 1 and domain 2. Solid and dotted lines indicate bar with uniform and non-uniform taperness respectively.

#### 4.2.4 Solution of the problem

The solution for the elasto-plastic displacement field of a body under equilibrium is obtained from the application of minimization of total potential energy principle ( $\delta(U+V)=0$ ). In the post elastic region of material behaviour the principle is applied by using Hencky's total deformation theory.  $U$  is the strain energy stored in the bar in form of increment in work of deformation and  $V$  is the potential energy developed by the applied force  $F$ . It is assumed that the principle of minimum potential energy remains valid for bilinear material model, unless one considers a cyclic loading problem.

The axial displacement field ( $u$ ) in the member can be computed from the linear-strain displacement relation,  $\varepsilon_x = du/dx$ , where,  $\varepsilon_x$  is the axial strain. On substituting  $\varepsilon_x$  and  $\Gamma$  in Eq. (4.8), the expression of  $U$ , under elastic conditions, is obtained as

$$U = \int_0^L \left( \frac{K(I-2\nu)^2}{2} + \frac{2G(I+\nu)^2}{3} \right) A(x) \left( \frac{\partial u}{\partial x} \right)^2 dx. \quad (4.11)$$

The expression for work potential is given by

$$V = -Fu \Big|_{\xi_f}. \quad (4.12)$$

Further analysis for solution of  $u$  starts with fully elastic domain which goes into post-elastic domain when applied load exceeds elastic limit load ( $F_y$ ).

##### 4.2.4.1 Elastic solution

When domain 1 and domain 2 are considered fully elastic, substituting Eq. (4.11) and Eq. (4.12) in the energy principle  $\delta(U+V)=0$ , the governing equilibrium equation becomes,

$$\delta \left[ \int_0^L \left( \frac{K(I-2\nu)^2}{2} + \frac{2G(I+\nu)^2}{3} \right) A(x) \left( \frac{\partial u}{\partial x} \right)^2 dx - Fu \Big|_{\xi_f} \right] = 0. \quad (4.13)$$

Eq. (4.13) is expressed in the global normalized co-ordinate,  $\xi$  and is obtained as,

$$\left( \frac{K(I-2\nu)^2}{2} + \frac{2G(I+\nu)^2}{3} \right) \left( \frac{1}{L} \right) \int_0^1 \left\{ A(\xi) \left( \frac{\partial u}{\partial \xi} \right) \delta \left( \frac{\partial u}{\partial \xi} \right) \right\} d\xi - F \delta \left[ u(\xi) \Big|_{\xi=\xi_f} \right] = 0. \quad (4.14)$$

Eq. (4.14) provides the governing equation of the global system, which is subsequently expressed in terms of domain 1 and 2,

$$\left( \frac{K(I-2\nu)^2}{2} + \frac{2G(I+\nu)^2}{3} \right) \left( \frac{I}{L} \right) \left[ \int_0^{\xi_f} A(\xi) \left( \frac{\partial u}{\partial \xi} \right) \delta \left( \frac{\partial u}{\partial \xi} \right) d\xi + \int_{\xi_f}^I A(\xi) \left( \frac{\partial u}{\partial \xi} \right) \delta \left( \frac{\partial u}{\partial \xi} \right) d\xi \right] - F \delta \left[ u(\xi) \Big|_{\xi=\xi_f} \right] = 0. \quad (4.15)$$

To facilitate the numerical computation, Eq. (4.15) is expressed in domain specific normalized co-ordinates  $\xi_1$  and  $\xi_2$ , and the governing equation takes the form,

$$\left( \frac{K(I-2\nu)^2}{2} + \frac{2G(I+\nu)^2}{3} \right) \left( \frac{I}{L} \right) \left[ \left( \frac{2}{\xi_f} \right)^I \int_0^I A(\xi_1) \left( \frac{\partial u}{\partial \xi_1} \right) \delta \left( \frac{\partial u}{\partial \xi_1} \right) d\xi_1 + \left( \frac{2}{\xi_b} \right)^I \int_0^I A(\xi_2) \left( \frac{\partial u}{\partial \xi_2} \right) \delta \left( \frac{\partial u}{\partial \xi_2} \right) d\xi_2 \right] - F \delta \left[ u(\xi) \Big|_{\xi=\xi_f} \right] = 0. \quad (4.16)$$

The global displacement function  $u(\xi)$  is approximated by a linear combination of sets of orthogonal coordinate functions as  $u(\xi) = \sum c_i \phi_i$ ,  $i = 1, 2, \dots, n_f$ , where  $\phi_i$  is the set of orthogonal functions developed through Gram–Schmidt scheme and  $n_f$  is number of functions.  $\{c\}$  is a set of unknown parameters, which indicates the contribution of individual displacement functions, and need to be evaluated for obtaining  $u(\xi)$ . The necessary starting function to generate the higher order orthogonal functions is selected by satisfying the relevant geometric boundary conditions, i.e.  $u = 0$  at  $\xi = 0$ ,  $u = 0$  at  $\xi = 1$  and  $\frac{du}{d\xi} = 0$  at  $\xi = \xi_f$ .

For the purpose of computation, the respective portions of global displacement functions in domain 1 and domain 2 are expressed as  $u(\xi_1) \cong \sum c_i \phi_{i1}$  and  $u(\xi_2) \cong \sum c_i \phi_{i2}$ , where  $\phi_{i1}$  and  $\phi_{i2}$  are portions of the function  $\phi_i$  in domain 1 and domain 2. Substituting these assumed displacement functions in Eq. (4.16) and replacing operator  $\delta$  by  $\partial/\partial c_j$ , the governing equation in matrix form is obtained as

$$\left( \frac{K(I-2\nu)^2}{2} + \frac{2G(I+\nu)^2}{3} \right) \sum_{i=1}^n \sum_{j=1}^n \left[ \left( \frac{2}{L_f} \right) \int_0^l (A(\xi_1) \phi'_{i1} \phi'_{j1}) d\xi_1 + \left( \frac{2}{L_b} \right) \int_0^l (A(\xi_2) \phi'_{i2} \phi'_{j2}) d\xi_2 \right] \{c_i\} \quad (4.17)$$

$$= \left\{ F \cdot \phi_j \Big|_{\xi_f} \right\},$$

where ( )' indicates differentiation with respect to normalized coordinate  $\xi (= x/L)$ . Solution of Eq. (4.17) is quite straight forward, which yields the solution for axial displacement  $u$  for any prescribed value of concentrated axial load  $F$ . Strain field is computed from the displacement field and subsequently stress field is obtained. The stress field yields reaction forces  $F_0$  and  $F_l$  at fixed ends, which are developed to establish static equilibrium of the clamped bar system. The formulation holds for any bar geometry and load application point but fails when the magnitude of  $F$  is high enough ( $F > F_y$ ) to induce stress beyond yield value.

#### 4.2.4.2 Solution for post-elastic domain

For statically indeterminate bar, yielding will occur with increasing load at a particular point and its location depends on the geometry and load application point of the bar. It is obvious that yielding initiates at the heavily stressed region and hence, yielding may initiate at any one of the domain end points: ( $x = L_f$ ) or ( $x = L$ ). Afterwards with increase in load intensity the yield region grows, thereby giving rise to three-regions. The interface between elastic and plastic region is termed as plastic front location. Three-region formulation contains a part elastic and a part plastic region for one domain and a fully elastic region for another domain and remains valid until the yielding starts at another domain as well. When yielding exists at both the domains, four-region formulation holds good, in which, each of the domains contain elastic and plastic region simultaneously.

The particular value of axial load at which yielding initiates at the location of load application point ( $x = L_f$ ) in the bar is termed as elastic limit load ( $F_{y1}$ ) of domain 1 and the value of load at which yielding occurs at  $x = L$  is termed as elastic limit load ( $F_{y2}$ ) of domain 2. Hence  $F_{y1}$  and  $F_{y2}$  are domain specific elastic limit loads and not dependent on the order of occurrence of yielding. With further increase in load intensity, the plastic front of domain 1 proceeds towards the origin  $x = 0$  and elastic-plastic region coalesces at a particular load,

termed as plastic collapse load ( $F_{c1}$ ) for domain 1. For domain 2, the plastic front proceeds towards the domain 1 and elastic-plastic region coalesces at the location of load application point  $x = L_f$  at a particular load, termed as plastic collapse load ( $F_{c2}$ ) of domain 2. In view of the variations in the location of initiation of yielding and the behavior in the growth of post-elastic region, mathematical formulations have been reported in two different sections. In both the cases, location(s) of plastic front at any load is obtained numerically by an iterative method.

#### 4.2.4.2.1 Three region formulation

In this section, it is assumed that yielding initiates at  $x = L$  of domain 2. So, the whole bar has now three regions with fully elastic domain 1 and elasto-plastic domain 2. The notations for a statically indeterminate taper bar for this case have been indicated in Figure 4.2(a). But for some combination of geometry and load application point, yielding may also initiate at domain 1 (three-region of second kind). In this case, the bar has three regions with elasto-plastic domain 1 and fully elastic domain 2. To maintain brevity, the condition is not shown in Figure 4.2(a). It is to be mentioned here that identification for three region formulation becomes obvious when yielding initiates at any one of the domain. There is a particular situation when yielding will occur simultaneously in both the domains and it would give rise to four region problem directly which is discussed in the next section.

In the three region problem, as shown in Figure 4.2(a),  $L_{be}$  and  $L_{bp}$  are the lengths of the elastic and the plastic regions of domain 2 and the corresponding normalized length parameters are denoted by  $\xi_2^e$  and  $\xi_2^p$  respectively. Hence in line with the earlier notation,  $\xi_2^e = (x - L_f)/L_{be}$  and  $\xi_2^p = (x - L_f - L_{be})/L_{bp}$ . Displacement functions for domain 1 is expressed as  $u(\xi_1) \cong \sum c_i \phi_{i1}$ , as mentioned previously in fully elastic problem and for domain 2,  $u(\xi_2)$  is broken up into elastic and plastic domains, as  $u(\xi_2^e) \cong \sum c_i \phi_{i2}^e$  and  $u(\xi_2^p) \cong \sum c_i \phi_{i2}^p$  respectively, where  $\phi_{i2}^e$  and  $\phi_{i2}^p$  are portions of the functions  $\phi_{i2}$  in elastic and plastic regions respectively. Substituting these assumed displacement functions, the governing equation is obtained in matrix form and is given as



$$\begin{aligned}
 & \sum_{i=1}^n \sum_{j=1}^n c_i \left[ \left( \frac{K(1-2\nu)^2}{2} + \frac{2G(1+\nu)^2}{3} \right) \left( \frac{2}{L_f} \right) \int_0^l (A(\xi_1) \phi'_{i1} \phi'_{j1}) d\xi_1 \right. \\
 & + \left( \frac{K(1-2\nu)^2}{2} + \frac{2G(1+\nu)^2}{3} \right) \left( \frac{2}{L_{be}} \right) \int_0^l (A(\xi_2^e) \phi'_{i2} \phi'_{j2}) d\xi_2^e \\
 & \left. + \left( \frac{K(1-2\nu)^2}{2} + \frac{2g(\Gamma)(1+\nu_p)^2}{3} \right) \left( \frac{2}{L_{bp}} \right) \int_0^l (A(\xi_2^p) \phi'_{i2} \phi'_{j2}) d\xi_2^p \right] = \{ F \cdot \phi_j |_{\xi_f} \}.
 \end{aligned} \tag{4.18}$$

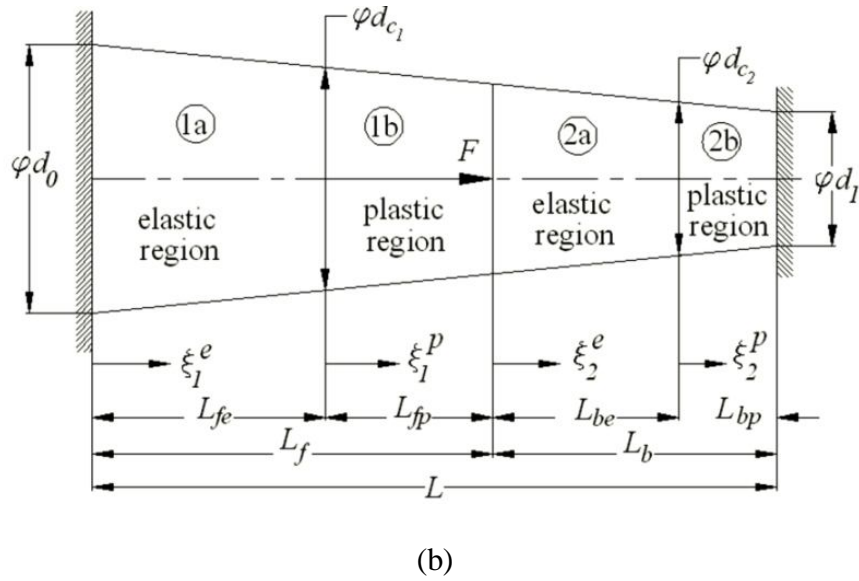
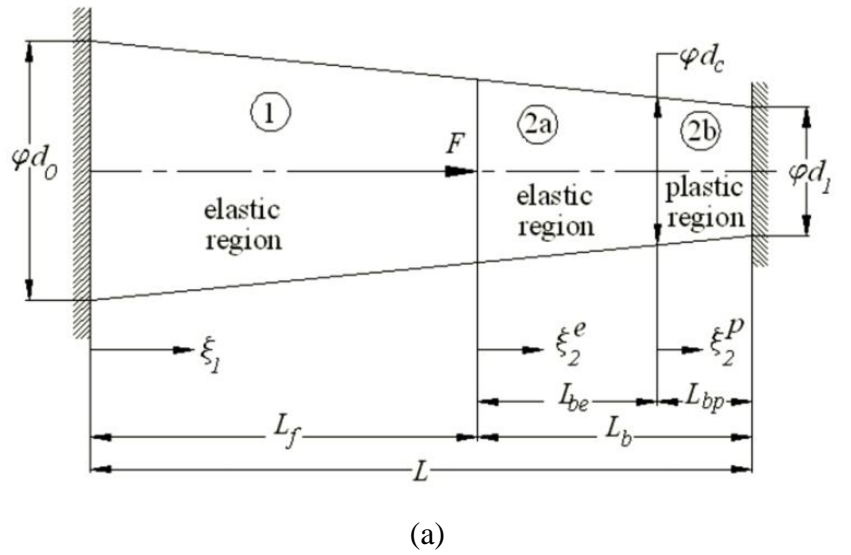


Figure 4.2. Representation of nomenclatures: (a) Three region and (b) Four region.

The expressions of the strain energies in the three different regions, necessary in the derivation of the above equation, are not mentioned to maintain brevity. The solution procedure of Eq. (4.18) is identical to that of Eq. (4.17) although it requires some more iterative numerical computations.  $g(\Gamma)$  is the modulus of plasticity which is set equal to modulus of rigidity  $G$ , at the zeroth approximation, and the problem is solved as an extension of elastic solution. In subsequent approximations the value of  $g(\Gamma)$  is updated until a final convergence is achieved, following the iterative scheme of Kachanov (1971). The mathematical relations for the three region problem of second kind are not reported here to maintain brevity and due to its similarity with the present formulation.

#### 4.2.4.2.2 Four region formulation

In this case, yielding occurs in both the domains and so, the whole bar now has four regions, namely, 1a, 1b, 2a and 2b, out of which 1a and 2a are elastic regions whereas 1b and 2b are plastic regions as shown in Figure 4.2(b).  $L_{fe}$  and  $L_{fp}$  denote the lengths of the elastic and plastic regions of domain 1 respectively, and hence the corresponding normalized coordinates are  $\xi_1^e = x/L_{fe}$  and  $\xi_1^p = (x - L_{fe})/L_{fp}$ .  $L_{be}$  and  $L_{bp}$  are the lengths of the elastic and plastic regions of domain 2 and the corresponding normalized coordinates are  $\xi_2^e = (x - L_f)/L_{be}$  and  $\xi_2^p = (x - L_f - L_{be})/L_{bp}$ .

Displacement functions of elastic and plastic regions for domain 1 and domain 2 is expressed as  $u(\xi_1^e) \cong \sum c_i \phi_{i1}^e$ ,  $u(\xi_1^p) \cong \sum c_i \phi_{i1}^p$ ,  $u(\xi_2^e) \cong \sum c_i \phi_{i2}^e$  and  $u(\xi_2^p) \cong \sum c_i \phi_{i2}^p$  respectively, where  $\phi_{i1}^e$  and  $\phi_{i1}^p$  are portions of the functions  $\phi_{i1}$  in elastic and plastic regions and  $\phi_{i2}^e$  and  $\phi_{i2}^p$  are portions of the functions  $\phi_{i2}$  in elastic and plastic regions respectively. Substituting these assumed displacement functions, the governing equation is obtained as

$$\begin{aligned}
 & \sum_{i=1}^n \sum_{j=1}^n c_i \left[ \left( \frac{K(I-2\nu)^2}{2} + \frac{2G(I+\nu)^2}{3} \right) \left( \frac{2}{L_{fe}} \right)_0^l \int_0^l (A(\xi_1) \phi_{i1}^{e'} \phi_{j1}^{e'}) d\xi_1^e + \right. \\
 & \left( \frac{K(I-2\nu)^2}{2} + \frac{2g(\Gamma_1)(I+\nu_p)^2}{3} \right) \left( \frac{2}{L_{fp}} \right)_0^l \int_0^l (A(\xi_1) \phi_{i1}^{p'} \phi_{j1}^{p'}) d\xi_1^p + \\
 & \left( \frac{K(I-2\nu)^2}{2} + \frac{2G(I+\nu)^2}{3} \right) \left( \frac{2}{L_{be}} \right)_0^l \int_0^l (A(\xi_2) \phi_{i2}^{e'} \phi_{j2}^{e'}) d\xi_2^e + \\
 & \left. \left( \frac{K(I-2\nu)^2}{2} + \frac{2g(\Gamma_2)(I+\nu_p)^2}{3} \right) \left( \frac{2}{L_{bp}} \right)_0^l \int_0^l (A(\xi_2) \phi_{i2}^{p'} \phi_{j2}^{p'}) d\xi_2^p \right] = \left\{ F \cdot \phi_j \Big|_{\xi_f} \right\},
 \end{aligned} \tag{4.19}$$

where  $g(\Gamma_1)$  and  $g(\Gamma_2)$  are the modulus of plasticity as applicable for domain 1 and domain 2 respectively.

### 4.3 Validation study

The present analysis is mainly carried out for bilinear (linear elastic and linear strain hardening elasto-plastic) material behavior, as shown in Figure 4.3. From the stress-strain diagram of Figure 4.3(a), elastic modulus ( $E$ ) and tangent modulus ( $E_t$ ) of the bar material are obtained. In Figure 4.3(b), the relations of deviatoric stress ( $S$ ) and shear strain ( $\Gamma$ ) are shown, which yields shear modulus ( $g(\Gamma) = G'$ ) of the bar material at each state of the post-elastic region. Results are generated using  $E = 210$  GPa,  $E_t = 70$  GPa and yield stress of the bar material  $\sigma_y = 350$  MPa. The value of Poisson's ratio  $\nu$  of the bar in elastic state is taken as 0.3 and after initiation of yielding, Poisson's ratio in post-elastic state ( $\nu_p$ ), is taken as 0.5. The length of the bar  $L$  is taken as 1.2 m.

Another trilinear material model has also been used to establish generalized applicability of the present method. The results are presented for trilinear material behavior using tangent modulus  $E_{tA} = 90$  GPa and  $E_{tB} = 58$  GPa as shown in Figure 4.4(a). In Figure 4.4(b), relations of deviatoric stress ( $S$ ) with shear strain ( $\Gamma$ ) are shown for the trilinear material model.

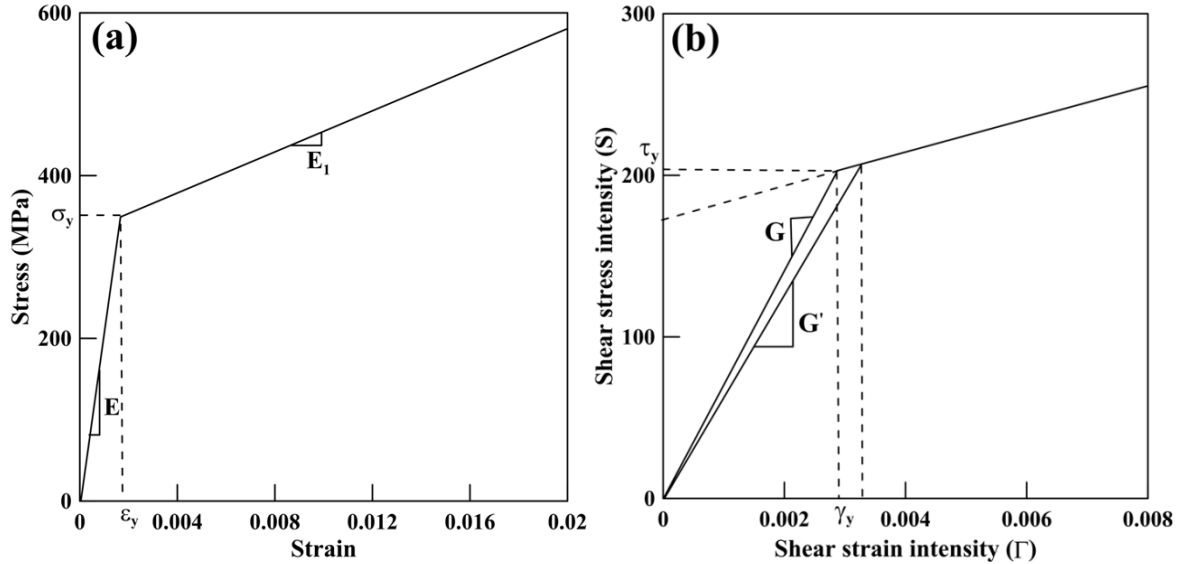


**Figure 4.3.** (a) Linear elastic and linear strain hardening elasto-plastic behavior and (b) deviatoric stress-shear strain diagram, for linear strain hardening material.

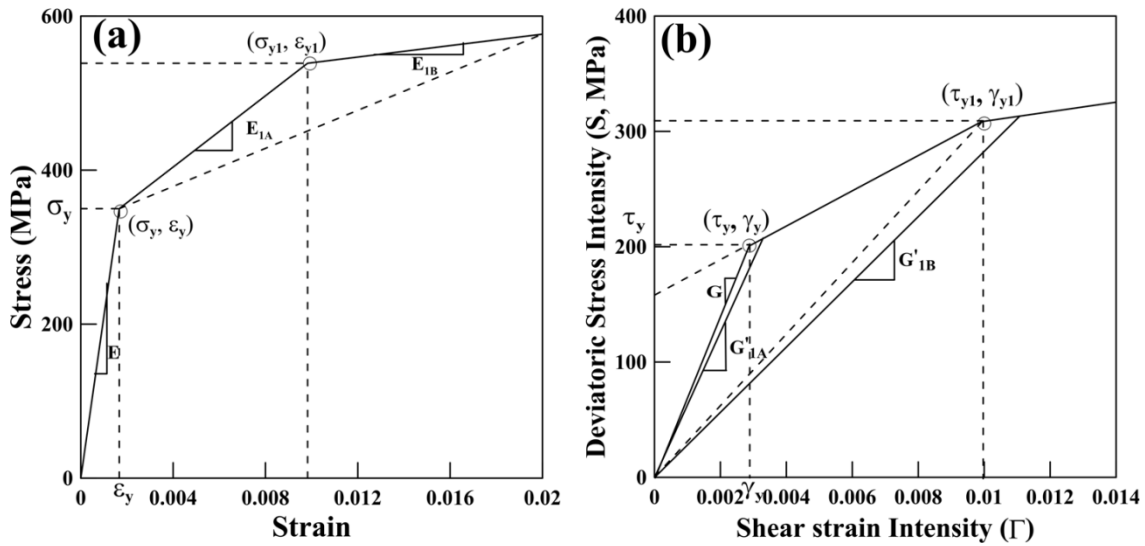


**Figure 4.4.** (a) Linear elastic and bilinear strain hardening elasto-plastic behavior and (b) deviatoric stress-shear strain diagram for bilinear strain hardening material.

Convergence study is carried out to ascertain the minimum number of orthogonal functions required to represent the displacement field. Convergence study is undertaken for a clamped-clamped bar with increasing number of functions. It is found that converged results are

obtained when  $n_f > 9$ . Therefore, numbers of functions are taken as eleven for all subsequent analysis.

The results are generated with aspect ratio ranging from 0 to 0.1 and slenderness ratio ranging from 20 to 100. The smaller diameter  $d_l$  is calculated from the slenderness ratio as  $d_l = (2\sqrt{2}L)/S_R$  and the larger diameter  $d_o$  is calculated from the aspect ratio relation as  $d_o = d_l + (2LA_R)$ . Although critical buckling load may be exceeded for certain combinations of parameter values, the elastic instability consideration is not included in the scope of the present analysis.

To determine the applicability of present formulation, a comparative study has been carried out between the present method and analytical method for a clamped-free taper bar under uniaxial tensile load  $F$  acting at the free end. The expression of stress field, as given below, comes directly from applied load and beam geometry and it is independent on material type,

$$\sigma_x = \frac{4F}{\pi d^2}. \quad (4.20)$$

For the clamped-free taper bar, validation plot for normalized plastic front location with normalized load is provided in Figures 4.5(a1,a2) for bilinear and trilinear material behaviour which shows very good agreement with the same results obtained using analytical method and hence the correctness of the present formulation is established. In another comparison, plot of normalized stress field  $(\sigma/\sigma_y)$  has been validated in Figures 4.5(b1,b2), indicating excellent agreement. The normalized stress fields correspond to collapse load  $(F_c)$  for three different geometries, as specified in the figure. A similar validation plot has been provided in Figures 4.6(a1,b1) and (a2,b2) for a clamped free non-uniform taper bar with bilinear and trilinear material behaviour and in this case also good agreement is observed.

Two different cases of taperness, uniform and non-uniform taper has been considered. In both the cases, initiation of yielding occur at the tip and the particular value tensile loading is termed as elastic limit load  $F_y (= A_l \sigma_y)$ . With increase in load the plastic front gradually proceeds towards the fixed end and ultimately coalesces there at a load termed as plastic collapse load  $F_c$ . Beyond yielding the normalized load is given by  $F^* = F/F_y$  and corresponding to it the

normalized plastic front location is given by  $\xi_p = x_p/L$ , where  $x_p$  represents the location of the plastic front.

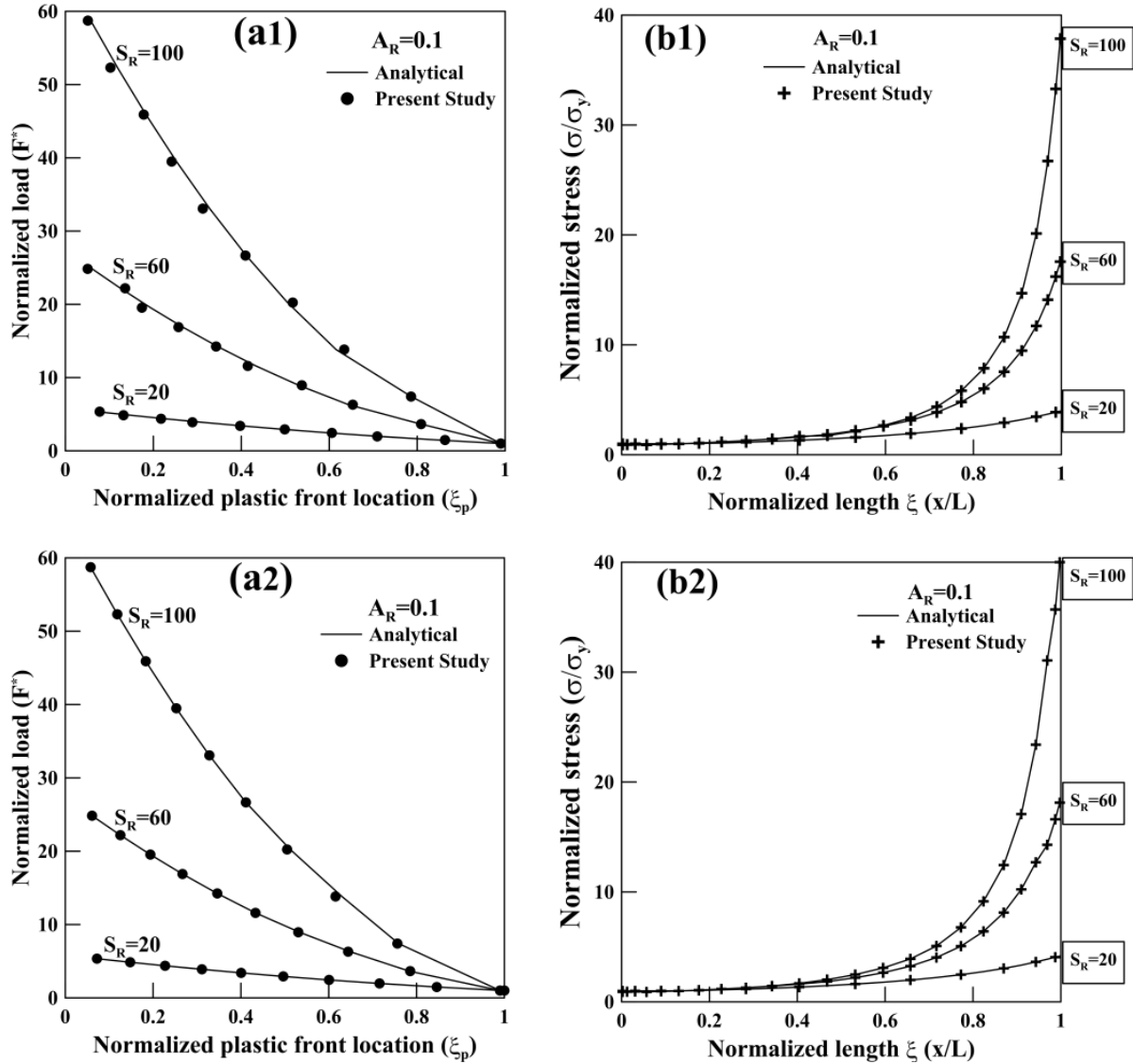


**Figure 4.5.** Validation plots for a uniform taper bar ( $A_R = 0.1$ ) with different values for  $S_R$  for (a#) normalized load vs. normalized plastic front location and (b#) normalized stress vs. normalized length with (#1) bilinear and (#2) trilinear material behaviour.

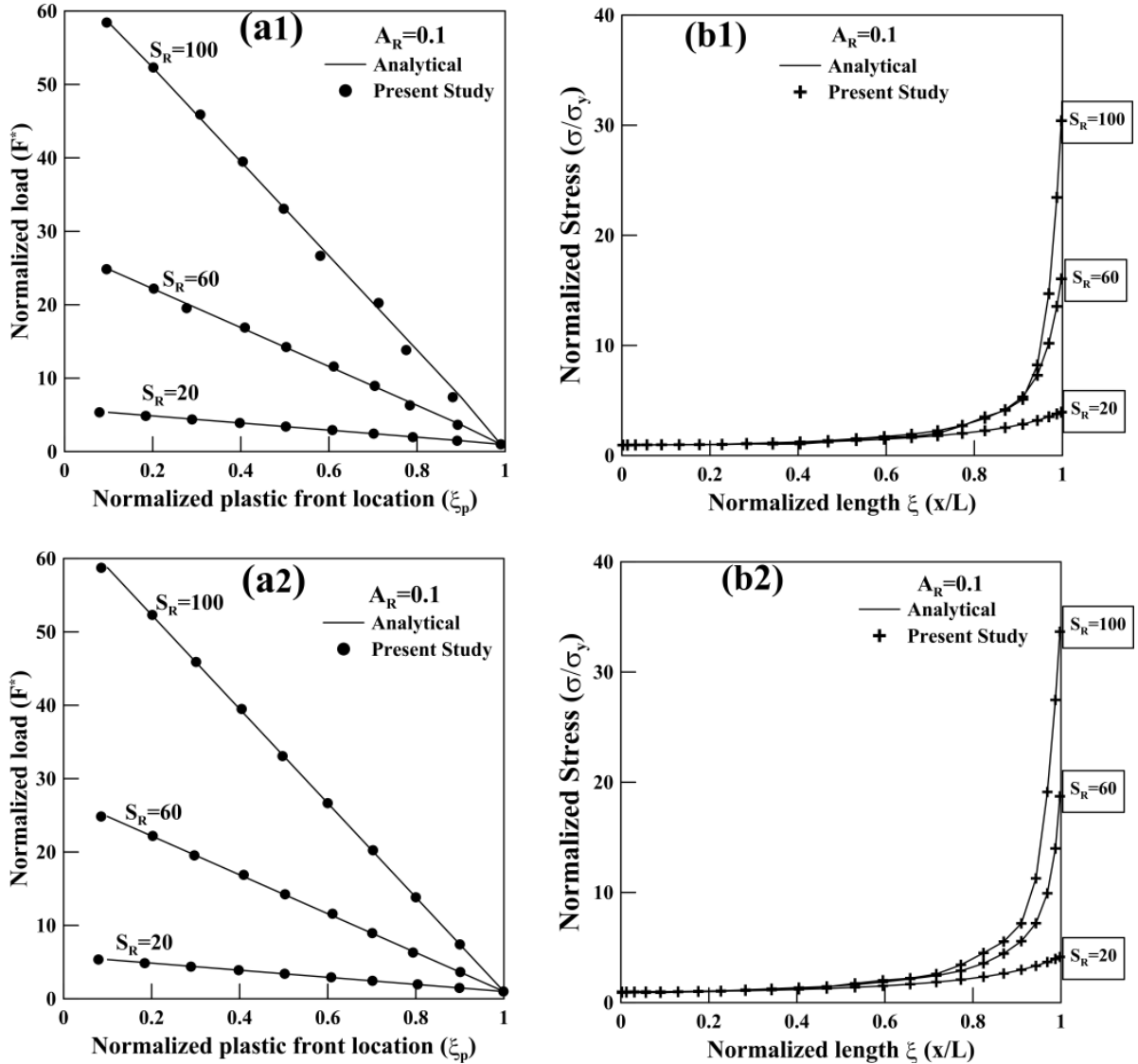


**Figure 4.6.** Validation plots for a non-uniform taper bar ( $A_R = 0.1$ ) with different values for  $S_R$  for (a#) normalized load vs. normalized plastic front location and (b#) normalized stress vs. normalized length with (#1) bilinear and (#2) trilinear material behaviour.

A comparative study for a statically indeterminate problem has also been carried out with that of finite element analysis software Abaqus CAE (version 6.8) for clamped-clamped taper bar with  $L = 1.2$  m,  $\xi_f = 0.5$ ,  $S_R = 100$  and  $A_R = 0.025$  as shown in Figures 4.7(a) and (b). The two figures have been clubbed together and presented again in Figure 4.10(b) at a later stage. The bar subjected to a concentrated load at the midpoint, is modeled by using 8 node linear brick element with 1920 elements in Abaqus. The continuous non-uniform stress field obtained in the present

study at four different load levels shows a discrepancy with that of the results obtained from Abaqus CAE, where a singularity in stress field is observed at load application point. Hence the present mathematical formulation has been revised with domain decomposition method, to accommodate singularity in the solution field.

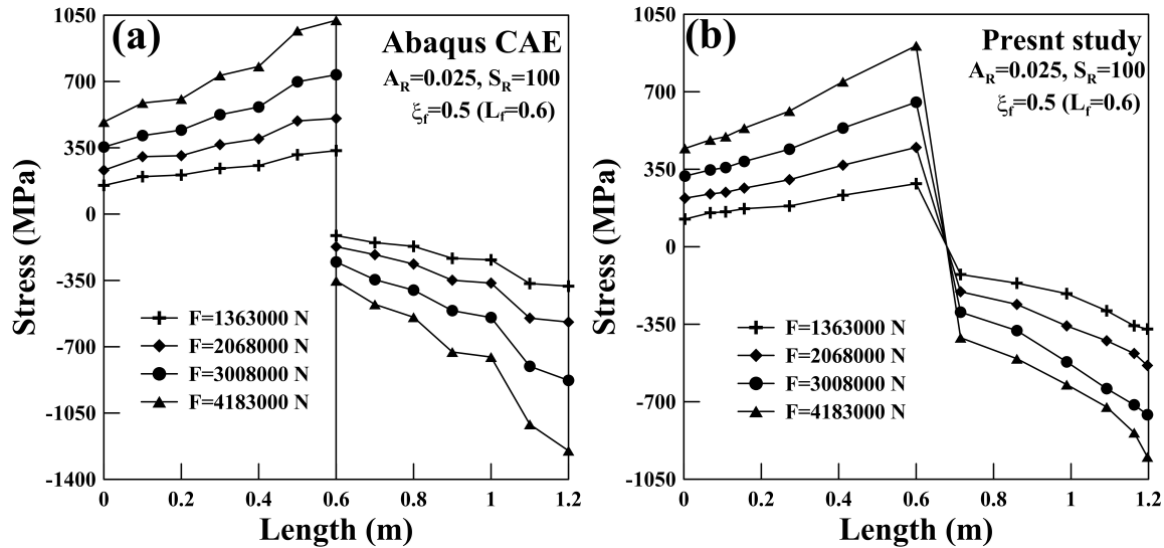


**Figure 4.7.** Plot of stress fields for a clamped-clamped taper bar as obtained in (a) Abaqus CAE and (b) Present study.

### 4.3.1 Revised formulation using iterative variational method

In domain decomposition method, the whole domain is decomposed into two sub-domains about the point of application of the load  $F$ . The reaction forces of axial load  $F$ , developed at the two fixed ends are denoted by  $F_0$  and  $F_1$  respectively where  $F = F_0 + F_1$ , as shown in Figure 4.8. The notations of the bar and the nomenclatures of the two domains remain identical.



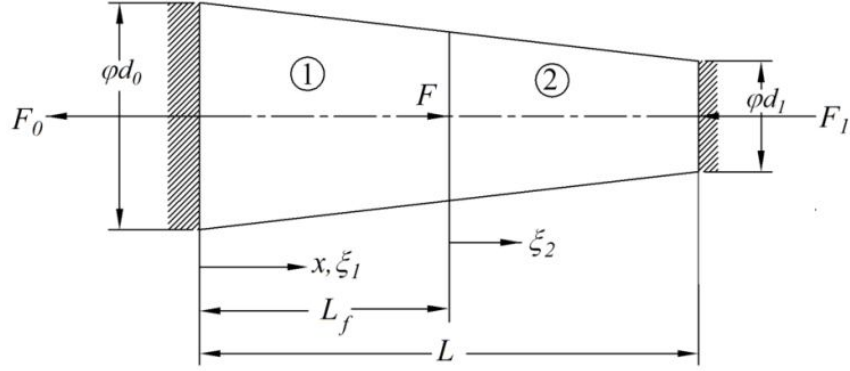


Figure 4.8. Taper bar with reaction forces at fixed ends.

#### 4.3.1.1 Iterative variational method (IVM) using domain decomposition (DDM)

The expression of strain energy and work potential for domain 1 under elastic conditions is obtained as:

$$U_1 = \int_0^{L_f} \left( \frac{K(I-2\nu)^2}{2} + \frac{2G(I+\nu)^2}{3} \right) A(x_1) \left( \frac{\partial u_1}{\partial x_1} \right)^2 dx_1 \quad (4.21)$$

and

$$V_1 = -F_0 u(\xi_1) \Big|_{\xi_1=L}. \quad (4.22)$$

On substituting Eqs. (4.21) and (4.22) in the energy principle  $\delta(U_1 + V_1) = 0$ , the governing equilibrium equation for domain 1 is expressed in normalized coordinate  $\xi_1$  as

$$\left( \frac{K(I-2\nu)^2}{2} + \frac{2G(I+\nu)^2}{3} \right) \left( \frac{2}{L_f} \right) \left[ \int_0^1 A(\xi_1) \left( \frac{\partial u}{\partial \xi_1} \right) \delta \left( \frac{\partial u}{\partial \xi_1} \right) d\xi_1 \right] - F_0 \delta [u(\xi_1) \Big|_{\xi_1=L}] = 0. \quad (4.23)$$

Similarly, the governing equation for domain 2 in normalized coordinate  $\xi_2$  is given by

$$\left( \frac{K(I-2\nu)^2}{2} + \frac{2G(I+\nu)^2}{3} \right) \left( \frac{2}{L_b} \right) \left[ \int_0^1 A(\xi_2) \left( \frac{\partial u}{\partial \xi_2} \right) \delta \left( \frac{\partial u}{\partial \xi_2} \right) d\xi_2 \right] - F_1 \delta [u(\xi_2) \Big|_{\xi_2=0}] = 0. \quad (4.24)$$

The global displacement function  $u(\xi)$  is approximated by a linear combination of sets of orthogonal coordinate functions as before.

For the purpose of computation, the respective portions of displacement functions in domain 1 and domain 2 are expressed as  $u(\xi_1) \cong \sum c_i \phi_{i1}$  and  $u(\xi_2) \cong \sum d_i \phi_{i2}$ , where  $\phi_{i1}$  and  $\phi_{i2}$  are portions of the function  $\phi_i$  in domain 1 and domain 2. Substituting these assumed displacement functions in Eqs. (4.23) and (4.24) and replacing operator  $\delta$  by  $\partial/\partial c_j$ , the governing equation in matrix form is obtained as

$$\left( \frac{K(I-2\nu)^2}{2} + \frac{2G(I+\nu)^2}{3} \right) \sum_{i=1}^n \sum_{j=1}^n \left[ \left( \frac{2}{L_f} \right) (A(\xi_1) \phi'_{i1} \phi'_{j1}) d\xi_1 \right] \{c_i\} = \{F_0 \cdot \phi_j|_{\xi_1=1}\} \quad (4.25)$$

and

$$\left( \frac{K(I-2\nu)^2}{2} + \frac{2G(I+\nu)^2}{3} \right) \sum_{i=1}^n \sum_{j=1}^n \left[ \left( \frac{2}{L_b} \right) (A(\xi_2) \phi'_{i2} \phi'_{j2}) d\xi_2 \right] \{d_i\} = \{F_1 \cdot \phi_j|_{\xi_2=0}\}. \quad (4.26)$$

Eqs. (4.25) and (4.26) can be clubbed together in matrix form as  $[K]\{C\} = \{f\}$  where,  $[K]$  is the stiffness matrix,  $\{C\}$  is the column matrix of displacement coefficients and  $\{f\}$  is the column matrix of forces which are of the form given below:

$$[K] = \begin{bmatrix} k_{11} & k_{12} \\ k_{21} & k_{22} \end{bmatrix}, \quad \{C\} = \begin{bmatrix} \{c_i\} \\ \{d_i\} \end{bmatrix} \quad \text{and} \quad \{f\} = \begin{bmatrix} \{F_0\} \\ \{F_1\} \end{bmatrix}$$

The elements of the stiffness matrix are easy to identify from Eqs. (4.25) and (4.26).

#### 4.3.1.2 The iterative scheme for revised formulation

In this method it is needed to estimate the contribution of the axial load ( $F$ ) in both the regions ( $F_0$  for domain 1 and  $F_1$  for domain 2). In order to estimate these loads an iterative technique is employed based on the compatibility condition ( $u|_{\xi_1=1} = u|_{\xi_2=0}$ ). The procedure followed is mentioned below and flow chart of the solution algorithm is shown in Figure 4.9.

1. Load  $F$  is initiated at a very low value and an increment  $\Delta F$  is selected suitably. Yield load is achieved at  $i^{\text{th}}$  load step ( $F_i = F_y$ ) and elastic relations are valid upto this point. Hence sharing of  $F_i$  at the two boundaries ( $F_{i0}$  and  $F_{i1}$ ) are obtained analytically.

2. Set  $x_p^o = L$  and for the next load step  $F_{i+1} = F_i + \Delta F$ , the plastic front location ( $x_p$ ) is determined first from elastic domain assumption.
3. A load sharing parameter ( $\alpha$ ) for load increment  $\Delta F$  is assumed and another loop with counter  $j$  is initiated. Corresponding to  $F_{i+1}$ , the actual load sharing is obtained at  $j^{\text{th}}$  step, when compatibility condition is satisfied, Corresponding to this load values of  $F_0$  and  $F_1$  are  $F_{0(i+1)} = F_{0i} + j\alpha\Delta F$  and  $F_{1(i+1)} = F_{1i} + (1 - j\alpha)\Delta F$ .
4. Here it is assumed that domain 1 remains fully elastic and based on the yield front location ( $x_p$ ),  $\phi_{i2}^e$  and  $\phi_{i2}^p$  are portions of the functions  $\phi_{i2}$  in elastic and plastic regions of domain 2 and function  $\phi_{i1}$  is defined for fully elastic domain 1. Using these functions elastic stiffness matrix for domain 1  $[K_e]$  and elastoplastic stiffness matrix  $[K_{ep}]$  for domain 2 is obtained. Using  $F_{0(i+1)}$  and  $F_{1(i+1)}$ , load vectors  $\{F_0\}$  and  $\{F_1\}$  for both the domains are obtained. Coefficients  $\{c_i\}$  and  $\{d_i\}$  are computed as  $\{c_i\} = [K_e]^{-1} \{F_0\}$  and  $\{d_i\} = [K_{ep}]^{-1} \{F_1\}$ . From the displacement fields of both the domains, the difference in displacements at load application point  $(u_{(i+1)}|_{\xi_1=1} - u_{(i+1)}|_{\xi_2=0})$  is found to be zero at  $j^{\text{th}}$  step.
5. Corresponding strain and stress fields are obtained and location of yield front ( $x_p$ ) is calculated, and updated as  $x_p^o = x_p$ . For same load step  $F_{i+1}$  but with updated  $g(\Gamma)$  displacement fields are computed again as mentioned above. The process of updating the material parameter  $g(\Gamma)$  is well documented in Kachanov (1971) and it was implemented in the earlier part of the analysis as well. Once the convergence in  $x_p$  is obtained load step  $F_{i+1}$  is solved.
6. Increment  $F_{i+2} = F_{i+1} + \Delta F$  is given and the entire procedure is repeated for subsequent load steps.
7. Once a particular value of  $F$  is reached yielding also starts at domain 1 and both the region becomes elastoplastic which leads to four region formulation. The solution procedure is identical and other details are not mentioned here to maintain brevity.

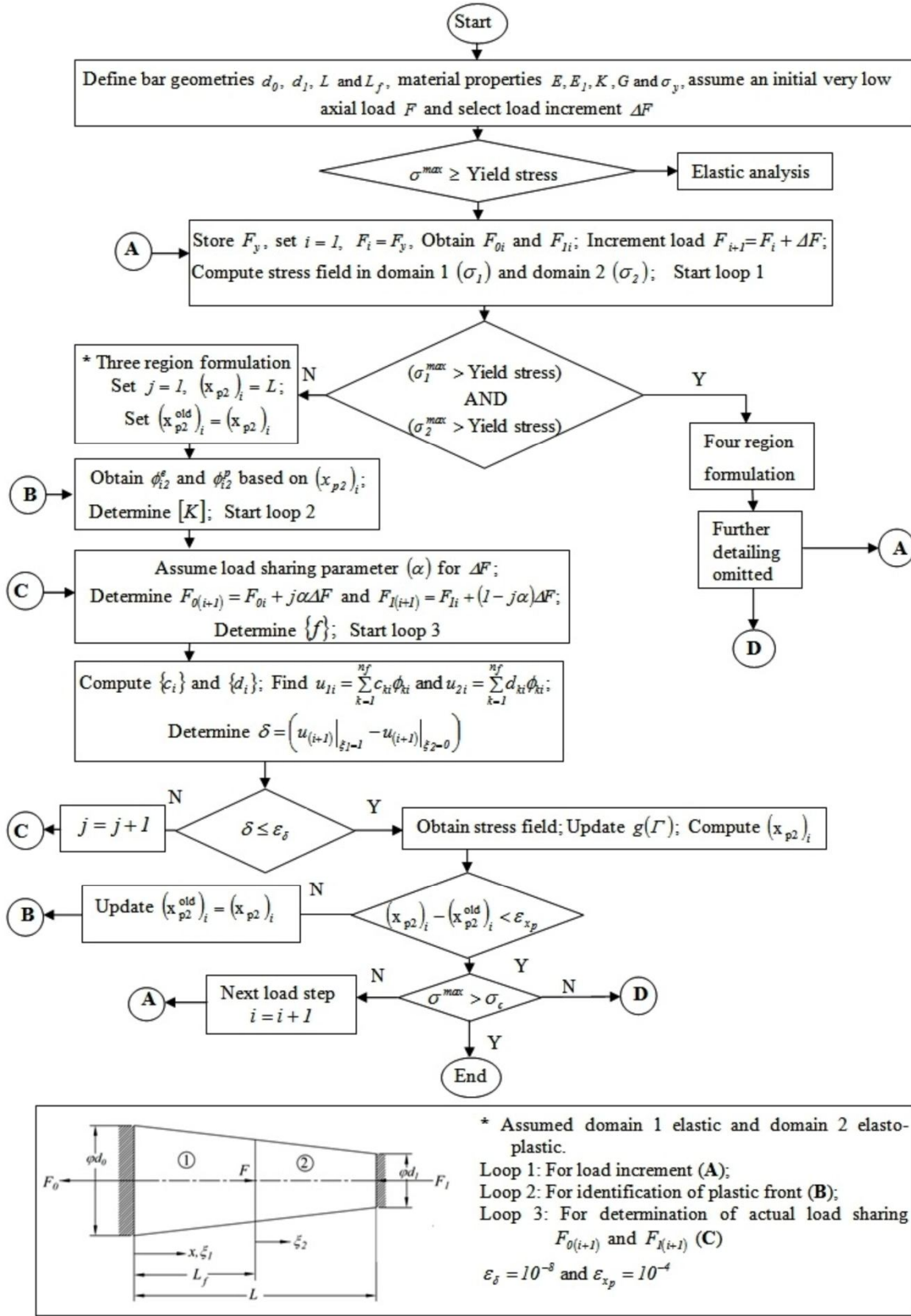
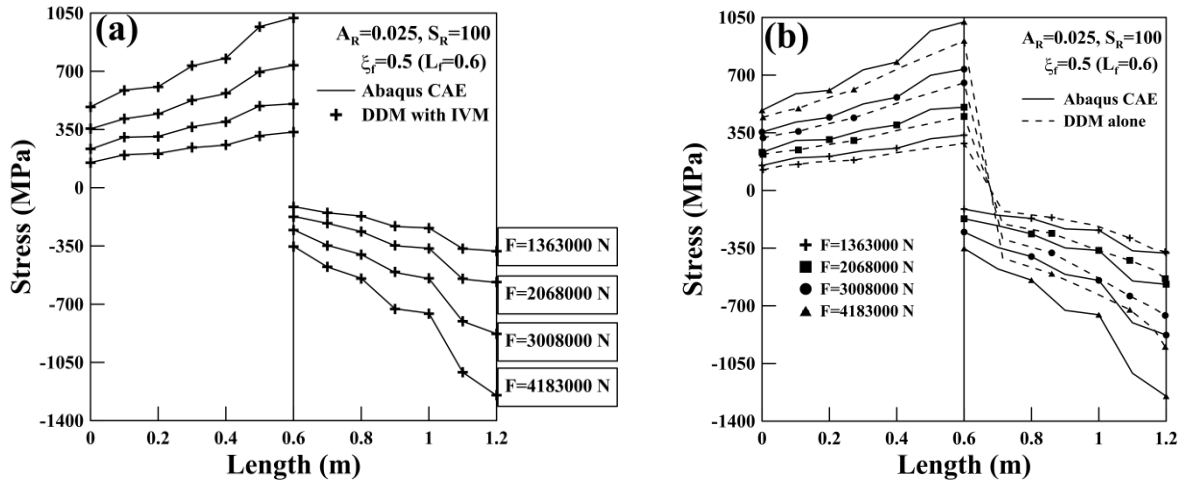


Figure 4.9. Flow chart for the solution algorithm.

Results obtained from the revised formulation using domain decomposition method with iterations for the clamped-clamped taper bar is shown in Figure 4.10(a), which successfully validates the present method with that of the finite element analysis software. For ready reference, the earlier results of comparative study are also shown in Figure 4.10(b). The percent error of the results of the present method (DDM and DDM with IVM) and Abaqus CAE are also presented in Table 4.1.



**Figure 4.10.** Validation plot for a clamped-clamped taper bar with Abaqus CAE using (a) DDM with IVM and (b) DDM alone.

**Table 4.1:** Validation of results on  $F = 300800$  N for a clamped-clamped taper bar

Axial length (m)	DDM	DDM with IVM	Abaqus	Error (%) (DDM and Abaqus)	Error (%) (DDM with IVM and Abaqus)
0.2	280.7	312.14	306.83	8.52	1.73
0.4	369.72	397.48	399.93	7.55	0.61
0.8	-234.21	-401.63	-403.17	41.90	0.38
1.0	-364.47	-552.30	-546.58	33.32	1.05
1.2	-535.97	-877.74	-879.33	39.04	0.18

### 4.3.2 Analytical solution of the problem with variationally based boundary conditions

To determine the applicability of the present formulation, a further validation study with the present method and analytical method for a clamped-clamped taper bar under elastic

conditions have also been carried out. In order to calculate the exact displacement fields for domain 1 and domain 2, the stationary condition of  $\Pi_1 (=U_1 + V_1)$  and  $\Pi_2 (=U_2 + V_2)$  is used and the governing differential equations and the natural boundary conditions are generated as mentioned in Bathe (2006).

For domain 1, we have

$$\Pi_1 = \frac{E}{2} \left[ \int_0^{L_f} A(x_1) \left( \frac{\partial u}{\partial x_1} \right)^2 dx_1 \right] - F_0 \left[ u \Big|_{x_1=L_f} \right]. \quad (4.27)$$

Setting  $\delta \Pi_1 = 0$  and using integration by parts, we obtain

$$\frac{d}{dx_1} \left( EA(x_1) \frac{du(x_1)}{dx_1} \right) = 0 \quad (4.28)$$

$$EA(x_1) \frac{du(x_1)}{dx_1} \Big|_{x_1=L_f} = F_0 \quad (4.29)$$

The solution of Eq. (4.28) subjected to the natural boundary condition in Eq. (4.29) and the essential boundary condition  $u|_{x_1=0} = 0$  gives the exact solution of the given problem. For uniform taper bar, the analytical displacement field for domain 1 is obtained as

$$u(x_1) = \frac{4F_0L}{\pi E(d_0 - d_1)} \left( \frac{1}{d_0 - \frac{x_1}{L}(d_0 - d_1)} - \frac{1}{d_0} \right). \quad (4.30)$$

Similarly, the analytical displacement field for domain 2 is obtained as

$$u(x_2) = \frac{-4F_1L}{\pi E(d_0 - d_1)} \left( \frac{1}{d_0 - \frac{x_2}{L}(d_0 - d_1)} - \frac{1}{d_1} \right). \quad (4.31)$$

The analytical displacement fields for the two domains of non-uniform taper bar is obtained in a similar way and they are given by

$$u(x_1) = \frac{4F_0L}{\pi E(d_0^2 - d_1^2)} \ln \left( \frac{d_0^2}{d_0^2 - \frac{x_1}{L}(d_0^2 - d_1^2)} \right) \quad (4.32)$$

and

$$u(x_2) = \frac{-4F_1L}{\pi E(d_0^2 - d_1^2)} \ln \left( \frac{d_1^2}{d_0^2 - \frac{x_2}{L}(d_0^2 - d_1^2)} \right). \quad (4.33)$$

The reaction forces  $F_0$  and  $F_1$  at the two boundaries are unknown initially as the problem is statically indeterminate.  $F_0$  and  $F_1$  is determined by setting  $u(x_1) = u(x_2)$  at  $x = L_f$  and satisfying the force relation  $F = F_0 + F_1$ . Plot for displacement fields with length for uniform and non-uniform taperness is provided in Figures 4.11(a) and (b) for two different load application points which matches exactly with the results obtained using present method. The analytical solution of the problem, as reported in Eqs. (4.30)-(4.33) is possible for elastic material only, because in post-elastic state  $E$  becomes dependent on space variable  $x$ . So, exact analytical solution in post-elastic state is not possible and implementation of the numerical solution scheme is appreciable for such problem, as exemplified earlier in Figures 4.5 and 4.6 for statically determinate clamped free bars. In case of the present statically indeterminate clamped-clamped bar implementation of numerical solution scheme becomes much more involved.

## 4.4 Results and discussion

The purpose of this study is to reveal the yield front propagation of statically indeterminate taper bar in axial direction with uniform and non-uniform taperness in post-elastic regime. In addition the effect of aspect ratio and slenderness ratio on non-dimensional collapse load of clamped-free and clamped-clamped taper bar is studied in subsequent sections. The range of values of  $A_R$  and  $S_R$  are kept identical as mentioned in the previous validation sections. For clamped-free taper bar, non-dimensional collapse load is given by  $\lambda_c = F_c/F_y$  whereas for clamped-clamped taper bar, two different non-dimensional collapse load  $\lambda_{c1}$  and  $\lambda_{c2}$  are used.

Results are presented for two different types of taperness. However, for uniform taperness, load application point is considered at five different locations but for non-uniform taperness, result is provided for a particular load application point.

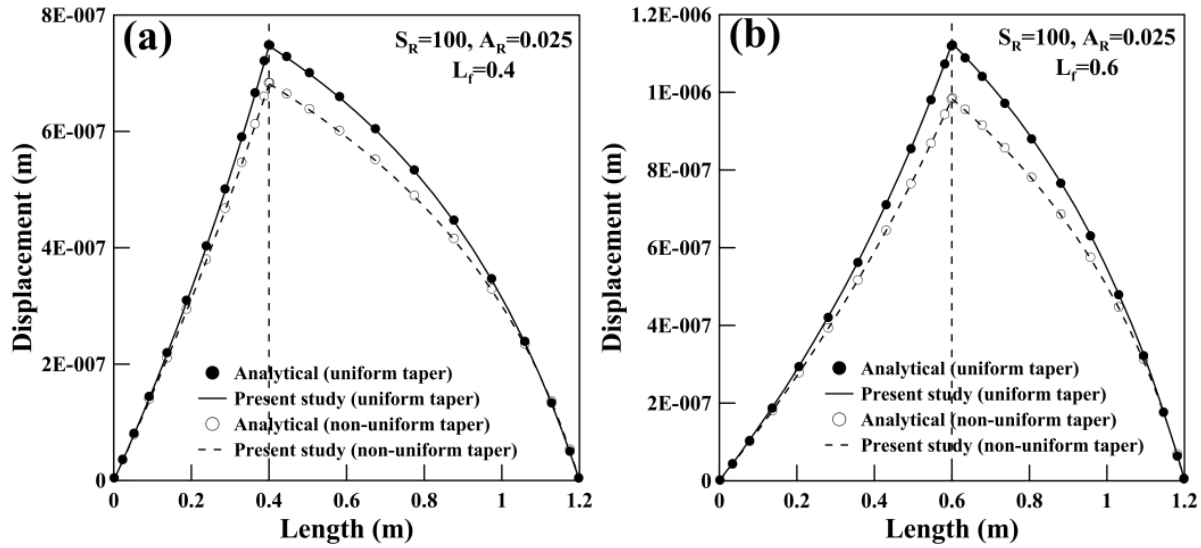


**Figure 4.11.** Plot of displacement fields for a clamped-clamped uniform and non-uniform taper bar as obtained in analytical method and present study for (a)  $L_f = 0.4$  and (b)  $L_f = 0.6$ .

#### 4.4.1 Effect of aspect ratio and slenderness ratio on clamped-free taper bar

For clamped-free bar with uniform and non-uniform taper, 3D and contour plots of non-dimensional collapse load showing its simultaneous variation with aspect ratio and slenderness ratio has been presented in Figures 4.12(a) and (b). In both the cases, it is observed that with increase in  $A_R$  as well as  $S_R$ ,  $\lambda_c$  increases.

#### 4.4.2 Post-elastic behaviour of clamped-clamped uniform taper bar

For clamped-clamped bar, results are presented for non-dimensional collapse load in domain 1 and domain 2. Non-dimensional collapse load for domain 1 and domain 2 are given by  $\lambda_{c1} = F_{c1}/F_{y1}$  and  $\lambda_{c2} = F_{c2}/F_{y2}$ . Change in geometry of uniform taper bar for typical values of  $A_R$  and  $S_R$  are shown in Table 4.2 through graphical representation. For better understanding the



elastic and plastic limit loads for domain 1 and 2 have been furnished in Table. 4.3 for different load application points for two different geometries (case A and B) of Table 4.2.

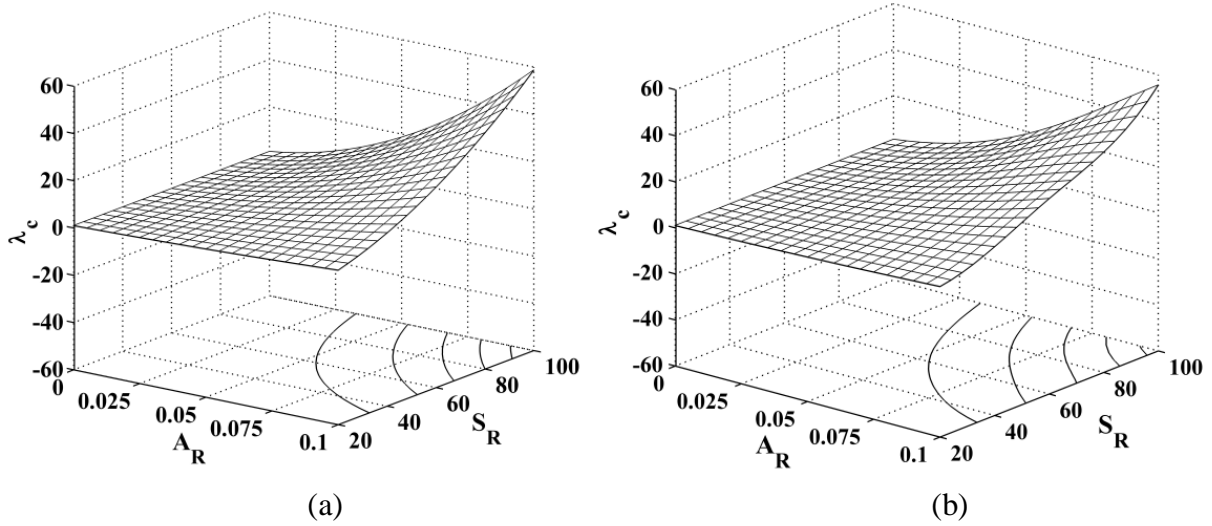


**Figure 4.12.** 3D and contour plots of non-dimensional collapse load ( $\lambda_c$ ) showing its variation with  $A_R$  and  $S_R$  for (a) uniform taper and (b) non-uniform taper.

**Table 4.2:** Graphical representation of clamped-clamped uniform taper bar

$S_R \backslash A_R$	20	50	100	
0	$d_o = d_l = 169.70$ mm 	$d_o = d_l = 67.88$ mm 	$d_o = d_l = 33.94$ mm 	<b>C</b>
0.05	$d_o = 289.70$ mm, $d_l = 169.70$ mm 	$d_o = 187.88$ mm, $d_l = 67.88$ mm 	$d_o = 153.94$ mm, $d_l = 33.94$ mm 	<b>B</b>
0.1	$d_o = 409.70$ mm, $d_l = 169.70$ mm 	$d_o = 307.88$ mm, $d_l = 67.88$ mm 	$d_o = 273.94$ mm, $d_l = 33.94$ mm 	<b>A</b>

**Table 4.3:** Elastic and plastic limit loads for domain 1 and domain 2 of taper bar for two different geometries with bilinear material model (case A and B of Table 4.1)

	Case A				Case B			
$\xi_f$	$F_{y1}$ (kN)	$F_{c1}$ (kN)	$F_{y2}$ (kN)	$F_{c2}$ (kN)	$F_{y1}$ (kN)	$F_{c1}$ (kN)	$F_{y2}$ (kN)	$F_{c2}$ (kN)
0.3	39221.47	72559.72	62754.35	112957.83	7178.85	13404.05	11342.59	20416.66
0.4	35786.23	66920.25	39364.85	97624.84	6481.43	11472.12	6999.94	15949.92
0.5	34280.93	82058.30	26992.86	81788.37	6596.65	13852.96	4780.18	12906.48
0.6	33573.83	67147.67	16786.92	65468.98	6263.33	11900.33	2940.53	10291.86
0.7	33206.38	56107.34	16357.83	48746.32	6033.90	9171.53	2832.82	7931.89

3D and contour plots of non-dimensional collapse load for domain 1 and domain 2 showing its variation with aspect ratio and slenderness ratio for five different load application points have been presented in Figures 4.13((a1,a2)-(e1,e2)). It is evident from the figures that with increase in  $A_R$  as well as with  $S_R$ ,  $\lambda_{c1}$  and  $\lambda_{c2}$  attain highest values at  $A_R = 0.1$  and  $S_R = 100$  for all load application points.  $\lambda_{c1}$  decreases and  $\lambda_{c2}$  increases as the load application points shift from higher diameter end to lower diameter end.

To analyze the growth of yield front in greater details, the variation of stress field with load for a uniform taper bar is reported in Figures 4.14(a-d) through waterfall plots. Figures are provided for four different load application points ( $\xi_f = 0.4, 0.5, 0.6$  and  $0.7$ ) and in each figure several stress profiles are shown for loads ranging from initial yield limit to ultimate collapse limit. It is observed for all the cases that stress increases with increase in load, initial yielding occurs at ( $x=L$ ) and with increase in load intensity yielding also occurs at ( $x=L_f$ ). When the load reaches  $F_{c2}$  entire bar becomes elastoplastic.

From the stress fields, as shown in waterfall plots of Figure 4.14, plastic front locations are captured at different load levels and their location with load is provided in Figures 4.15(a-d). For a clamped-clamped uniform taper bar, the figures capture the advancement of plastic front with increasing load for domain 1 and domain 2, for the four load application points.

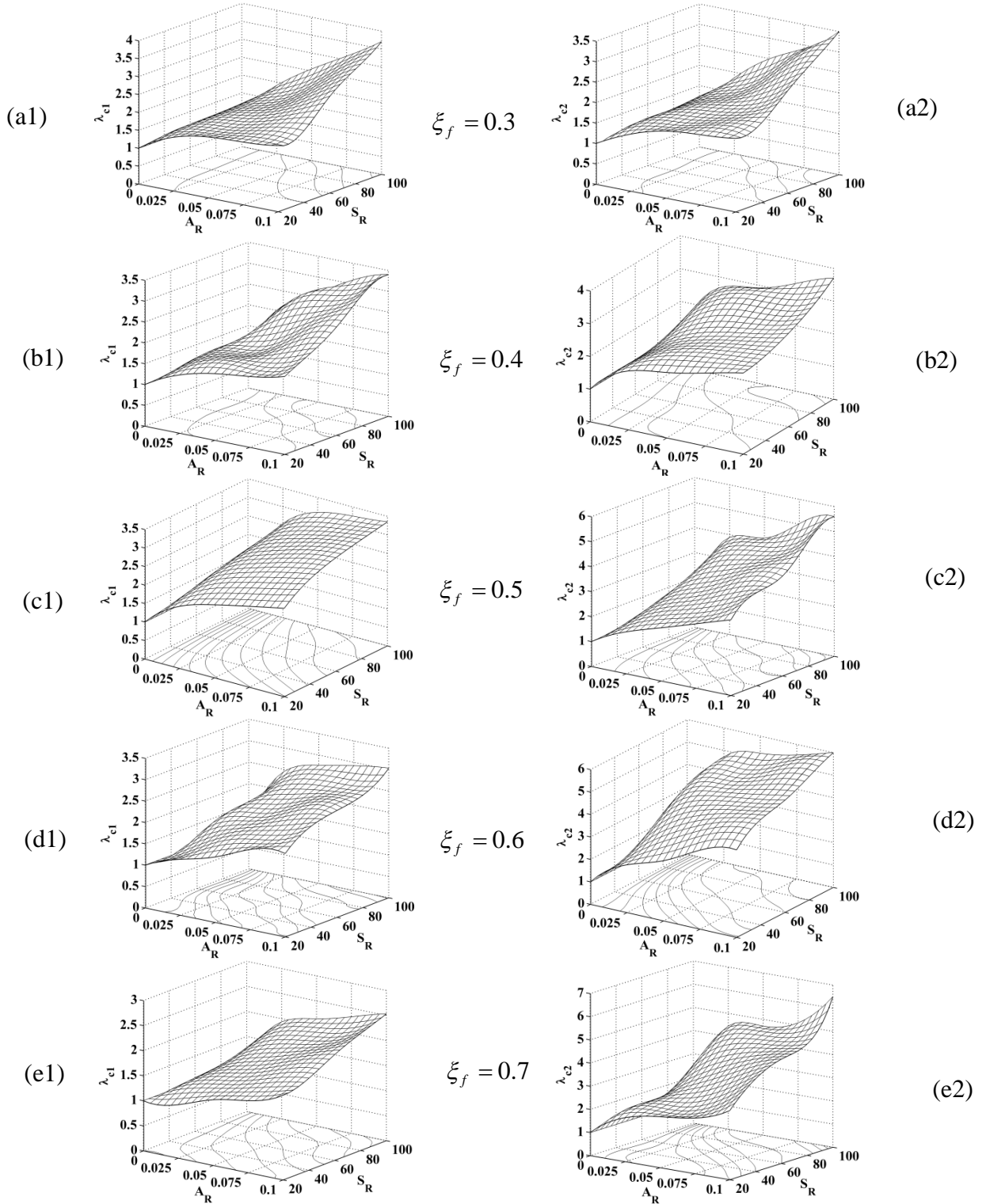


**Figure 4.13.** 3D and contour plots of non-dimensional collapse load  $\lambda_{c1}$  and  $\lambda_{c2}$  showing its variation with  $A_R$  and  $S_R$  for load application point (a1, a2)  $\xi_f = 0.3$  (b1, b2)  $\xi_f = 0.4$  (c1, c2)  $\xi_f = 0.5$  (d1, d2)  $\xi_f = 0.6$  and (e1, e2)  $\xi_f = 0.7$ .

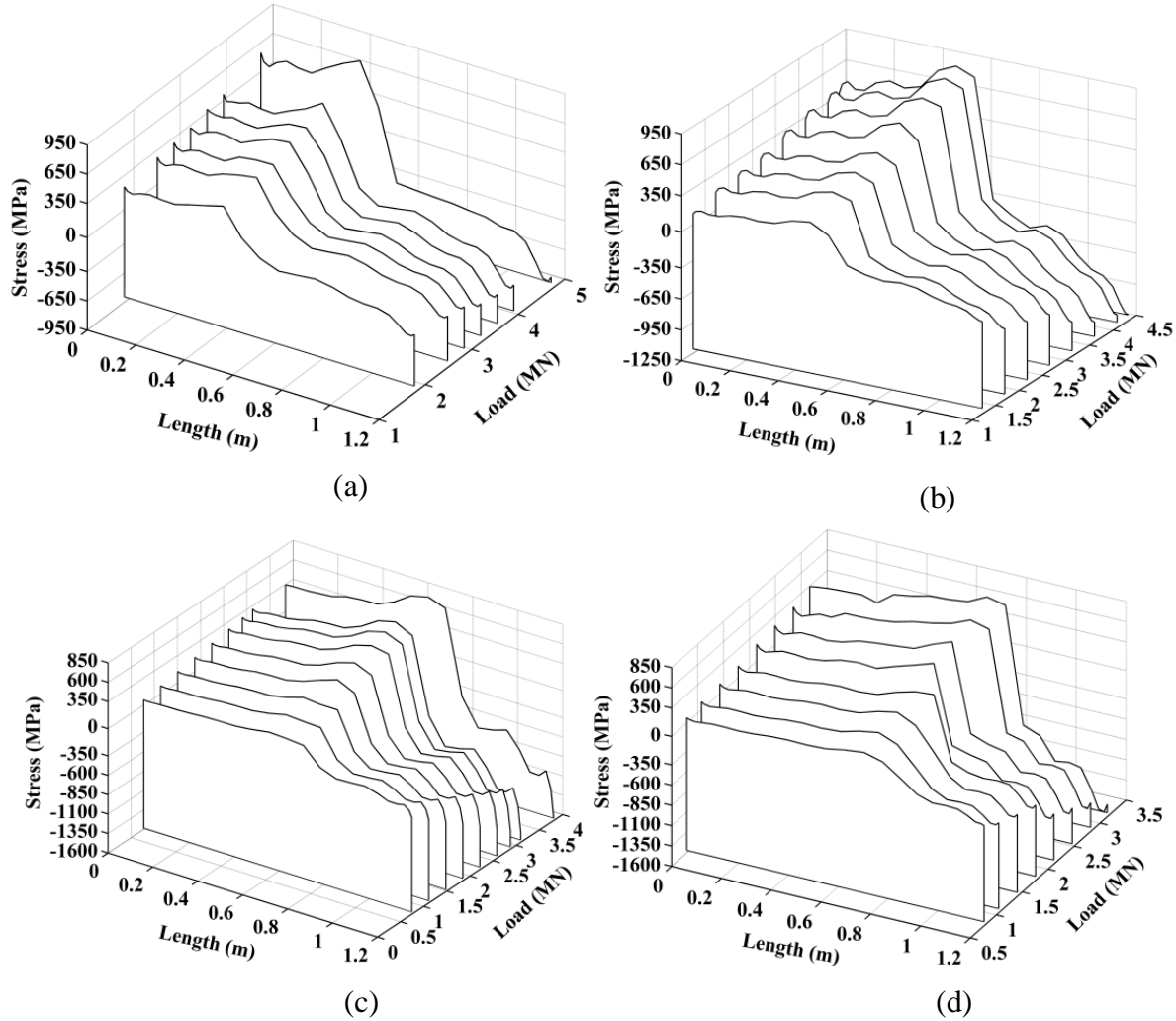


**Figure 4.14.** Waterfall plot of stress variation with load for a uniform taper bar with  $A_R = 0.025$  and  $S_R = 100$  for different load application point (a)  $\xi_f = 0.4$  (b)  $\xi_f = 0.5$  (c)  $\xi_f = 0.6$  (d)  $\xi_f = 0.7$ .

### 4.4.3 Post-elastic behaviour of clamped-clamped non-uniform taper bar

For a clamped-clamped non-uniform taper bar, 3D and contour plots of non-dimensional collapse load, showing its variation with aspect ratio and slenderness ratio for load application point ( $\xi_f = 0.5$ ) are presented in Figures 4.16(a, b), for domain 1 and domain 2 respectively. The observation for this case remains almost same as that mentioned for uniform taper bars except for the fact that the increase in  $\lambda_{c2}$  is much more than  $\lambda_{c1}$ . Similar observations as that for load

application point at  $\xi_f = 0.5$ , are found for all the other load application points but are not reported here to maintain brevity.

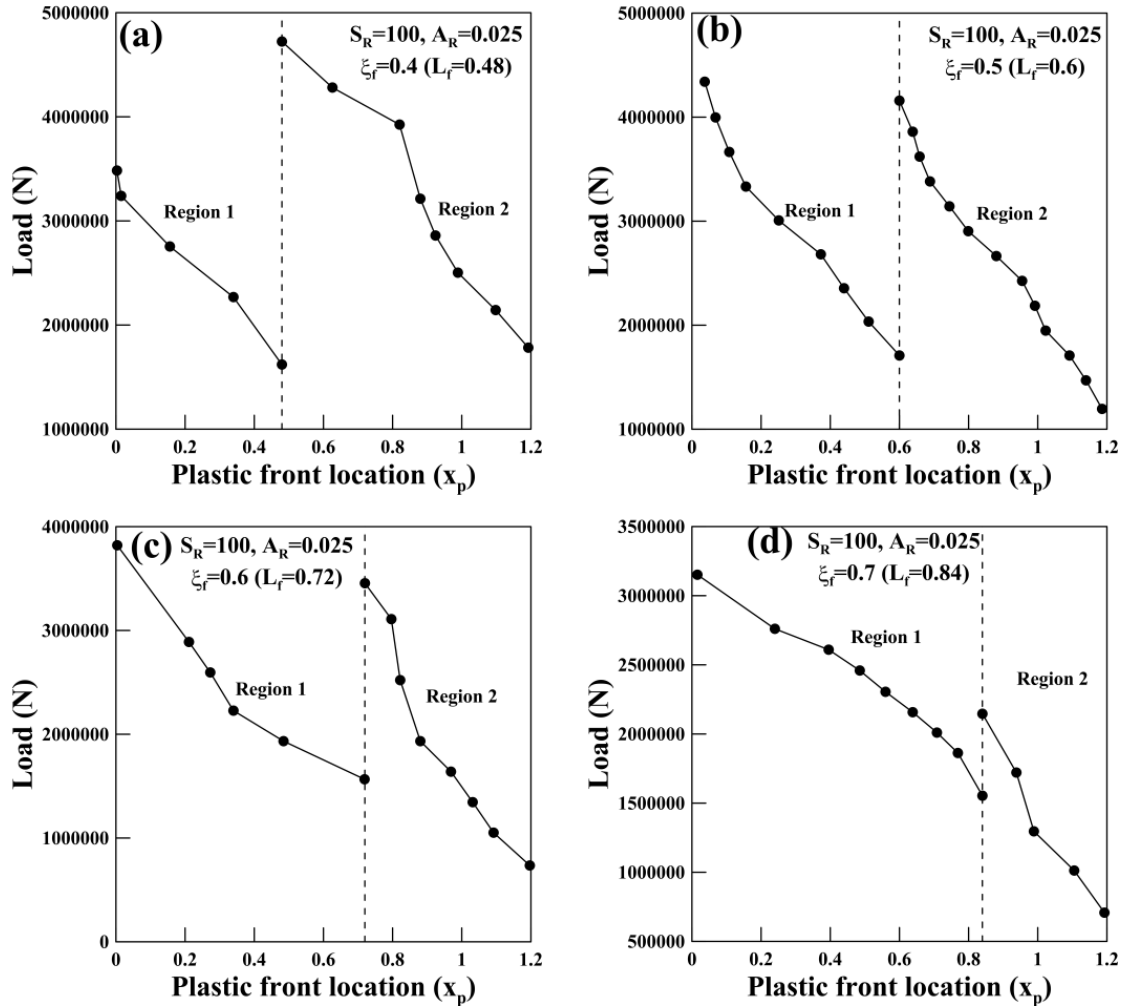


**Figure 4.15.** Plot of plastic front location variation with load for a uniform taper bar for load application point (a)  $\xi_f = 0.4$  (b)  $\xi_f = 0.5$  (c)  $\xi_f = 0.6$  (d)  $\xi_f = 0.7$ .

In Figures 4.17(a-d) the variation of stress field in the bar is reported through waterfall plots and the observation for this case also remains same as that for uniform taper bars, but in this case the yield load and plastic collapse load for both the domains ( $F_{y1}$ ,  $F_{y2}$  and  $F_{c1}$ ,  $F_{c2}$ ) are higher. From these waterfall plots the plastic front locations are captured at different load levels and their location has been provided in Figures 4.18(a-d) with increasing load for domain 1 and domain 2.

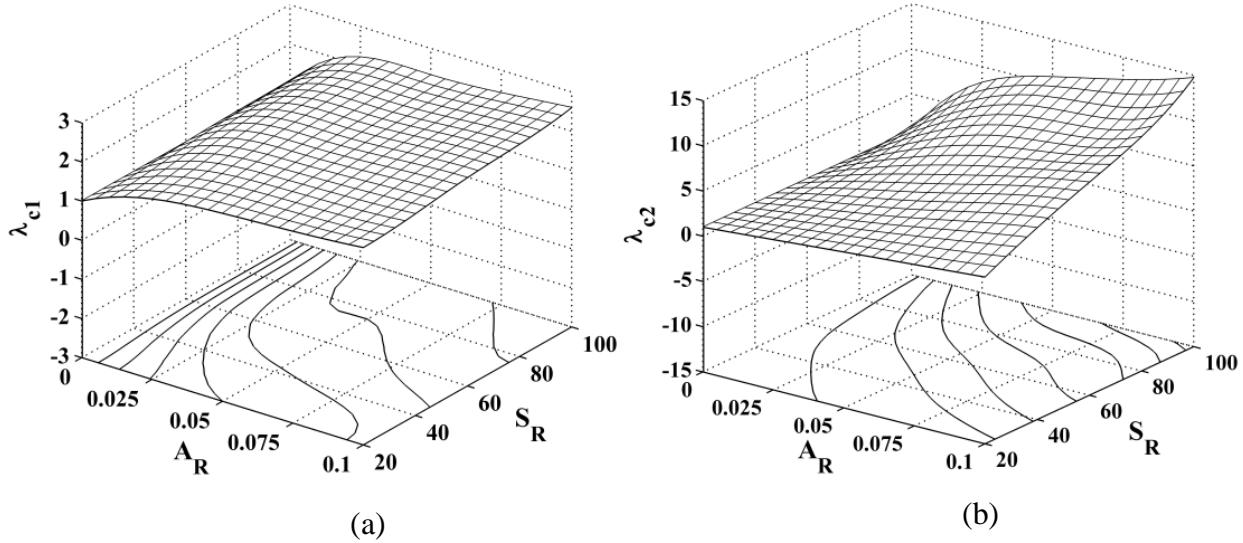


**Figure 4.16.** 3D and contour plots of non-dimensional collapse load  $\lambda_{c1}$  and  $\lambda_{c2}$  showing it's variation with  $A_R$  and  $S_R$  for load application point (a, b).

#### 4.4.4 Results for clamped-clamped uniform taper bar with trilinear material model

The elastic and plastic limit loads for domain 1 and 2 have been furnished in Table. 4.4 for different load application points for two different geometries (case A and B of Table 4.2). The values of  $F_y$  and  $F_c$  for uniform geometry bar (case C of Table 4.2) remains same, as expected for a material with given  $\sigma_y$  and  $\sigma_{ult}$  values. From Table 4.4, it is also observed that the elastic limit loads for both the domains ( $F_{y1}$  and  $F_{y2}$ ) remain same for bilinear and trilinear material model. There is a change in plastic collapse loads and it is observed that the plastic collapse load is more in case of trilinear material model for all the load application points and for both the domains. For better understanding, sample 3D and contour plots of non-dimensional collapse load, showing it's variation with aspect ratio and slenderness ratio for load application point ( $\xi_f = 0.5$ ) are presented in Figures 4.19(a, b). The plots are compared with cases (c1, c2) of Figure 4.13 and it is found that but the nature of plots are identical but magnitudes of loads are more.

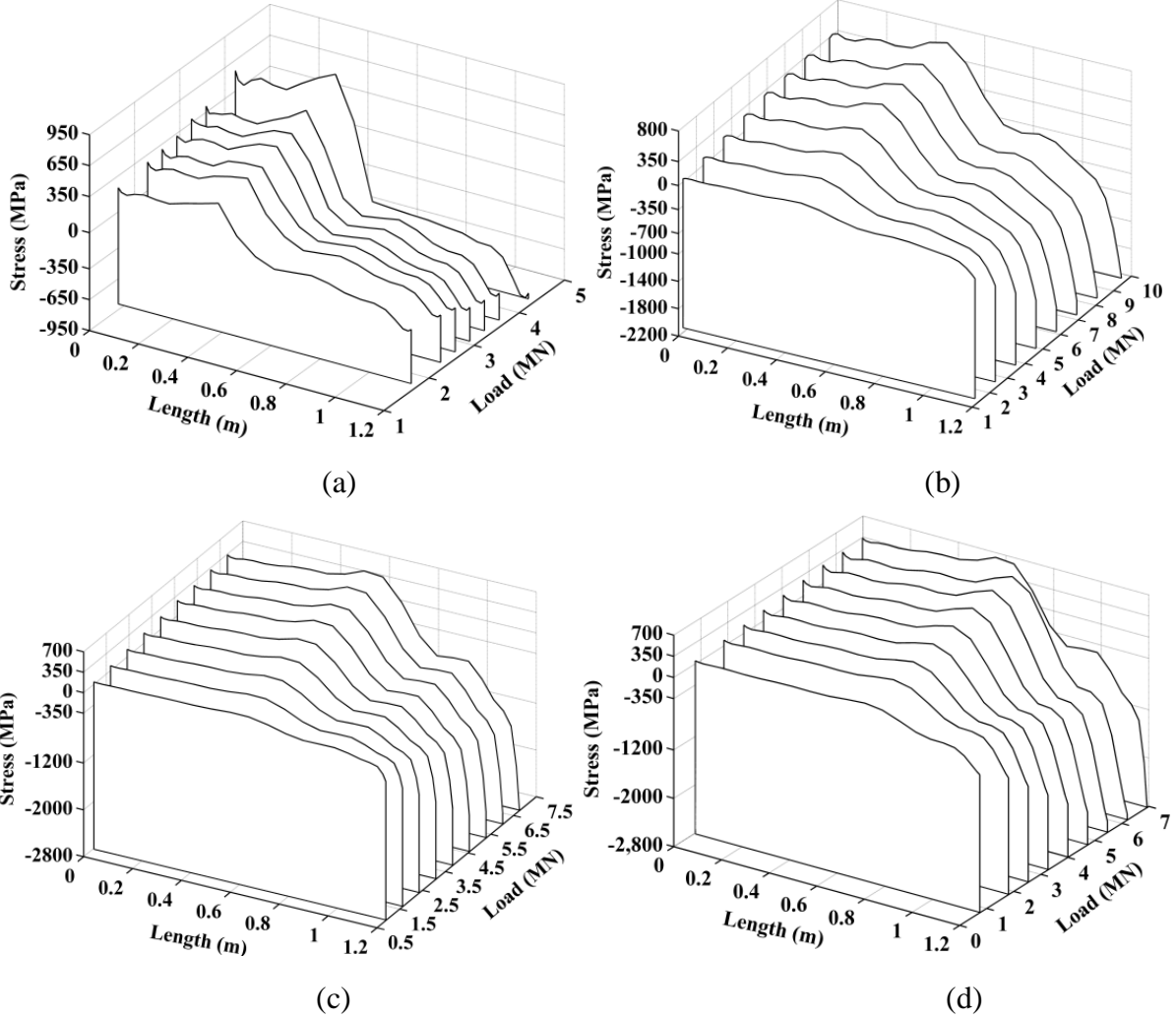


**Figure 4.17.** Waterfall plot of stress variation with load for a non-uniform taper bar with  $A_R = 0.025$  and  $S_R = 100$  for load application point (a)  $\xi_f = 0.4$  (b)  $\xi_f = 0.5$  (c)  $\xi_f = 0.6$  (d)  $\xi_f = 0.7$ .

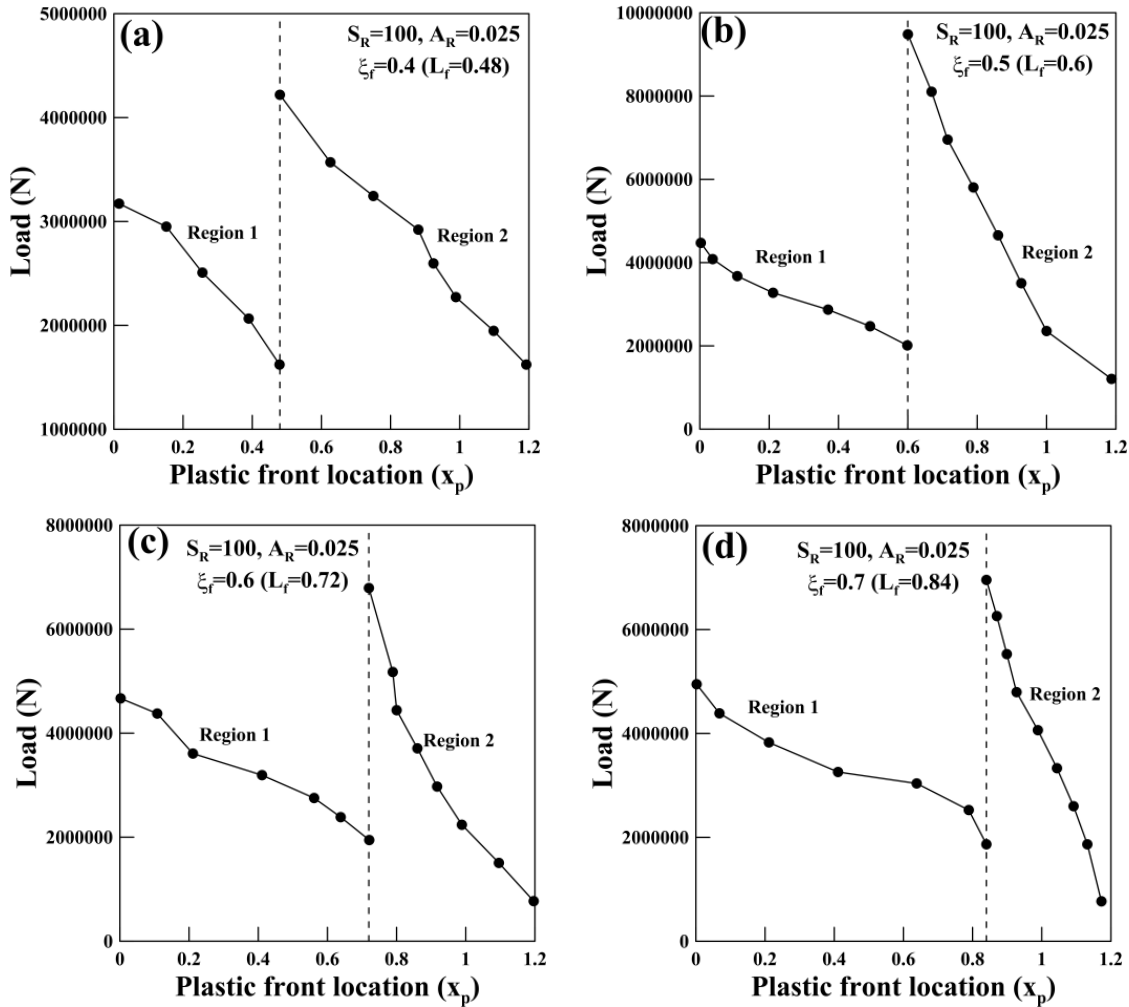


**Figure 4.18.** Plot of plastic front location variation with load for a taper bar with linear variation in area for load application point (a)  $\xi_f = 0.4$  (b)  $\xi_f = 0.5$  (c)  $\xi_f = 0.6$  (d)  $\xi_f = 0.7$ .

**Table 4.4:** Elastic and plastic limit loads for domain 1 and domain 2 of taper bar for two different geometries with trilinear material model

$\xi_f$	Case A				Case B			
	$F_{y1}$ (kN)	$F_{c1}$ (kN)	$F_{y2}$ (kN)	$F_{c2}$ (kN)	$F_{y1}$ (kN)	$F_{c1}$ (kN)	$F_{y2}$ (kN)	$F_{c2}$ (kN)
0.3	39221.47	76481.87	62754.35	117664.41	7178.85	14057.70	11342.59	21870.30
0.4	35786.23	71572.46	39364.85	100201.44	6481.43	12162.85	6999.94	16203.57
0.5	34280.93	82617.05	26992.86	82328.23	6596.65	14550.15	4780.18	13826.24
0.6	33573.83	67987.01	16786.92	66476.19	6263.33	12379.42	2940.53	11785.37
0.7	33206.38	60523.96	16357.83	58888.17	6033.90	11039.48	2832.82	9756.20



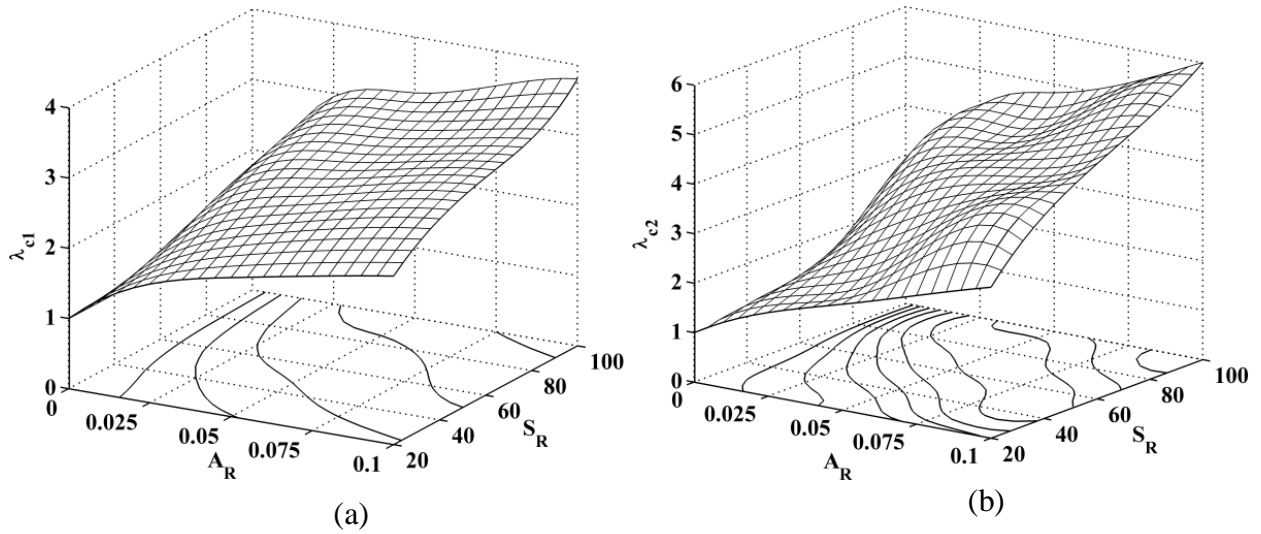


**Figure 4.19.** 3D and contour plots of non-dimensional collapse load  $\lambda_{c1}$  and  $\lambda_{c2}$  showing its variation with  $A_R$  and  $S_R$  for load application point (a, b) for trilinear model.

## 4.5 Summary

In this chapter, the investigation of yield front propagation of statically indeterminate taper bar is formulated through the extension and application of minimum potential energy principle in Hencky's deformation theory based on von-Mises yield criterion and for linear strain hardening behaviour. Both determinate and indeterminate problems have been considered. For determinate problems domain decomposition method has been established and to overcome its insufficiency for indeterminate problems, an iterative variational method has been proposed successfully. The results obtained by the present methodology have been validated with that of analytical results of a clamped-free taper bar under uniaxial tensile load and excellent agreement is obtained. The results obtained through the revised formulation using domain decomposition method are validated successfully by finite element analysis software Abaqus CAE for a clamped-clamped taper bar. Some new results are presented which show that the variations in aspect ratio and slenderness ratio have significant effect on the yield front propagation of clamped-clamped bar. The results are presented graphically to become design friendly. Waterfall plots showing the variation in stress field with increase in load have also been presented.



# GROWTH OF YIELD FRONT IN THERMO-MECHANICALLY LOADED ISOTROPIC AND FG BARS

## 5.1 Introduction

The thermo-elasto-plastic analyses of non-uniform bars are important for efficient designing of mechanical, aerospace and civil structures. The phenomenon of elastic-plastic regime in the bar material is exhibited when thermal load exceeds the critical load to produce initial yielding condition in the bar. Due to the absence of comprehensive analytical solution of the problem, several efforts have been made to obtain effective methods of solution in the elasto-plastic region due to induced thermal stress.

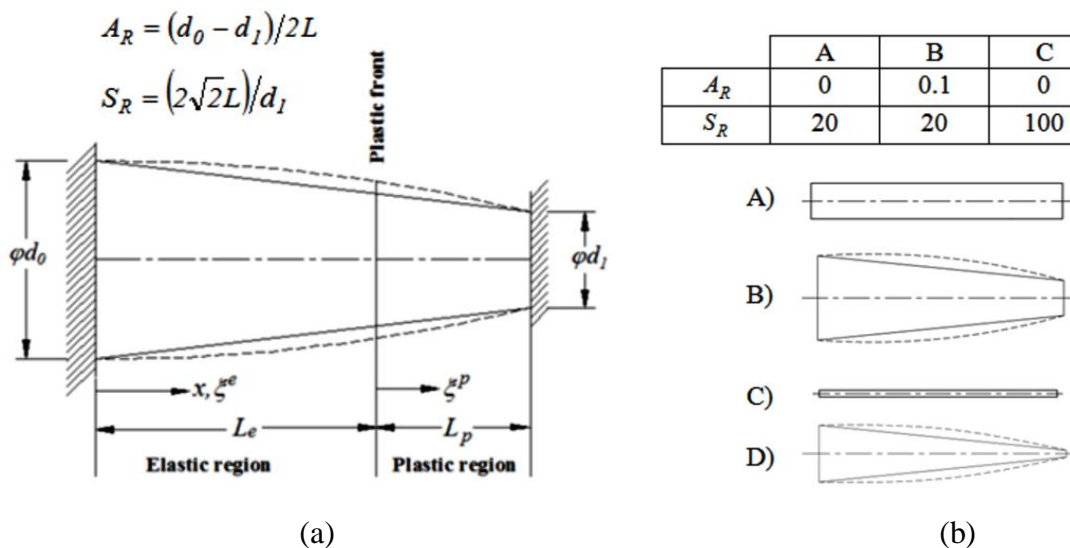


**Figure 5.1.** (a) Schematic diagram of geometry of taper bar and (b) four typical geometries for  $L=1.2$  m.

A taper bar of solid circular cross-section with linear and parabolic variation in diameter is considered in the present analysis as represented by the solid and dotted lines in Figure 5.1. For linear taper geometry, the diameter at location  $x$  is given by,  $d = d_0 - \xi(d_0 - d_1)$ , where  $d_0$  is the largest diameter at  $x = 0$ ,  $d_1$  is the smallest diameter at the other clamped end and  $\xi$  is the normalized axial coordinate. Total length of the bar  $L$  is used to frame the normalizing

parameter  $\xi(=x/L)$ . For parabolic geometry, the variation in diameter is given by  $d = d_1 + ((d_0 - d_1)\sqrt{1-\xi})$ . The geometry of the bar is also characterized by the aspect ratio ( $A_R$ ) and slenderness ratio ( $S_R$ ), as detailed in Figure 5.1(a). Four typical geometries for different  $A_R$  and  $S_R$  values are shown in the Figure 5.1(b) for a bar of length 1.2 m. Moreover, various other types of geometries are furnished in Table 4.1 of the preceding chapter 4 of the thesis.

The basic method of analysis for both these problems remains the same and is similar to the one presented in the preceding chapter for the analysis of statically indeterminate non-uniform bar problem in post elastic domain by an iterative variational method. The present chapter endeavors to address the thermo-elasto-plastic behaviour of isotropic and functionally graded non-uniform bars by using a numerical technique based on variational principle. The solution algorithm of the governing equation has been proposed for predicting the unknown displacement field in an iterative manner based on von-Mises yield criterion and Hencky's deformation theory of plasticity by assuming an isotropic material model.

## 5.2 Thermo-elasto-plastic analysis of isotropic non-uniform bars

This section deals with the analysis of elasto-plastic behaviour of isotropic non-uniform bars subjected to thermal load. A quick review of the available literatures significantly related to this problem is provided here. Theoretical investigation of elastic-plastic behaviour of solid slender bars of various types of geometry as well as loading is a relevant area of work for the designers (Kachanov (1971); Hill (1950); Chakrabarty (1987); Johnson and Mellor (1962)). Grysa and Kozlowski (1982) presented one-dimensional transient thermoelastic problems of heat flux and determined the unknown functions describing heat flux and temperature on the surface of an isotropic infinite slab. Horgan and Chan (1999) investigated the effects of material inhomogeneity on the torsion response of linearly elastic isotropic bars. In this analysis, optimal upper and lower bounds for the torsional rigidity for non-homogeneous bars of arbitrary cross-section were established.

Aleksandrov and Lyamaina (2012) obtained a semi-analytical solution of the formulated boundary value problem of a thin hollow disk subjected to thermo-mechanical loading with a uniform pressure distribution on the inner contour and a gradually increasing thermal load. Alexandrov and Alexandrova (2001) gave a closed-form solution, predicting thermal effect on

the development of plastic zones in thin plates. They assumed uniform temperature field which varies monotonically with time. Haslinger et al. (2016) introduced an incremental procedure for numerical evaluation and estimation of limit load in deformation plasticity based on variational formulation.

From the literature review, it is revealed that stress and deformation problem of uniform geometry bar subjected to thermal loading is mainly addressed in elastic domain only and literatures clarifying elasto-plastic behaviour of clamped non-uniform bars under thermo-mechanical loading are rare. The purpose of the present study is to investigate the growth of yield front in post-elastic domain of a thermo-mechanically loaded non-uniform bar with clamped ends. The problem is solved through an extension of the variational method in post-elastic regime. It is assumed that yield stress is the only physical parameter dependent on temperature variation of the bar and all other material properties remain constant corresponding to the value at ambient temperature. The bar is axisymmetric and during thermal loading its plane cross-sections remain plane maintaining axisymmetry. This analysis of the energy based variational formulation is carried out by Galerkin's principle, using a linear combination of sets of orthogonal co-ordinate functions which satisfy prescribed boundary conditions. The approximate solution additionally needs an iterative technique to find the growth in yield front for the type of prescribed temperature field manner based on von-Mises yield criterion and deformation theory of plasticity by assuming an isotropic material model. The solution algorithm is actualized with the assistance of MATLAB<sup>®</sup> computational simulation software. Uniform, linear and parabolic types of temperature distribution over the length of the bar are assumed and some numerical results in dimensional form are presented and discussed for a clamped-clamped mild steel bar. The temperatures corresponding to onset of yielding and total collapse are considered as markers of yield limit and collapse loads. The temperatures and limit load factors for different bar geometries and temperature distributions are provided. Results obtained from the proposed mathematical model are compared with those of finite element analyses using the commercial software, Abaqus. The results reveal that the thermo-elasto-plastic deformation of clamped bar is significantly influenced by the effect of geometry parameters and by the nature of thermal load.

### 5.2.1 Mathematical formulation

The present section performs analysis for clamped-clamped taper bars subjected to thermal load. Both bilinear and multilinear models of material behaviors are considered for the present analysis. An energy based variational approach is used by employing von-Mises criterion and total deformation theory of plasticity to get the governing equations. In the presence of temperature field the analysis of plastic behaviour becomes more complicated, because the yield limit and stress-strain relation depends on temperature. It is assumed that the temperature rise is not permanent so that effect of creep can be neglected. In the presence of a variable temperature field the relative volumetric change will produce strain, which is given by the well-known expression  $\varepsilon = 3k\sigma + 3\alpha T$  where  $k(=(1-2\nu)/E)$  is the coefficient of volumetric compression,  $\alpha$  is the coefficient of linear thermal expansion and  $T$  is the temperature rise. It is assumed that the stress and strain deviatorics are coaxial and their principal values are proportional i.e.,  $e_{ij} = \psi s_{ij}$ , where  $\psi$  is a scalar. It is also obvious that the components of strain deviatoric  $e_{ij}$  does not involve thermal expansions and so, using total deformation theory of plasticity, the total strain can be expressed as

$$\varepsilon_{ij} = \frac{\varepsilon}{3} \delta_{ij} + e_{ij} = k\sigma\delta_{ij} + \alpha T\delta_{ij} + \psi s_{ij}. \quad (5.1)$$

The solution for the thermo-elasto-plastic displacement field of a body under equilibrium is obtained from the application of minimum potential energy principle ( $\delta(U+V)=0$ ) in Hencky's total deformation theory.  $U$  is the strain energy stored in the bar in form of increment in work of deformation and  $V$  is the potential energy developed by the thermal loading. The expression of total potential energy under elastic conditions can be reduced to an identical expression given by Eq. (4.13) in section 4.2.4.1 of the thesis with the effect of thermal loading contributed to the work potential and is given by,

$$\Pi = \int_0^L \left[ \left( \frac{K(1-2\nu)^2}{2} + \frac{2G(1+\nu)^2}{3} \right) (u')^2 - 3K(1-2\nu)\alpha Tu' \right] A(x) dx, \quad (5.2)$$

where  $( )'$  indicate first derivative with respect to the coordinate variable.  $\Pi$  is the total potential energy in which one part is similar to the strain energy  $U$  stored in the bar and the

other part is work function due to temperature gradient loading. So, the expression for strain energy  $U$  is given by,

$$U = \int_0^L \left\{ \left( \frac{K(1-2\nu)^2}{2} + \frac{2G(1+\nu)^2}{3} \right) (u')^2 \right\} A(x) dx, \quad (5.3)$$

where  $u'$  is the axial strain  $\varepsilon_x$ . The expression for potential energy  $V$ , arising from the thermal loading is given by,

$$V = -\int_0^L \{ 3K(1-2\nu)\alpha T u' \} A(x) dx. \quad (5.4)$$

As the bar remains axisymmetric, the shear deformation consideration is not included in the present analysis.

The initiation of yielding occurs at the smaller fixed end ( $x = L$ ) of the taper bar at a particular value of temperature  $T_y$  termed as elastic limit thermal load. With increase in temperature the plastic front gradually proceeds towards the larger fixed end ( $x = 0$ ) and ultimately coalesces there at a temperature  $T_c$  termed as plastic collapse thermal load. The domain of the bar beyond elastic limit load gets divided into two regions, an elastic region ( $0$  to  $L_e$ ) of higher diameter and a relatively smaller diameter plastic region ( $L_e$  to  $L$ ). Hence in the post elastic state the total strain energy  $U$  consists of an elastic ( $U_e$ ) and a plastic ( $U_p$ ) part.

Expression of strain energy in the elastic part is given by,

$$U_e = \int_0^{L_e} \left( \frac{K(1-2\nu)^2}{2} + \frac{2G(1+\nu)^2}{3} \right) A(x) (u')^2 dx \quad (5.5)$$

and the strain energy for the post-elastic region is obtained from the expression

$$U_p = \int_{L_e}^L \left( \frac{K(1-2\nu)^2}{2} + \frac{2g(\Gamma)(1+\nu_p)^2}{3} \right) A(x) (u')^2 dx, \quad (5.6)$$

where  $g(\Gamma)$  is the modulus of plasticity and  $\nu_p$  is the Poisson's ratio in post-elastic region.

Substituting Eqs. (5.3) to (5.6) in the energy principle  $\delta(U + V) = 0$ , the governing equilibrium equation becomes

$$\delta \left[ \begin{array}{l} \int_0^{L_e} \left( \frac{K(I-2\nu)^2}{2} + \frac{2G(I+\nu)^2}{3} \right) A(x)(u')^2 dx \\ + \int_{L_e}^L \left( \frac{K(I-2\nu)^2}{2} + \frac{2g(\Gamma)(I+\nu_p)^2}{3} \right) A(x)(u')^2 dx \\ - \int_0^L \{ 3K(I-2\nu)\alpha T u' \} A(x) dx \end{array} \right] = 0. \quad (5.7)$$

The normalized length parameters are denoted by  $\xi^e$  and  $\xi^p$  in elastic and post-elastic regions, respectively and they are framed by  $\xi^e = x/L_e$  and  $\xi^p = (x - L_e)/L_p$ , where  $L_e$  and  $L_p$  are the lengths of the elastic and post-elastic regions respectively. The displacement function  $u(\xi)$  in Eq. (5.7) is approximated by a linear combination of sets of orthogonal coordinate functions as  $u(\xi) = \sum c_i \phi_i$ ,  $i = 1, 2, \dots, n_f$ , where  $\phi_i$  is the set of  $n_f$  number of orthogonal functions developed through Gram–Schmidt scheme and  $c_i$  is the set of unknown coefficients. The necessary start function  $\phi_0$  is given by  $\phi_0 = \xi(1 - \xi)$  which satisfies the geometric boundary conditions of the bar, i.e.,  $u = 0$  at  $\xi = 0$  and  $u = 0$  at  $\xi = 1$ . Displacement functions in the elastic and post-elastic regions are expressed as  $u(\xi^e) \cong \sum c_i \phi_i^e$  and  $u(\xi^p) \cong \sum c_i \phi_i^p$  respectively. Substituting these assumed displacement functions and replacing operator  $\delta$  by  $\partial/\partial c_j$ ,  $j = 1, 2, \dots, n$ , according to Galerkin error minimization principle, we obtain the governing differential equation in matrix form

$$\begin{aligned} & \sum_{i=1}^n \sum_{j=1}^n c_i \left[ \left( \frac{K(I-2\nu)^2}{2} + \frac{2G(I+\nu)^2}{3} \right) \left( \frac{2}{L_e} \right) \int_0^1 (A(\xi^e) \phi_i^{e'} \phi_j^{e'}) d\xi^e \right. \\ & \left. + \left( \frac{K(I-2\nu)^2}{2} + \frac{2g(\Gamma)(I+\nu_p)^2}{3} \right) \left( \frac{2}{L_p} \right) \int_0^1 (A(\xi^p) \phi_i^{p'} \phi_j^{p'}) d\xi^p \right] \\ & = 3K(I-2\nu)\alpha T \sum_{j=1}^n \int_0^1 (A(\xi) \phi_j) d\xi. \end{aligned} \quad (5.8)$$

Solution of Eq. (5.8) yields the solution vector  $\{c_i\}$ , obtained through a single step matrix inversion process. The axial displacement field ( $u$ ) can be found out for any prescribed value of temperature  $T$  which in turn gives strain and stress fields. However, the numerical scheme



requires some more iterative numerical computations to ascertain the location of yield front, i.e., the elastic-plastic boundary. The modulus of plasticity  $g(\Gamma)$  is set equal to modulus of rigidity  $G$ , at the zeroth approximation, and the problem is solved as an extension of elastic solution. In subsequent approximations the value of  $g(\Gamma)$  is updated until a final convergence is achieved, following the iterative scheme of Kachanov (1971). A flowchart of the iterative solution algorithm is similar to that of Figure 4.9 of the preceding chapter 4 of the thesis.

## **5.2.2 Results and discussion**

This chapter mainly presents result for thermo-elasto-plastic behavior of non-uniform bars taking uniform as well as non-uniform thermal load for various bar geometries. The present analysis is carried out for linear elastic and linear strain hardening elasto-plastic material behavior, as shown in Figure 5.2 for a mild steel (MS) bar. Another multilinear material model with four segments has also been incorporated afterwards in the present study. From the idealized stress-strain diagram of Figure 5.2(a), elastic modulus ( $E$ ) and tangent modulus ( $E_t$ ) of the bar material are obtained. In Figure 5.2(b), the relations of deviatoric stress ( $S$ ) and shear strain ( $\Gamma$ ) are shown, which yields shear modulus ( $g(\Gamma)=G'$ ) of the bar material. As the prevailing state of stress is different at each location of the bar in post elastic region, value of ( $G$ ) is also different. From the idealized post-elastic behaviour of linear strain hardening material, the values of elasticity modulus and tangent modulus are obtained as  $E = 210$  GPa,  $E_t = 12.23$  GPa and initial yield stress of the bar material  $\sigma_o = 260$  MPa. The value of Poisson's ratio  $\nu$  is taken as 0.3 in elastic state and  $\nu_p$  in post-elastic region is taken as 0.5. The length of the bar  $L$  is taken as 1.2 m and coefficient of thermal expansion,  $\alpha = 11.5e-6 / ^\circ\text{C}$ .

For the various geometries of the bar, the range for aspect ratio is 0 to 0.1 and slenderness ratio varies from 20 to 100. The smaller diameter  $d_1$  is calculated from the slenderness ratio as  $d_1 = (2\sqrt{2}L)/S_R$  and the larger diameter  $d_o$  is calculated from the aspect ratio relation as  $d_o = d_1 + (2LA_R)$ .

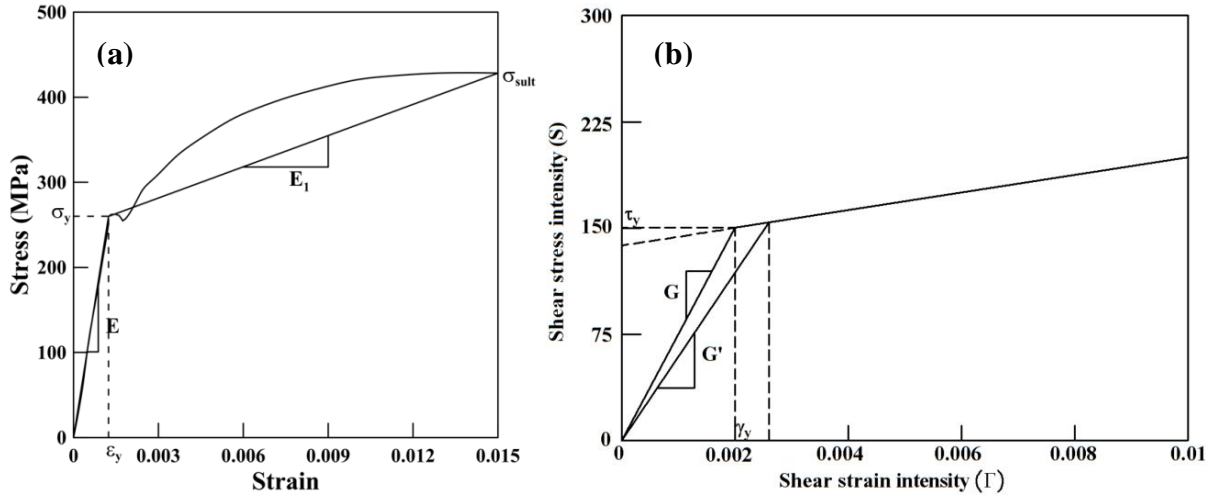


**Figure 5.2.** (a) Stress-strain plot for mild steel (MS) at 20 °C showing linear elastic and linear strain hardening elasto-plastic behavior and (b) deviatoric stress-shear strain diagram, for linear strain hardening material.

The analysis is also carried out for three different types of temperature distributions: uniform  $T(\xi)=T_l$ , linearly decreasing  $T(\xi)=T_l - (\{T_l - T_o\}\xi)$  and parabolically decreasing  $T(\xi)=T_l - (\{T_l - T_o\}\xi^2)$  where  $T_o$  = ambient temperature and  $T_l$  = maximum temperature. A sample of the nature of temperature variations are shown in Figure 5.3 taking  $T_o = 20^\circ\text{C}$  and  $T_l = 100^\circ\text{C}$ . When  $T_o$  and  $T_l$  appears at  $x=0$  and  $x=L$ , we get increasing temperature distribution and the relations for linearly increasing and parabolically increasing ones are given by  $T(\xi)=T_o + (\{T_l - T_o\}\xi)$  and  $T(\xi)=T_o + (\{T_l - T_o\}\xi^2)$ . The elastic limit loads  $T_y$  for linearly increasing and decreasing temperature distributions are same as the induced elastic strains remain same for both the cases. However, there is a change in plastic collapse temperature  $T_c$  for these two cases as shown in Figure 5.4(a) for linearly varying temperature distributions. The same phenomenon is also observed for parabolically increasing and decreasing temperature distributions and the elasto-plastic strains are presented in Figure 5.4(b).

The effect of aspect ratio and slenderness ratio on elastic limit thermal load ( $T_y$ ) and plastic collapse thermal load ( $T_c$ ) of clamped bar is studied in subsequent sections. Results for the two different geometries namely taper and parabolic under three different types of temperature distributions are presented in elasto-plastic regime of material behaviour. Results are

presented for both the material models: bilinear and multilinear with four segments. However, for bilinear material model, both linear taper and parabolic geometries are considered but for multilinear material model, results are provided for only linear taper geometry. Results are also presented for clamped-clamped linear taper bars for bilinear material model considering yield stress variation with temperature.

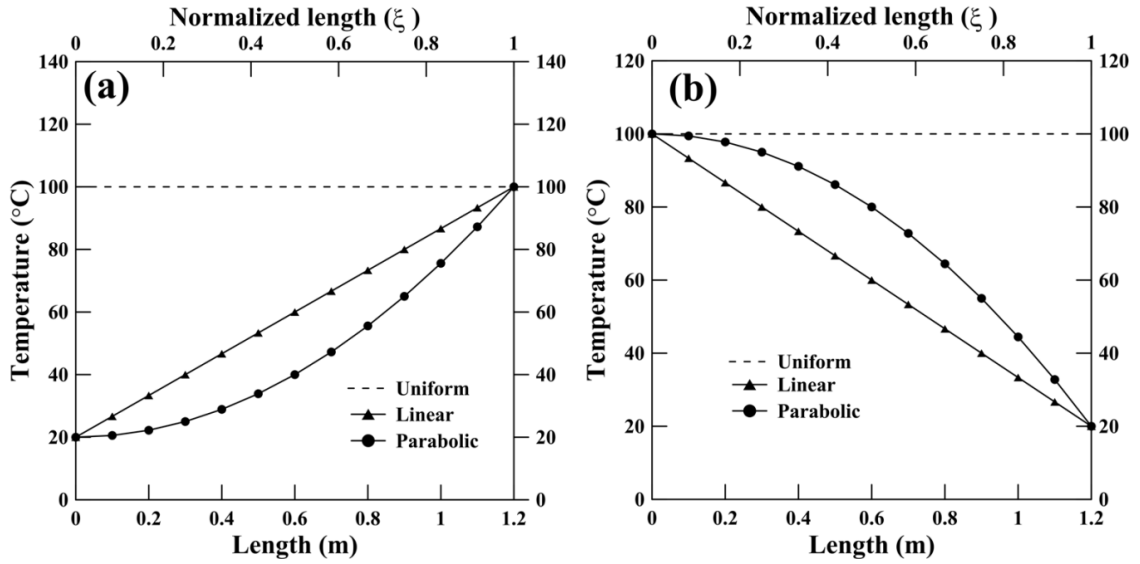


Figure 5.3. Variations in temperature (a) increasing and (b) decreasing.

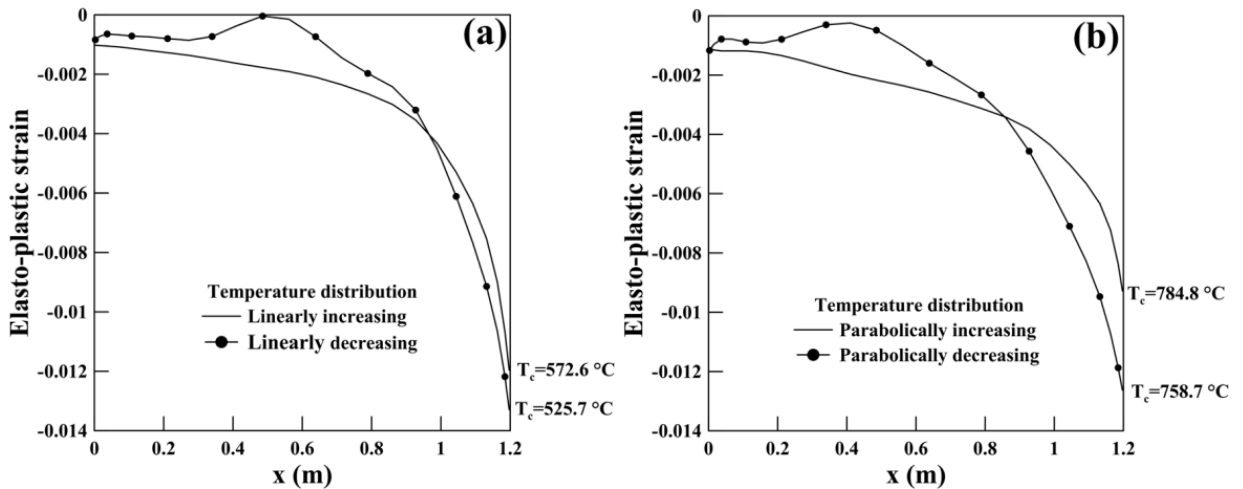


Figure 5.4. Plot of elasto-plastic strain for clamped taper bar ( $A_R = 0.025$  and  $S_R = 100$ ) corresponding to plastic collapse temperature  $T_c$ : (a) linear and (b) parabolic temperature distribution.

5.2.2.1 Validation study

Figure 5.5 shows the validation of the present method with that of finite element analysis software Abaqus CAE (version 6.8) for a clamped linear taper bar with  $L = 1.2$  m,  $S_R = 20$  and  $A_R = 0.1$ . The bar, subjected to uniform temperature, is modeled by using 8 node thermally coupled linear brick element with 2400 elements in Abaqus. This comparison successfully validates the present method for both elastic and post-elastic regime of bar material. The percent error of the results of the present method and Abaqus CAE are also presented in Table 5.1.

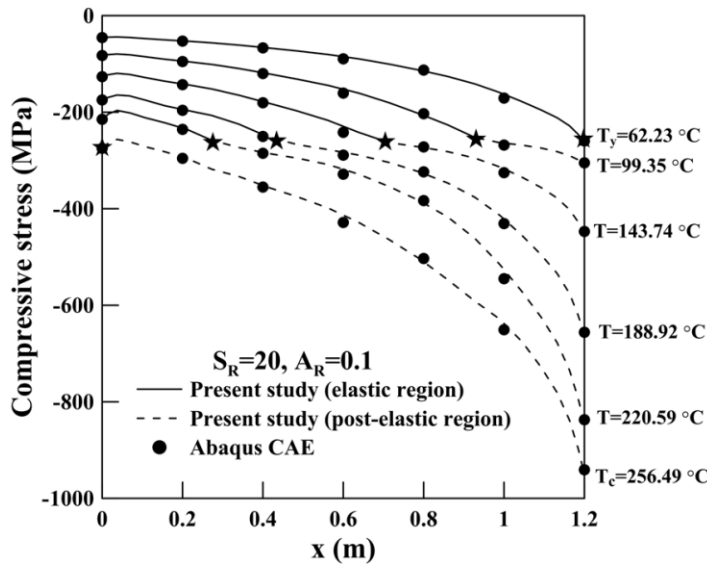
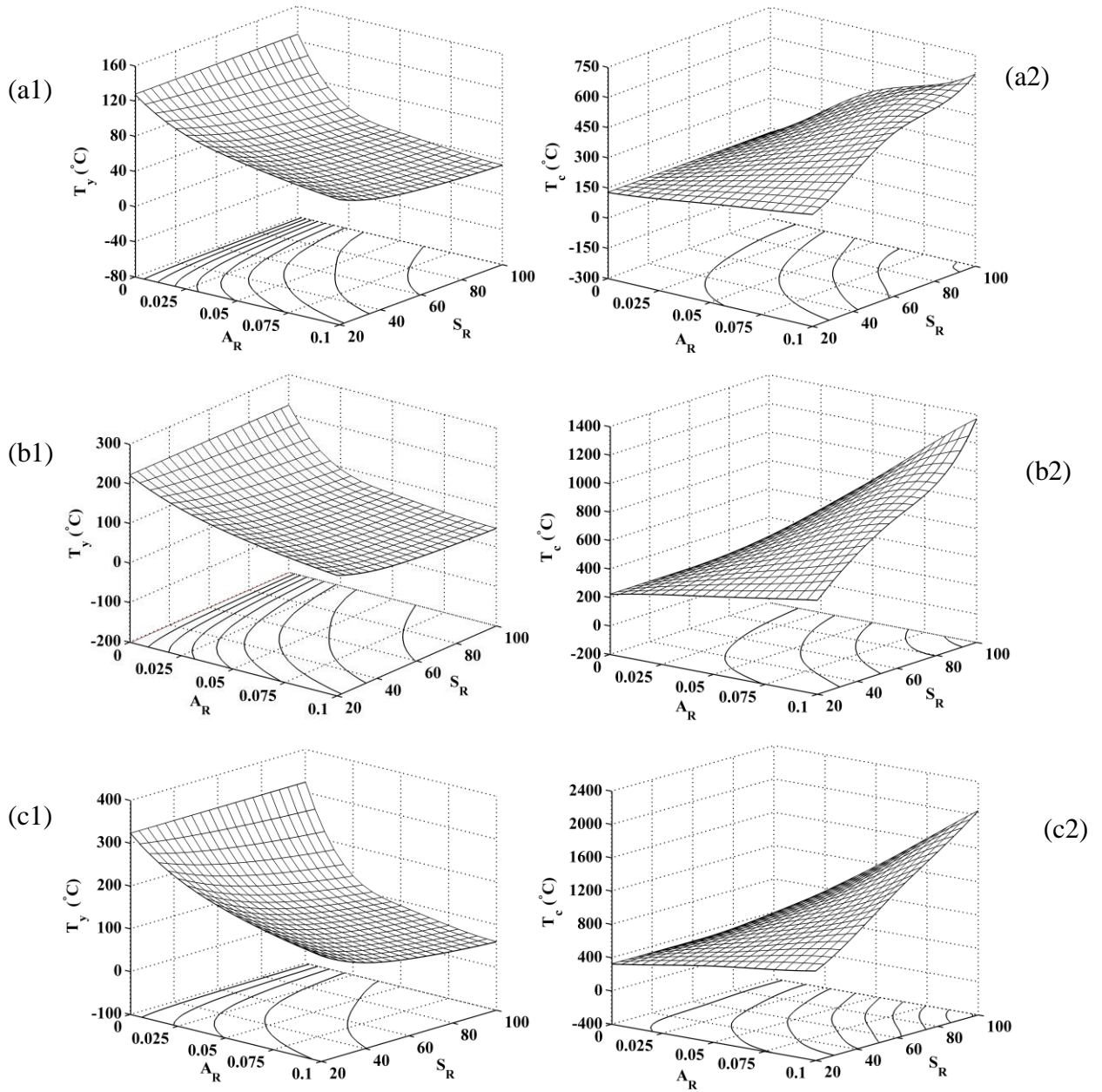


Figure 5.5. Validation plot of stress field for clamped taper bar.

Table 5.1: Validation of compressive stress for clamped linear taper bar

Axial length (m)	$T_y = 62.23^\circ\text{C}$			$T_c = 256.49^\circ\text{C}$		
	Compressive stress (MPa)			Compressive stress (MPa)		
	Present method	Abaqus	Error (%)	Present method	Abaqus	Error (%)
0.2	-51	-53	3.77	-292.67	-295.89	1.09
0.4	-65.14	-67.17	3.02	-351	-355	1.13
0.6	-85.33	-88.13	3.39	-411.50	-413.47	0.48
0.8	-115.50	-113.43	1.82	-510	-507.28	0.54
1.0	-163.83	-165.79	1.18	-641	-644.33	0.52
1.2	-260	-260.79	0.30	-940.83	-942.33	0.16



**Figure 5.6.** 3D and contour plots of elastic limit temperature ( $T_y$ ) and plastic collapse temperature ( $T_c$ ) with its variation with  $A_R$  and  $S_R$  for clamped taper bars under (a1,a2) uniform, (b1,b2) linearly decreasing and (c1,c2) parabolically decreasing temperatures.

### 5.2.2.2 Elasto-plastic behaviour of clamped-clamped linear taper bar

For clamped taper bars, 3D and contour plots of elastic limit temperatures and plastic collapse temperatures are shown in Figure 5.6 depicting simultaneous variation in aspect ratio

and slenderness ratio. The figures has been presented for three types of temperature distribution: uniform (a1,a2), linearly decreasing (b1,b2) and parabolically decreasing (c1,c2). It is observed that with increase in  $A_R$  as well as  $S_R$ , the elastic limit temperature ( $T_y$ ) decreases whereas the plastic collapse temperature ( $T_c$ ) increases for all the three cases of temperature distribution.

The observations are obvious, because at lower values of  $A_R$  and high values of  $S_R$ , bar geometry tends to be uniform and smaller in diameter. It should be noted that the higher temperature regions (say  $T \geq 1000$  °C) shown in the diagram are not physically realizable and the effect of variations in material properties with temperature are not considered. The elastic limit and plastic collapse temperatures are higher for parabolic temperature distributions and lower for uniform temperature distributions for all values of  $A_R$  as well as  $S_R$ . Temperatures  $T_y$  and  $T_c$  as presented in Figure 5.6 represent cases of different bar geometries having different material volume, as shown in Figure 5.7. Figure 5.7(a) represents the volume of a taper bar with variation in aspect ratio and slenderness ratio.

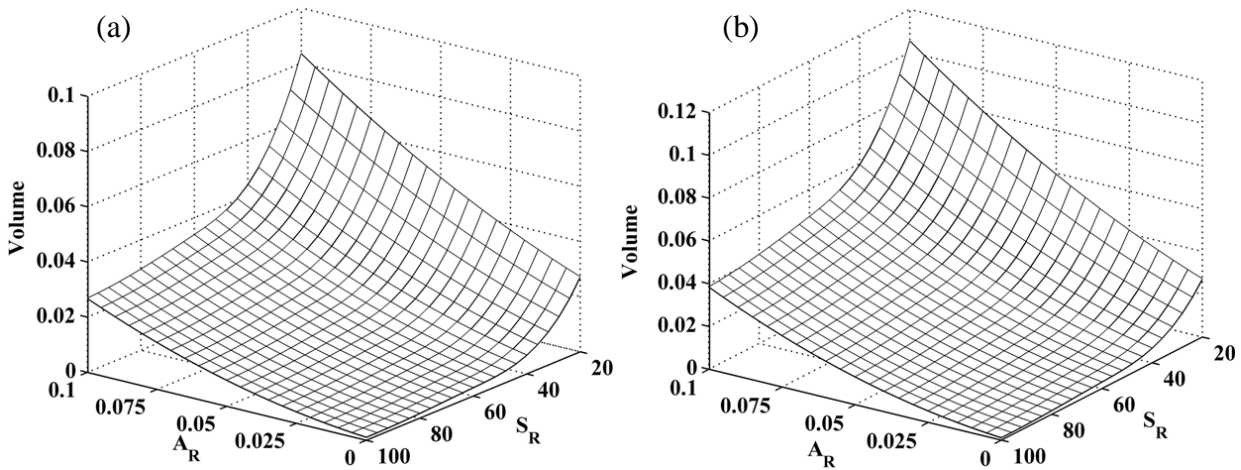


**Figure 5.7.** 3D plot of volume showing its variation with  $A_R$  and  $S_R$  for (a) taper and (b) parabolic bars.

For a more meaningful comparison, 3D and contour plots of  $T_y$  and  $T_c$  are expressed per unit volume of bar and presented in Figure 5.8 for different temperature distributions. From these figures, it is observed that, with increasing  $A_R$  and  $S_R$  values,  $T_y/V$  remains constant over a

wide region of  $S_R$ ,  $A_R$  values but  $T_c/V$  is continuously decreasing for all the temperature distributions.

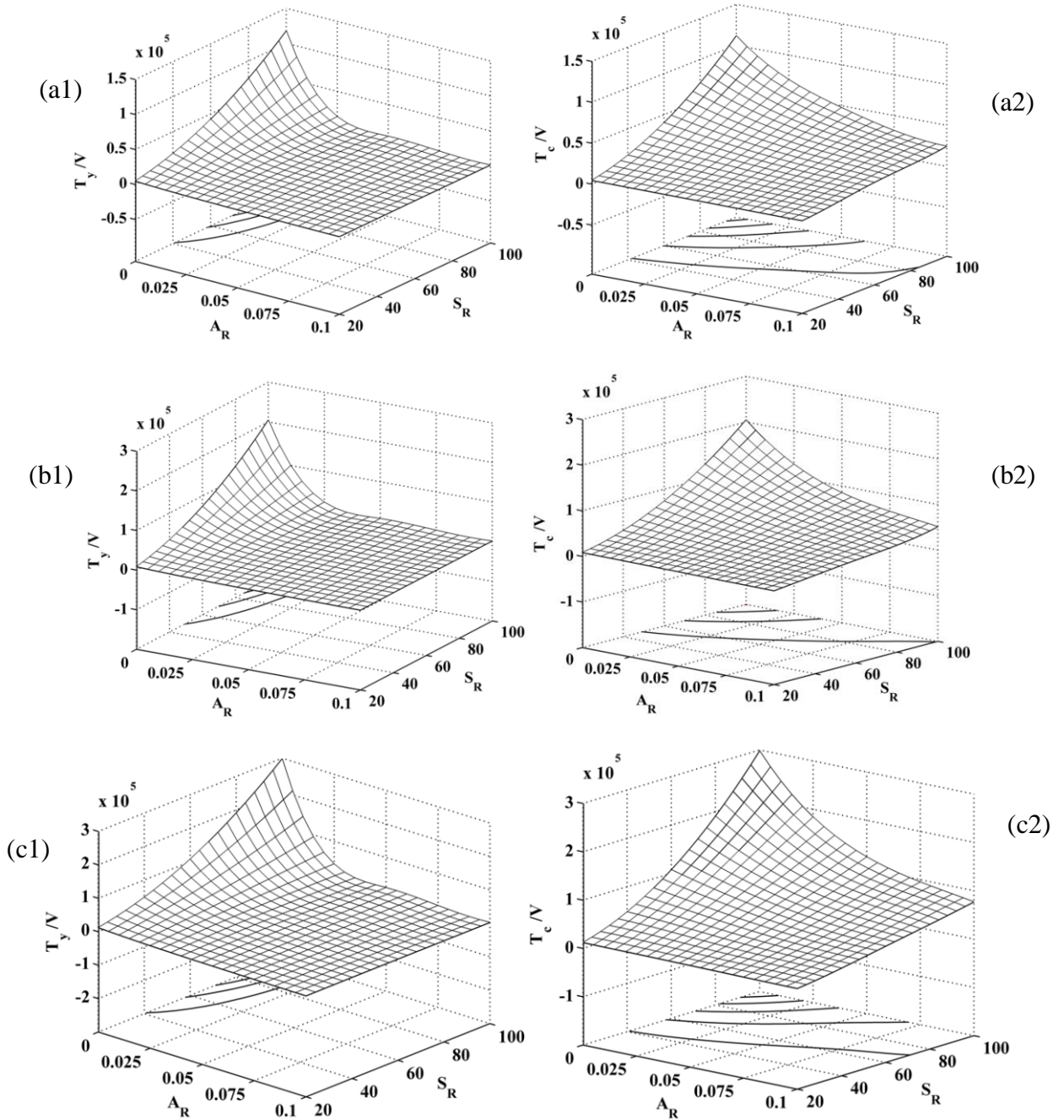


**Figure 5.8.** 3D and contour plots of elastic limit temperature and plastic collapse temperature per unit volume with its variation with  $A_R$  and  $S_R$  for taper bars under (a1,a2) uniform, (b1,b2) linearly decreasing and (c1,c2) parabolically decreasing temperatures.

The concept of limit load factor, defined by the ratio of collapse load to yield limit load, is also used in this work, but here it is defined by the ratio  $T_c/T_y$ . 3D plots of this factor is shown in Figure 5.9 for various combinations of  $A_R$  and  $S_R$  values. It is observed that  $T_c/T_y$  increases with increase in  $A_R$  and  $S_R$  for all the cases. It is also evident from the figures that with increase in  $A_R$  as well as with  $S_R$ ,  $T_c/T_y$  attain highest values at  $A_R = 0.1$  and  $S_R = 100$  for all the temperature distributions. The 2D representations of  $T_c/T_y$  with  $A_R$  for different  $S_R$  values are presented in Figure 5.10.

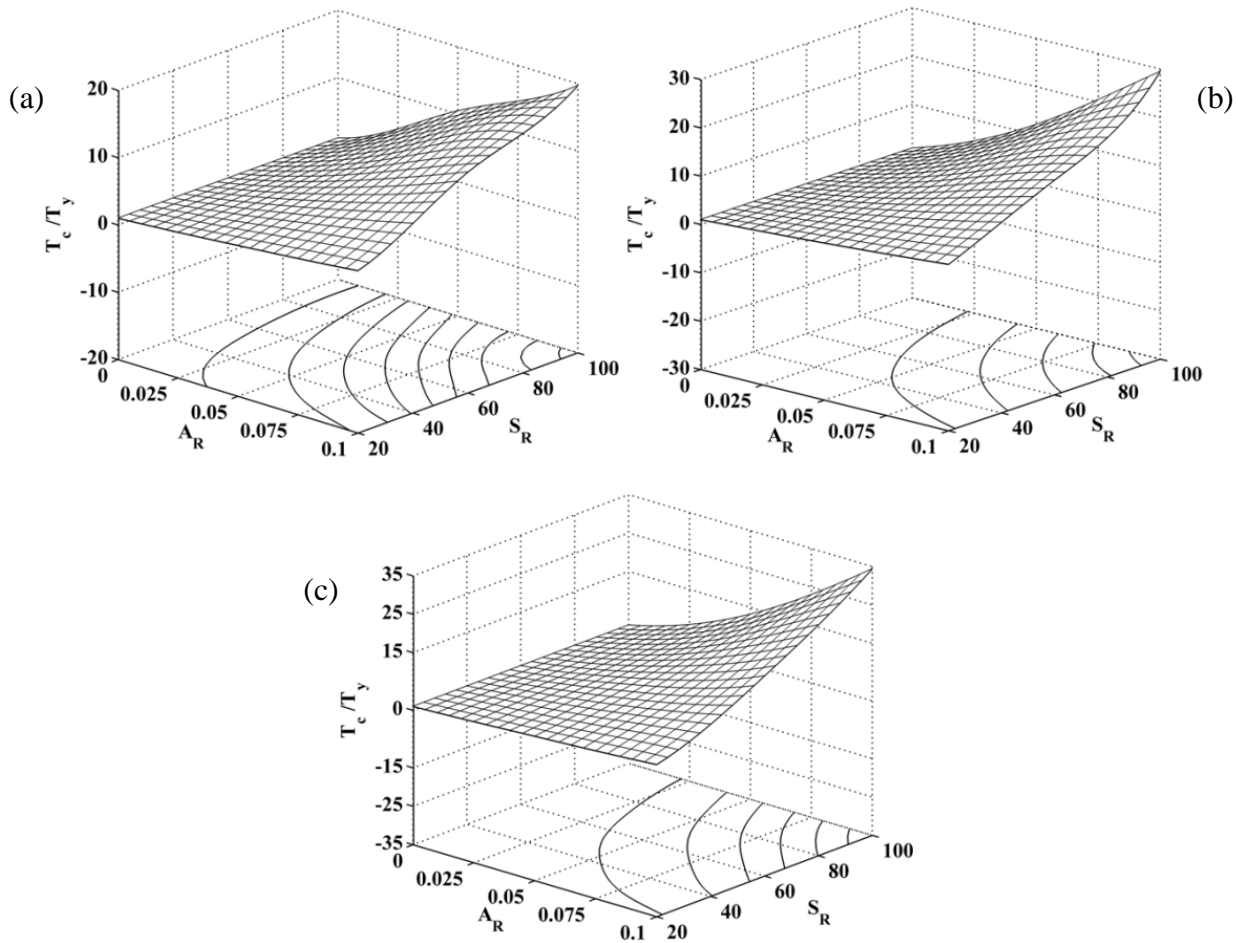


**Figure 5.9.** 3D and contour plots of limit load factor ( $T_c/T_y$ ) showing its variation with  $A_R$  and  $S_R$  for a taper bar of  $L=1.2$  m for (a) uniform, (b) linear and (c) parabolic temperature variations.



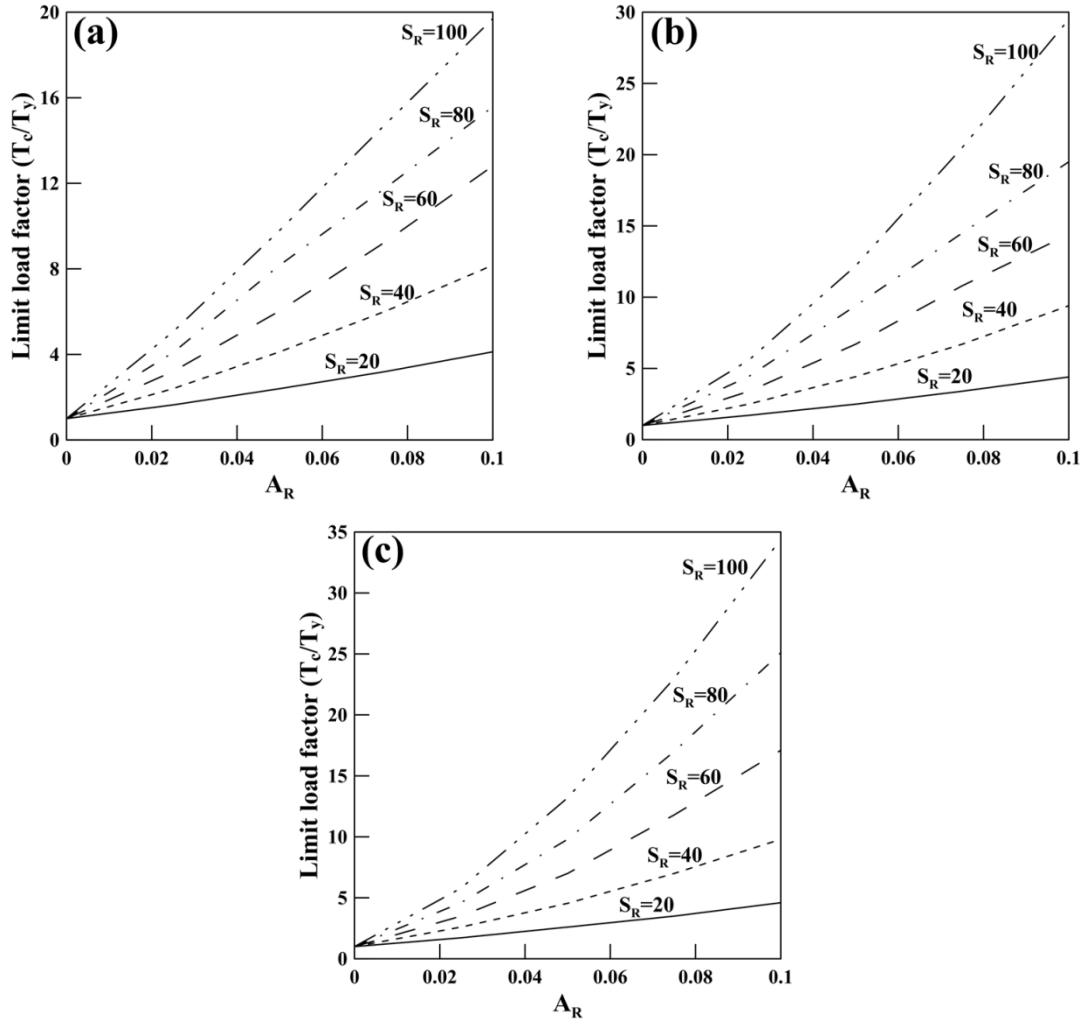


**Figure 5.10.** Plot of limit load factor  $(T_c/T_y)$  variation with  $A_R$  for different  $S_R$  for a taper bar of  $L=1.2$  m for (a) uniform, (b) linear and (c) parabolic temperature variations.

To analyze the growth of yield front in a taper bar under thermal loading, the stress fields are reported in Figures 5.11(a)-(c) at different temperatures through waterfall plots and their superimposed projected views. The plots are shown for three types of temperature distributions and in each of them temperature range from initial yield limit to ultimate collapse limit. The plots are shown for a particular bar geometry  $A_R = 0.1$ ,  $S_R = 20$ ,  $L = 1.2$  m as indicated in case (B) of Figure 5.1(b). It is observed that the compressive stress increases with increase in temperature for all the three cases of temperature distributions, yielding initiates at the smallest fixed end ( $x = L$ ) of the bar and with increase in temperature the yield front starts propagating towards the largest fixed end and the entire bar becomes elasto-plastic. The compressive stress is

more for uniform temperature as compared to decreasing linear and parabolic temperature distributions.

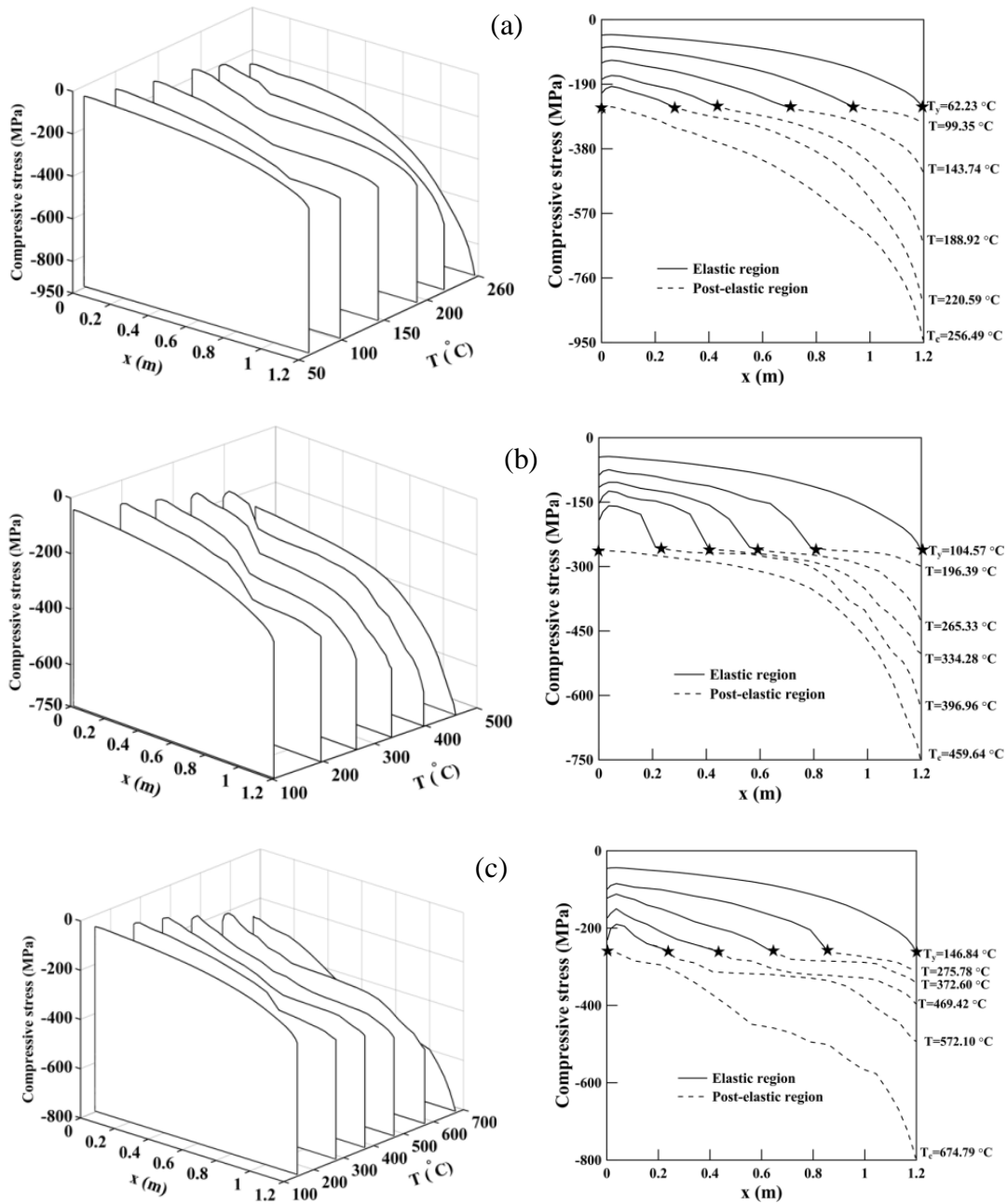


**Figure 5.11.** Waterfall plot and projections of stress fields at different temperatures for a taper bar of  $A_R = 0.1$  and  $S_R = 20$ , under (a) uniform, (b) linearly decreasing and (c) parabolically decreasing temperatures.

From the stress fields of waterfall plots in Figure 5.11, the plastic front locations are captured at different temperature levels and their location with temperature is provided in Figures 5.12(a)-(c), for the clamped-clamped linear taper bar. The figures indicate the advancement of plastic front locations with increasing temperatures for all the three types of temperature distributions.

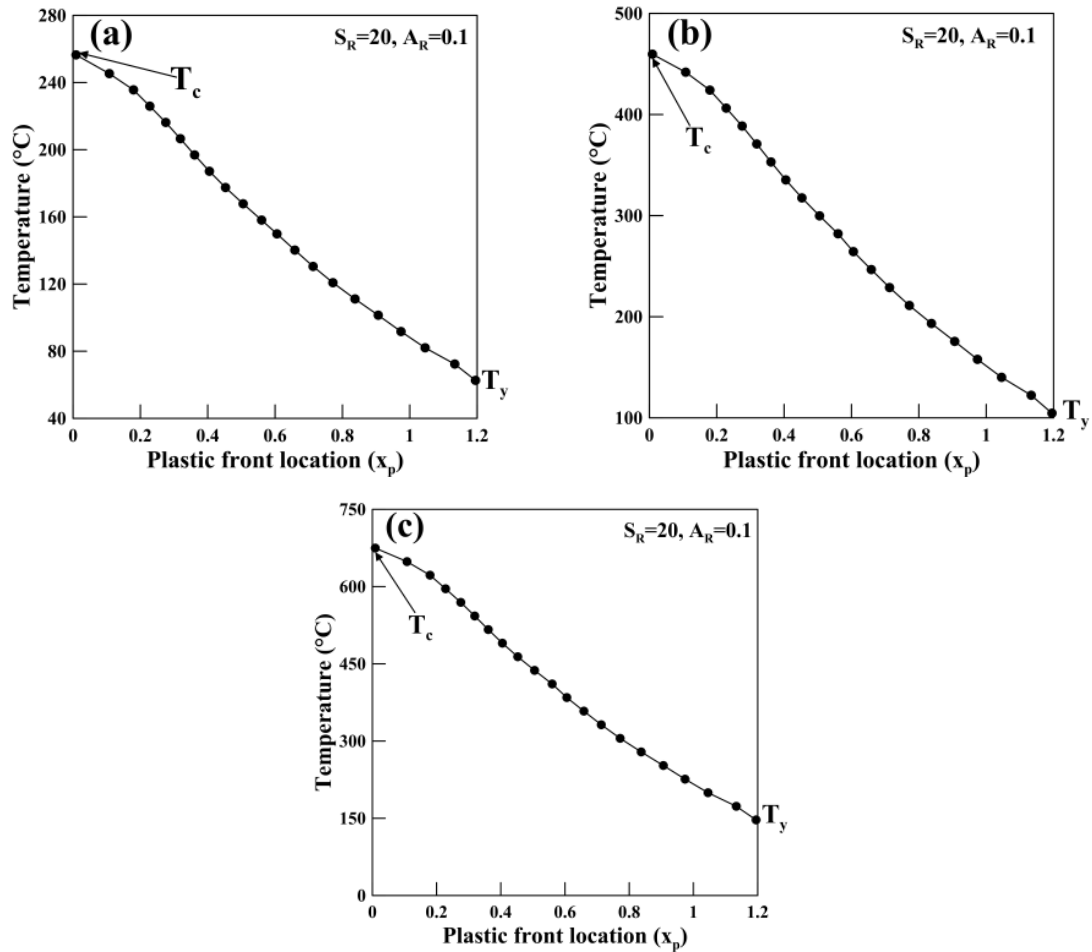


**Figure 5.12.** Plot of plastic front location variation with temperature for a taper bar of  $A_R = 0.1$  and  $S_R = 20$ , under (a) uniform, (b) linearly decreasing and (c) parabolically decreasing temperatures.

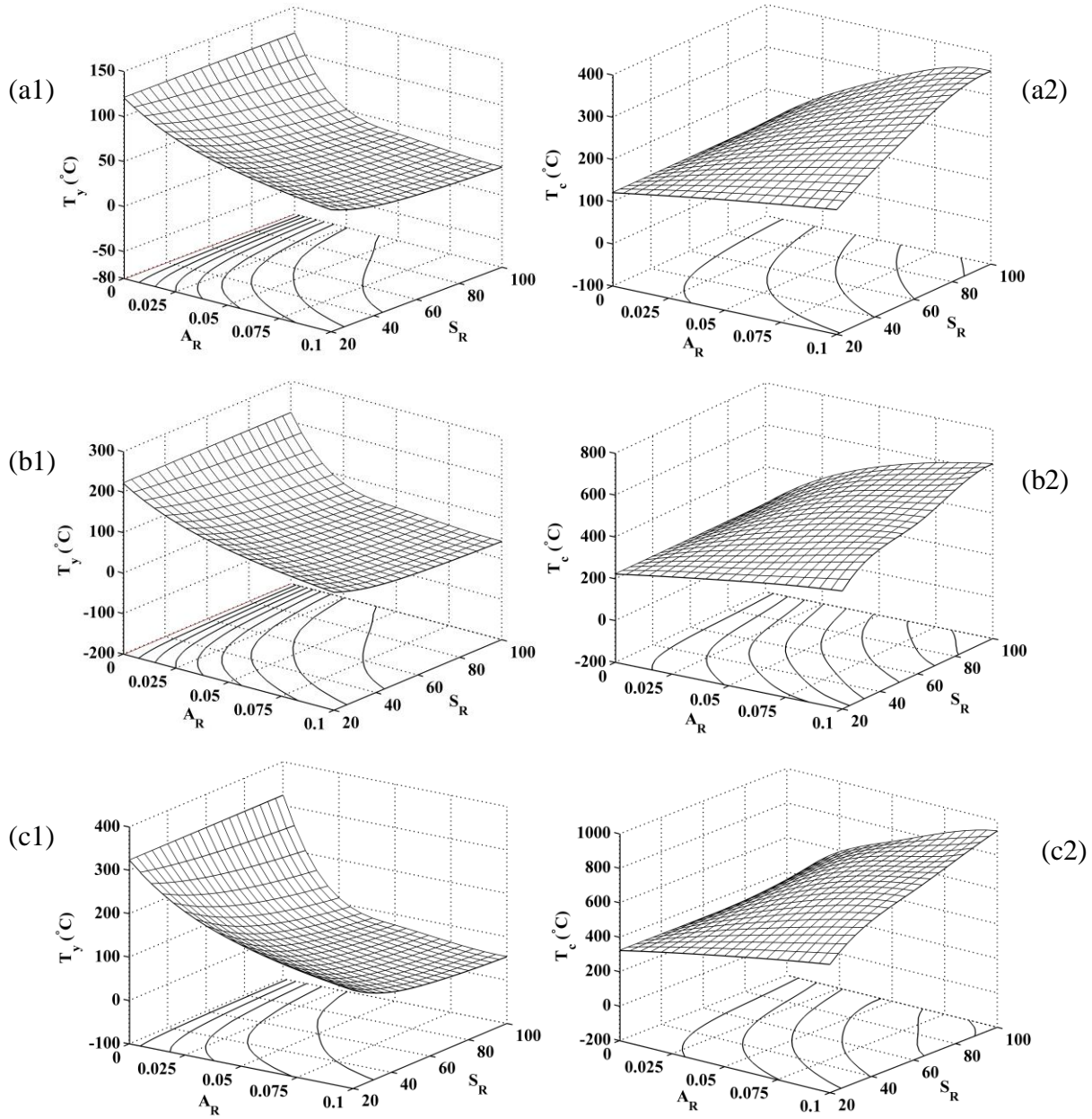


**Figure 5.13.** 3D and contour plots of elastic limit temperature ( $T_y$ ) and plastic collapse temperature ( $T_c$ ) with its variation with  $A_R$  and  $S_R$  for parabolic bars under (a1,a2) uniform, (b1,b2) linearly decreasing and (c1,c2) parabolically decreasing temperatures.

### 5.2.2.3 Elasto-plastic behaviour of clamped-clamped parabolic bar

For clamped parabolic bars, 3D and contour plots of elastic limit temperatures and plastic collapse temperatures are shown in Figure 5.13, depicting simultaneous variation in aspect ratio

and slenderness ratio. The figures has been presented for three types of temperature distribution: uniform (a1,a2), linearly decreasing (b1,b2) and parabolically decreasing (c1,c2).

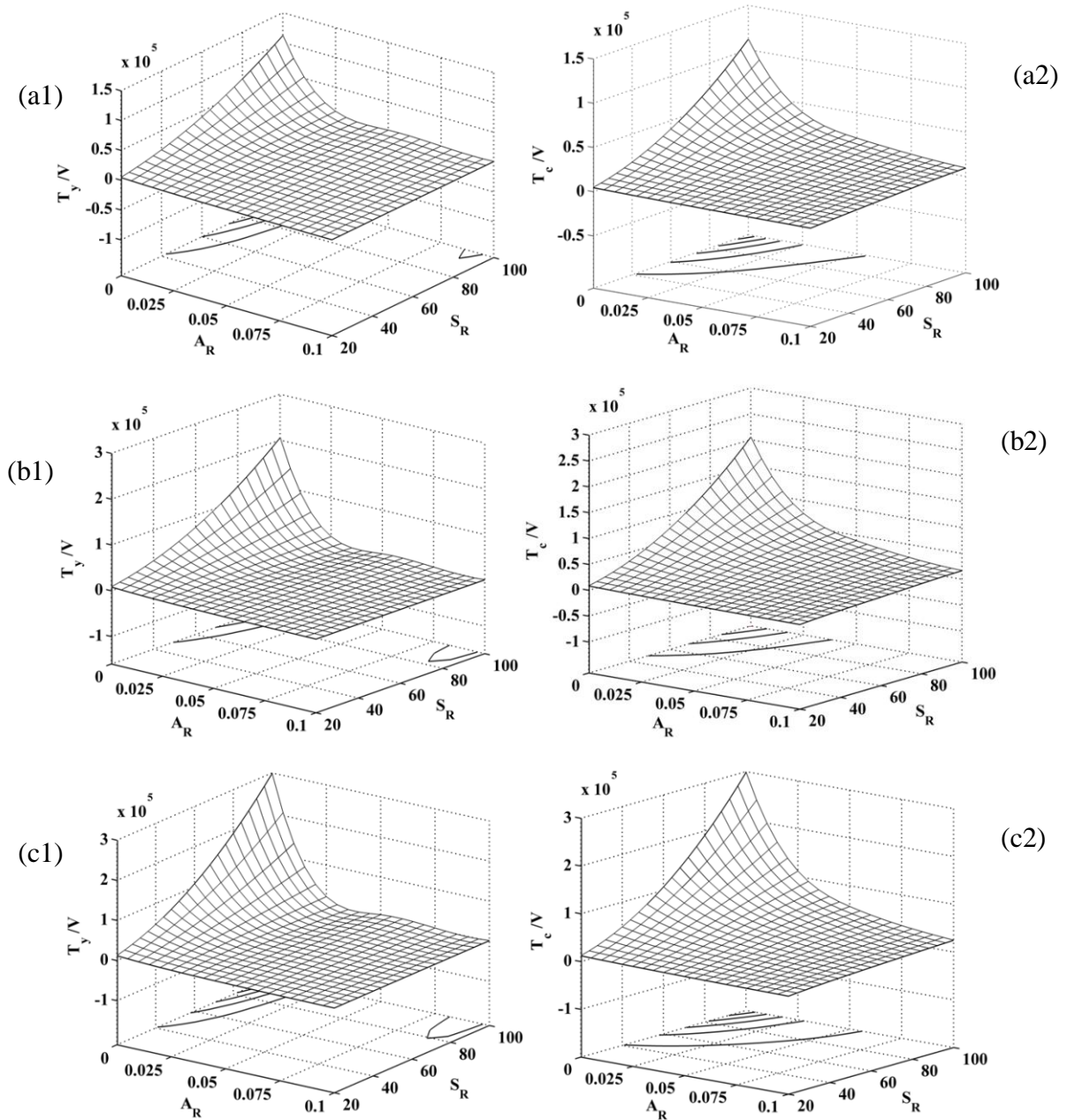


**Figure 5.14.** 3D and contour plots of elastic limit temperature and plastic collapse temperature per unit volume with its variation with  $A_R$  and  $S_R$  for parabolic bars under (a1,a2) uniform, (b1,b2) linearly decreasing and (c1,c2) parabolically decreasing temperatures.

The observation for this case remains same as that of taper bars but for parabolic geometry bars, the elastic limit temperature ( $T_y$ ) and the plastic collapse temperature ( $T_c$ ) are lower than that of linear taper bars for all  $A_R$  as well as  $S_R$  values.

The volume of a parabolic bar with variation in aspect ratio and slenderness ratio is presented in Figure 5.7(b) is used to obtain 3D and contour plots of  $T_y$  and  $T_c$  per unit volume of bar and they are presented in Figure 5.14 for different temperature distributions. The observation for this case remains almost same as that mentioned for taper bars except for the fact that there is more decrease in  $T_c/V$ .

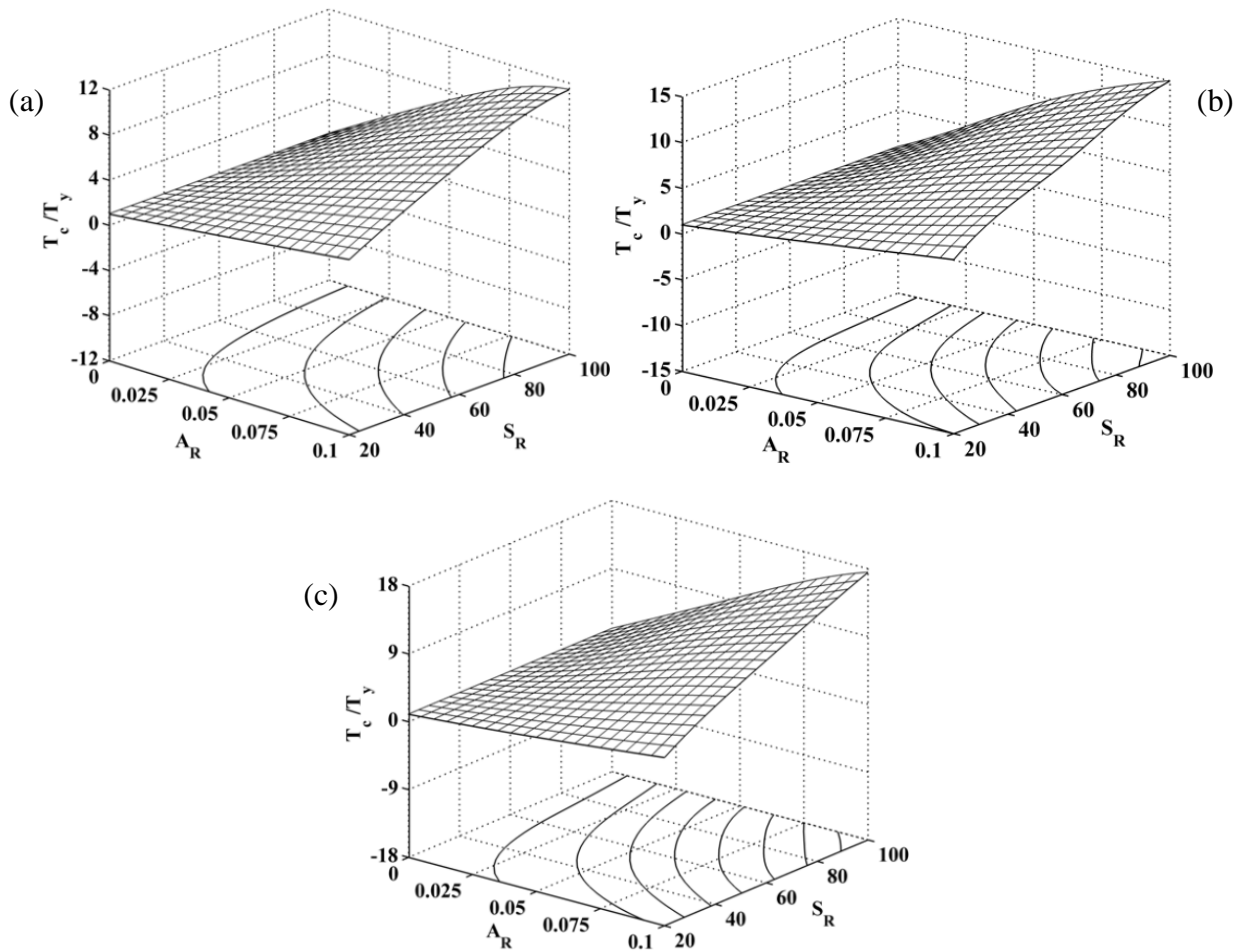


**Figure 5.15.** 3D and contour plots of limit load factor ( $T_c/T_y$ ) showing its variation with  $A_R$  and  $S_R$  for a parabolic bar under (a1,a2) uniform, (b1,b2) linear and (c1,c2) parabolic temperature variations.

3D and contour plots of limit load factor are shown in Figure 5.15 for various combinations of  $A_R$  and  $S_R$  values for parabolic bars. The observation for this case also remains same as that mentioned for taper bars except for the fact that the limit load factors are lower. The 2D representations of  $T_c/T_y$  with  $A_R$  for different  $S_R$  values are presented for parabolic bars in Figure 5.16.

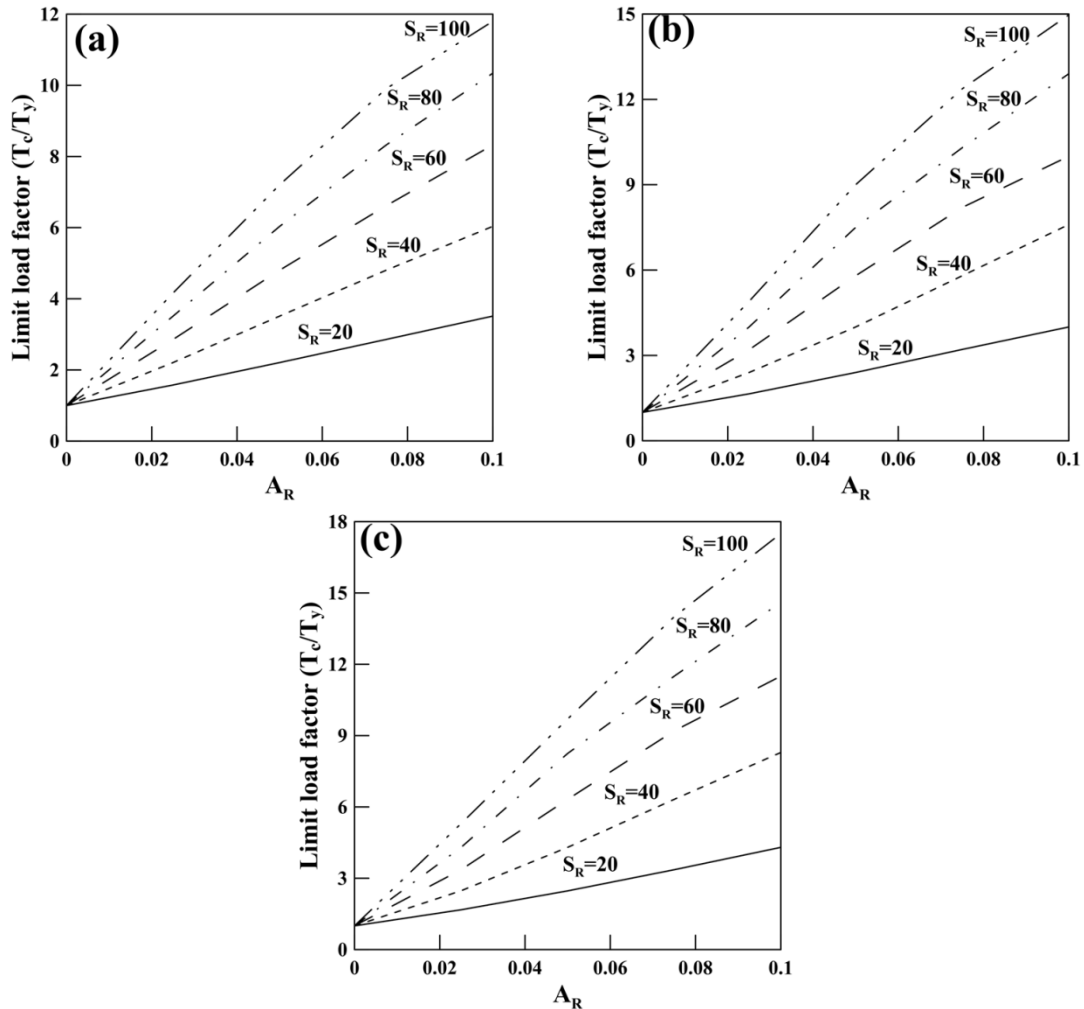


**Figure 5.16.** Plot of limit load factor ( $T_c/T_y$ ) variation with  $A_R$  for different  $S_R$  for a parabolic bar of  $L=1.2$  m for (a) uniform, (b) linear and (c) parabolic temperature variations.

In Figures 5.17, the variation of stress field in parabolic bar is reported through waterfall plots with their superimposed projected views for three types of temperature distributions. The compressive stress for this case also increases with increase in temperature for all the three types

of temperature distributions. However the compressive stress is more for linearly decreasing temperature distribution as compared to other two temperature distributions.

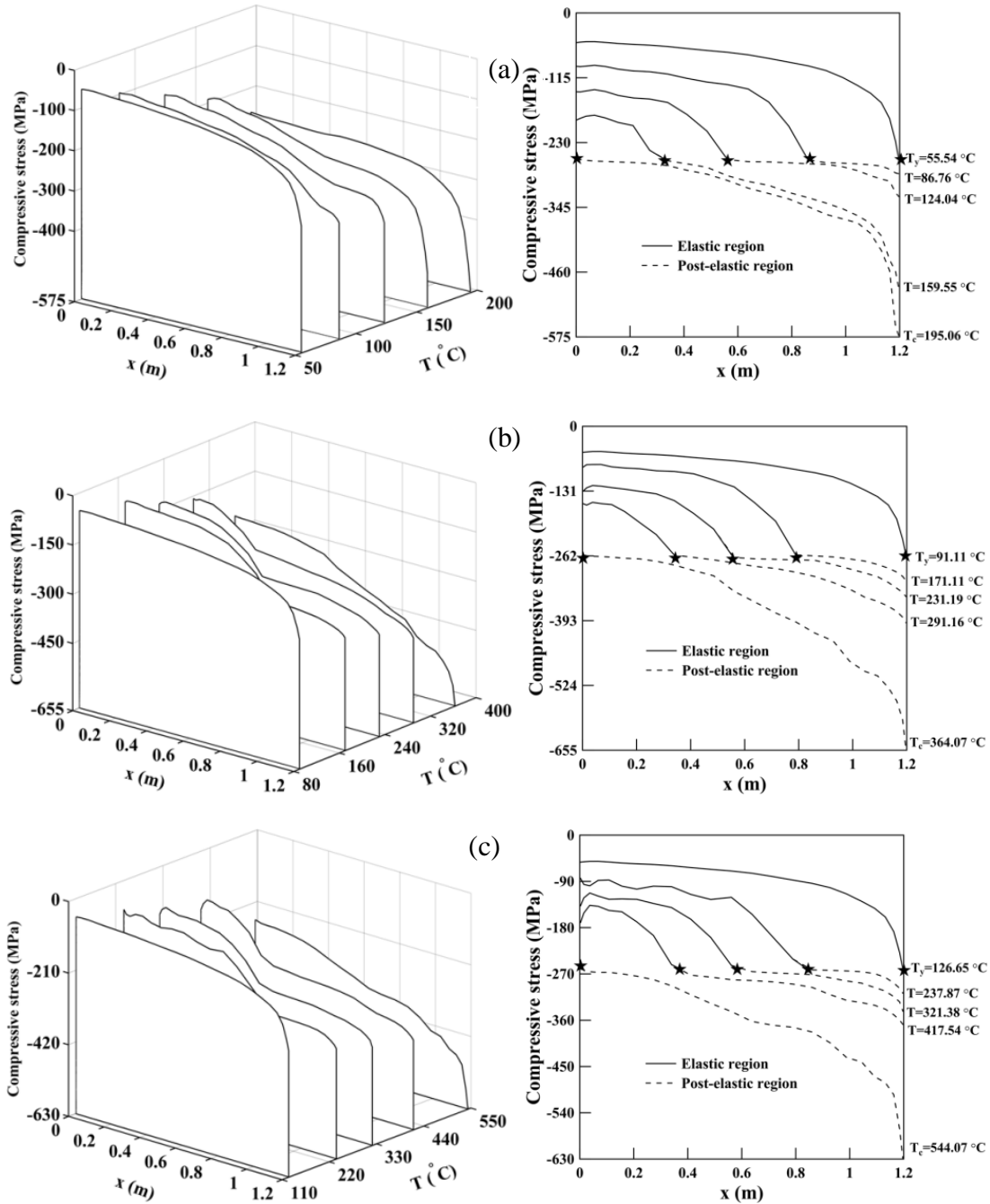


**Figure 5.17.** Waterfall plot and projections of stress fields at different temperatures for a parabolic bar of  $A_R = 0.1$  and  $S_R = 20$ , under (a) uniform, (b) linearly decreasing and (c) parabolically decreasing temperatures.



From these waterfall plots, the plastic front locations are captured at different temperature levels and their locations has been provided in Figures 5.18.

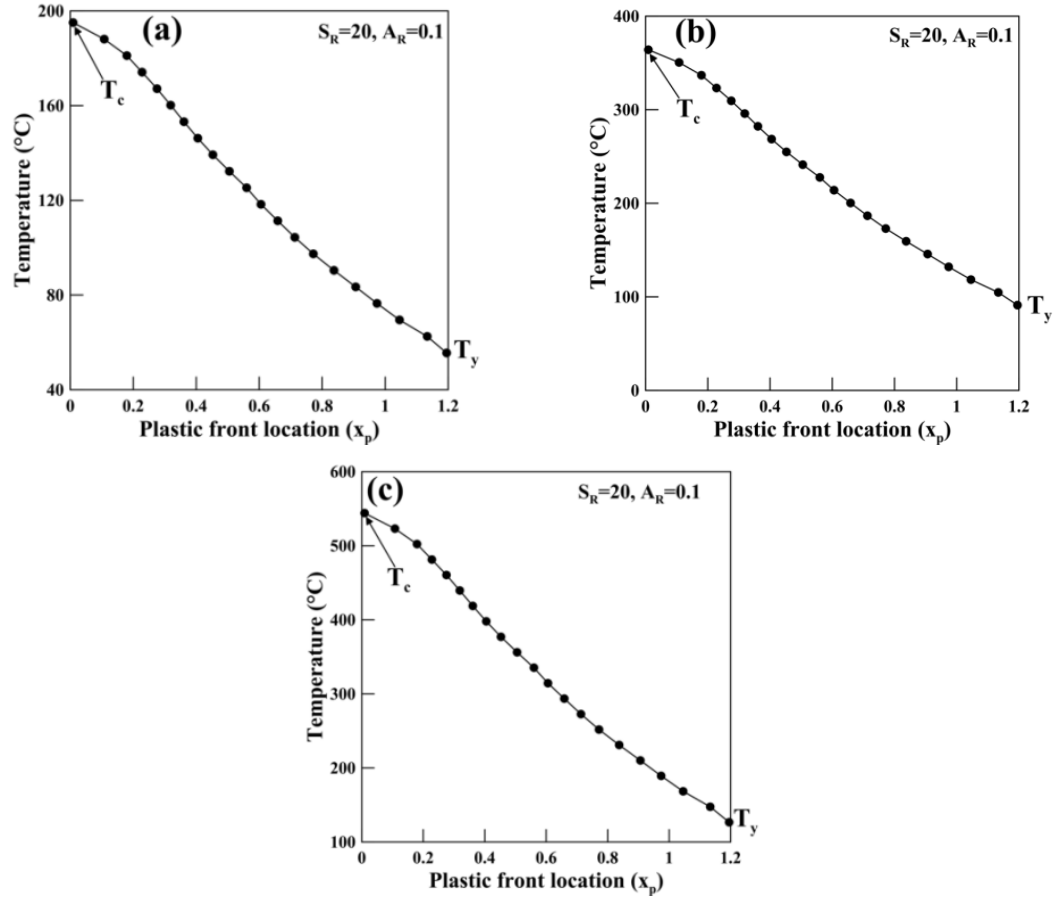


**Figure 5.18.** Plot of plastic front location variation with temperature for a parabolic bar of  $A_R = 0.1$  and  $S_R = 20$ , under (a) uniform, (b) linearly decreasing and (c) parabolically decreasing temperatures.

#### 5.2.2.4 Results for multilinear (four segment) material model

The results are also presented for multilinear material behavior with four segments using tangent modulus  $E_{IA} = 26.47$  GPa,  $E_{IB} = 17.39$  GPa and  $E_{IC} = 3.80$  GPa as shown in Figure 5.19(a). In Figure 5.19(b), relations of deviatoric stress ( $S$ ) with shear strain ( $\Gamma$ ) are shown for multilinear material model.

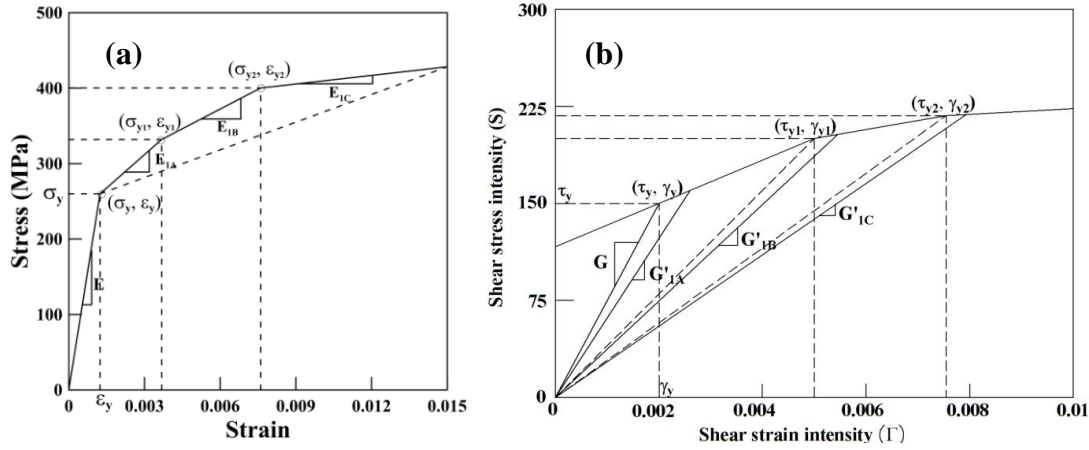


**Figure 5.19.** Linear elastic and trilinear elasto-plastic behaviour (multilinear with four segment material model).

3D and contour plots of elastic limit and plastic collapse temperatures with simultaneous variation in aspect ratio and slenderness ratio has also been presented in Figures 5.20(a1,a2)-(c1,c2) for multilinear material model. These plots are compared with Figures 5.6(a1,a2)-(c1,c2) and it is observed that the elastic limit temperatures remain same for both bilinear and multilinear material model, as expected. However, there is a change in the plastic collapse temperatures and is more for multilinear material model for all the cases of temperature variations.

The nature of waterfall plots and their projections depicting variation of stress field at different temperatures are shown in Figures 5.21(a)-(c) for multilinear material model. It is apparent that the nature of stress fields are identical but the compressive stress is more for all the temperature variations as compared to bilinear material model.

The plastic front locations with temperatures are plotted in Figures 5.22(a)-(c) for multilinear material model, and their change with the corresponding plot for bilinear model are obvious. It is observed that the elastic limit temperature ( $T_y$ ) remain same for both the material models but the plastic collapse temperature ( $T_c$ ) is more for multilinear material model for all the cases of temperature variations. For uniform temperature distribution, there is not much difference in plastic front locations for both the models at lower temperatures. However, the difference in plastic front locations is prominent for linear and parabolic temperature distributions.

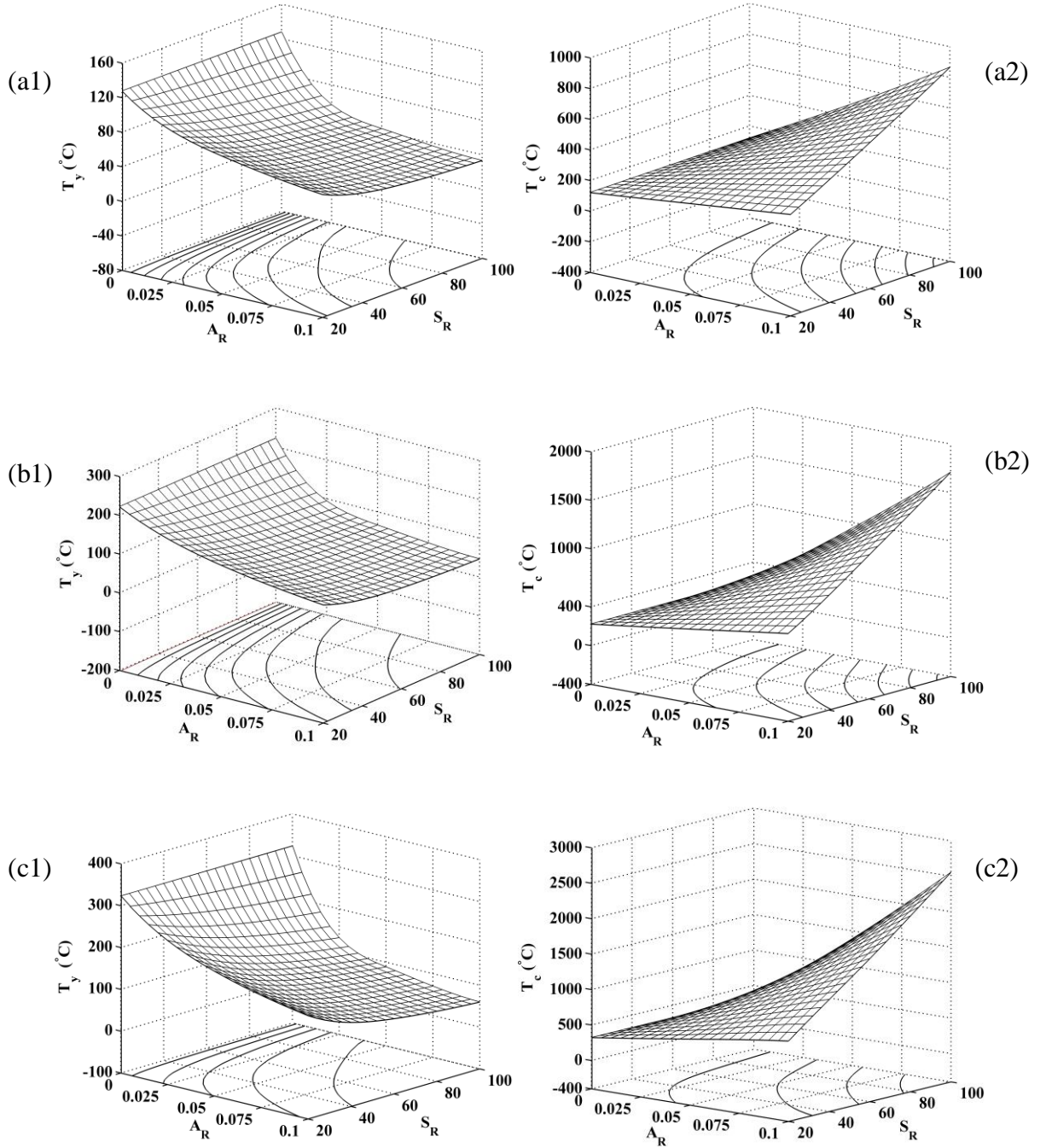


**Figure 5.20.** 3D and contour plots of elastic limit temperature ( $T_y$ ) and plastic collapse temperature ( $T_c$ ) with its variation with  $A_R$  and  $S_R$  for clamped taper bar with multilinear material model under (a1,a2) uniform, (b1,b2) linearly decreasing and (c1,c2) parabolically decreasing temperatures.

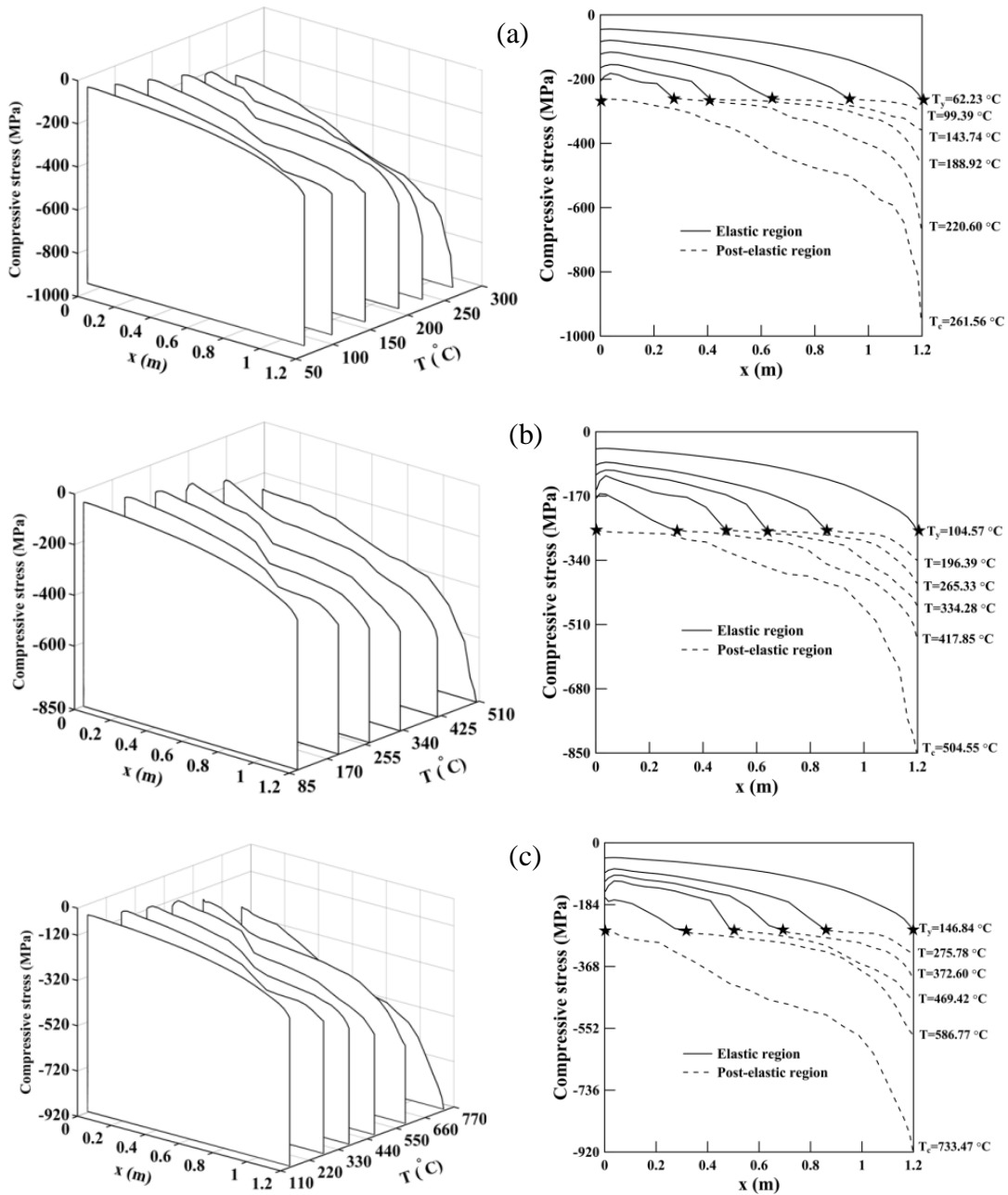


**Figure 5.21.** Waterfall plot and projections of stress fields at different temperatures for a taper bar of  $A_R = 0.1$  and  $S_R = 20$  for multilinear material model under (a) uniform, (b) linearly decreasing and (c) parabolically decreasing temperatures.

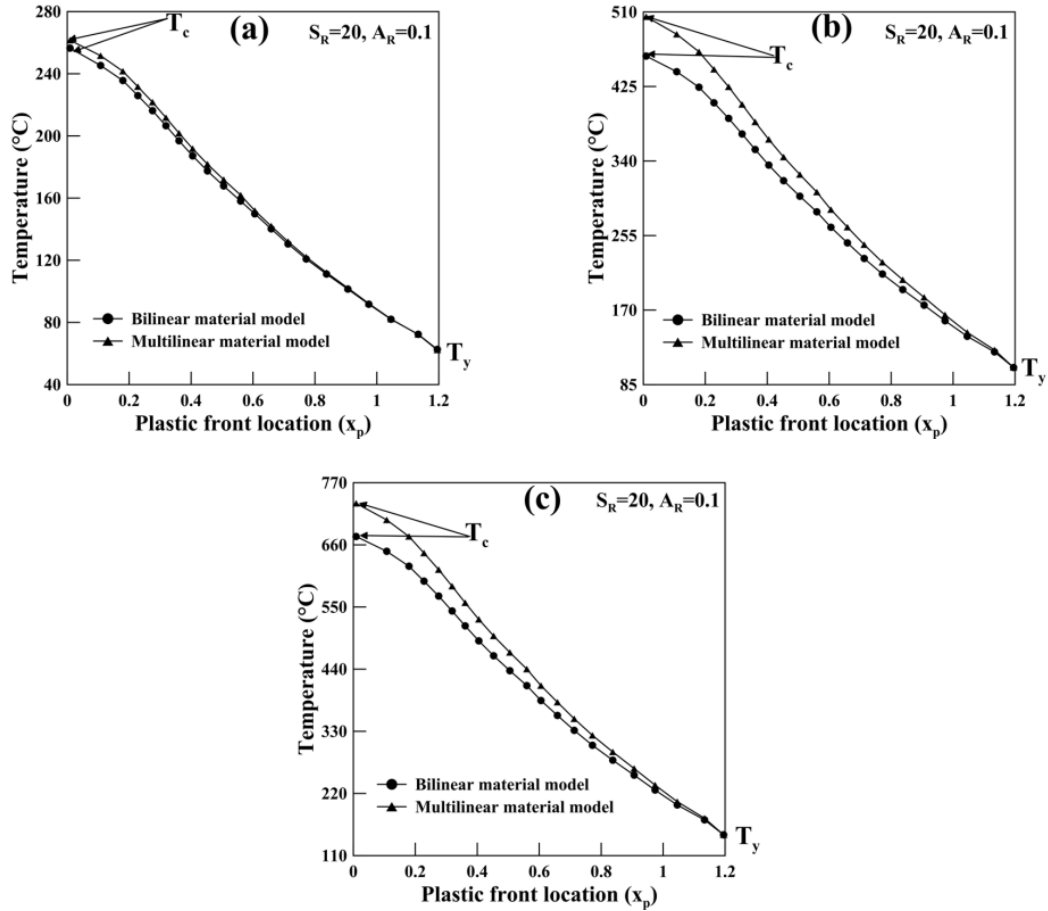


**Figure 5.22.** Plot of variation in plastic front location variation with temperature for taper bar with multilinear material model under (a) uniform, (b) linearly decreasing and (c) parabolically decreasing temperatures.

### 5.2.2.5 Elasto-plastic behaviour considering yield stress variation with temperature

The results are presented for clamped taper bar considering the effect of temperature on yield stress of mild steel as obtained from an article by Martinez (2016). The experimental data points taken from Martinez (2016) are presented graphically by best fit curve in Figure 5.23(a) where initial yield stress,  $\sigma_o = 260$  MPa. 3D and contour plots of elastic limit and plastic collapse temperatures with simultaneous variation in aspect ratio and slenderness ratio has been presented in Figures 5.24(a1,a2)-(c1,c2) considering bilinear material behaviour. In Figure 5.23(b), the initial yield stress at three different temperatures are considered as 100 MPa, 180 MPa and 260 MPa. From this figure, it is obvious that the  $E$  value remains constant but there is a decrease in  $E_I$  value with increase in yield stress. However, the effect of  $E_I$  is not considered for

the present analysis. These plots are compared with Figures 5.6(a1,a2)-(c1,c2) with constant yield stress and it is observed that there is a decrease in elastic limit temperatures and plastic collapse temperatures for yield stress variation for all the cases of temperature variations.

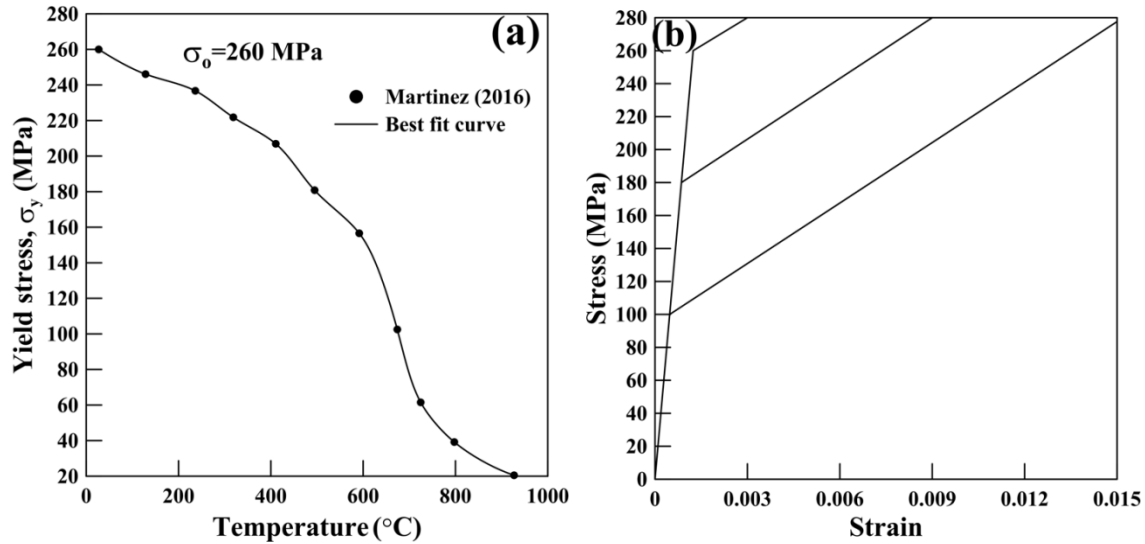


**Figure 5.23.** (a) Yield stress variation with temperature of mild steel, after Martinez (2016) and (b) Stress-strain plot for yield stress variation showing bilinear material behaviour.

The stress field variation and their projected views at different temperatures are presented in Figures 5.25(a)-(c) considering yield stress variation with temperature. These plots are compared with the waterfall plots of Figure 5.11 and it is observed that the nature of stress fields are identical in this case also but the compressive stress is more for linear and parabolic temperature distributions. From these waterfall plots in Figure 5.25, the plastic front locations with temperatures are plotted in Figures 5.26(a)-(c) and their comparison with the corresponding plot for constant yield stress are shown. It is observed that the elastic limit temperature ( $T_y$ ) and the plastic collapse temperature ( $T_c$ ) is less for all the cases of temperature variations considering yield stress variation in temperature.

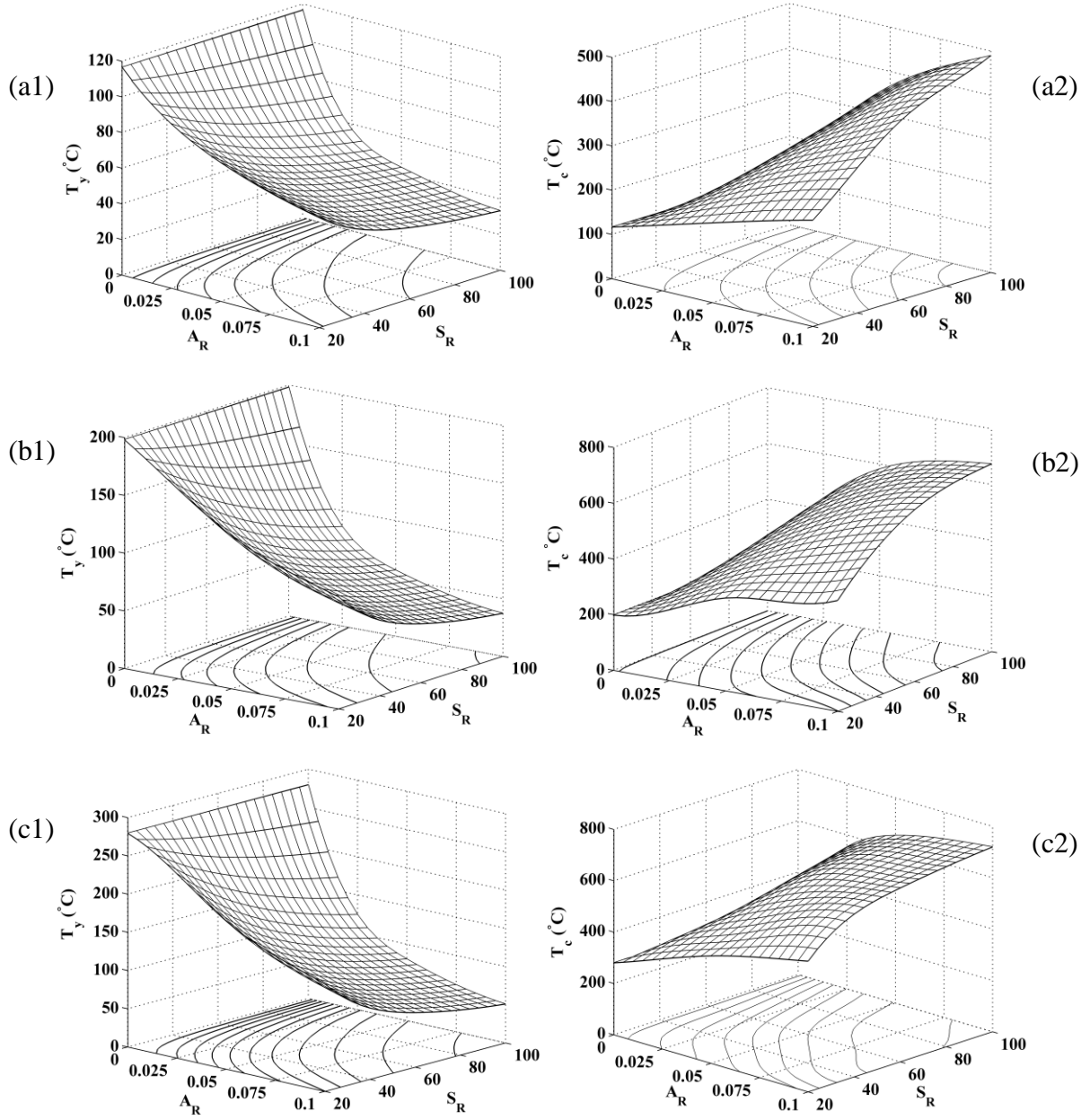


**Figure 5.24.** 3D and contour plots of elastic limit temperature ( $T_y$ ) and plastic collapse temperature ( $T_c$ ) with its variation with  $A_R$  and  $S_R$  for taper bars considering yield stress variation with temperature under (a1,a2) uniform, (b1,b2) linearly decreasing and (c1,c2) parabolically decreasing temperatures.

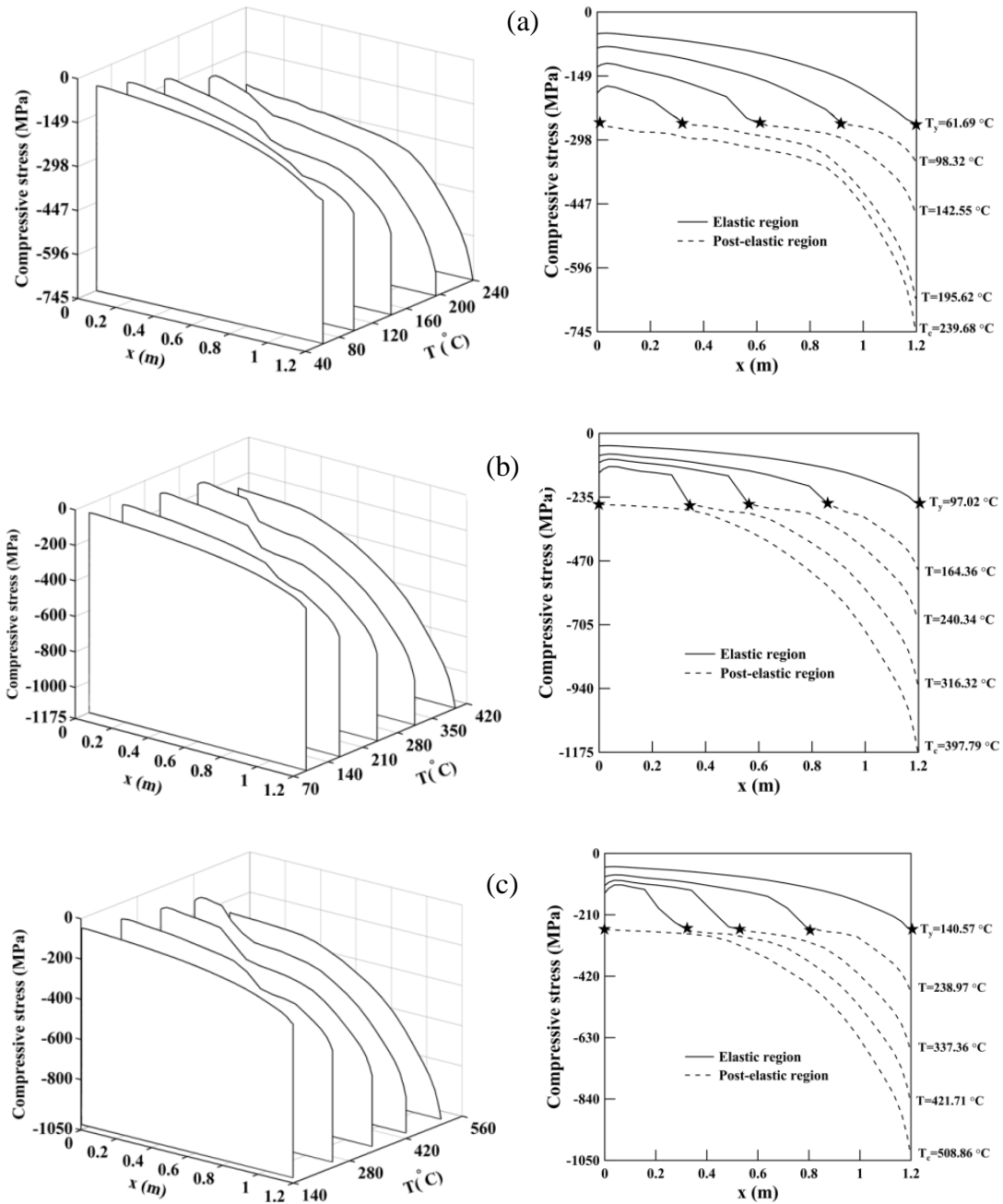


**Figure 5.25.** Waterfall plot and projections of stress fields at different temperatures for a taper bar with yield stress variation of  $A_R = 0.1$  and  $S_R = 20$ , under (a) uniform, (b) linearly decreasing and (c) parabolically decreasing temperatures.



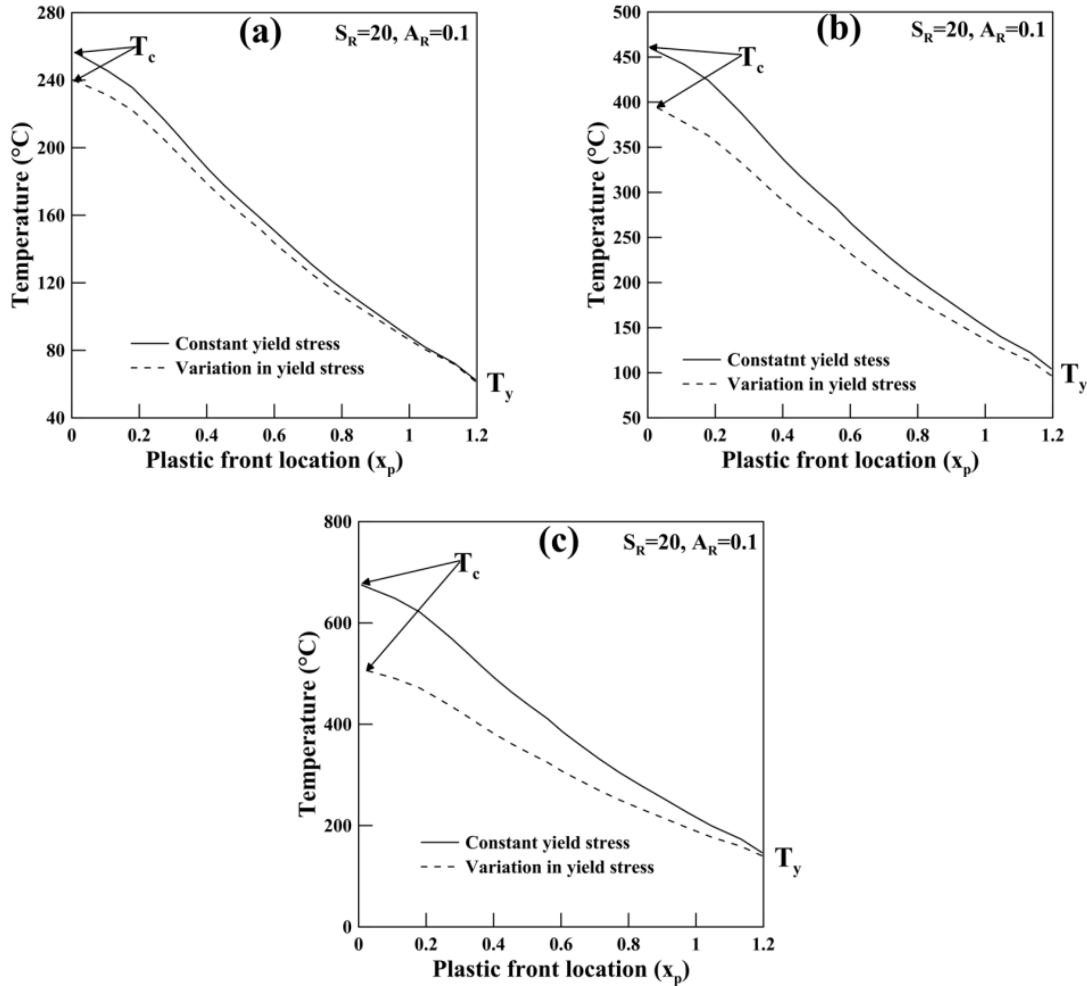


**Figure 5.26.** Plot of variation in plastic front location variation with temperature for taper bar considering yield stress variation under (a) uniform, (b) linearly decreasing and (c) parabolically decreasing temperatures.

### 5.3 Thermo-elasto-plastic analysis of functionally graded non-uniform bars

Elasto-plastic analysis of functionally graded non-uniform bars subjected to thermal loads is reported in this section. The earliest FGMs were introduced by Japanese scientists in the mid-1980s as ultra-high temperature resistant materials for aerospace applications (Yamanoushi et al. (1990)). Miyamoto et al. (1999) discussed the methods of FGM fabrication and general information about FGMs including microstructure analysis of the graded materials. Suresh and Mortensen (1998) provided an introduction to the fundamentals of FGMs. Noda (1991)

presented an extensive review that covers a wide range of topics from thermoelastic to thermo inelastic problems. The author discussed the importance of temperature dependent properties on stresses and suggested that those properties of the material should be taken into account in order to perform more accurate analysis.

Cho and Oden (2000) studied the thermal stress characteristics of functionally graded materials using finite element method. Different thermal stress characteristics for different material variations and sizes of FGM were observed. Shabana et al. (2000) analyzed the elasto-plastic thermal stresses in functionally graded materials by using microscopic combination law. The finite element model of the formulation is developed by considering elasto-plasticity theory. Pitakthapanaphong and Busso (2002) described the thermo-elastic and thermo-elasto-plastic behaviour of FGM through analytical and semi-analytical solutions. The homogenization of the local elasto-plastic FGM behaviour in terms of the properties of its individual phases was performed using a self-consistent approach and power-law strain hardening behaviour was assumed for the FGM metallic phase. Eraslan and Akis (2005) obtained the plane strain analytical solutions for functionally graded elastic and elastic-plastic pressurized tube problems. The plastic modeling was based on Tresca's yield criterion, its associated flow rule and ideally plastic material behaviour.

Alibeigloo (2010) studied FG beams integrated with piezoelectric actuator and sensor subjected to an applied electric field and thermo-mechanical load using analytical solution. In this study, the FGM properties were assumed to vary exponentially in the thickness direction and the poisson's ratio was held constant. Wattanasakulpong et al. (2011) employed an improved third order shear deformation theory to investigate thermal buckling load of FGM beam under uniform temperature rise. Ma and Lee (2012) obtained closed form solution for the non-linear static responses of FGM beams subjected to a uniform in-plane thermal loading. The governing equations for the axial and transverse deformations of FGM beams were based on the non-linear first order shear deformation theory. Bayat and Toussi (2015) solved the elasto-plastic torsion problem of hollow FGM circular shafts. The torsional shaft is considered as a thick-walled axisymmetric inhomogeneous cylindrical object, while the FG material is composed of ceramic and metallic parts with power function distribution only across the radial direction. Xin et al. (2016) investigated the elasto-plastic response of FG thick-walled tube subjected to internal pressure by using the relation of the volume average stresses of constituents and the macroscopic

stress of composite material. Garg and Pant (2017) simulated thermal fracture in functionally graded materials by implementing element-free Galerkin method (EFGM). Zhang and Liew (2016) presented post buckling analysis of axially compressed functionally graded carbon nano tube resting on Pasternak foundations by utilizing an element-free approach. Shen et al. (2017) investigated the non-linear vibration behaviour of functionally graded graphene-reinforced composite laminated cylindrical shells in thermal environments. Tsiatas and Babouskos (2017) employed a new integral equation solution to the elasto-plastic torsion problem of functionally graded bars of arbitrary cross-section, by using deformation theory of plasticity. Huang et al. (2014) presented a semi-analytic solution to analyze the buckling behaviour of elasto-plastic functionally graded cylindrical shells under torsional loading by assuming multilinear hardening model for materials. Niknam et al. (2014) investigated the non-linear bending of tapered functionally graded beams by implementing analytical and numerical approaches subjected to thermal and mechanical loading. Paul and Das (2016) presented non-linear post-buckling load of FGM Timoshenko beam under non-uniform temperature rise across the thickness of the beam at steady-state condition.

The present study concentrates on the growth of yield front of functionally graded material (FGM) non-uniform bars subjected to thermal loads. FGM is modeled by considering continuous distribution of metal and ceramic constituents across the length using power law variation of volume fraction. Moreover, the FGM bar is assumed to be modeled as linear elastic ceramic and the metal as an elastic-linear hardening material. The problem is solved through a variational method, taking yield stress and elasticity modulus of the metallic part, being a function of temperature whereas the elasticity modulus corresponding to the value at ambient temperature is considered for the ceramic part. The elasto-plastic analysis based on deformation theory of plasticity and von-Mises yield criterion is carried out by assuming a series approximation of the unknown displacement field. Galerkin's principle is used to obtain the solution of the governing differential equation. An iterative process is applied to locate the growth of the yield front for the approximate solution and for the prescribed temperature field. MATLAB<sup>®</sup> computational simulation software is used to implement the solution algorithm. Some numerical results of the thermo-elasto-plastic field are presented graphically showing the effect of material parameters on clamped-clamped functionally graded non-uniform bars having various geometries subjected to uniform and non-uniform thermal loads.

### 5.3.1 Mathematical formulation

A functionally graded bar comprised of a ceramic phase and metal phase is considered in this investigation. For FGM modeling, a continuous variation of volume fraction of metal and ceramic along the axial direction is assumed. The volume fraction of ceramic ( $V_c$ ) and metal ( $V_m$ ) constituents along the axial direction follows the power law distribution (Farimani and Toussi (2013))

$$V_c(x) = V_{c0} \left( \frac{x}{L} \right)^n \quad (5.9a)$$

and

$$V_c + V_m = 1, \quad (5.9b)$$

where,  $V$  is the volume fraction of the constituents with subscripts  $c$  and  $m$ , which corresponds to the ceramic and metallic constituents.  $V_{c0}$  is volume fraction of the ceramic in the right fixed end of the bar and  $n$  is the volume fraction exponent. The FG bar becomes a pure metallic bar when  $V_{c0} = 0$  and  $n = 0$  denotes a bar with uniform distribution of ceramic phase. For  $V_{c0} = 1$ , the left and right ends of the bar comprises of purely metal and purely ceramic parts, respectively.

For the elasto-plastic analysis of FGM bars, it is assumed that the metal matrix has bilinear elastic-plastic behaviour model with elastic modulus  $E_m$ , tangent modulus  $E_{tm}$  and yield stress  $\sigma_{ym}$ , whereas the ceramic is assumed to be linear elastic with elastic modulus,  $E_c$  as shown in Figure 5.27. In the present investigation, TTO homogenization scheme is adopted for the modeling of elasto-plastic FGMs as defined by Tamura et al. (1973) for the estimation of FGM effective properties. The model was extended by Bocciarelli (2008) for ceramic/metal compound to depict the elasto-plastic behaviour of FGMs.

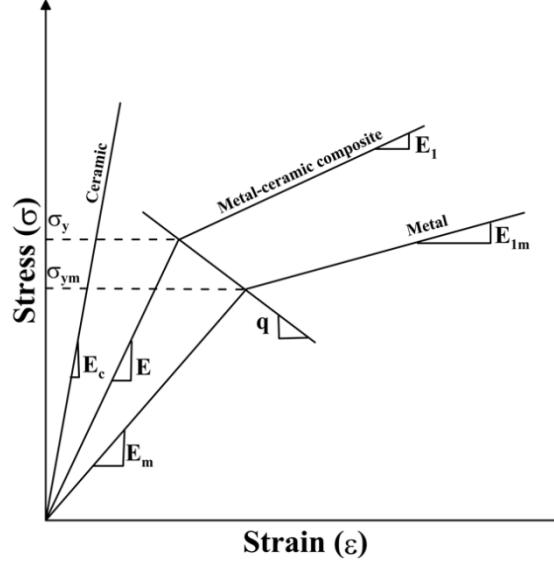


**Figure 5.27.** Schematic bilinear stress-strain curve for the FGM.

The TTO model assumes that the composite yields once the metal constituent yields (Gao and Ogden (2003)). Thus, the elasto-plastic behaviour of FGM is obtained by the introduction of the ratio of stress to strain transfer  $q(= \tilde{q}E_c)$  where,  $\tilde{q}$  is the stress transfer parameter ( $\tilde{q} \geq 0$ ). It should be noted  $\tilde{q} = 0$  represents that FGMs flow plastically once the metallic constituents reach their yield limit. The value of  $q$  depends on many factors such as composition, material microstructure, loading condition, etc. However,  $q$  is assumed to be constant beyond the elastic range due to lack of experimental data. The elasto-plastic material properties of FGM bar along the axial location can be defined by Nakamura et al. (2000) as

$$E(x) = \left[ V_m E_m \left( \frac{q + E_c}{q + E_m} \right) + V_c E_c \right] / \left[ V_m \left( \frac{q + E_c}{q + E_m} \right) + V_c \right] \quad (5.10a)$$

$$\sigma_y(x) = \sigma_{ym} \left[ V_m + \left( \frac{q + E_m}{q + E_c} \right) \frac{E_c}{E_m} V_c \right] \quad (5.10b)$$

$$E_1(x) = \left[ V_m E_{1m} \left( \frac{q + E_c}{q + E_{1m}} \right) + V_c E_c \right] / \left[ V_m \left( \frac{q + E_c}{q + E_{1m}} \right) + V_c \right] \quad (5.10c)$$

where  $E(x)$  is elastic modulus,  $\sigma_y(x)$  is the overall yield stress and  $E_1(x)$  is the tangent modulus of the FGM bar as shown in Figure 5.25.

The coefficient of linear thermal expansion  $\alpha(x)$  of FGM bar can be determined by using the modified rule of mixtures (Suresh and Mortensen (1998)) as provided below.

$$\alpha(x) = \alpha_m V_m + \alpha_c V_c. \quad (5.10d)$$

However, Poisson's ratio is assumed to be constant in this analysis for both the phases (metal and ceramic) as there is small change in value between ceramic and metal; therefore an average value is considered throughout the FGM. However,  $\nu$  and  $\nu_p$  are Poisson's ratios in elastic and post-elastic regions respectively.

### 5.3.1.1 Solution of the problem

The present section performs analysis for clamped-clamped FGM taper bars subjected to thermal load. Both bilinear (Figure 5.2) and multilinear (Figure 5.19) models of material behaviors are considered for the present analysis. The FGM bar is considered to be locally isotropic and an energy based variational approach is used by following von-Mises criterion and Hencky's total deformation theory of plasticity to get the governing equations. In the presence of temperature field the analysis of plastic behaviour becomes more complicated, because the yield limit and stress-strain relation depends on temperature. It is assumed that the temperature rise is not permanent so that effect of creep can be neglected. Using the similar expressions from Eq. (5.1) to Eq. (5.7), the governing differential equation for the FGM bar is given by

$$\begin{aligned} & \sum_{i=1}^n \sum_{j=1}^n c_i \left[ \left( \frac{2}{L_e} \right) \int_0^l \left( \frac{K(1-2\nu)^2}{2} + \frac{2G(1+\nu)^2}{3} \right) (A(\xi^e) \phi_i^{e'} \phi_j^{e'}) d\xi^e \right. \\ & \left. + \left( \frac{2}{L_p} \right) \int_0^l \left( \frac{K(1-2\nu)^2}{2} + \frac{2g(\Gamma)(1+\nu_p)^2}{3} \right) (A(\xi^p) \phi_i^{p'} \phi_j^{p'}) d\xi^p \right] = \sum_{j=10}^n \int 3K(1-2\nu)\alpha T (A(\xi) \phi_j') d\xi. \end{aligned} \quad (5.11)$$

The solution procedure of Eq. (5.11) is identical to that of Eq. (5.8).

### 5.3.2 Results and discussion

The present analysis is carried out for functionally graded non-uniform bars subjected to thermal load. The material properties of the bar are represented in Table 5.2 that is used in the analyses taken from Farimani and Toussi (2013). The value of Poisson's ratio  $\nu$  is taken as 0.3

in elastic state and  $v_p$  in post-elastic region is taken as 0.5 for the FGM bar. The length of the bar  $L$  is taken as 1.2 m.

**Table 5.2:** Material properties of the FGM bar

	$E$ (GPa)	$\sigma_y$ (MPa)	$\alpha$ ( $10^{-6}/^{\circ}\text{C}$ )	$E_I$ (GPa)	$q$ (GPa)
Metal	208	260	11.5	80	17.2
Ceramic	324	-	7.7	-	

The results are presented for three different volume fraction of the ceramic content in the right fixed end,  $V_{c0}$ , considering their values as 0.5, 0.8 and 1. The volume fraction exponent,  $n$  is taken as 0.5 and 2. A plot of Eq. (5.9) is presented in Figure 5.28 for different  $n$  and  $V_{c0}$  values for six materials, FGM AI, FGM BI, FGM AII, FGM BII, FGM AIII and FGM BIII.

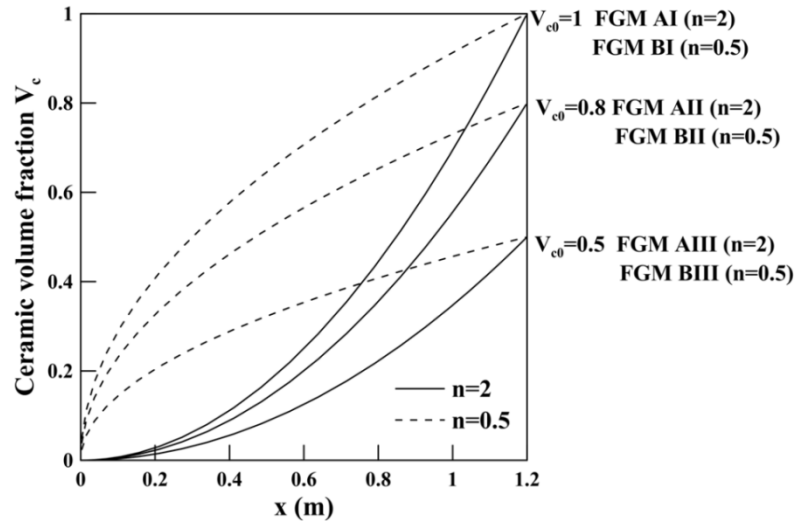


**Figure 5.28.** Plots for ceramic volume fraction  $V_c$  for six materials, FGM AI, FGM BI, FGM AII, FGM BII, FGM AIII and FGM BIII.

As the  $V_c$  and  $V_m$  values are functions of axial location, it is obvious from Eqs. 5.10(a)-(c), that the material properties of the bar are also functions of axial location. The material properties of the FGM bar are given in detail in Table 5.3, indicating the elasticity modulus,

tangent modulus and yield stress of the bar. The analysis is carried out for three different types of temperature distributions as described in Figure 5.3(b).

**Table 5.3:** Material properties of the bar at different normalized co-ordinates for FGM AI

Normalized length ( $\xi$ )	Elasticity modulus, $E$ (GPa)	Tangent modulus, $E_t$ (GPa)	Yield stress, $\sigma_y$ (MPa)
0.00	208.00	80.00	260.00
0.01	208.01	80.01	260.00
0.03	208.07	80.06	260.00
0.06	208.24	80.20	260.01
0.09	208.61	80.51	260.02
0.13	209.27	81.07	260.03
0.18	210.35	81.99	260.06
0.23	211.95	83.37	260.10
0.28	214.19	85.35	260.16
0.34	217.18	88.06	260.23
0.40	221.03	91.69	260.32
0.47	225.81	96.42	260.43
0.53	231.60	102.50	260.56
0.60	238.43	110.22	260.70
0.66	246.29	119.97	260.86
0.72	255.12	132.17	261.02
0.77	264.77	147.34	261.19
0.82	275.03	165.99	261.35
0.87	285.53	188.55	261.50
0.91	295.82	215.03	261.64
0.94	305.33	244.61	261.77
0.97	313.45	274.96	261.87
0.99	319.56	301.79	261.94
1.00	324.00	320.00	262.00



The present analysis is carried out by considering the effect of temperature on yield stress and elasticity modulus of the metallic part of the bar as obtained from Martinez (2016) whereas the elasticity modulus value at ambient temperature is considered for the ceramic part although. The plot for normalized yield stress and elasticity modulus with temperature are presented graphically by best fit curve from the experimental data points taken from Martinez (2016) in Figure 5.29, where  $\sigma_{y_0} = 260\text{MPa}$  and  $E_0 = 208\text{GPa}$  are the values at the ambient temperature.

The effect of aspect ratio, slenderness ratio, the volume fraction of ceramic in the right end ( $V_{c0}$ ), the volume fraction exponent ( $n$ ) and temperature field distributions on elastic limit thermal load ( $T_y$ ) and plastic collapse thermal load ( $T_c$ ) of clamped FGM bar are studied and presented in subsequent sections. Results are presented for both bilinear and multilinear material models. However, for bilinear material model, both linear taper and parabolic geometries are considered but for multilinear material model, results are provided for only linear taper geometry.

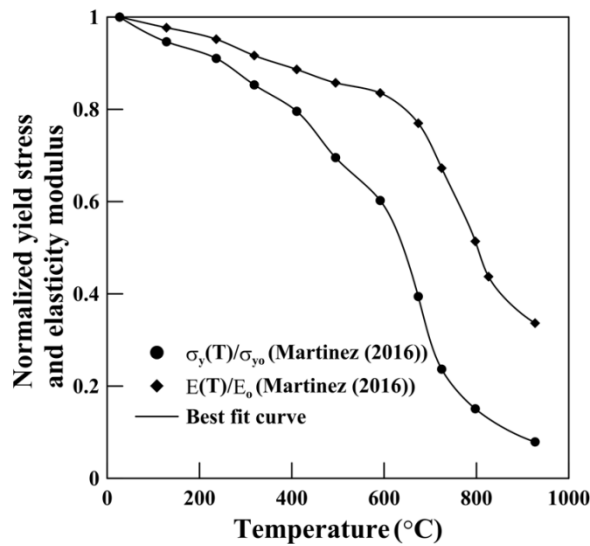


**Figure 5.29.** Normalized yield stress and elasticity modulus variation with temperature of mild steel, after Martinez (2016).

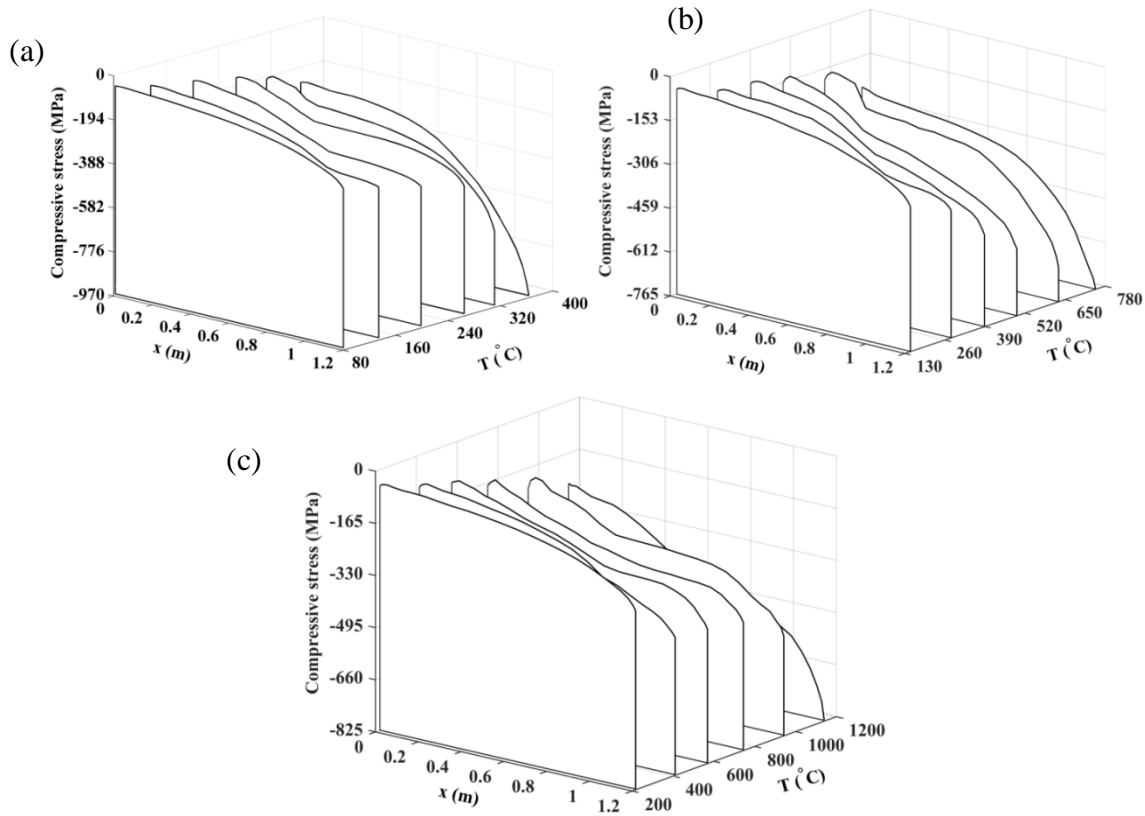


**Figure 5.30.** Waterfall plot of stress fields at different temperatures for FGM taper bar of  $A_R = 0.1$  and  $S_R = 20$ , under (a) uniform, (b) linearly decreasing and (c) parabolically decreasing temperatures.

### 5.3.2.1 Elasto-plastic behaviour of FGM taper bar

For clamped-clamped FGM bar, to analyze the growth of yield front under thermal loading, the axial distribution of stress fields are reported in Figures 5.30(a)-(c) at different temperatures through waterfall plots. The ceramic volume fraction at the right fixed end,  $V_{c0} = 1$  and volume fraction exponent,  $n=2$  is considered for this analysis. The plots are shown for three types of temperature distributions and in each of them temperature range from initial yield limit to ultimate collapse limit.

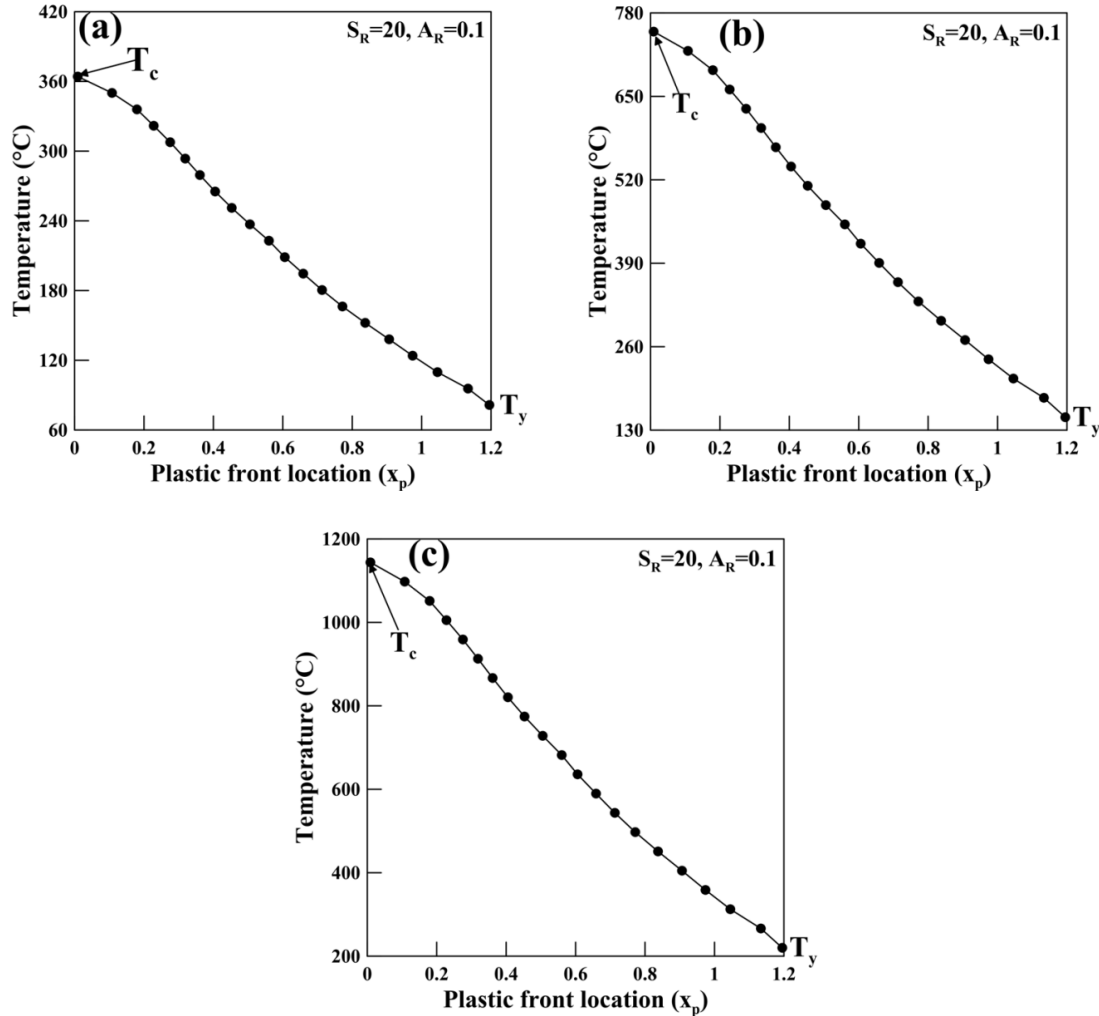


**Figure 5.31.** Plot of propagation of yield front location with increase in temperature for FGM taper bar of  $A_R = 0.1$  and  $S_R = 20$ , under (a) uniform, (b) linearly decreasing and (c) parabolically decreasing temperatures.

The plots are presented for a particular bar geometry  $A_R = 0.1$ ,  $S_R = 20$  and  $L = 1.2$  m. It is observed for all the cases of temperature distributions that the compressive stress increases with increase in temperature, initial yielding occurs at the smallest fixed end ( $x = L$ ) of the bar and when the temperature reaches  $T_c$ , entire bar becomes elastoplastic. For uniform temperature field, the compressive stress is more as compared to decreasing linear and parabolic temperature field distributions. From the waterfall plots of stress fields in Figure 5.30 for the clamped FGM taper bar, the yield front locations are captured at various temperature levels and their

temperature with location are given in Figures 5.31(a)-(c). These figures indicate the yield front locations advancement with increasing temperatures for all the three types of temperature field distributions.

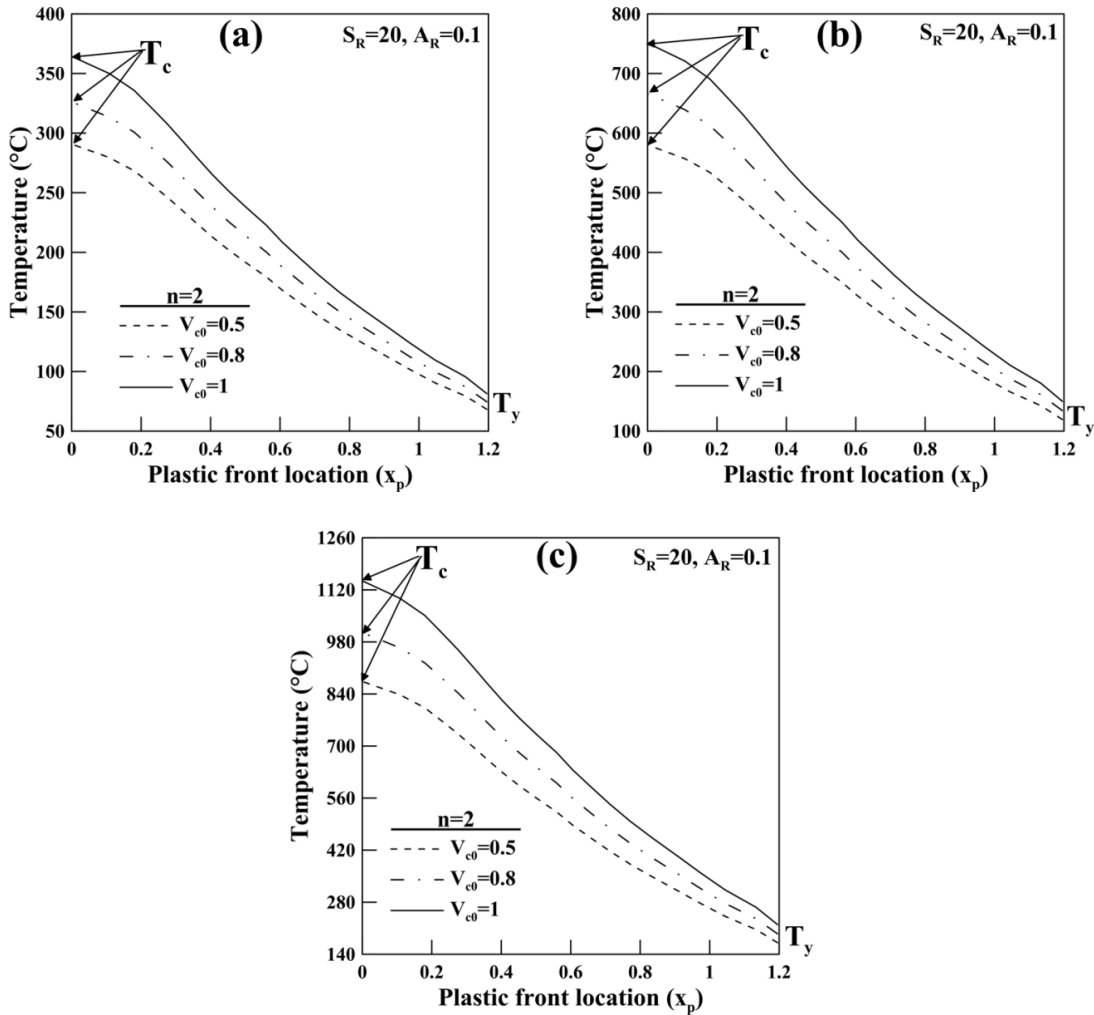


**Figure 5.32.** Plot of propagation of yield front location with increase in temperature for different  $V_{c0}$  values for FGM taper bar under (a) uniform, (b) linearly decreasing and (c) parabolically decreasing temperatures.

### 5.3.2.2 Effect of material parameters $V_{c0}$ and $n$

To understand the significance of the material parameters on FGM taper bar, a parametric study by changing the values of  $V_{c0}$  for a particular volume fraction exponent,  $n$  is carried out.

The results are also obtained by changing the values of  $n$  for a particular ceramic content at the right end,  $V_{c0}$ .

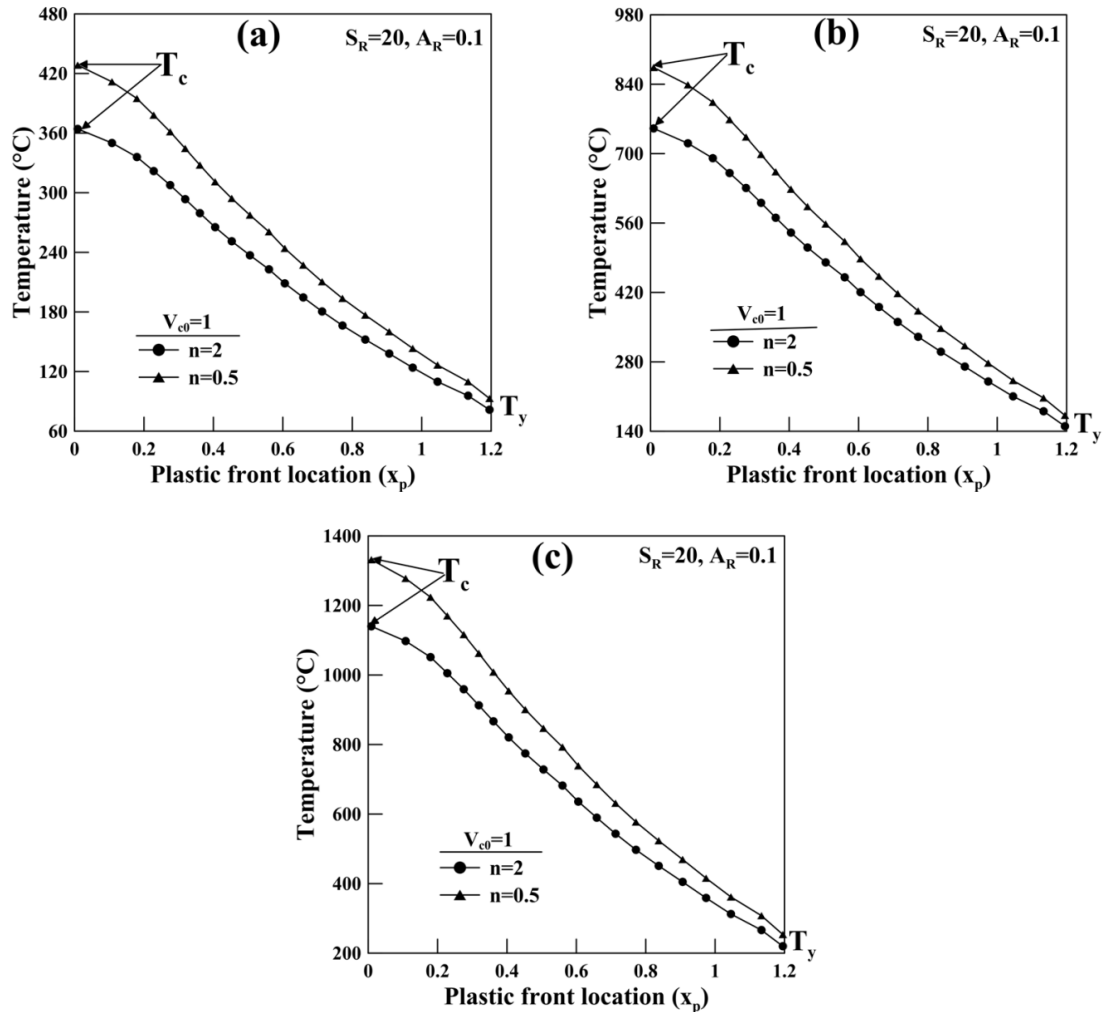


**Figure 5.33.** Plot of propagation of yield front location with increase in temperature for different  $n$  values for FGM taper bar under (a) uniform, (b) linearly decreasing and (c) parabolically decreasing temperatures.

### 5.3.2.2.1 Effect of the ceramic content at the right fixed end, $V_{c0}$

The yield front locations with temperatures are plotted in Figures 5.32(a)-(c) for FGM taper bar under different types of temperature distributions. Each plot contains three different values for  $V_{c0}$  (equals to 0.5, 0.8 and 1) with  $n=2$  and the effect of the  $V_{c0}$  values are observed. It

is obvious that the elastic limit thermal load ( $T_y$ ) and plastic collapse thermal load ( $T_c$ ) increases when  $V_{c0}$  is increased for all the temperature field distributions. From this analysis it is evident that the increase in ceramic content in a ceramic-metal FGM bar improves the limit temperatures.

#### 5.3.2.2.2 Effect of the volume fraction exponent, $n$

The plots for yield front locations with temperatures for FGM taper bar under different types of temperature distributions are presented in Figures 5.33(a)-(c). In each plot two different values for  $n$  (equals to 0.5 and 2) with  $V_{c0} = 1$  is considered and the effect of change in  $n$  values are observed. It is found that the elastic limit thermal load ( $T_y$ ) and plastic collapse thermal load ( $T_c$ ) increases when  $n$  is decreased for all the temperature field distributions. Here, it may be presumed that a smaller value of ' $n$ ' which means more percentage of ceramic in a ceramic-metal FGM bar increases the plastic collapse thermal load.

#### 5.3.2.3 Elasto-plastic behaviour of FGM parabolic bar

In Figure 5.34, the yield front locations at different temperature locations are captured and their locations have been provided for FGM parabolic bar for different temperature distributions. These figures also furnish the results of Figure 5.31 for FGM taper bar in solid lines and it is observed that the elastic limit thermal load ( $T_y$ ) and plastic collapse thermal load ( $T_c$ ) are lower for parabolic bar for all the temperature distributions.

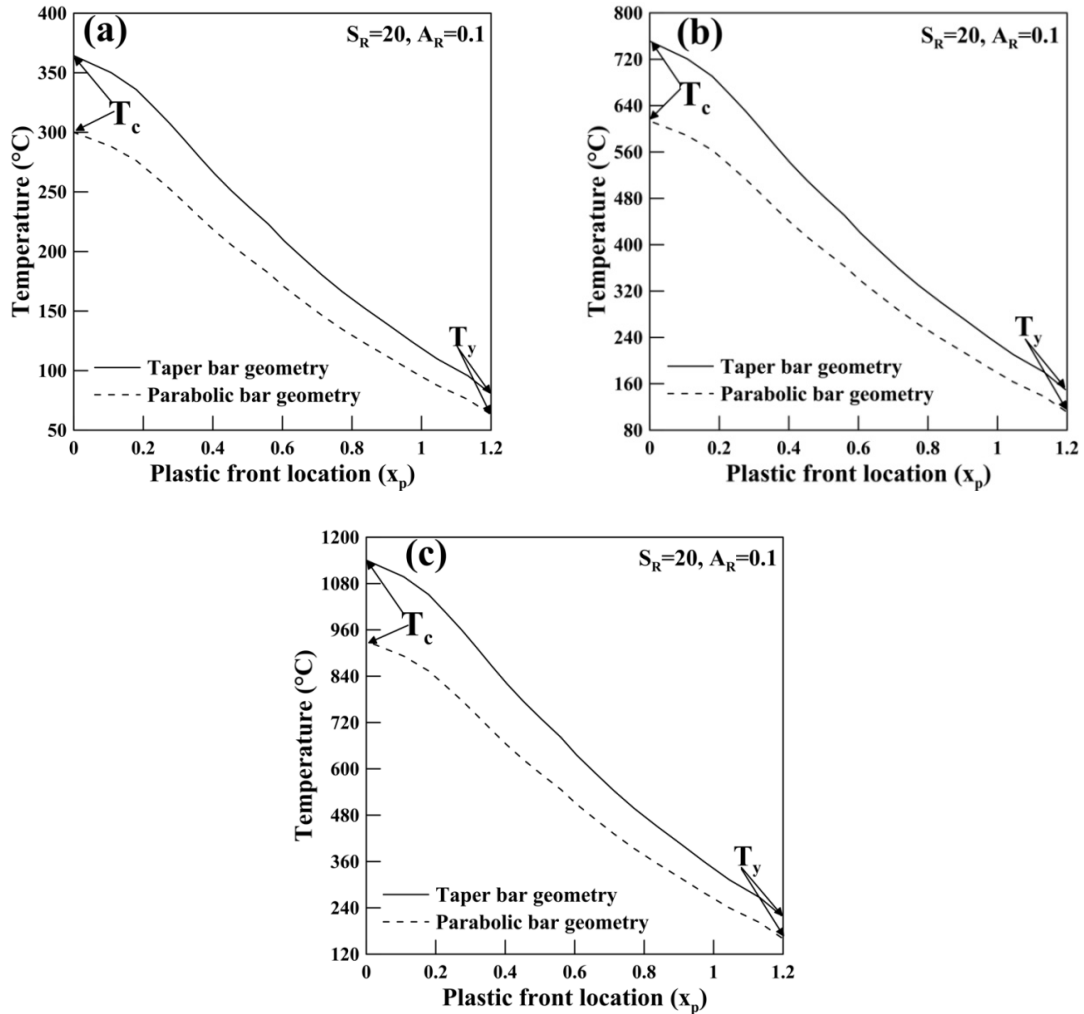


**Figure 5.34.** Plot of propagation of yield front location with increase in temperature for FGM taper and parabolic bar under (a) uniform, (b) linearly decreasing and (c) parabolically decreasing temperatures.

### 5.3.2.4 Results for multilinear (four segment) material model for FGM taper bar

The results are presented for multilinear material model for FGM taper bar under different types of temperature distributions. In this analysis the ceramic volume fraction at the right fixed end  $V_{c0} = 1$  and volume fraction exponent,  $n=2$ . The waterfall of stress fields at different temperatures is presented in Figures 5.35(a)-(c) for multilinear material behaviour. These plots are compared with the corresponding waterfall plots of Figure 5.30 for bilinear material model. It is found that the nature of stress fields are identical but the compressive stress is more for multilinear model for all the temperature field distributions.

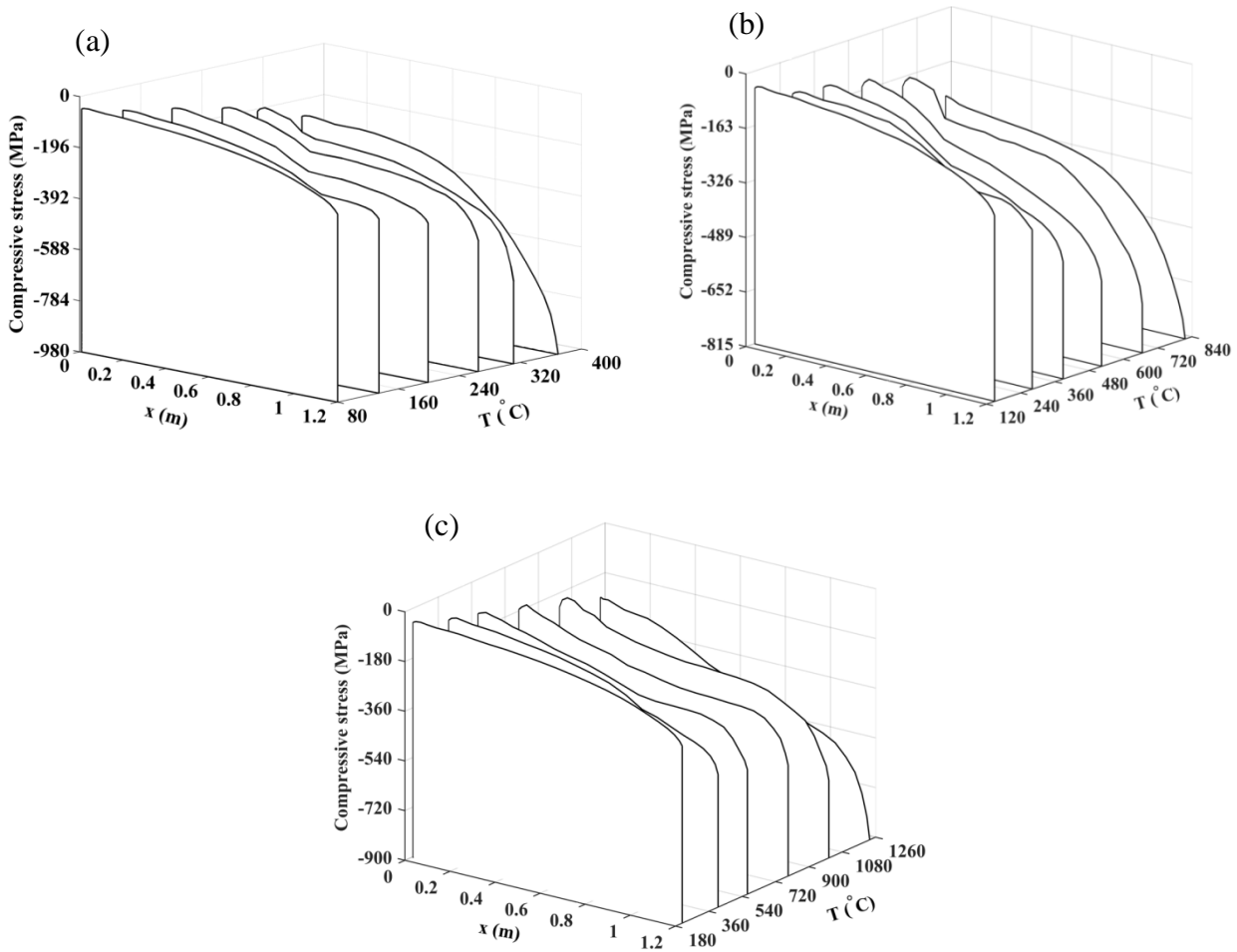


**Figure 5.35.** Waterfall plot of stress fields at different temperatures for FGM taper bar of  $A_R = 0.1$  and  $S_R = 20$ , for multilinear material model under (a) uniform, (b) linearly decreasing and (c) parabolically decreasing temperatures.

The yield front locations with temperatures are presented in Figures 5.36(a)-(c) for multilinear material behaviour which depicted their change with the corresponding plot for bilinear material model. These figures showed that the elastic limit temperature ( $T_y$ ) remain same for both bilinear and multilinear material models. However, there is an increase in plastic collapse temperature ( $T_c$ ) for multilinear model for all cases of temperature field distributions. There is not significant difference in yield front locations for uniform temperature distribution at lower temperatures for both the material models. However, the difference is prominent in yield front locations for linear and parabolic temperature field distributions.



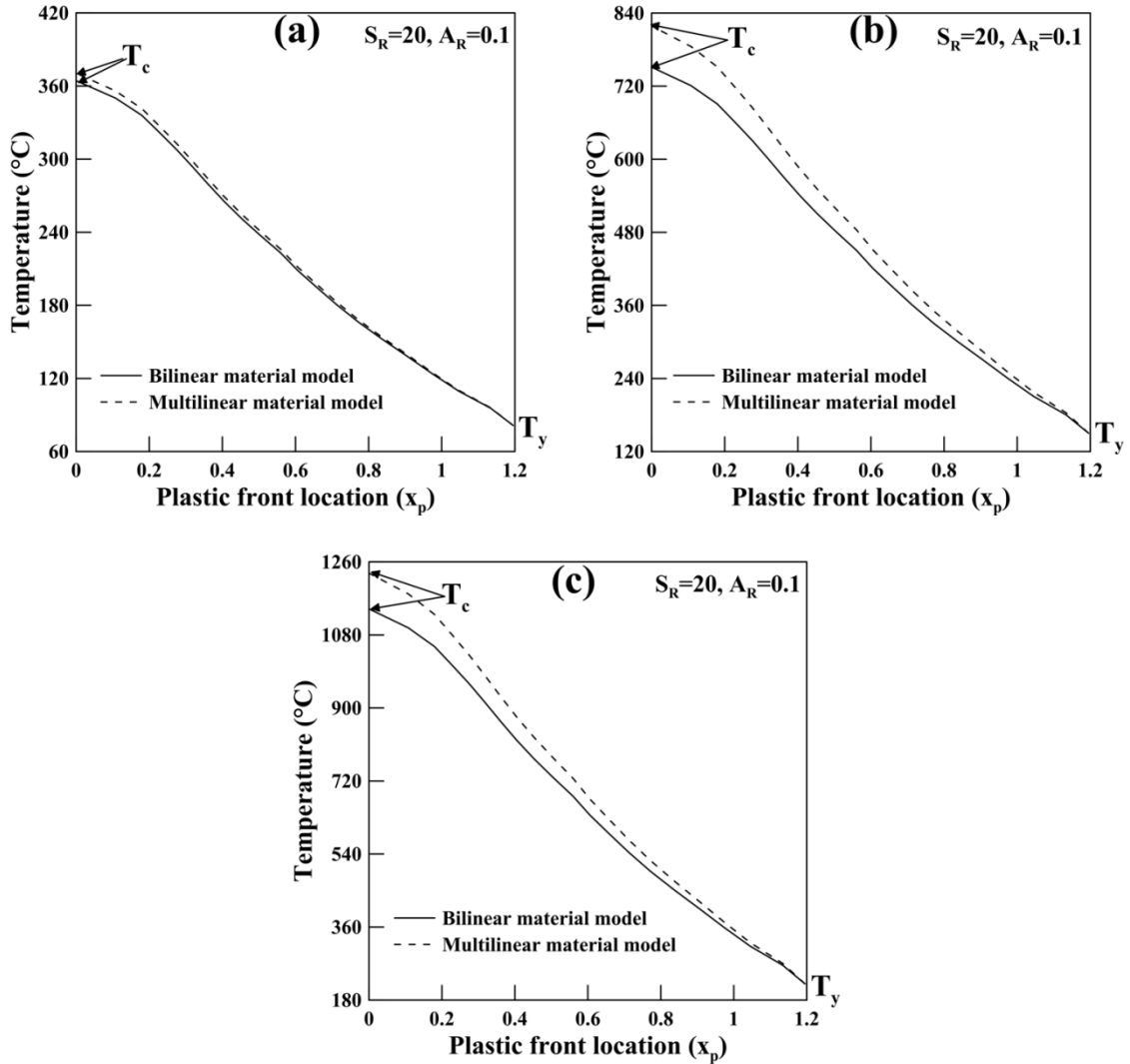


**Figure 5.36.** Plot of propagation of yield front location with increase in temperature for FGM taper bar of  $A_R = 0.1$  and  $S_R = 20$ , for both the material models under (a) uniform, (b) linearly decreasing and (c) parabolically decreasing temperatures.

## 5.4 Summary

The chapter presents the yield front propagation of thermo-mechanically loaded clamped-clamped isotropic and functionally graded bars. The problem is formulated through the extension of minimum potential energy principle in Hencky's deformation theory using von-Mises yield criterion and for both bilinear and multilinear material models. The results obtained by the proposed methodology are validated successfully with that of finite element analysis software

Abaqus CAE for a clamped linear taper bar under uniform temperature field. Some new results are presented which indicates that the yield front propagation of clamped-clamped bar with various temperature distributions are affected significantly by the variations in aspect ratio and slenderness ratio. The variation in stress fields with increase in temperature has been presented through waterfall plots and from the projection of these plots, growth in yield front is captured. Effect of temperature on yield stress is considered for isotropic bars and from the waterfall plots of stress field, it is observed that there is decrease in elastic limit and plastic collapse temperatures. Various results are presented to show the effects of material parameters  $V_{c0}$  and  $n$  on FGM bars and it is observed that increase in ceramic content in a ceramic-metal FGM bar improves the limit temperatures. The results are also presented for the stress fields through waterfall plots and growth of plastic fronts for FGM taper and parabolic bar geometries under different types of temperature distributions and it is observed for all the cases that for parabolic temperature variation, the yield and collapse temperature are higher.

## **ELASTOPLASTIC ANALYSIS OF THERMO-MECHANICALLY LOADED FGM DISKS**

### **6.1 Introduction and literature review**

Functionally graded materials (FGMs) with spatially varying properties are mainly constructed to work in high temperature environments that find their application in turbine rotors, flywheels, gears and in aerospace industries which operate under complex thermal and mechanical loading conditions. In the past two decades, there have been many works relating to the studies on FGM disks. In particular, various numerical and analytical investigations have been extensively used by several researchers to predict the elastic and thermo-elastic analysis of functionally graded disks under different loading conditions (Bayat et al. (2009), Kordkheili and Naghdabadi (2007), Afsar and Go (2010) and Peng and Li (2010)). However, optimizing the design of a rotating disk and understanding its behavior in the elasto-plastic regime provides a better insight towards effective usage of the disk material.

The necessity of post-elastic analysis of mechanical structures arises from demand of complete use of strength resources of bodies and leads to a progressive method of calculating the load bearing ability of machines and structures. The economic value of the use of processes involving plastic deformation of metals in hot and cold conditions is well known and as a result the analysis of forces necessary to accomplish these processes constitutes an important area for the application of plasticity theory. The problem of stresses in rotating disks is important in practical engineering applications to rotating machinery, such as turbines and generators, and wherever large rotational speeds and temperatures are involved. The phenomenon of the elastic-plastic state in the rotating disks is exhibited corresponds to a load exceeding the required critical load to produce initial yielding condition in the material. For a designer, apart from the limit elastic load of the rotating disks, another important parameter is the fully plastic load at which the entire disk has undergone yielding.

Nowadays the use of FGMs are extending, new methodologies need to be developed to characterize, analyze and design structural components made of these materials. The main reason for using FGM rotating disks is their reduced weight and material consumptions which may result in the fabrication of high rotational speed disks as reported in many papers. The non-

linearity associated with the study of stresses in elastic-plastic regimes is an important aspect as the analysis requires advanced and efficient computational techniques, developed during the last two decades. A very brief account of the research work related to the elasto-plastic analysis of thermo-mechanically loaded FGM disks is mentioned here. The theoretical investigation of elastic-plastic behaviour of rotating disks subject to various end conditions has been treated at great length in standard textbooks (Kachanov (1971), Hill (1950), Timoshenko (1930) and Chakrabarty (1987)). For the elasto-plastic analysis of disks, the Tresca yield criterion in conjunction with its associated flow rule presented simple and easy analytical solution to the stresses and strains in rotating disks under plane stress conditions (Gamer (1984), Eraslan and Orcan (2002) and Eraslan (2003)). Based on von Mises yield criterion, You et al. (2000) developed a unified numerical method based on polynomial stress strain relationship and deformation theory of plasticity for the analysis of elasto-plastic rotating disk of varying thickness. Bhowmick et al. (2010) performed a variational formulation based on von Mises yield criterion and linear strain hardening material behaviour to locate the growth of yield front in rotating disks.

Jahromi et al. (2012) provided an analytical method for evaluating the elasto-plastic stresses in a functionally graded rotating disk with varying elastic and plastic properties in the radial direction. The effect of different metal-ceramic grading patterns as well as the relative elastic moduli and densities of the ceramic and metallic constituents on the developed stresses were studied. Hassani et al. (2012) presented semi-exact method of Liao's homotopy analysis method (HAM) and finite element method (FEM) to obtain the stress and strain components of functionally graded elastic-strain hardening rotating disks with non-uniform thickness and material properties subjected to thermo-elasto-plastic loading. Farimani and Toussi (2013) studied the effect of volume fraction distribution on the plastic radius and limit speed in FG disks subjected to centrifugal and isothermal loadings. The variable material property theory was used for the determination of stress and deformation fields. Callioglu et al. (2015) studied the elasto-plastic stress of functionally graded rotating disks by using analytical and numerical methods. The yielding behaviour of the disk material is supposed to be non-work hardening using von-Mises yield condition. In another study, Demir et al. (2017) analyzed the elasto-plastic stresses of functionally graded hyperbolic disks subjected to uniform temperature. Mahdavi et al. (2016) presented thermo-mechanical analysis of elasto-plastic FG disk with variable thickness by using

variable material property theory. The authors investigated the effect of the boundary conditions, temperature gradient, and thickness profile on the stress behavior of disk by the VMP method.

In the present study, the elasto-plastic analysis of FG disks has been proposed by a numerical method based on variational principle. The material of the FG disk is considered to be metal-ceramic composite with a continuous variation of volume fraction of metal and ceramic along the radial direction. The solution of the unknown displacement field from the governing equation is achieved in an iterative manner based on von-Mises yield criterion and Hencky's deformation theory of plasticity by assuming elastic linear strain hardening material behaviour. The results obtained from the present mathematical model are validated with those of other researchers for appropriate values of system parameters and good agreement is obtained. Furthermore, some numerical results of the elasto-plastic field problem under thermo-mechanical loading are presented showing the effect of variation of material properties on rotating FG disks having various geometries and temperature distributions. The results depicting the initiation of yield front and its growth with increase in rotational speed and temperature are also furnished in the present study.

## **6.2 Mathematical formulation**

Post-elastic study of a thermo-mechanically loaded functionally graded rotating disk having inner radius,  $a$  and outer radius,  $b$  is considered. The symmetry of the loading, geometry and boundary condition of the problem makes the analysis axisymmetric. The disk rotates at an angular velocity  $\omega$  and simultaneously is subjected to thermal loading, thus producing radial and tangential strain field coming from both the effects. At a certain speed, the maximum value of stress field of the disk exceeds the yield limit value giving rise to yield initiation corresponding to the relevant temperature. The particular speed is termed as elastic limit speed  $\omega_{IT}$  and the corresponding location of the maximum stress point is termed as yield front location  $(r_y)^\omega$ . Similarly, at a given rotational speed, if temperature of the disk is increased, the induced stress will exceed yield limit at a particular temperature known as yield limit temperature  $T_{I\omega}$  corresponding to that rotational speed and the associated yield front location is designated by  $(r_y)^T$ . Analysis of these two types of limit loads is considered for FGM disks.

### 6.2.1 Material properties determination for FGM

A functionally graded disk composed of ceramic and metal constituents is considered in this section. In a ceramic-metal disk, the ceramic reinforcement particles are distributed in the metal matrix of the compound. For FGM modeling, a continuous variation of volume fraction of metal and ceramic along the radial direction is assumed while in the axial direction it is assumed to be constant. The continuous variation of volume fraction of ceramic reinforcement along the radial direction is given by the power law distributions (Farimani and Toussi (2013))

$$V_c(r) = V_{c0} \left( \frac{r-a}{b-a} \right)^n \quad (6.1a)$$

and

$$V_c + V_m = 1. \quad (6.1b)$$

In Eq. (6.1),  $V$  denotes the volume fraction with subscripts  $c$  and  $m$ , which corresponds to the ceramic and metallic constituents.  $V_{c0}$  is the ceramic volume fraction in the outer radius and  $n$  is the power exponent. In this model,  $V_{c0} = 0$  represents a pure metallic disk and  $n = 0$  signifies a uniform distribution of ceramic phase in the disk. For  $V_{c0} = 1$ , the inner and outer radii of the disk comprises of purely metal and purely ceramic parts, respectively.

In the present analysis, FGM disks are also analysed in the post-elastic regime of the FGM material. Linear hardening model is assumed for the metal matrix with elastic modulus  $E_m$ , tangent modulus  $E_{lm}$  and yield stress  $\sigma_{ym}$ , whereas the ceramic is assumed to have linear elastic behaviour althrough with elastic modulus,  $E_c$  as shown in Figure 5.25 of the preceding chapter 5.

For elasto-plastic modelling of FGMs, Tamura et al. (1973) defined the rule of mixtures for metallic constituents and it is named TTO model. The model was extended by Bocciarelli (2008) for metal ceramic compound in which the material flow of FGMs is assumed to be induced by plastic deformation of ductile metallic constituents. According to Nakamura et al. (2000), the elasto-plastic material properties of FGMs can be calculated using the modified rule of mixtures  $P_{FGM} = P_m V_m + P_c V_c$ ,  $V_c + V_m = 1$  where  $P_c$  and  $P_m$  are the material properties of the ceramic and metal constituents respectively. The post-elastic behaviour of FGM is obtained by

introducing the ratio of stress to strain transfer parameter  $q(= \tilde{q}E_c)$  where,  $\tilde{q}$  is the stress transfer parameter  $\tilde{q}(\geq 0)$ . It should be noted  $\tilde{q} = 0$  represents that FGMs flow plastically once the metallic constituents reach their yield limit. Generally, the parameter  $q$  depends on several factors (e.g. mechanical characteristics of each constituent, material microstructure and loading condition, etc.). However,  $q$  is assumed constant in most applications even beyond the elastic range due to lack of experimental data. The material properties of the metal-ceramic composite disk at radius  $r$  is given by

$$E(r) = \left[ V_m E_m \left( \frac{q + E_c}{q + E_m} \right) + V_c E_c \right] / \left[ V_m \left( \frac{q + E_c}{q + E_m} \right) + V_c \right] \quad (6.2a)$$

$$\sigma_y(r) = \sigma_{ym} \left[ V_m + \left( \frac{q + E_m}{q + E_c} \right) \frac{E_c}{E_m} V_c \right] \quad (6.2b)$$

$$E_t(r) = \left[ V_m E_{tm} \left( \frac{q + E_c}{q + E_{tm}} \right) + V_c E_c \right] / \left[ V_m \left( \frac{q + E_c}{q + E_{tm}} \right) + V_c \right] \quad (6.2c)$$

where  $E(r)$  is elastic modulus,  $\sigma_y(r)$  is the overall yield stress and  $E_t(r)$  is the tangent modulus of the FGM disk as shown in Figure 5.25 of the previous chapter 5.

To determine the density  $\rho(r)$  and the coefficient of thermal expansion  $\alpha(r)$  of FGM disks, modified rule of mixture are used as provided below.

$$\rho(r) = \rho_m V_m + \rho_c V_c \quad (6.2d)$$

$$\alpha(r) = \alpha_m V_m + \alpha_c V_c \quad (6.2e)$$

As before, the subscripts  $m$  and  $c$  in Eqs. (6.2d) and (6.2e) stand for metallic and ceramic parts, respectively. In this analysis, the Poisson's ratios are assumed to be constant for both the phases (metal and ceramic) and an overall value is considered throughout the FGM. However, when the disk is in post-elastic state,  $\nu$  and  $\nu_p$  are Poisson's ratios in elastic and plastic regions respectively.

The FGM disk is considered to be locally isotropic and yields following von-Mises criterion. The TTO model in conjunction with Hencky's deformation theory of plasticity is used to describe the mechanical behavior of FGM disk beyond the elastic limit.

## 6.2.2 Formulation of the thermo-mechanical problem

In the presence of temperature field  $T(r)$ , the analysis of plastic behaviour of a FGM disk becomes more complicated due to additional material parameters. The additional parameters considered in the present work include the elastic modulus, the tangent modulus and the yield stress. The parameter values at a particular radius are now evaluated corresponding to the temperature at that location. It is assumed that the temperature rise is not permanent so that effect of creep can be neglected. Further, the analysis is carried out based on the assumptions that the relative volumetric change induced by variable temperature field  $T$  is elastic in the entire regime of deformation and is given by the expression  $\varepsilon = 3k\sigma + 3\alpha T$  where  $k(= (1 - 2\nu)/E)$  is the coefficient of volumetric compression,  $\sigma$  is the mean stress and  $\alpha$  is the coefficient of thermal expansion. It is assumed that the stress and strain deviatorics are coaxial and their principal values are proportional i.e.,  $e_{ij} = \psi s_{ij}$ , where  $\psi$  is a scalar. As deviatoric strains do not produce any change in volume, it is obvious that the components of strain deviatoric  $e_{ij}$  do not involve thermal expansions. Hence using total deformation theory of plasticity, the total strain can be expressed as

$$\varepsilon_{ij} = \frac{\varepsilon}{3} \delta_{ij} + e_{ij} = k\sigma \delta_{ij} + \alpha T \delta_{ij} + \psi s_{ij}. \quad (6.3)$$

Under thermo-mechanical loading, radial displacements will occur in a disk due to the centrifugal load as well as due to the thermal load. The magnitude of this displacement field is also governed by the boundary conditions of the disk. It is assumed that the disk is symmetric with respect to the mid-plane, and a state of plane stress ( $\sigma_z = 0$ ) persists in the loaded disk. The solution for the displacement field is obtained from the application of minimum potential energy principle ( $\delta(U+V)=0$ ) in Hencky's total deformation theory.  $U$  is the strain energy stored in the disk in form of increment in work of deformation and  $V$  is the potential energy developed from both the centrifugal and thermal load. For axisymmetric problems, the relations between strain components and radial displacement are given by  $\varepsilon_r = du(r)/dr$  and  $\varepsilon_\theta = u(r)/r$ , where  $u(r)$  is the radial displacement. As the disk remains axisymmetric, the shear deformation is not



taken into consideration in the present analysis. It should be noted that  $\varepsilon_z = -\frac{\nu}{(1-\nu)}(\varepsilon_r + \varepsilon_\theta)$

does not produce any work as  $\sigma_z = 0$ .

The expression of total potential energy under elastic conditions can be reduced to an identical expression given by Eq. (4.13) in section 4.2.4.1 of the thesis and is given by,

$$\begin{aligned} \Pi = 2\pi \int_a^b & \left[ \left( \frac{K}{2} \left( \frac{1-2\nu}{1-\nu} \right)^2 + \frac{2G}{3} \frac{(1+\nu^2-\nu)}{(1-\nu)^2} \right) \left( \frac{u^2}{r^2} + \left( \frac{du}{dr} \right)^2 \right) \right. \\ & \left. + \left( K \left( \frac{1-2\nu}{1-\nu} \right)^2 + \frac{2G}{3} \frac{(-1-\nu^2+4\nu)}{(1-\nu)^2} \right) \frac{u}{r} \frac{du}{dr} \right] \\ & - \rho\omega^2 ru - 3K\alpha T \left( \frac{1-2\nu}{1-\nu} \right) \left( \frac{u}{r} + \frac{du}{dr} \right) \Big] h r dr. \end{aligned} \quad (6.4)$$

Here, the total potential energy  $\Pi$  is decomposed into two parts in which one part is similar to the strain energy  $U$  stored in the disk coming from the associated stress field and the other part is work function due to centrifugal and thermal loading. The first part of potential energy  $V_{\text{centrifugal}}$  comes from centrifugal force field, while the second part  $V_{\text{thermal}}$ , comes from the thermal load. The expressions for  $U$ ,  $V_{\text{centrifugal}}$  and  $V_{\text{thermal}}$  are given below.

$$U = 2\pi \int_a^b \left\{ \left( \frac{K}{2} \left( \frac{1-2\nu}{1-\nu} \right)^2 + \frac{2G}{3} \frac{(1+\nu^2-\nu)}{(1-\nu)^2} \right) \left( \frac{u^2}{r^2} + \left( \frac{du}{dr} \right)^2 \right) + \left( K \left( \frac{1-2\nu}{1-\nu} \right)^2 + \frac{2G}{3} \frac{(-1-\nu^2+4\nu)}{(1-\nu)^2} \right) \frac{u}{r} \frac{du}{dr} \right\} h r dr \quad (6.5)$$

$$V_{\text{centrifugal}} = -2\pi\omega^2 \int_a^b \rho u r^2 h dr \quad (6.6)$$

$$V_{\text{thermal}} = -2\pi \int_a^b 3K\alpha T \left( \frac{1-2\nu}{1-\nu} \right) \left( \frac{u}{r} + \frac{du}{dr} \right) h r dr \quad (6.7)$$

So, the expression for potential energy  $V$  under combined loading becomes,

$$V = -2\pi\omega^2 \int_a^b \rho u r^2 h dr - 2\pi \int_a^b 3K\alpha T \left( \frac{1-2\nu}{1-\nu} \right) \left( \frac{u}{r} + \frac{du}{dr} \right) h r dr. \quad (6.8)$$

### 6.2.3 Total PE in post elastic state of FGM

The von-Mises theory is taken as the failure criteria and in the present analysis von-Mises stress is determined from the relation  $\sigma_{vm}^2 = \sigma_r^2 - \sigma_r \sigma_\theta + \sigma_\theta^2$ . The stress components  $\sigma_r$  and  $\sigma_\theta$  for a given thermo-mechanical loading are obtained from the post processing of displacement field  $u(r)$ , which becomes known from the solution of Eq. (6.4).

Whenever the von-Mises stress at a particular radial location of a thermally loaded rotating disk reaches the uniaxial yield stress value, the plastic front initiates at that location and the rotational speed corresponding to the relevant temperature is termed as elastic limit speed  $\omega_{IT}$ . On further increase in rotational speed, a certain region of the disk attains post-elastic state and when this region encompasses the entire disk we get plastic limit speed or collapse speed ( $\omega_{2T}$ ). Similarly, the entire disk will undergo yielding with increase in temperature corresponding to a given rotational speed and it is termed as collapse temperature ( $T_{2\omega}$ ). For a uniform thickness disk, initiation of yielding occurs at the inner radius, but for typical disk geometries it may occur at any radius (Bhowmick et al. (2010)).

However, the geometry and loading conditions of the present FG disk is considered to be such that yielding initiates at the root of the disk corresponding to the particular value of elastic limit speed  $\omega_{IT}$  or yield limit temperature  $T_{I\omega}$ . Hence in the present analysis,  $(r_y)^\omega = (r_y)^T = a$ . With further increase in rotational speed or temperature, the plastic front gradually proceeds towards the disk periphery.

The domain of the disk beyond elastic limit state gets divided into two regions, an inner plastic region ( $r = a$  to  $r = r_y$ ) and an outer elastic region ( $r = r_y$  to  $r = b$ ). Hence in the post elastic state the total strain energy  $U$  consists of an elastic ( $U_e$ ) and a plastic ( $U_p$ ) part. The interface between the outer elastic and the inner post elastic region is demarcated by the radius  $r = r_y$ .

Expression of strain energy in the elastic part for the outer region is given by,

$$U_e = 2\pi \int_{r_y}^b \left\{ \left( \frac{K}{2} \left( \frac{1-2\nu}{1-\nu} \right)^2 + \frac{2G}{3} \frac{(1+\nu^2-\nu)}{(1-\nu)^2} \right) \left( \frac{u^2}{r^2} + \left( \frac{du}{dr} \right)^2 \right) + \left( K \left( \frac{1-2\nu}{1-\nu} \right)^2 + \frac{2G}{3} \frac{(-1-\nu^2+4\nu)}{(1-\nu)^2} \right) \frac{u}{r} \frac{du}{dr} \right\} hrdr \quad (6.9)$$

and the strain energy for the inner post-elastic region is obtained from the expression

$$U_p = 2\pi \int_a^{r_y} \left\{ \left( \frac{K}{2} \left( \frac{1-2\nu}{1-\nu} \right)^2 + \frac{2g(\Gamma)}{3} \frac{(1+\nu_p^2-\nu_p)}{(1-\nu_p)^2} \right) \left( \frac{u^2}{r^2} + \left( \frac{du}{dr} \right)^2 \right) + \left( K \left( \frac{1-2\nu}{1-\nu} \right)^2 + \frac{2g(\Gamma)}{3} \frac{(-1-\nu_p^2+4\nu_p)}{(1-\nu_p)^2} \right) \frac{u}{r} \frac{du}{dr} \right\} hrdr, \quad (6.10)$$

where  $g(\Gamma)$  is the modulus of plasticity and  $\nu_p$  is the Poisson's ratio in post-elastic region.

Substituting Eqs. (6.8)-(6.10) in the energy principle  $\delta(U+V)=0$ , the governing equilibrium equation becomes

$$\delta \left[ \begin{aligned} & 2\pi \int_a^{r_y} \left\{ \left( \frac{K}{2} \left( \frac{1-2\nu}{1-\nu} \right)^2 + \frac{2g(\Gamma)}{3} \frac{(1+\nu_p^2-\nu_p)}{(1-\nu_p)^2} \right) \left( \frac{u^2}{r^2} + \left( \frac{du}{dr} \right)^2 \right) + \left( K \left( \frac{1-2\nu}{1-\nu} \right)^2 + \frac{2g(\Gamma)}{3} \frac{(-1-\nu_p^2+4\nu_p)}{(1-\nu_p)^2} \right) \frac{u}{r} \frac{du}{dr} \right\} hrdr \\ & + 2\pi \int_{r_y}^b \left\{ \left( \frac{K}{2} \left( \frac{1-2\nu}{1-\nu} \right)^2 + \frac{2G}{3} \frac{(1+\nu^2-\nu)}{(1-\nu)^2} \right) \left( \frac{u^2}{r^2} + \left( \frac{du}{dr} \right)^2 \right) + \left( K \left( \frac{1-2\nu}{1-\nu} \right)^2 + \frac{2G}{3} \frac{(-1-\nu^2+4\nu)}{(1-\nu)^2} \right) \frac{u}{r} \frac{du}{dr} \right\} hrdr \\ & - 2\pi \omega^2 \int_a^b \rho ur^2 h dr \\ & - 2\pi \int_a^b 3K\alpha T \left( \frac{1-2\nu}{1-\nu} \right) \left( \frac{u}{r} + \frac{du}{dr} \right) hrdr \end{aligned} \right] = 0. \quad (6.11)$$

The normalized parameters are denoted by  $\xi$ ,  $\xi^p$  and  $\xi^e$  in total, post-elastic and elastic regions, respectively and they are framed by  $\xi = (r-a)/(b-a)$ ,  $\xi^p = (r-a)/(r_y-a)$  and  $\xi^e = (r-r_y)/(b-r_y)$ , where  $\bar{r} = b-a$ ,  $\bar{r}_1 = r_y-a$  and  $\bar{r}_2 = b-r_y$ . To facilitate the

numerical computation, Eq. (6.11) is expressed in specific normalized co-ordinates, and the governing equation takes the form,

$$\delta \left[ \begin{array}{l} 2 \int_0^1 \left\{ \left( \frac{K}{2} \left( \frac{1-2\nu}{1-\nu} \right)^2 + \frac{2g(\Gamma)(1+\nu_p^2-\nu_p)}{3(1-\nu_p)^2} \right) \left( \frac{-u^2}{r_1(\bar{r}_1\xi^p+a)} + \frac{(\bar{r}_1\xi^p+a)}{r_1} \left( \frac{du}{d\xi^p} \right)^2 \right) \right\} hd\xi^p \\ + \left( K \left( \frac{1-2\nu}{1-\nu} \right)^2 + \frac{2g(\Gamma)(-1-\nu_p^2+4\nu_p)}{3(1-\nu_p)^2} \right) u \frac{du}{d\xi^p} \\ \left( \frac{K}{2} \left( \frac{1-2\nu}{1-\nu} \right)^2 + \frac{2G}{3} \frac{(1+\nu^2-\nu)}{(1-\nu)^2} \right) \left( \frac{-u^2}{r_2(\bar{r}_2\xi^e+r_y)} + \frac{(\bar{r}_2\xi^e+r_y)}{r_2} \left( \frac{du}{d\xi^e} \right)^2 \right) \right\} hd\xi^e \\ + \left( K \left( \frac{1-2\nu}{1-\nu} \right)^2 + \frac{2G}{3} \frac{(-1-\nu^2+4\nu)}{(1-\nu)^2} \right) u \frac{du}{d\xi^e} \\ - 2\omega^2 \bar{r} \int_0^1 \rho u (\bar{r}\xi + a)^2 hd\xi \\ - 2\bar{r} \int_0^1 3K\alpha T \left( \frac{1-2\nu}{1-\nu} \right) \left( \frac{u}{(\bar{r}\xi+a)} + \frac{du}{rd\xi} \right) (\bar{r}\xi + a) hd\xi \end{array} \right] = 0. \quad (6.12)$$

The displacement function  $u(\xi)$  in Eq. (6.12) is approximated by a linear combination of sets of orthogonal coordinate functions as  $u(\xi) = \sum c_i \phi_i$ ,  $i = 1, 2, \dots, n_f$ , where  $\phi_i$  is the set of  $n_f$  number of orthogonal functions developed through Gram–Schmidt scheme and  $c_i$  is the set of unknown coefficients. The necessary start function  $\phi_0$  which satisfies the boundary conditions of the annular disk, i.e.,  $\sigma_r|_{(a)} = 0$  and  $\sigma_r|_{(b)} = 0$  is given by

$$\phi_0(r) = \frac{\rho\omega^2 r(3+\nu)}{8E} \left[ (b^2 + a^2)(1-\nu) - \left\{ \frac{(1-\nu^2)r^2}{(3+\nu)} \right\} + b^2 a^2 \frac{(1+\nu)}{r^2} \right] + \frac{\alpha}{r} \left[ (1+\nu) \int_a^r T(r) r dr + \frac{(1-\nu^2)r^2 + (1+\nu)a^2}{b^2 - a^2} \int_a^b T(r) r dr \right]. \quad (6.13)$$

For the purpose of computation, displacement functions in the elastic and post-elastic regions are expressed as  $u(\xi^e) \cong \sum c_i \phi_i^e$  and  $u(\xi^p) \cong \sum c_i \phi_i^p$  respectively. Substituting these assumed displacement functions and replacing operator  $\delta$  by  $\partial/\partial c_j$ ,  $j = 1, 2, \dots, n$ , according to Galerkin error minimization principle, we obtain the governing differential equation in matrix form

$$\begin{aligned}
 & \left[ \sum_{i=1}^n \sum_{j=1}^n c_i \int_0^1 \left\{ \begin{aligned} & 2 \left( \frac{K(1-2\nu)}{2} \frac{(1-2\nu)^2}{(1-\nu)} + \frac{2g(\Gamma)(1+\nu_p^2-\nu_p)}{3(1-\nu_p)^2} \right) \left( \frac{\phi_i^p \phi_j^p}{r_1(\bar{r}_1 \xi^p + a)} + \frac{(\bar{r}_1 \xi^p + a)}{r_1} (\phi_i^{p'} \phi_j^{p'}) \right) \right. \\ & \left. + \left( K \frac{(1-2\nu)^2}{(1-\nu)} + \frac{2g(\Gamma)(-1-\nu_p^2+4\nu_p)}{3(1-\nu_p)^2} \right) (\phi_i^p \phi_i^{p'} + \phi_i^{p'} \phi_j^p) \right\} hd\xi^p \right] \\
 & + \sum_{i=1}^n \sum_{j=1}^n c_i \int_0^1 \left\{ \begin{aligned} & 2 \left( \frac{K(1-2\nu)}{2} \frac{(1-2\nu)^2}{(1-\nu)} + \frac{2g(\Gamma)(1+\nu^2-\nu)}{3(1-\nu)^2} \right) \left( \frac{\phi_i^e \phi_j^e}{r_2(\bar{r}_2 \xi^e + r_y)} + \frac{(\bar{r}_2 \xi^e + r_y)}{r_2} (\phi_i^{e'} \phi_j^{e'}) \right) \right. \\ & \left. + \left( K \frac{(1-2\nu)^2}{(1-\nu)} + \frac{2g(\Gamma)(-1-\nu^2+4\nu)}{3(1-\nu)^2} \right) (\phi_i^e \phi_i^{e'} + \phi_i^{e'} \phi_j^e) \right\} hd\xi^e \right] \quad (6.14) \\
 & = \omega^2 \bar{r} \sum_{j=10}^n \int_0^1 \{ (\bar{r} \xi + a)^2 \phi_j \} \rho h d\xi + \sum_{j=10}^n \int_0^1 3K\alpha T \left( \frac{1-2\nu}{1-\nu} \right) \{ \phi_j \bar{r} + (\bar{r} \xi + a) \phi_j' \} h d\xi
 \end{aligned}
 \right.
 \end{aligned}$$

where ( ) indicates differentiation with respect to normalized coordinate  $\xi$ . The solution of Eq. (6.14) yields the solution vector  $\{c_i\}$ , obtained numerically through a single step matrix inversion process. The radial displacement field ( $u$ ) can be found out for any prescribed value of rotational speed  $\omega$  and temperature  $T$  from which the strain components of the field are evaluated. From these strains, the effective and shear strains are calculated as available in section 4.2.1 of the thesis. However, the numerical scheme requires some more iterative numerical computations to ascertain the location of yield front, i.e., the elastic-plastic boundary. The modulus of plasticity  $g(\Gamma)$  is set equal to modulus of rigidity  $G$ , at the zeroth approximation, and the problem is solved as an extension of elastic solution. In subsequent approximations the value of  $g(\Gamma)$  is updated until a final convergence on yield front location is achieved, following the iterative scheme of Kachanov (1971). If convergence is achieved then the stress and strain values are finally post-processed, else, the procedure is repeated until convergence is achieved. Once convergence is achieved, the problem is then post-processed and taken to next load step with the updated yield front location.

## 6.2.4 Post-processing

For a converged load step speed above limit elastic speed at a particular temperature, the radial and tangential strains can be calculated from the radial displacement field as stated earlier.

Using the radial and tangential strains the effective and shear strains are calculated. The effective plastic strain is calculated from a relation obtained as given below,

$$\varepsilon_{vm}^p = \varepsilon_{vm} - \frac{2(1+\nu)}{3E} \sigma_{vm}. \quad (6.15)$$

In Eq. (6.15),  $\varepsilon_{vm}^p$  is the effective plastic strain and  $\sigma_{vm}$  is the effective or von-Mises stress. The radial, tangential and axial strains at each coordinate inside the post-elastic region of the disk can be decomposed into elastic and plastic parts as given below

$$\varepsilon_r = \varepsilon_r^e + \varepsilon_r^p + \alpha T \quad (6.16a)$$

$$\varepsilon_\theta = \varepsilon_\theta^e + \varepsilon_\theta^p + \alpha T \quad (6.16b)$$

$$\varepsilon_z = \varepsilon_z^e + \varepsilon_z^p + \alpha T \quad (6.16c)$$

where the superscript ‘e’ and ‘p’ denote the elastic and plastic part of the strains respectively. The relations between stresses and elastic strains can be derived from generalized Hooke’s law. The deformation theory of plasticity is used with the usual assumptions that the directions of the principal strains coincide with the direction of the principal stresses and that the volume remains constant in the plastic range. These assumptions imply (Mendelson and Manson (1957)),

$$\frac{\varepsilon_r - \varepsilon_\theta}{\sigma_r - \sigma_\theta} = \frac{\varepsilon_\theta - \varepsilon_z}{\sigma_\theta - \sigma_z} = \frac{\varepsilon_z - \varepsilon_r}{\sigma_z - \sigma_r} = k_1 \quad (6.17a)$$

$$\frac{\varepsilon_r^p - \varepsilon_\theta^p}{\sigma_r - \sigma_\theta} = \frac{\varepsilon_\theta^p - \varepsilon_z^p}{\sigma_\theta - \sigma_z} = \frac{\varepsilon_z^p - \varepsilon_r^p}{\sigma_z - \sigma_r} = k_2 \quad (6.17b)$$

where  $k_1 = k_2 + \frac{(1+\nu)}{E}$

and  $\varepsilon_r^p + \varepsilon_\theta^p + \varepsilon_z^p = 0$ . (6.17c)

Using Eqs. 6.17(a-c), the plastic part of radial and tangential strain is calculated as

$$\varepsilon_r^p = \frac{1}{3} \frac{\varepsilon_{vm}^p}{\varepsilon_{vm}} (2\varepsilon_r - \varepsilon_\theta - \varepsilon_z) \quad (6.18)$$

$$\varepsilon_{\theta}^p = \frac{1}{3} \frac{\varepsilon_{vm}^p}{\varepsilon_{vm}} (2\varepsilon_{\theta} - \varepsilon_r - \varepsilon_z) \quad (6.19)$$

## 6.3 Results and discussion

The present section performs analysis for functionally graded rotating disks subjected to thermo-mechanical loading. The parameters of the present problem are described first, next some validation studies are carried out and finally results of the present study are furnished.

### 6.3.1 The description of parameters

The geometry of disk, its material properties and the induced temperature field are described in the following sections.

#### 6.3.1.1 Geometrical properties of the disk

The inner and outer radii of the disks are  $a=0.1$  m and  $b=0.6$  m, respectively. Four types of thickness profile  $h$  of the disk are considered: uniform, taper, exponential and parabolic. The thickness is considered to vary radially according to the relations

$$h(\xi) = h_o \exp[-n(\xi)^k] \text{ and} \quad (6.20)$$

$$h(\xi) = h_o [1 - n(\xi)^k] \quad (6.21)$$

following exponential and parabolically thickness variation respectively. In these equations, the non-dimensional radial co-ordinate,  $\xi = (r - a)/\bar{r}$  where  $\bar{r} = (b - a)$ , and  $h_o$  is the root thickness of the disk (i.e. at  $\xi = 0.0$ ). The variation in the geometry is controlled through the parameters  $n$  and  $k$  of Eqs. (6.20) and (6.21) and it may be noted that uniform and taper disks are two special cases of thickness variation. The detail values of the parameters for complete specification of the geometries are indicated in Table 3.1 in chapter 3 of the thesis.

**6.3.1.2 Material properties of the disk**

The material properties of the disks that are used in the analyses are taken from Farimani and Toussi (2013) and provided in Table 6.1. For the FGM disk, the value of Poisson’s ratio  $\nu$  is taken as 0.3 in elastic state and  $\nu_p$  in post-elastic region is taken as 0.5.

**Table 6.1:** Material properties of the FGM disk

	$E$ (GPa)	$\sigma_y$ (MPa)	$\rho$ (kg/m <sup>3</sup> )	$\alpha$ (10 <sup>-6</sup> /°C)	$E_l$ (GPa)	$q$ (GPa)
Metal	208	300	7860	11.5	80	17.2
Ceramic	324	-	5000	7.7	-	

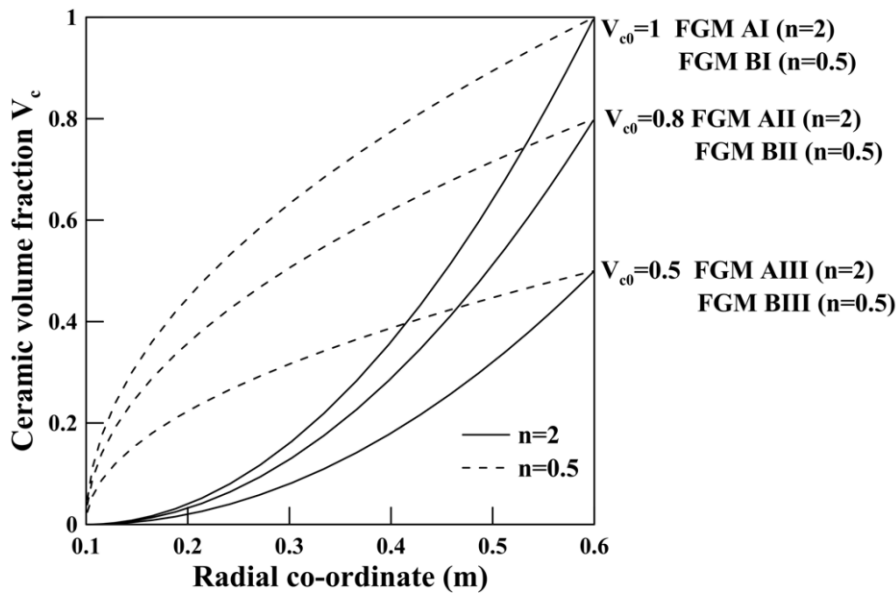


**Figure 6.1.** Plots for ceramic volume fraction  $V_c$  for six materials, FGM AI, FGM BI, FGM AII, FGM BII, FGM AIII and FGM BIII.

In this analysis, the results are presented for three different volume fraction of the ceramic content in the outer radius,  $V_{c0}$ , considering their values as 0.5, 0.8 and 1. The ceramic distribution coefficient,  $n$  is taken as 0.5 and 2. A plot of Eq. (6.1) is presented in Figure 6.1 by considering the different  $n$  and  $V_{c0}$  values for six materials, FGM AI, FGM BI, FGM AII, FGM



BII, FGM AIII and FGM BIII. As the  $V_c$  and  $V_m$  values are functions of radial location, it is obvious from Eqs. (6.2a)-(6.2c), that the material properties of the disks are also functions of radial location. For FGM AI, some sample plots of material properties, considering bilinear material model, are presented in Figures 6.2(a)-(c) at three different locations,  $r=0.2$  m, 0.3m and 0.5m, of the disk.

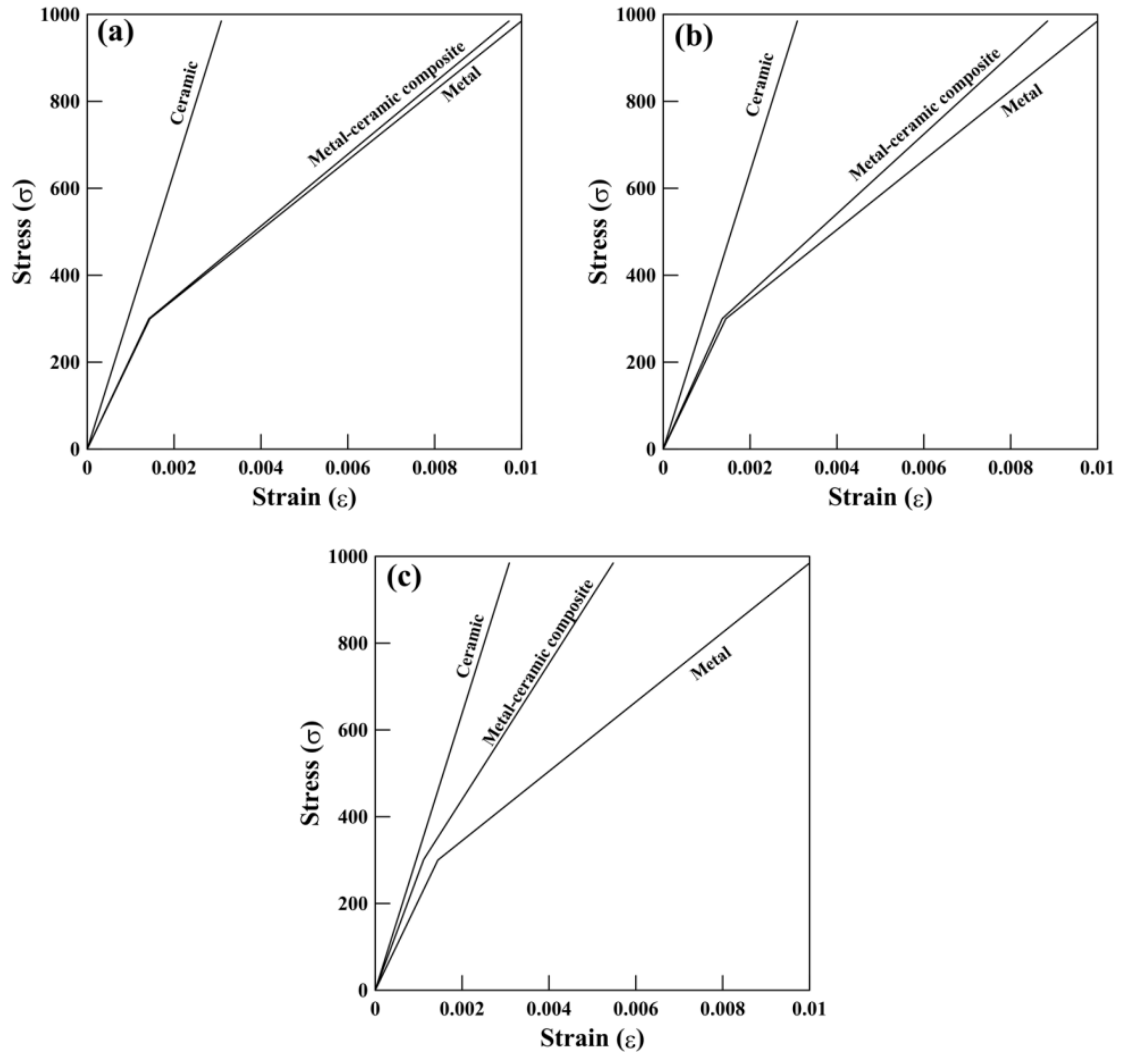


**Figure 6.2.** Stress-strain plots at locations (a)  $r=0.2$ m, (b)  $r=0.3$  m and (c)  $r= 0.5$  m for FGM AI.

The material properties of the FGM disk are given in detail in Table 6.2, indicating the elasticity modulus, tangent modulus and yield stress of the disk. A graphical representation of the

variation of the material properties with radial co-ordinate are shown in Figure 6.3 for six FGM materials.

**Table 6.2:** Material properties of the disk at different normalized co-ordinates for FGM AI

Normalized radial co-ordinate ( $\xi$ )	Elasticity modulus, $E$ (GPa)	Tangent modulus, $E_t$ (GPa)	Yield stress, $\sigma_y$ (MPa)
0.0	208	80	300
0.12	209.27	81.07	300.03
0.22	211.95	83.37	300.12
0.31	217.18	88.06	300.27
0.40	221.03	91.68	300.37
0.53	231.60	102.50	300.65
0.64	246.28	119.97	300.99
0.72	255.12	132.17	301.18
0.82	275.03	165.99	301.56
0.91	295.82	215.03	301.90
0.99	323.14	319.51	302.28

### 6.3.1.3 Effect of temperature on FGM disk

The analysis is carried out for various varying temperature profiles following uniform  $T(\xi) = T_a$ , linear  $T(\xi) = T_a + (T_b - T_a)\xi$ , exponential  $T(\xi) = \frac{(T_a - T_b)\ln(b/\xi)}{\ln(b/a)} + T_b$  and parabolic  $T(\xi) = T_a + (T_b - T_a)\xi^2$  temperature distributions, where  $T_a$  and  $T_b$  are the inner and outer surface temperature of the FGM disk at  $r = a$  and  $r = b$  respectively. A sample plot for temperature variations are shown in Figure 6.4 taking,  $T_a = 100^\circ\text{C}$  and  $T_b = 300^\circ\text{C}$ .

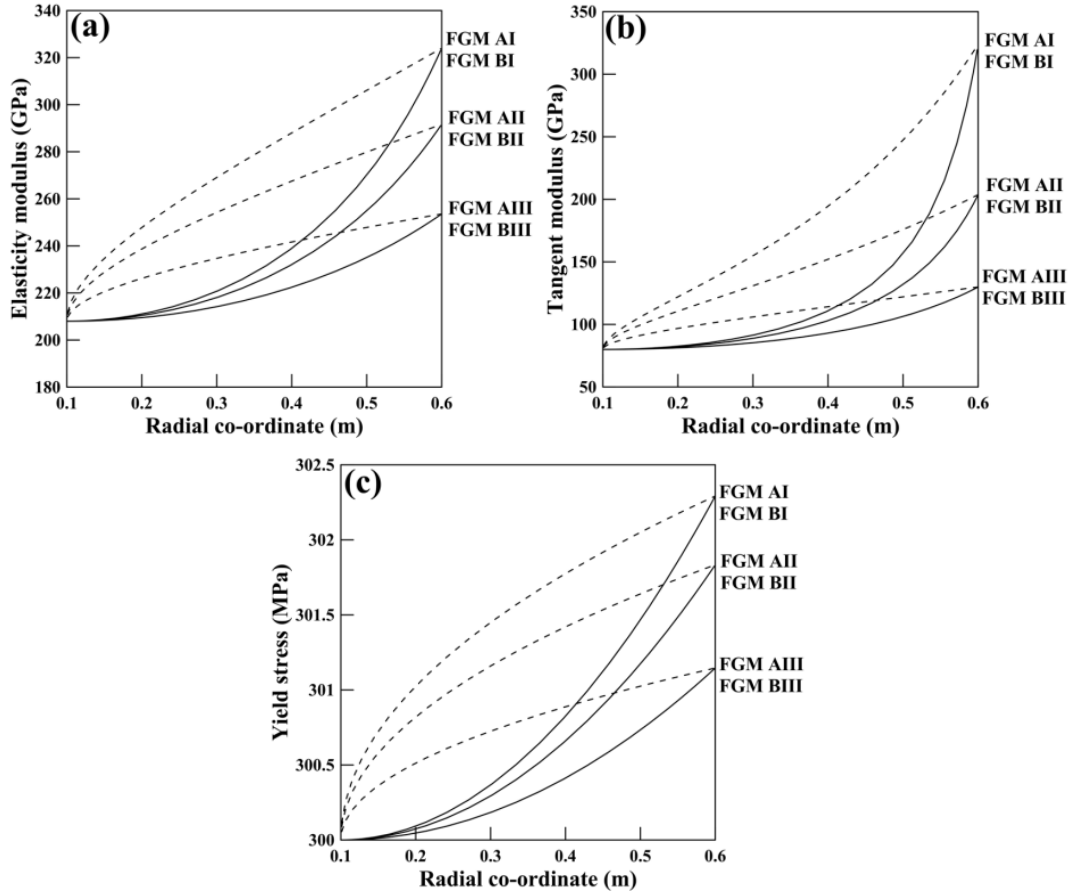


**Figure 6.3.** Variation in material properties of the disk: (a) elasticity modulus, (b) tangent modulus and (c) yield stress.

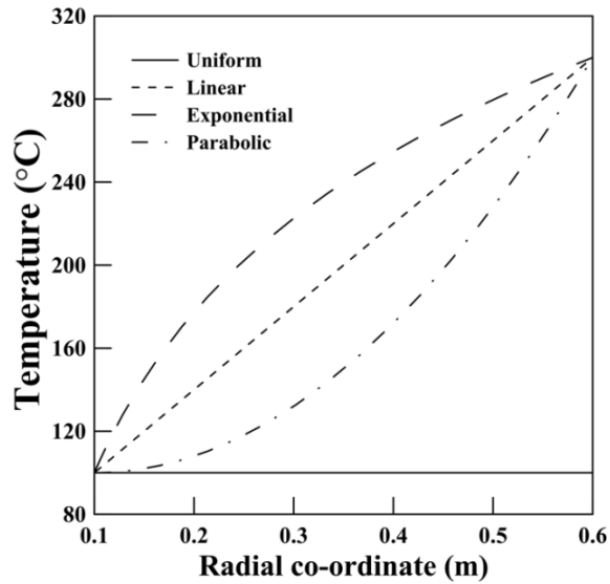


**Figure 6.4.** Plot for temperature variation.

The degradation of normalized yield stress and elasticity modulus with increasing temperature is shown in Figure 6.5 (Seif et al. (2016)), where  $\sigma_{y0} = 300\text{MPa}$  and  $E_0 = 208\text{GPa}$  are the values at the ambient temperature. The effect of temperature on elasticity modulus and yield stress of the metallic part of the disk is considered in the present analysis whereas the value of elasticity modulus at ambient temperature is considered for the ceramic part although.

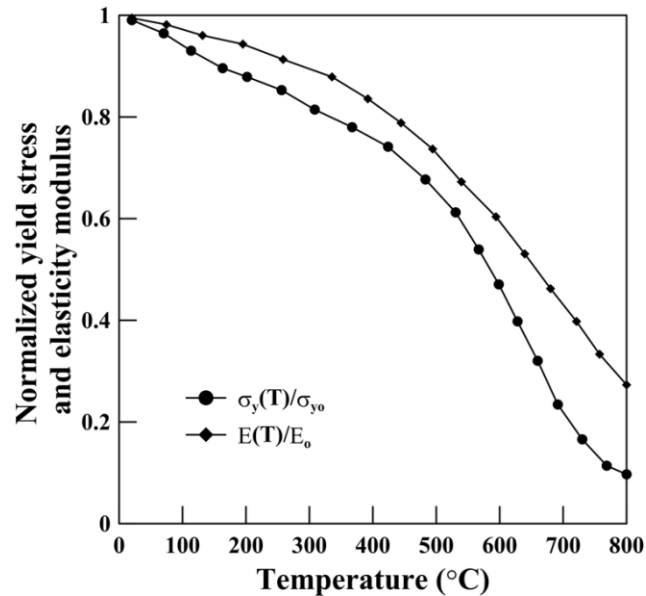


**Figure 6.5.** Normalized yield stress and elasticity modulus variation with temperature for mild steel (Seif et al. (2016)).

### 6.3.2 Validation study

The validation of the present method is carried out for elasto-plastic functionally graded disk without considering thermal load with the result reported by Farimani and Toussi (2013). The material properties of the FG disk along the radial direction used for validation are modelled by using modified rule of mixtures in Eq. (6.1). The inner and outer radii of the disks are  $a=0.1$  m and  $b=0.6$  m. The thickness variation of the FG rotating disk is used for validation in the following form:

$$h(r) = h_o \left( \frac{r}{b} \right)^d \quad (6.22)$$

where  $d = -0.2$ . The plot for plastic limit speed ( $\omega_2$ ) versus ceramic distribution coefficient ( $n$ ) for two different  $V_{c0}$  values has been validated and is presented in Figure 6.6(a) for the disk geometry as shown in Figure 6.6(b). A fairly good agreement is obtained in this case.

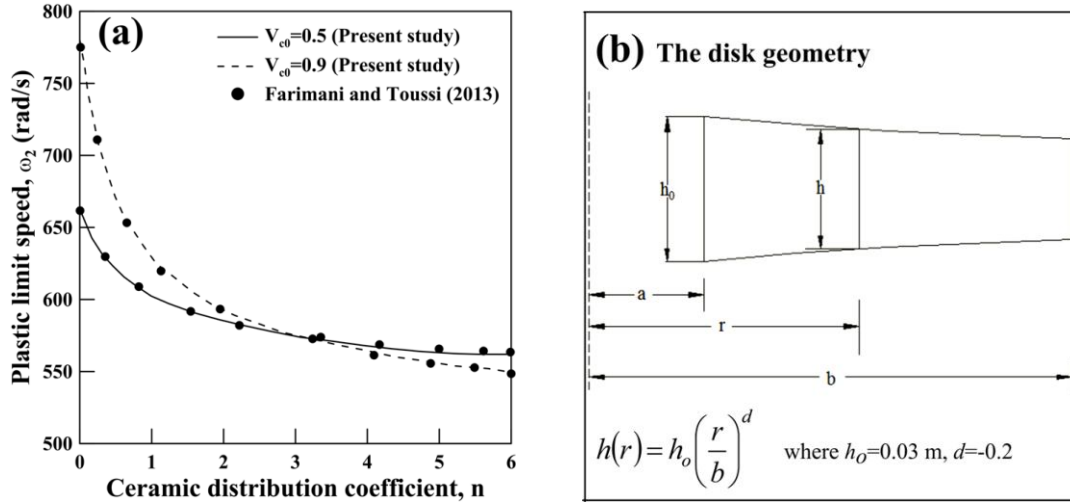


**Figure 6.6.** (a) Plastic limit speed ( $\omega_2$ ) versus ceramic distribution coefficient ( $n$ ) for two different ceramic volume fraction ( $V_{c0}$ ) values, (b) the disk geometry.

A further validation of the present method is also carried out for elasto-plastic functionally graded disks subjected to thermo-mechanical loading with the results of Hassani et al. (2012). The similar modified rule of mixtures, as given in Eq. (6.1), is used. The same thickness variation is used by Hassani et al. (2012) as in Eq. (6.22) with  $d = -0.5$ . The temperature field distribution of the FG rotating disk is used for validation is given by:

$$T(r) = (T_b - T_a) \xi^3 + T_a, \quad (6.23)$$

where  $T_a = 100^\circ\text{C}$  and  $T_b = 300^\circ\text{C}$ . The inner and outer radii of the disks are  $a=0.1$  m and  $b=0.6$  m. The disk is rotating at angular velocity,  $\omega = 535$  rad/s. The plots for radial, tangential and von-Mises presented in Figures 6.7 (a, b) along with the results of Hassani et al. (2012), indicating good validation. The plots for total radial and tangential strains are plotted next in

Figure 6.8. This plot also exhibits very good agreement establishing validity of the present elasto-plastic analysis method. The percent error of the results of the present method and Hassani et al. (2012) are also presented in Table 6.3 for radial, tangential and von-Mises stresses as shown in Figures 6.7.

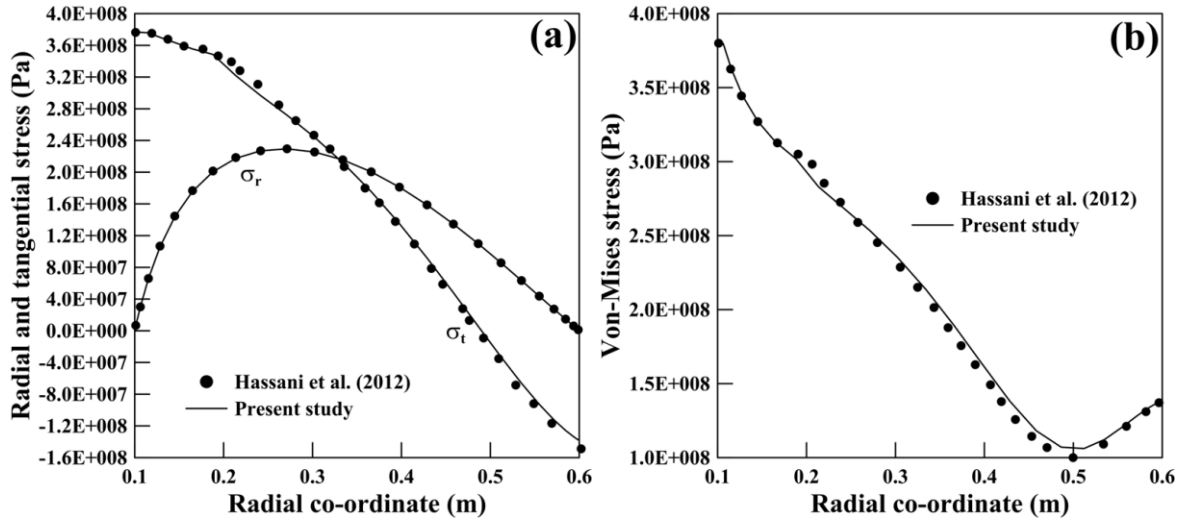


Figure 6.7. Validation of (a) radial and tangential stresses and (b) von-Mises stress.

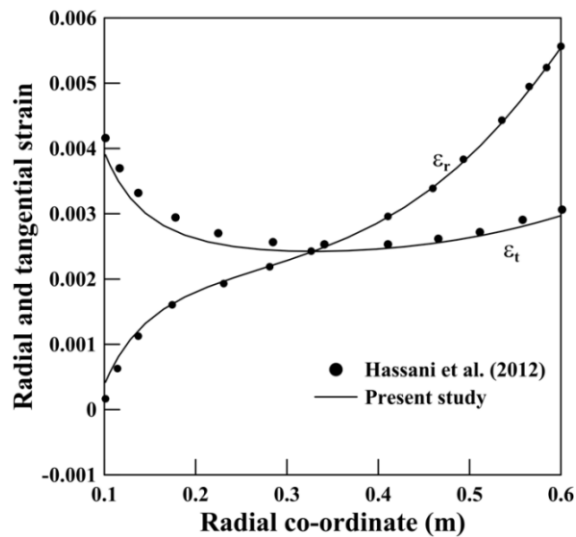


Figure 6.8. Validation of total radial and tangential strains.

**Table 6.3:** Validation of stresses for FG ( $V_{c0}=1$  and  $n=2$ ) disk subjected to thermo-mechanical loading

Radial co-ordinate (m)		0.1	0.2	0.3	0.4	0.5	0.6
$(\sigma_r)$ (MPa)	Present method	-	194.6	227.15	178.43	98.53	-
	Hassani et al. (2012)	-	184	211.54	171.05	93.31	-
	% error	-	5.76	7.38	4.31	5.59	-
$(\sigma_t)$ (MPa)	Present method	377.13	336.25	248.61	129.71	-16.36	-137.13
	Hassani et al. (2012)	372.02	344.96	248.99	131.32	-16.03	-136.56
	% error	1.37	2.52	0.15	1.22	2.05	0.41
$(\sigma_{vm})$ (MPa)	Present method	377.13	292.40	238.60	159.74	109.65	137.13
	Hassani et al. (2012)	372.02	300.01	232.88	155.42	102.01	136.56
	% error	1.37	2.53	2.45	2.78	5.52	0.41

### 6.3.3 Present results

The effect of geometry variation, the volume fraction of the ceramic content in the outer radius ( $V_{c0}$ ), the ceramic distribution coefficient ( $n$ ) and temperature distributions on elastic limit speed ( $\omega_{IT}$ ) and collapse speed ( $\omega_{2T}$ ) of FGM disk are studied and presented in subsequent sections. The yield limit temperature ( $T_{I\omega}$ ) and collapse temperature ( $T_{2\omega}$ ) are also presented for different disk geometries considering linear temperature distribution field, while the disk is rotating at 20%, 40%, 60% and 80% of elastic limit speeds ( $\omega_{IT}$ ). Results are mainly presented for bilinear material model. However, for trilinear material model, results are provided only for linear temperature distribution for different disk geometries.

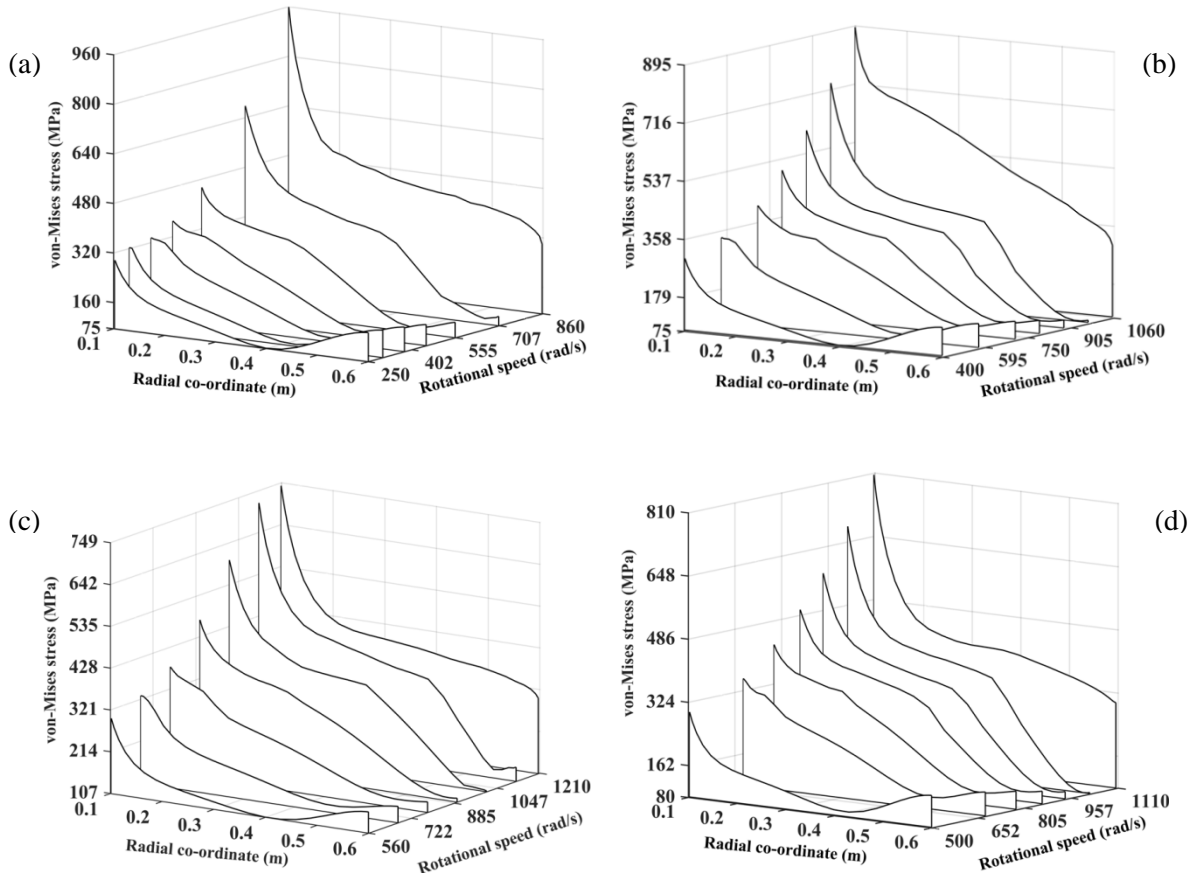


**Figure 6.9.** Waterfall plots of variation of von-Mises stress with rotational speed under linear temperature field for (a) uniform, (b) taper, (c) exponential and (d) parabolic disk geometries.

### 6.3.3.1 Effect of geometry variation on elasto-plastic behaviour of FGM annular disk

The effect of geometry variation on performance of functionally graded disk in elasto-plastic regime for four different disk geometries under linear temperature distributions is investigated in this section. In this analysis the ceramic volume fraction in the outer radius,  $V_{c0} = 1$  and ceramic distribution coefficient,  $n=2$ .



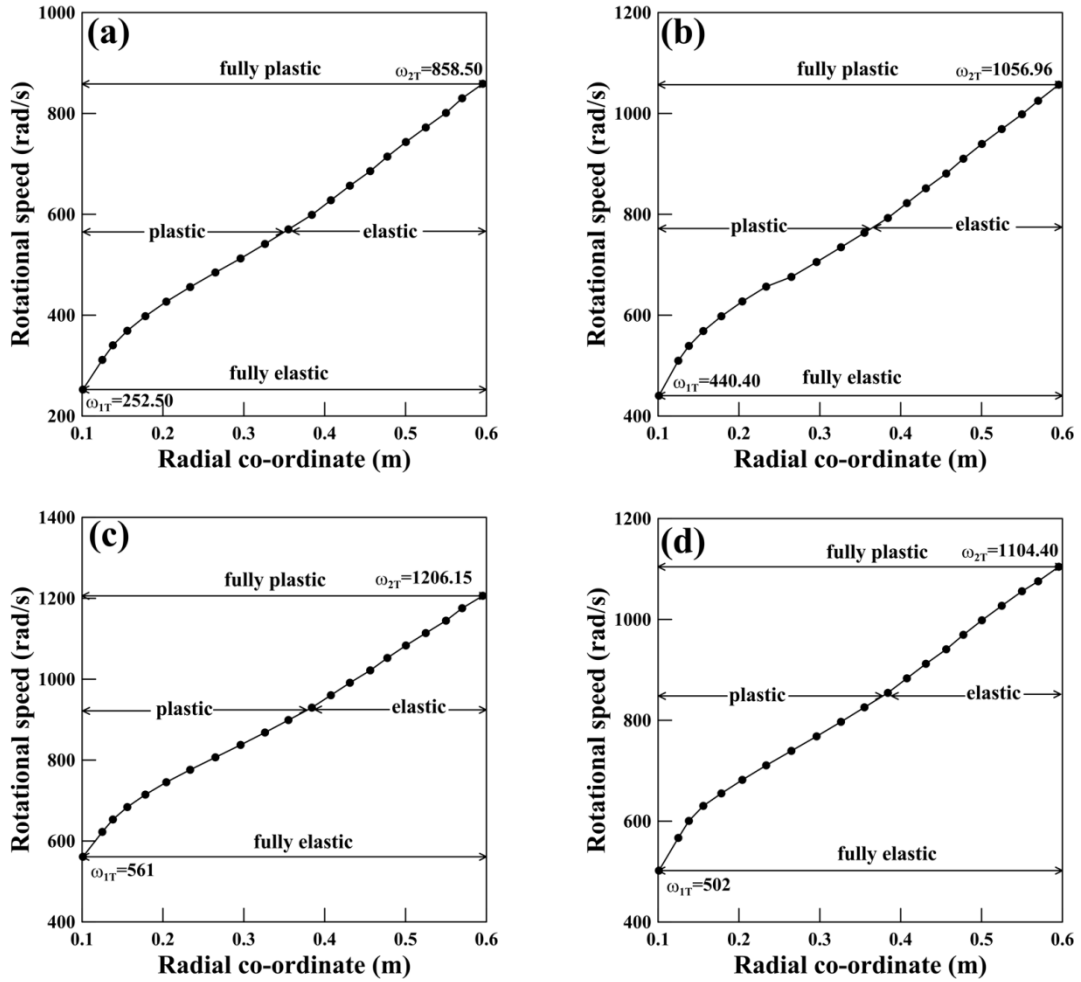


**Figure 6.10.** Plot of propagation of yield front with increase in rotational speed for (a) uniform, (b) taper, (c) exponential and (d) parabolic disk geometries, under linear temperature field.

To analyze the growth of yield front in a FGM disk under thermo-mechanical loading, the radial distribution of von-Mises stress are reported in Figures 6.9(a)-(d) at different rotational speeds through waterfall plots. The plots are shown for four types of disk geometry variations subjected to linear temperature distribution with  $T_a = 100^\circ\text{C}$  and  $T_b = 300^\circ\text{C}$  and in each of them rotational speed range from initial yield limit to ultimate collapse limit. From Figure 6.9, it is observed for all the cases that von-Mises stress increases with increase in rotational speed, initial yielding occurs at the inner radius at  $\omega_{1T}$  and when the rotational speed reaches  $\omega_{2T}$  entire disk becomes elasto-plastic. The von-Mises stress at fully plastic speed ( $\omega_{2T}$ ) is maximum for uniform disk geometry and minimum for exponential disk geometry at the inner radius of the

disk. Due to the effect of variation in thickness, higher rotational speed is required to yield at the inner surface of the disk, so the elastic limit speed and plastic collapse speeds are more for exponential disk thus resulting into higher strength disks.

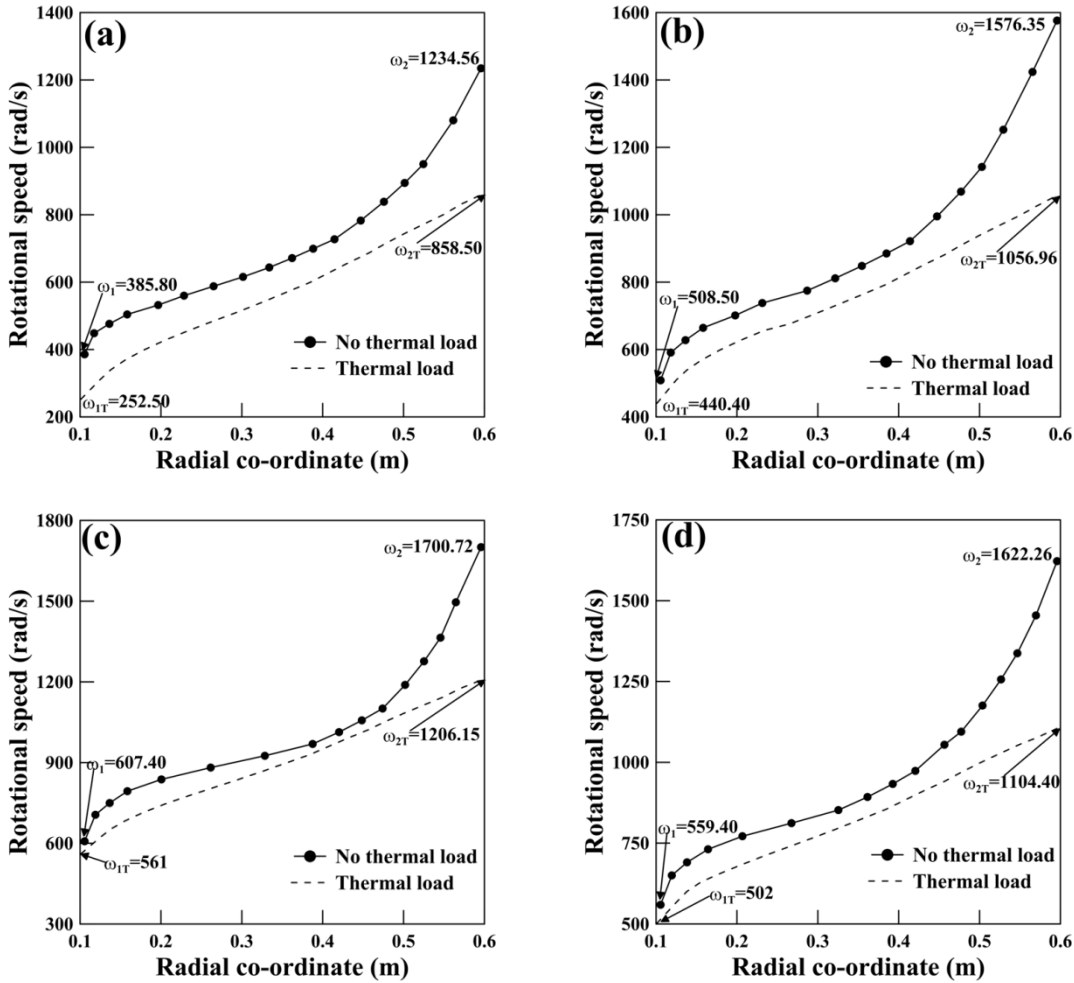


**Figure 6.11.** Plot of propagation of yield front with increase in rotational speed with and without thermal loading for (a) uniform, (b) taper, (c) exponential and (d) parabolic disk geometries.

From the stress fields of waterfall plots in Figure 6.9, the plastic front locations are captured at different rotational speeds and their location with rotational speed are provided in Figures 6.10(a)-(d), for the FGM annular disk. The figures indicate the advancement of plastic front locations with increasing rotational speeds for all the four types of disk geometries and the line demarcates the elastic-plastic region of the disk from fully elastic to fully plastic region.

In a subsequent study, the plastic front locations are captured at different rotational speeds without considering thermal load and their growth with rotational speed are provided in Figure 6.11. These figures also furnish the results of Figure 6.10 in dotted lines and it is observed that the elastic limit speed and plastic limit speed are higher for all the disk geometries without thermal load.

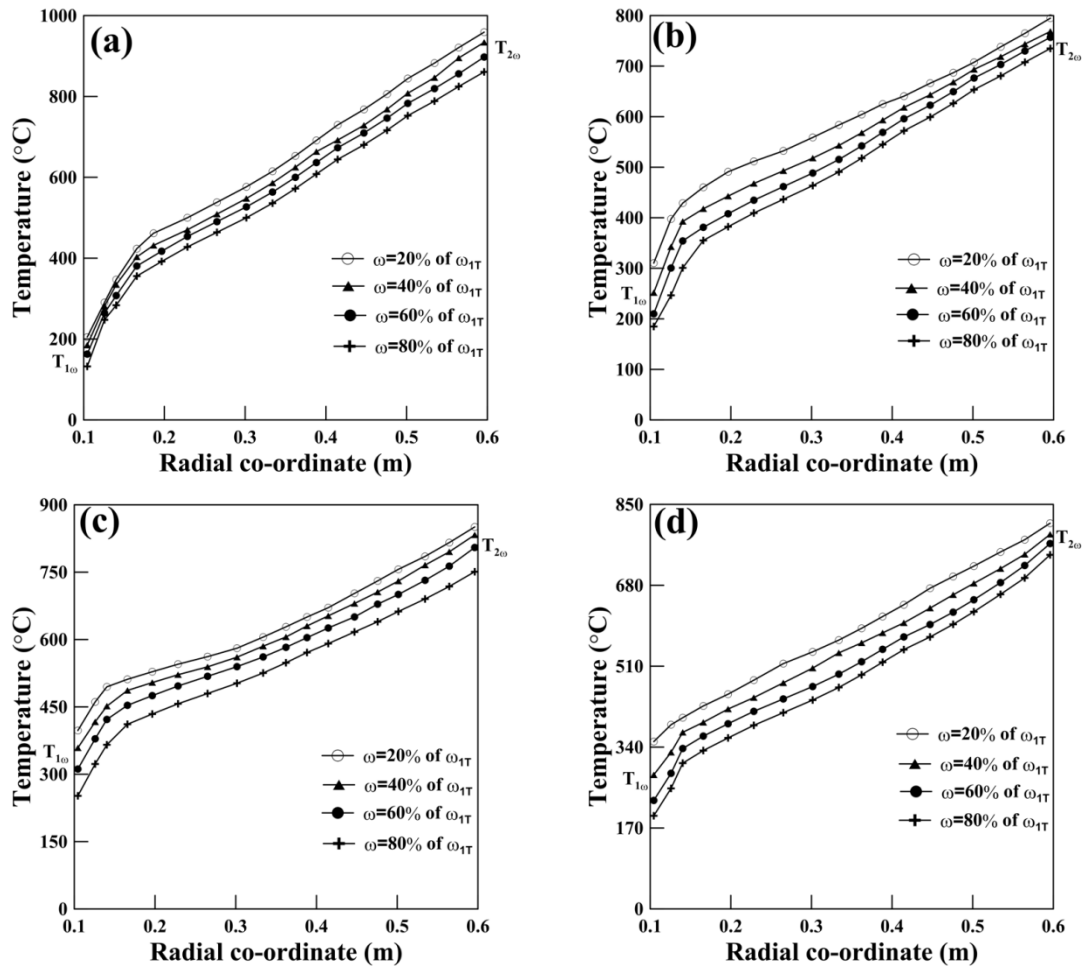


**Figure 6.12.** Plot of propagation of yield front with temperature for (a) uniform, (b) taper, (c) exponential and (d) parabolic disk geometries.

### 6.3.3.2 Study on the yield and collapse limit temperature

Figures 6.12(a)-(d) shows the advancement of yield front locations with increasing temperatures for all the four disk geometries considering linear temperature distribution with  $T_a = 100^\circ\text{C}$  and  $T_b = 300^\circ\text{C}$ . These figures are provided at 20%, 40%, 60% and 80% of elastic

limit speeds ( $\omega_{IT}$ ) as reported earlier in Figures 6.10(a)-(d). For all types of disk geometries, the yield limit and collapse temperature is more for lower value of rotational speed. With increase in rotational speed, the yield and collapse temperature decreases. It is also evident from these figures that the yield limit temperature is highest for exponential disk and lowest for uniform disk for all values of rotational speeds whereas the collapse temperature is highest for uniform disk and lowest for taper disk.

### 6.3.3.3 Effect of material parameters $V_{c0}$ and $n$

To understand the significance of the ceramic content at the outer radius  $V_{c0}$ , a parametric study is carried out by changing the values of  $V_{c0}$  for a particular ceramic distribution coefficient,  $n$ . Similarly, the results are also presented for two different  $n$  values considering a particular ceramic content at the outer radius,  $V_{c0}$ .

#### 6.3.3.3.1 Effect of the ceramic content at the outer radius, $V_{c0}$

The plastic front locations with rotational speed under linear temperature distribution with  $T_a = 100^\circ\text{C}$  and  $T_b = 300^\circ\text{C}$  are plotted in Figures 6.13(a)-(d) for the four different disk geometries. Each plot contains three different values for  $V_{c0}$  (equals to 0.5, 0.8 and 1) with  $n=2$  and the effect of the  $V_{c0}$  values are observed. It is obvious that the elastic limit speed ( $\omega_{IT}$ ) and the plastic limit speed ( $\omega_{2T}$ ) increases when  $V_{c0}$  is increased for all the disk geometries. This may be presumed that the ceramic part in a ceramic-metal FGM disk improves the limit speeds. As discussed earlier in Section 6.3.3.1, it is evident that for exponential disk geometry, the elastic limit speed and plastic limit speed are more for all the  $V_{c0}$  values as compared to other disk geometries.

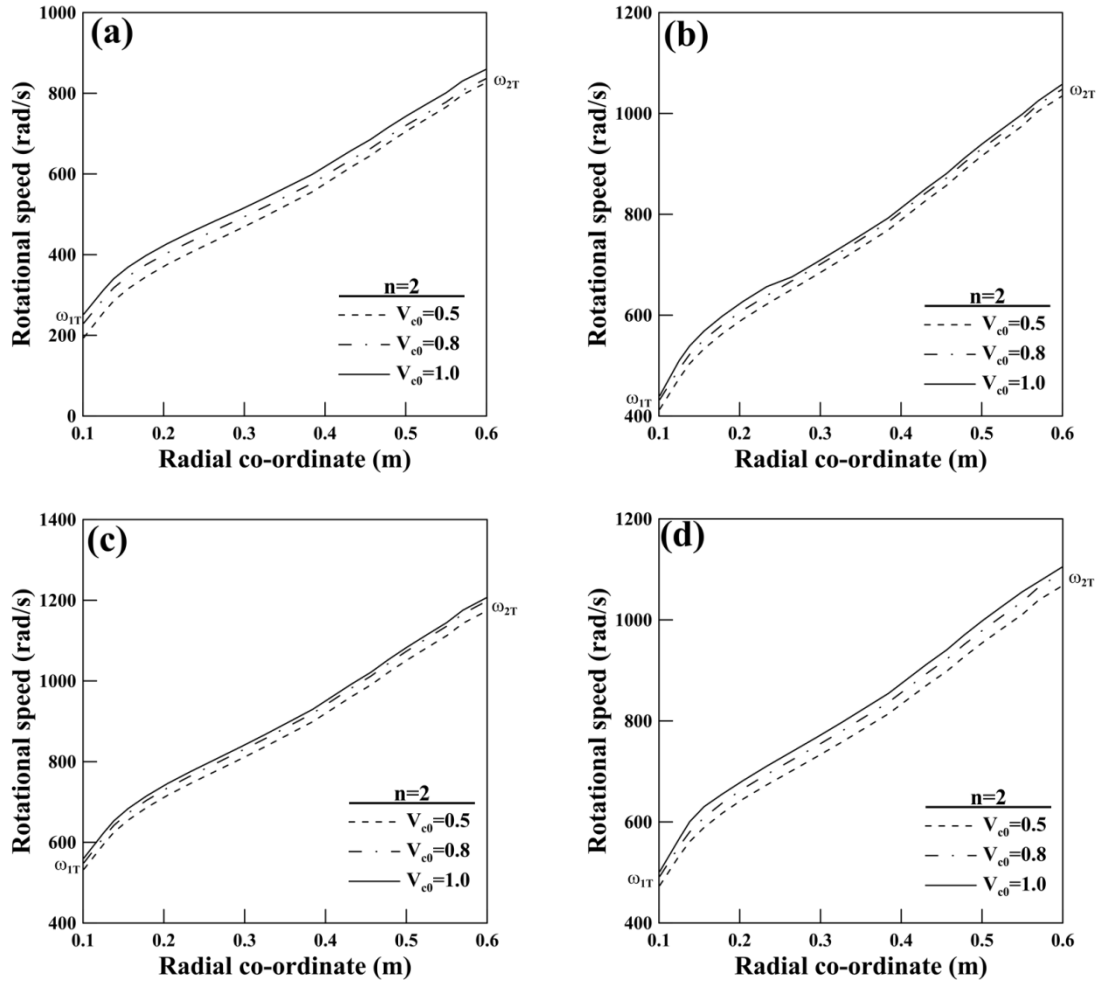


**Figure 6.13.** Effect of material parameter  $V_{c0}$  on propagation of yield front with increase in rotational speed for (a) uniform, (b) taper, (c) exponential and (d) parabolic disk geometries, while the disk is under linear temperature distribution.

### 6.3.3.3.2 Effect of the ceramic distribution coefficient, $n$

The plots for plastic front locations with rotational speed under linear temperature distribution are plotted in Figures 6.14(a)-(d) for the four different disk geometries. Each plot contains two different values for  $n$  (equals to 0.5 and 2) with  $V_{c0} = 1$  and the effect of  $n$  values are observed. It is observed that the elastic limit speed ( $\omega_{1T}$ ) and the plastic limit speed ( $\omega_{2T}$ ) increases when  $n$  is decreased for all the disk geometries. From this analysis, it is revealed that a smaller value of ‘ $n$ ’ which means increase of ceramic particles in a ceramic-metal FGM disk increases the plastic limit speed.

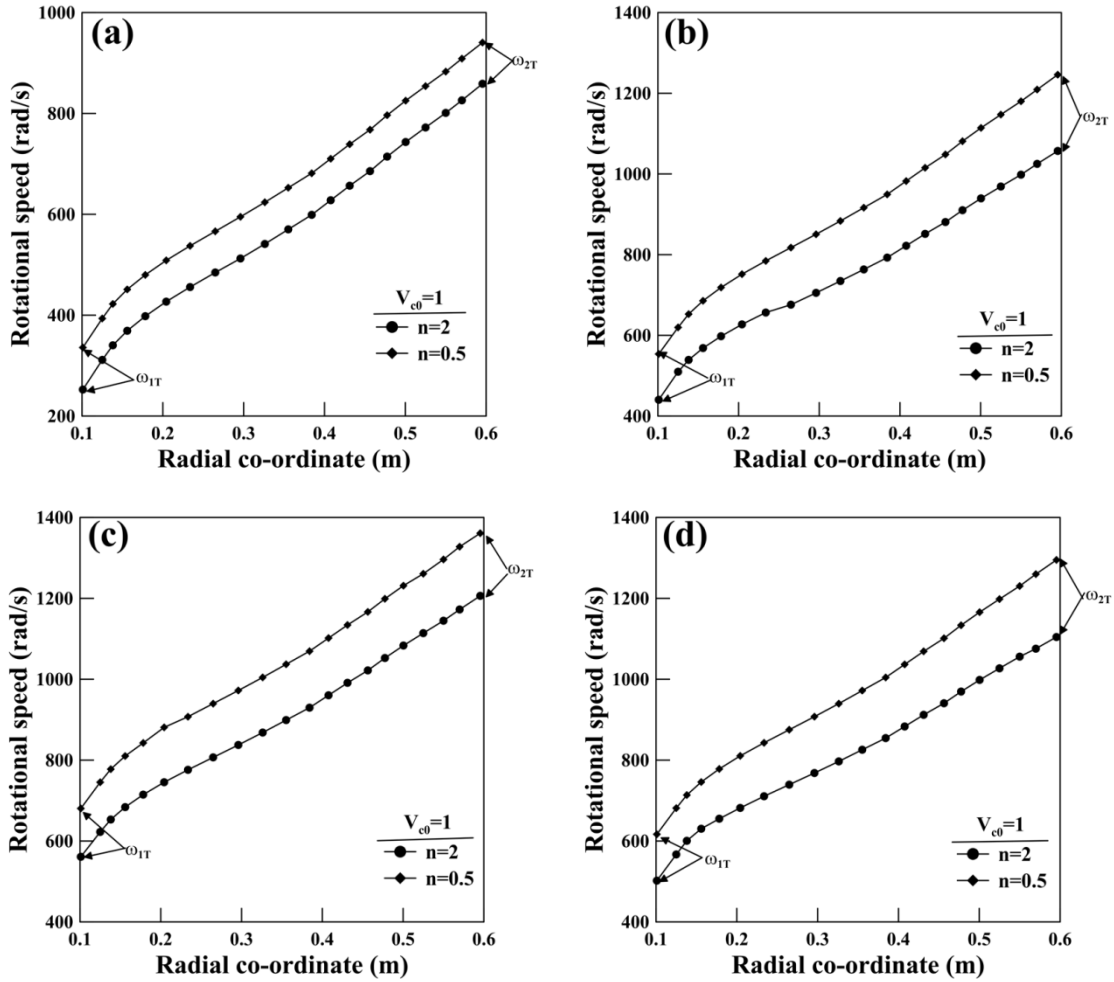


**Figure 6.14.** Effect of material parameter  $n$  on propagation of yield front with increase in rotational speed for (a) uniform, (b) taper, (c) exponential and (d) parabolic disk geometries, while the disk is under linear temperature distribution.

### 6.3.3.4 Effect of the nature of temperature distribution

To study the influence of different temperature distributions such as uniform, linear, exponential and parabolic, waterfall plots of von-Mises stress and yield front propagation are plotted in Figures 6.15 (a)-(d) and Figures 6.16 (a)-(d) for uniform disk. The ceramic volume fraction in the outer radius  $V_{c0} = 1$  and ceramic distribution coefficient,  $n=2$  for this analysis. In all the cases, the temperature field is considered as in Figure 6.4 by taking  $T_a = 100^\circ\text{C}$  and  $T_b = 300^\circ\text{C}$ . From Figure 6.15, it is observed that the von-Mises stress is

maximum for uniform temperature distribution for uniform disk and minimum for exponential temperature distribution.

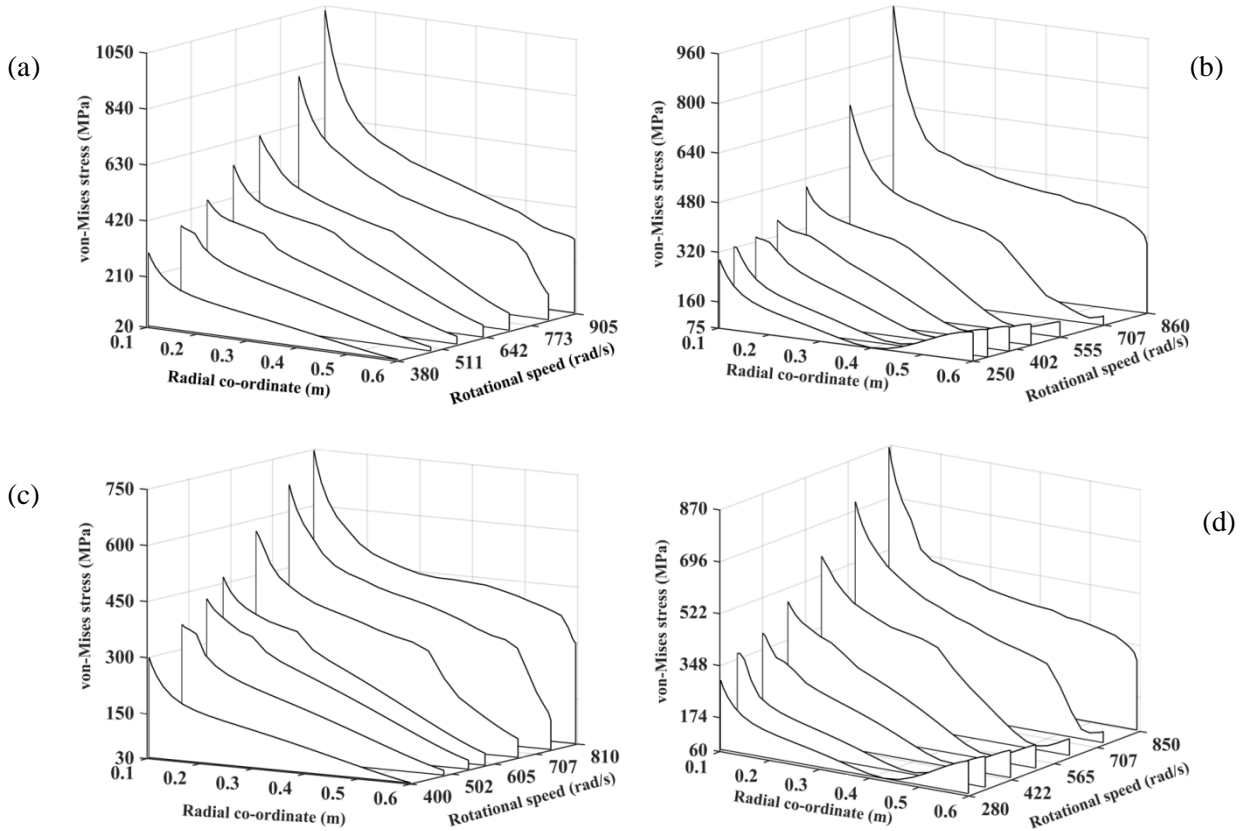


**Figure 6.15.** Waterfall plots of variation of von-Mises stress with rotational speed for uniform disk under (a) uniform, (b) linear, (c) exponential and (d) parabolic temperature distributions.

**6.3.3.5 Results for FGM disk with trilinear material model**

The results are presented for trilinear material model for the four different disk geometries under linear temperature distributions with  $T_a = 100^\circ\text{C}$  and  $T_b = 300^\circ\text{C}$ . In this analysis the ceramic volume fraction in the outer radius  $V_{c0} = 1$  and ceramic distribution coefficient,  $n=2$ . The waterfall plots of von-Mises stress at different rotational speeds are shown in Figures 6.17(a)-(d) for trilinear material model. These plots are compared with the corresponding waterfall plots of Figure 6.9 where bilinear material model was considered. It is observed that the nature of stress fields are identical but the von-Mises stress is more for trilinear model for all the disk geometries. The plastic front locations with rotational speed are plotted in

Figures 6.18(a)-(d) for trilinear material model and their change with the corresponding plot for bilinear model are shown. It is observed that the elastic limit speed ( $\omega_{1T}$ ) remain same for both bilinear and trilinear material model. However, there is a change in plastic collapse speed ( $\omega_{2T}$ ) and it is observed that the plastic collapse speed is less in case of trilinear material model for all the disk geometries considering linear temperature distribution.

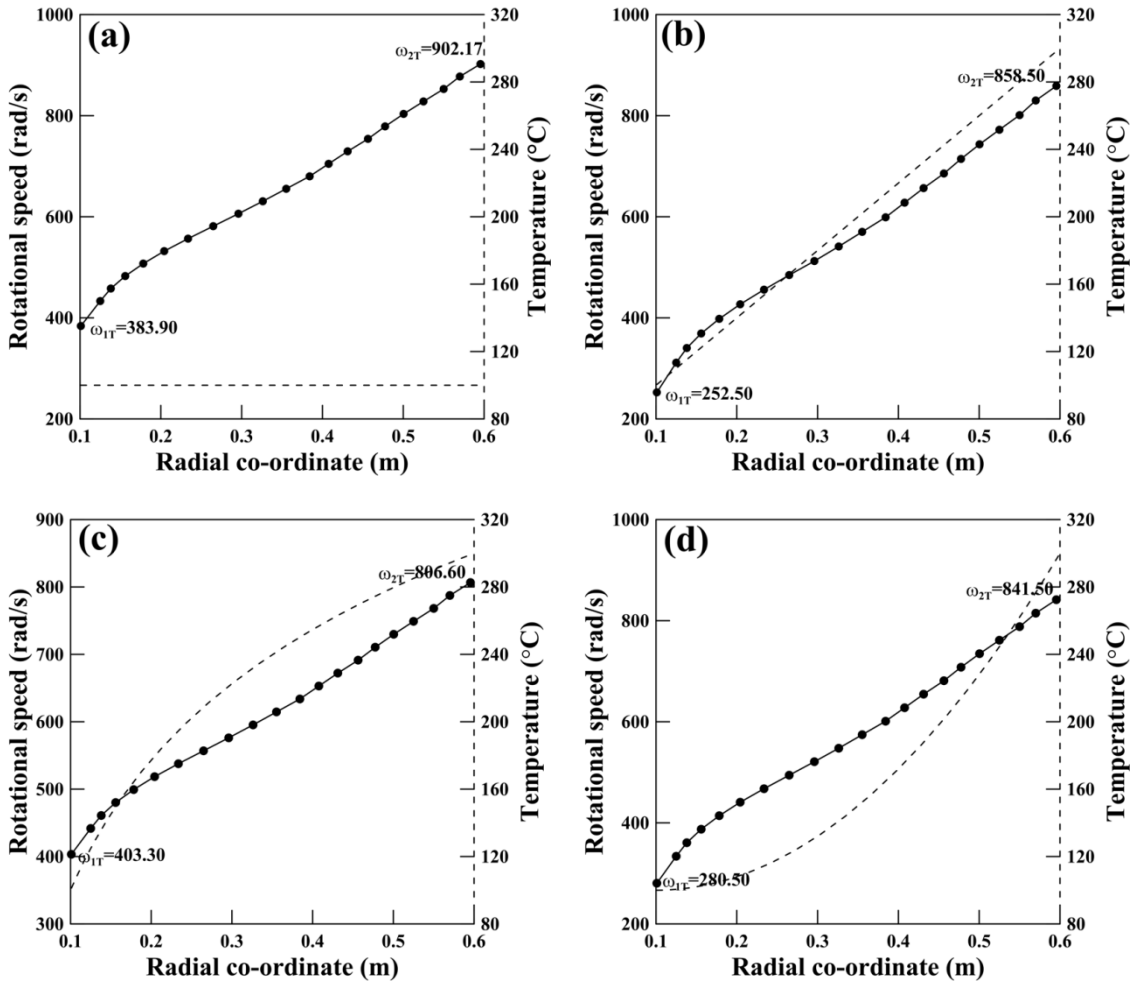


**Figure 6.16.** Yield front propagation with increase in rotational speed for uniform disk under (a) uniform, (b) linear, (c) exponential and (d) parabolic temperature distributions.



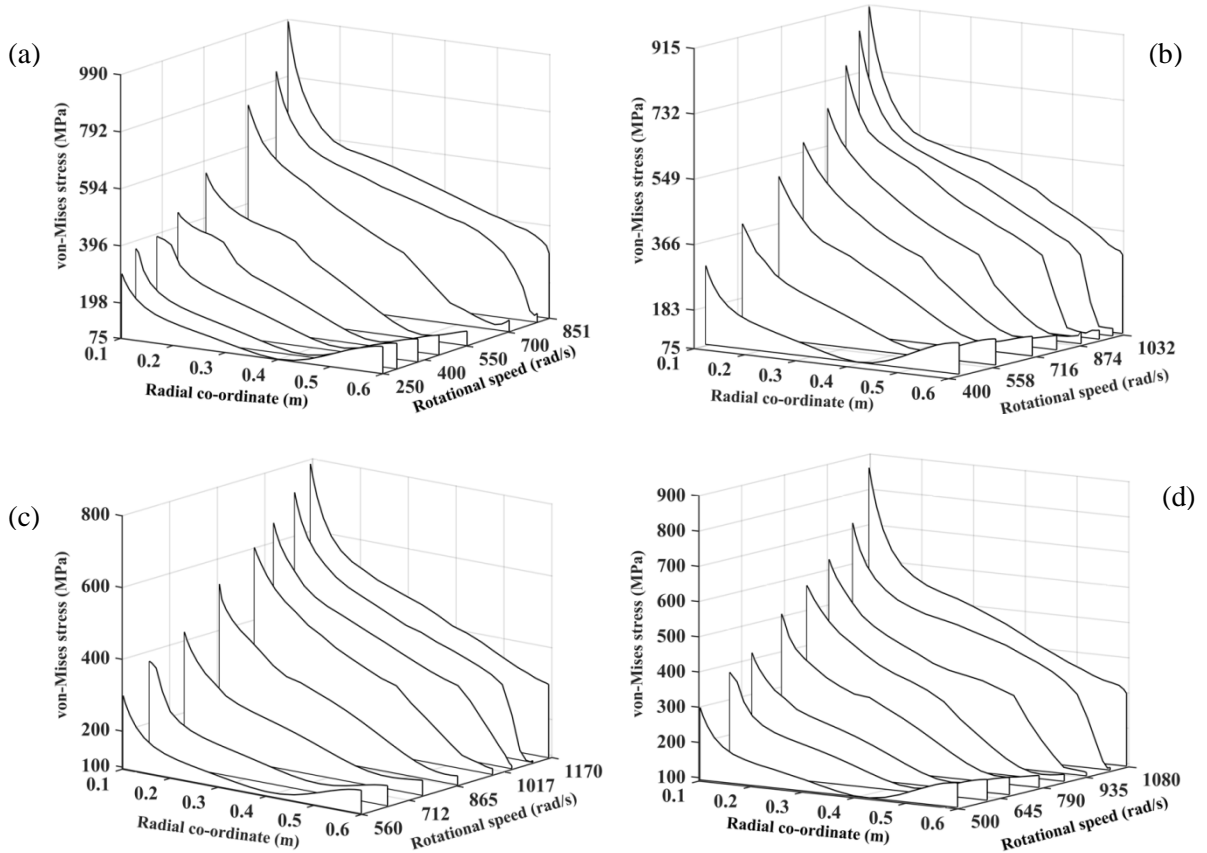


**Figure 6.17.** Waterfall plots of variation of von-Mises stress with rotational speed for trilinear material model for (a) uniform, (b) taper, (c) exponential and (d) parabolic disk geometries, while the disk is under linear temperature distribution.

### 6.3.3.6 Study on plastic strain

The plots of radial and tangential plastic strain at fully plastic speed for the respective disk geometries under linear temperature distribution are shown for bilinear material behaviour in Figures 6.19 (a)-(b). In Figures 6.20 (a)-(b), the radial and tangential plastic strains at fully plastic speed for different disk geometries under linear temperature distribution are plotted for trilinear material behaviour. The radial strain remains almost same as that for bilinear model but there is a decrease in tangential strain for trilinear model.

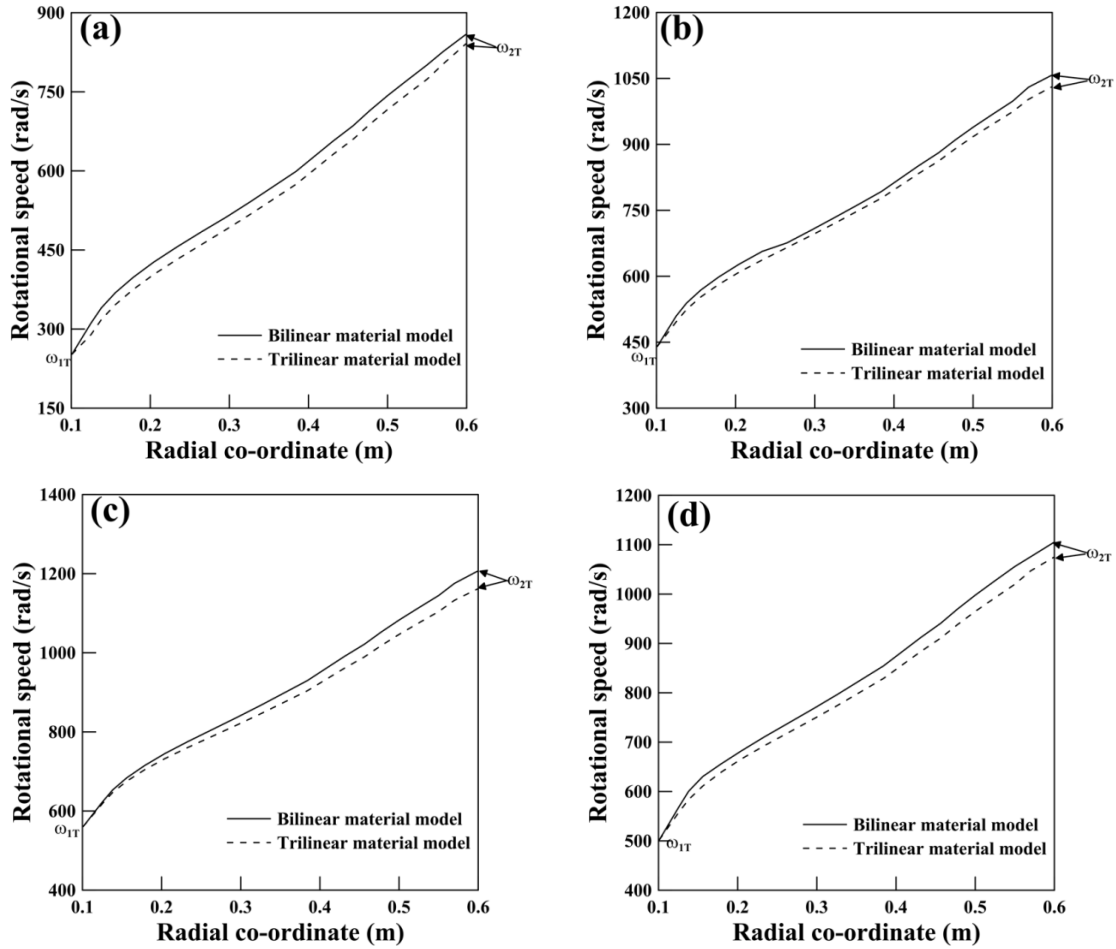


**Figure 6.18.** Plot of propagation of yield front with increase in rotational speed for (a) uniform, (b) taper, (c) exponential and (d) parabolic disk geometries, for trilinear material model.

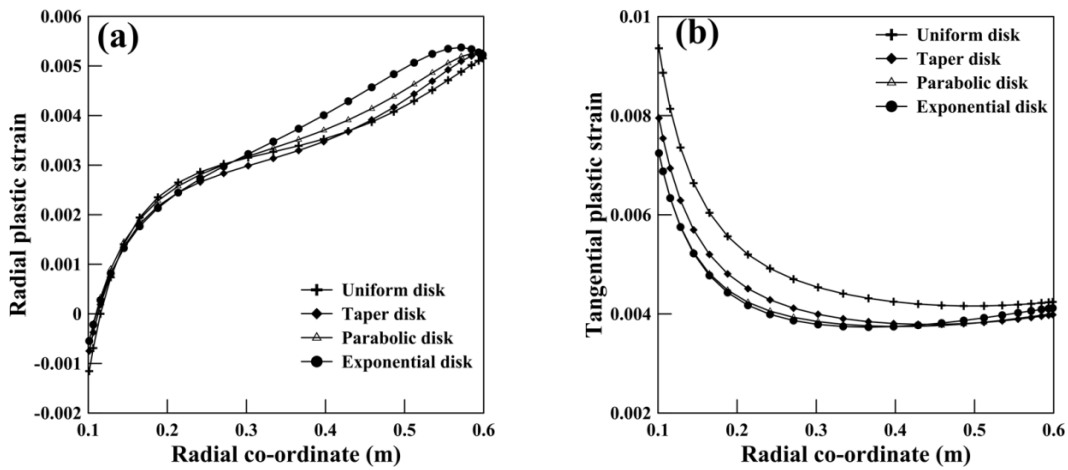


**Figure 6.19.** Plots of (a) radial and (b) tangential plastic strain at fully plastic speed for different geometries under linear temperature distribution for bilinear model.

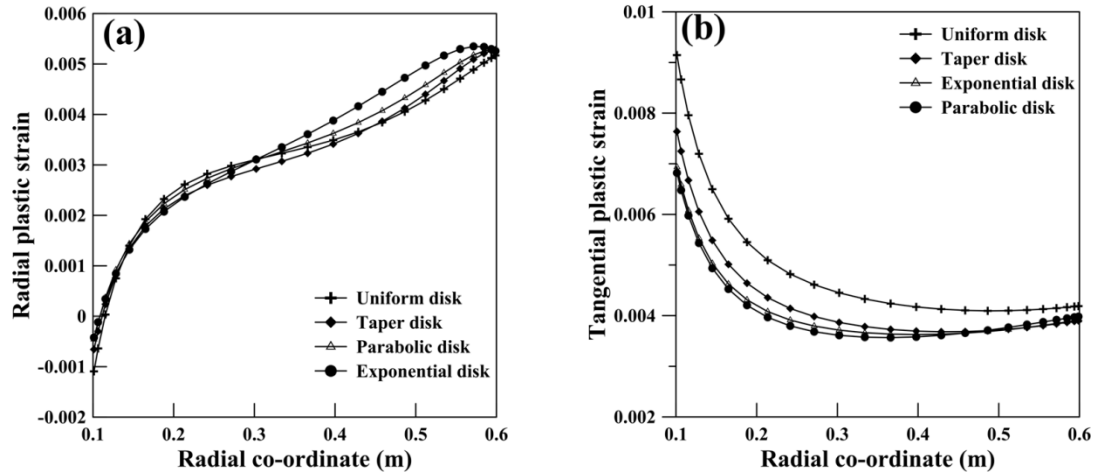


**Figure 6.20.** Plots of (a) radial and (b) tangential plastic strain at fully plastic speed for different geometries under linear temperature distribution for trilinear model.

## 6.4 Summary

The elasto-plastic stress fields and yield front propagation of thermo-mechanically loaded FGM rotating disk are presented in this chapter. The problem is formulated through a variational method in an iterative manner based on von-Mises yield criterion and Hencky's deformation theory of plasticity. Both the material models: bilinear and trilinear are considered. The results obtained from the present mathematical model are validated with those of other researchers for appropriate values of system parameters and good agreement is obtained. Some new results are presented for von-Mises stress fields through waterfall plots and growth of plastic fronts for different disk geometries under different types of temperature distribution fields and it is observed for all the cases that the elastic limit speed and plastic collapse speed are more for exponential disks. Furthermore, some numerical results of the elasto-plastic field problem under thermo-mechanical loading are presented showing the effect of material parameters  $V_{c0}$  and  $n$  on rotating FG disks having various geometries and temperature distributions. It is observed that the increase in ceramic content in a ceramic-metal FGM disk improves the limit speeds.



## **CLOSURE**

### **7.1 Conclusions**

The present thesis work focuses on the investigation of the elasto-plastic analysis of axisymmetric bars and rotating disks subjected to mechanical and thermal loads. The mathematical technique to carry out the above mentioned investigation is based on the extension and application of minimum potential energy principle in Hencky's deformation theory of plasticity. The von-Mises yield criterion and its associated flow rule assuming linear strain hardening (bilinear) material behaviour is adopted for the present work. The entire formulation for all the simulation studies of the present thesis work is displacement based and the unknown displacement field is approximated by finite linear combination of admissible orthogonal coordinate functions and unknown coefficients. The start functions for the above mentioned set of orthogonal functions are suitably selected so as to satisfy the boundary conditions. The higher order orthogonal functions are generated numerically by using Gram Schmidt scheme from the selected start functions. Due to the consideration of material non-linearity, the set of governing equations are found to be non-linear in nature. The set of non-linear equations are solved using an iterative variational method. The solution algorithm is actualized with the assistance of MATLAB<sup>®</sup> computational simulation software.

The elastic analysis of rotating disk upto limit (yield) state, for combined thermal load and rotational inertia effects, is reported. The attainment of yield state is defined on the basis of von-Mises yield criterion. The proposed method has been validated successfully with existing literatures and very good agreement is reported. The effect of geometry variation is reported by considering uniform, taper, exponential and parabolic variations. The effect of four types of temperature distributions, namely uniform, linear, exponential and parabolic, on the performance of rotating disks is considered. Limit angular speed of the disks is calculated under thermo-mechanical loading and reported in dimensional form as limit peripheral speed and in dimensionless form as normalized limit angular speed. The effects of temperature on material properties such as density, elasticity modulus, yield stress and combination of both density and elasticity modulus is also studied and the limit speed for any given temperature distribution and

boundary conditions is established under thermo-mechanical loading. The important conclusions are:

- a. The normalized limit angular speed remains constant for uniform temperature distributions for all the disk geometries and maximum for exponential disk geometry.
- b. For all other temperature distributions, the normalized limit angular speed decreases with increase in outer surface temperatures whereas increases with increase in inner surface temperature. The normalized limit angular speed is maximum for exponential disk geometry and minimum for uniform disk geometry.
- c. From the effect of temperature on von-Mises stress, it is observed that the induced von Mises stress profile increase with outer surface temperature values and the von Mises stress is higher for the rotating one as compared to the static disk.
- d. At a particular temperature, it is also observed that von Mises stress increases with increase in angular speeds but the increase is significantly lower in parabolic disk geometry as compared to uniform disk geometry.

The elasto-plastic analysis of statically indeterminate non-uniform bars is reported. The investigation of yield front propagation of statically indeterminate taper bar is formulated through the extension and application of minimum potential energy principle in Hencky's deformation theory based on von-Mises yield criterion. Bilinear and multilinear material model is considered. Domain decomposition method has been established for determinate problems and to overcome its insufficiency for indeterminate problems, an iterative variational method has been proposed successfully. The results obtained by the present methodology have been validated with that of analytical results of a clamped-free taper bar under uniaxial tensile load and excellent agreement is obtained. The results obtained through the revised formulation using domain decomposition method are validated successfully by finite element analysis software Abaqus CAE for a clamped-clamped taper bar. The effect of aspect ratio and slenderness ratio on yield front propagation of clamped-clamped bar has been studied. Waterfall plots showing the variation in stress field with increase in load have been presented. The important conclusions are:

- a. For clamped-clamped uniform taper bar, non-dimensional collapse load for domain 1 ( $\lambda_{c1}$ ) decreases and non-dimensional collapse load for domain 2 ( $\lambda_{c2}$ ) increases as the load application points shift from higher diameter end to lower diameter end.

- b. The observation for non-uniform taper bars remains almost same as that mentioned for uniform taper bars except for the fact that the increase in  $\lambda_{c2}$  is much more than  $\lambda_{c1}$ .
- c. The yield load and plastic collapse load for both the domains ( $F_{y1}$ ,  $F_{y2}$  and  $F_{c1}$ ,  $F_{c2}$ ) are higher for non-uniform taper bars as compared to uniform taper bars.
- d. The elastic limit loads for both the domains ( $F_{y1}$  and  $F_{y2}$ ) remain same for bilinear and trilinear material model. However, the plastic collapse load is more in case of trilinear material model for all the load application points and for both the domains.

The elasto-plastic analysis of isotropic and functionally graded non-uniform bars subjected to thermal load is carried out for both bilinear and multilinear material models through the extension of minimum potential energy principle in Hencky's deformation theory using von-Mises yield criterion. The results obtained by the proposed methodology are validated successfully with that of finite element analysis software Abaqus CAE for a clamped linear taper bar under uniform temperature field. The yield front propagation of clamped-clamped bar with various temperature distributions are affected significantly by the variations in aspect ratio and slenderness ratio. The temperatures and limit load factors for different bar geometries and temperature distributions are provided. The variation in stress fields with temperature are reported through waterfall plots. The conclusions are:

- a. The elastic limit temperature ( $T_y$ ) and plastic collapse temperature ( $T_c$ ) are higher for parabolic temperature distributions and lower for uniform temperature distributions for all values of aspect ratio and slenderness ratio.
- b. For taper bar geometry, the compressive stress is more for uniform temperature as compared to decreasing linear and parabolic temperature distributions.
- c. For parabolic bar geometry, ( $T_y$ ) and ( $T_c$ ) are lower than that of linear taper bars for all the temperature distributions.
- d. The limit load factors are lower for parabolic bars as compared to linear taper bars.
- e. There is a decrease in ( $T_y$ ) and ( $T_c$ ) values by considering yield stress variation with temperatures as compared to constant yield stress.

- f. The increase in ceramic content in a ceramic-metal FGM bar improves the limit temperatures.

Elasto-plastic analysis of functionally graded rotating disks under thermo-mechanical loading is performed. An extension of minimum total potential energy principle based on von-Mises yield criterion, its associated flow rule and Hencky's total deformation theory is used. Linear and bilinear strain hardening material behavior is assumed. The validation of the proposed formulation is established by comparing the results with benchmark solutions. The effect of disk geometries under different temperature distributions on the stress distribution of the disk is reported starting from the initiation of yielding till the attainment of fully plastic state. The representation of von-Mises stress in waterfall plots also give a good insight into the plastic state of the disk. The effect of material parameters on FG disk is also addressed for different disk geometries and temperature distributions. The important conclusions are:

- a. The von-Mises stress at fully plastic speed ( $\omega_{2T}$ ) is maximum for uniform disk geometry and minimum for exponential disk geometry at the inner radius of the disk.
- b. The elastic limit speed and plastic collapse speeds are more for exponential disk.
- c. The elastic limit speed and plastic limit speed are higher for all the disk geometries without considering thermal load.
- d. The increase in ceramic content in a ceramic-metal FGM disk improves the limit speeds.
- e. The von-Mises stress is maximum for uniform temperature distribution for uniform disk and minimum for exponential temperature distribution.
- f. The elastic limit speed ( $\omega_{1T}$ ) remain same for both bilinear and trilinear material model. However, the plastic collapse speed ( $\omega_{2T}$ ) is less in case of trilinear material model for all the disk geometries considering linear temperature distribution.

## 7.2 Future scope of work

Due to wide spread industrial applications, the study of axisymmetric bars and rotating disks working at elevated temperatures has been throughout an interesting area of research. The nature of application defines the type of material to be used, the initial and boundary conditions, the type of load and its range that acts on the structures, and possible modes of failure. Based on



these inputs, a researcher aims at finding the elasto-plastic solution for static and dynamic behaviour of these structures. In the present thesis, the elasto-plastic analysis of axisymmetric bars and rotating disks under mechanical and thermal loads is presented based on various assumptions. Each one of the assumptions may lead to different domains of research. The present method of formulation readily gives the kernel for solution of many other complicating effects. In addition, like any analysis software the present one also has the potential to save cost and time of prototype production process. Different aspects of the present work in which more elaborate studies can be directed are detailed below:

- The present thesis work considers linear elastic and linear strain hardening elasto-plastic material behaviour and the extension of the linear strain hardening model for multiple straight line segments for the post-elastic analysis of axisymmetric structures. However, the problem can be conveniently formulated for non-linear strain hardening behaviour wherein the local post-elastic stress-strain gradient can be calculated from the experimental uni-axial stress-strain diagram and incorporated into the formulation.
- The change in initial geometry of axisymmetric bars and disks should be considered in the mathematical modelling of elasto-plastic analysis and can be taken up as an extension of the present thesis work.
- The dynamic analysis of bars and disks in different loading conditions is also well within the future scope of work.
- The condition of buckling should be incorporated in the fixed-fixed bar problem.
- An investigation of the change in thermal material properties (thermal conductivity,  $k$  and convective heat transfer coefficient,  $h$ ), in the associated problem of temperature field determination needs to be conducted.
- The post-elastic analysis of non-uniform bars by using domain decomposition technique based on a direct variational method has been presently evaluated. The same domain decomposition method can be further taken up for rotating disk with attached mass problem.
- The present work can be extended to investigate the creep behaviour of rotating disks.
- Experimental studies can be taken up on the problems for which simulation studies have been carried out in the present thesis.



## *Bibliography*

- Abdalla H.F., Megahed M.M. and Younan M.Y.A., A simplified technique for shakedown limit load determination, *Nuclear Engineering and Design*, Vol. 237, pp. 1231-1240, 2007.
- Abdalla H.F., Megahed M.M. and Younan M.Y.A., A simplified technique for shakedown limit load determination of a large square plate with a small central hole under cyclic biaxial loading, *Nuclear Engineering and Design*, Vol. 241, pp. 657-665, 2011.
- Adali S., Verijenko V.E. and Chevallereau B., Design optimization of composite rotating disks under multiple loads, *AIAA/USAF/NASA/ISSMO Symposium on multidisciplinary analysis and optimization*, St. Louis, A98-39701, pp. 10-31, 1998.
- Afsar A.M. and Go J., Finite element analysis of thermo-elastic field in a rotating FGM circular disk, *Applied Mathematical Modelling*, Vol. 34, pp. 3309-3320, 2010.
- Alexandrov S. and Alexandrova N., Thermal effects on the development of plastic zones in thin axisymmetric plates, *Journal of Strain Analysis for Engineering Design*, Vol. 36, pp. 169-176, 2001.
- Alexandrov S., Chung K. and Jeong W., Stress and strain fields in rotating elastic/plastic annular disks of pressure-dependent material, *Mechanics Based Design of Structures and Machines*, Vol. 46, pp. 318-332, 2018.
- Alexandrova N. and Vila Real P. M. M., Elastic-plastic stress distributions and limit angular velocities in rotating hyperbolic annular disc, *Proceedings of the Institution of Mechanical Engineers, Part C: Journal of Mechanical Engineering Science*, Vol. 221, pp. 137-142, 2007.
- Alexandrova N. and Vila Real P.M.M., Effect of plastic anisotropy on stress-strain field in thin rotating disks, *Thin-walled structures*, Vol. 44, pp. 897-903, 2006.
- Alexandrova N., Application of Mises yield criterion to rotating solid disk problem, *International Journal of Engineering Science*, Vol. 51, pp. 333-337, 2012.
- Alexendrov S. and Lyamina E., Plastic limit state of a thin hollow disk under thermomechanical loading, *Journal of Applied Mechanics and Technical Physics*, Vol. 53, pp. 891–898, 2012.
- Alexendrov S., Lyamina E. and Jeng Y.R., Design of an Annular Disc Subject to thermomechanical loading, *Mathematical Problems in Engineering*, Hindawi Publishing Corporation, Article ID 709178, 2012.
- Alexendrova N. and Alexendrov S., Elastic-plastic stress distribution in a rotating annular disk, *Mechanics Based Design of Structures and Machines*, Vol. 32, pp. 1-15, 2004.

## *Bibliography*

- Alexandrova N. and Alexendrov S., Elastic-plastic stress distribution in a plastically anisotropic rotating disk, Transactions of the ASME, Journal of Applied Mechanics, Vol. 71, pp. 427-429, 2004a.
- Alexandrova N., Alexendrov S. and Real P.M.M.V., Displacement field and strain distribution in a rotating annular disk, Mechanics Based Design of Structures and Machines, Vol. 32, pp. 441-457, 2004.
- Alibeigloo A., Thermoelasticity analysis of functionally graded beam with integrated surface piezoelectric layers, Composite Structures, Vol. 92, pp. 1535-1543, 2010.
- Apatay T. and Eraslan A.N., Elastic deformations of rotating parabolic disks: an analytical solution, Journal of the Faculty of Engineering and Architecture of Gazi University, Vol. 18, pp. 115-135, 2003.
- Ari-Gur J. and Stavsky Y., On rotating polar-orthotropic circular disks, International Journal of Solids and Structures, Vol. 17, pp. 57-67, 1981.
- Arnold S.M., Saleeb A.F. and Al-Zoubi N.R., Deformation and life analysis of composite flywheel disk and multi-disk systems, NASA/TM-2001-210578, 2001.
- Arya V.K. and Bhatnagar N.S., Creep analysis of rotating orthotropic discs, Nuclear Engineering and Design, Vol. 55, pp. 326-330, 1979.
- Auciello N.M., On the transverse vibrations of non-uniform beams with axial loads and elastically restrained ends, International Journal of Mechanical Sciences, Vol. 43, pp. 193-208, 2001.
- Aurora C.D., Stelian A., Toader R.O., Luminita I. and Carmen C.F., FEA of stress concentrator effect from a rotating disk with a keyway, Fascicle of Management and Technological Engineering, Vol. IX, 2010.
- Babu R.N., Ramana K.V. and Rao K.M., Determination of stress concentration factors of a steam turbine rotor by FEA, International Journal of Mechanical and Mechatronics Engineering, Vol. 2, pp. 280-284, 2008.
- Bathe K.J., Finite Element Procedures, Prentice Hall, Pearson Education, Watertown, MA, 2006.
- Bayat M., Saleem M., Sahari B.B., Hamouda A.M.S and Mahdi E., Mechanical and thermal stresses in a functionally graded rotating disc with variable thickness due to radially symmetry loads, International Journal of Pressure Vessels and Piping, Vol. 86, pp. 357-372, 2009.

- Bayat M., Saleem M., Sahari B.B., Hamouda A.M.S. and Mahdi E., Analysis of functionally graded rotating disks with variable thickness, *Mechanics Research Communications*, Vol. 35, pp. 283-309, 2008.
- Bayat Y. and Toussi H.E., Elastoplastic torsion of hollow FGM circular shaft, *Journal of Computational and Applied Research in Mechanical Engineering*, Vol. 4, pp. 165-180, 2015.
- Bekta N.B., Topcu M., Callioglu H. and Atlan G., Elastic-plastic and residual stress analysis of an aluminium metal-matrix composite disk under internal pressures, *Journal of Reinforced Plastics and Composites*, Vol. 24, pp. 753-762, 2005.
- Bhavikatti S.S. and Ramakrishnan C.V., Optimum shape design of rotating disks, *Computers and Structures*, Vol. 11, pp. 397-401, 1980.
- Bhowmick S., Misra D. and Saha K.N., Approximate solution of limit angular speed for externally loaded rotating solid disk, *International Journal of Mechanical Sciences*, Vol. 50, pp. 163-174, 2008.
- Bhowmick S., Misra D. and Saha K.N., Variational formulation based analysis on growth of yield front in high speed rotating solid disks, *International Journal of Engineering Science and Technology, Multicraft*, Vol. 2, pp. 200-219, 2010.
- Biondi B. and Caddemi S., Euler-Bernoulli beams with multiple singularities in the flexural stiffness, *European Journal of Mechanics A/Solids*, Vol. 26, pp. 789-809, 2007.
- Bocciarelli M., Bolzon G. and Maie G., A constitutive model of metal-ceramic functionally graded material behaviour: formulation and parameter identification, *Computational Materials Science*, Vol. 43, pp. 16-26, 2008.
- Bose T. and Rattan M., Effect of thermal gradation on steady state creep of functionally graded rotating disc, *European Journal of Mechanics A/Solids*, Vol. 67, pp. 169-176, 2018.
- Bose T. and Rattan M., Modeling creep behavior of thermally graded rotating disc of functionally graded material, *Differential Equations and Dynamical Systems*, <http://dx.doi.org/10.1007/s12591-017-0350-1>, 2017.
- Budiansky B., A reassessment of deformation theories of plasticity, *Journal of Applied Mechanics*, Vol. 26, pp. 259-264, 1959.

## *Bibliography*

- Calderale P.M., Vivio F. and Vullo V., Thermal stresses of rotating hyperbolic disks as particular case of non-linearly variable thickness disks, *Journal of Thermal Stresses*, Vol. 35, pp. 877-891, 2012.
- Calladine C.R., *Engineering Plasticity*, Pergamon Press, 1969.
- Callioglu H., Demir E. and Sayer M., Thermal stress analysis of functionally graded rotating discs, *Scientific Research and Essays*, Vol. 6, pp. 3437-3446, 2011.
- Callioglu H., Sayer M. and Demir E., Elastic-plastic stress analysis of rotating functionally graded discs, *Thin-Walled Structures*, Vol. 94, pp. 38-44, 2015.
- Callioglu H., Stress analysis in a functionally graded disc under mechanical loads and a steady state temperature distribution, *Sadhana-Indian Academy of Sciences*, Vol. 36, pp. 53-64, 2011.
- Callioglu H., Stress analysis of an orthotropic rotating disk under thermal loading, *Journal of Reinforced Plastics and Composites*, Vol. 23, pp. 1859-1867, 2004.
- Callioglu H., Stress analysis of functionally graded isotropic rotating discs, *Advanced Composites Letters*, Vol. 17, pp. 147-153, 2008.
- Callioglu H., Thermal stress analysis of curvilinearly orthotropic rotating discs, *Journal of Thermoplastic Composite Materials*, Vol. 20, pp. 357-369, 2007.
- Callioglu H., Topcu M. and Tarakcilar A.R., Elastic-plastic stress analysis of an orthotropic rotating disc, *International Journal of Mechanical Sciences*, Vol. 48, pp. 985-990, 2006.
- Canales F.G. and Mantari J.L., Elasto-plastic vibrational analysis of tapered bars under uniform axial loading considering shear deformation and rotary inertia, *International Journal of Non-linear Mechanics*, Vol. 95, pp. 103-116, 2017.
- Chakrabarty J., *Theory of plasticity*, McGraw-Hill, New York, 1987.
- Chen J.S. and Fang Y.Y., Warping of stationary and rotating heavy disks, *International Journal of Solids and Structures*, Vol. 48, pp. 3032-3040, 2011.
- Chen P.C.T., The Bauschinger and hardening effect on residual stresses in an autofrettaged thick-walled cylinder, *Transactions of the ASME, Journal of Pressure Vessel Technology*, Vol. 108, pp. 108-112, 1986.
- Cho J.R. and Oden J.T., Functionally graded material: a parametric study on thermal-stress characteristics using the Crank-Nicolson-Galerkin scheme, *Computer Methods in Applied Mechanics and Engineering*, Vol. 188, pp. 17-38, 2000.

- Dai T. and Dai H.L., Thermo-elastic analysis of a functionally graded rotating hollow circular disk with variable thickness and angular speed, *Applied Mathematical Modelling*, Vol. 40, pp. 7689-7707, 2016.
- Danesh V. and Asghari M., Analysis of micro-rotating disks based on the strain gradient elasticity, *Acta Mechanica*, Vol. 225, pp. 1955-1965, 2014.
- Das D., Sahoo P. and Saha K.N., Dynamic analysis of non-uniform taper bars in post elastic regime under uniform axial loading, *Materials and Design*, Vol. 30, pp. 2113-2127, 2009a.
- Das D., Sahoo P. and Saha K.N., Dynamic analysis of non-uniform taper bars in post-elastic regime under body force loading, *Applied Mathematical Modelling*, Vol. 33, pp. 4163-4183, 2009b.
- Demir E., Callioglu H. and Sayer M., Elasto-plastic thermal stress analysis of functionally graded hyperbolic discs, *Structural Engineering and Mechanics*, Vol. 62, pp. 587-593, 2017.
- Dharmpal D., Garg M. and Gupta V.K., Creep behaviour of rotating FGM disc with linear and hyperbolic thickness profiles, *Kragujevac Journal of Science*, Vol. 37, pp. 35-48, 2015.
- Durban D. and Birman V., Elasto-plastic analysis of an anisotropic rotating disc, *Acta Mechanica*, Vol. 49, pp. 1-10, 1983.
- Durodola J.F. and Attia O., Deformation and stresses in functionally graded rotating disks, *Composites Science and Technology*, Vol. 60, pp. 987-995, 2000.
- Dwivedi J.P., Shah S.K., Upadhyay P.C. and Talukder N.K.D., Springback analysis of thin rectangular bars of non-linear work-hardening materials under torsional loading, *International Journal of Mechanical Sciences*, Vol. 44, pp. 1505-1519, 2002.
- Ecsedi I., Some analytical solutions for Saint-Venant torsion of non-homogeneous anisotropic cylindrical bars, *Mechanics Research Communications*, Vol. 52, pp. 95-100, 2013.
- Elhefny A. and Guozhu L., Stress and deformation of rocket gas turbine disk under different loads using finite element modeling, *Propulsion and Power Research*, Vol. 2, pp. 38-49, 2013.
- Ely J.F. and Zienkiewicz O.C., Torsion of compound bars-A relaxation solution, *International Journal of Mechanical Sciences*, Vol. 1, pp. 356-365, 1960.

## *Bibliography*

- Eraslan A.N. and Akis T., Elastoplastic response of a long functionally graded tube subjected to internal pressure, *Turkish Journal of Engineering and Environmental Sciences*, Vol. 29, pp. 361-368, 2005.
- Eraslan A.N. and Argeso H., Limit angular velocities of variable thickness rotating disks, *International Journal of Solids and Structures*, Vol. 39, pp. 3109-3130, 2002.
- Eraslan A.N. and Orcan Y., Elastic-plastic deformation of a rotating solid disk of exponentially varying thickness, *Mechanics of Materials*, Vol. 34, pp. 423-432, 2002a.
- Eraslan A.N. and Orcan Y., On the rotating elastic-plastic solid disks of variable thickness having concave profiles, *International Journal of Mechanical Sciences*, Vol. 44, pp. 1445-1466, 2002b.
- Eraslan A.N., Elastic-plastic deformations of rotating variable thickness annular disks with free, pressurized and radially constrained boundary conditions, *International Journal of Mechanical Sciences*, Vol. 45, pp. 643-667, 2003.
- Eraslan A.N., Inelastic deformations of rotating variable thickness solid disks by Tresca and von Mises criteria, *International Journal of Computational Engineering Science*, Vol. 3, pp. 89-101, 2002a.
- Eraslan A.N., Kaya Y. and Ciftci B., A computational model for partially-plastic stress analysis of orthotropic variable thickness disks subjected to external pressure, *Mathematical Sciences and Applications E-Notes*, Vol. 2, pp. 1-13, 2014.
- Eraslan A.N., Stress distributions in elastic-plastic rotating disks with elliptical thickness profiles using Tresca and von Mises criteria, *Zeitschrift für Angewandte Mathematik und Mechanik*, Vol. 85, pp. 252-266, 2005.
- Eraslan A.N., Von Mises yield criterion and nonlinearly hardening rotating shafts, *Acta Mechanica*, Vol. 168, pp. 129-144, 2004.
- Eraslan A.N., Von Mises yield criterion and nonlinearly hardening variable thickness rotating annular disks with rigid inclusion, *Mechanics Research Communications*, Vol. 29, pp. 339-350, 2002b.
- Eslami M.R., Jabbari M. and Sohrabpour S., Mechanical and thermal stresses in a functionally graded hollow cylinder due to radially symmetric loads, *International Journal of Pressure Vessels and Piping*, Vol. 79, pp. 493-497, 2002.



- Fanelli P., Fino A. and Vivio F., Analysis of elastic-plastic behaviour and plastic front evaluation in spot welded joints, *International Journal of Mechanical Sciences*, Vol. 90, pp. 122-132, 2015.
- Farimani M.R. and Toussi H.E., Plastic limit speed of FGM disc due to the variation of temperature and material composition, *Journal of Reinforced Plastics and Composites*, Vol. 32, pp. 1257-1267, 2013.
- Farshad M., Stresses in rotating disks of materials with different compressive and tensile moduli, *International Journal of Mechanical Sciences*, Vol. 16, pp. 559-564, 1974.
- Farshi B., Jahed H. and Mehrabian A., Optimum design of inhomogeneous non-uniform rotating discs, *Computers and Structures*, Vol. 82, pp. 773-779, 2004.
- Fukui Y., Yamanaka N. and Wakashima K., The stresses and strains in a thick-walled tube for functionally graded material under uniform thermal loading, *JSME International Journal Series A Solid Mechanics and Material Engineering*, Vol. 36, pp. 156-162, 1993.
- Gamer U. and Lance R.H., Stress distribution in a rotating elastic-plastic tube, *Acta Mechanica*, Vol. 50, pp. 1-8, 1983.
- Gamer U. and Mack W., Entlastungsvorgänge in der durch eine kreisringförmige Wärmequelle plastisch deformierten Scheibe, *Ingenieur-Archiv*, Vol. 57, pp. 368-376, 1987b.
- Gamer U. and Mack W., Thermal stress in an elastic-plastic disk exposed to a circular heat source, *Zeitschrift für angewandte Mathematik und Physik*, Vol. 36, pp. 568-580, 1985.
- Gamer U. and Mack W., Zur elastisch-plastischen Deformation dreh-symmetrisch erhitzter Kreisscheiben, *Zeitschrift für angewandte Mathematik und Physik*, Vol. 38, pp. 137-142, 1987a.
- Gamer U., Ein Beitrag zur Spannungsermittlung in Querschnittsverbindungen, *Ingenieur-Archiv*, Vol. 53, pp. 209-217, 1984c.
- Gamer U., Ein radialsymmetrischer Spannungszustand in der ideal-plastischen Scheibe, *Ingenieur-Archiv*, Vol. 36, pp. 174-191, 1967.
- Gamer U., Elastic-plastic deformation of the rotating solid disk, *Ingenieur-Archiv*, Vol. 54, pp. 345-354, 1984a.
- Gamer U., Mack W. and Varga I., Rotating elastic-plastic solid shaft with fixed ends, *International Journal of Engineering Science*, Vol. 35, pp. 253-267, 1997.

## *Bibliography*

- Gamer U., Stress distribution in the rotating elastic-plastic disk, *Zeitschrift für Angewandte Mathematik und Mechanik*, Vol. 65, pp. T136-T137, 1985.
- Gamer U., The elastic-plastic stress distribution in the rotating annulus and in the annulus under external pressure, *Zeitschrift für Angewandte Mathematik und Mechanik*, Vol. 64, pp. T126-T128, 1984d.
- Gamer U., The rotating solid disk in the fully plastic state, *Forschung Im Ingenieurwesen Engineering Research*, Vol. 50, pp. 137-140, 1984b.
- Gamer U., Tresca's yield condition and the rotating solid disk, *Transactions of the ASME, Journal of Applied Mechanics*, Vol. 50, pp. 676-678, 1983.
- Gang C., Yinghua L. and Bingye X., Plastic limit load analysis of defective pipelines, *Acta Mechanica Solida Sinica*, Vol. 16, pp. 102-109, 2003.
- Gao D.Y. and Ogden R.W., *Advances in mechanics and mathematics, Volume II.*, Kluwer Academic Publishers, Boston, 2003.
- Garg S. and Pant M., Numerical simulation of thermal fracture in functionally graded materials using element-free Galerkin method, *Sadhana-Academy Proceedings in Engineering Sciences*, Vol. 42, pp. 417-431, 2017.
- Genna F. and Symonds P.S., Dynamic plastic instabilities in response to short-pulse excitation: effects of slenderness ratio and damping, *Proceedings of the Royal Society of London A*, Vol. 417, pp. 31-44, 1988.
- Ghadimi B., Kowsary F. and Khorami M., Thermal analysis of locomotive wheel-mounted brake disc, *Applied Thermal Engineering*, Vol. 51, pp. 948-952, 2013.
- Ghafoori E. and Asghari M., Three-dimensional elasticity analysis of functionally graded rotating cylinders with variable thickness profile, *Proceedings of the Institution of Mechanical Engineers, Part C: Journal of Mechanical Engineering Science*, Vol. 226, pp. 585-594, 2012.
- Ghosh Dastidar D. and Ghosh P., Stresses and strains in the plastic range in an annular disk due to steady-state radial temperature variation, *International Journal of Mechanical Sciences*, Vol. 14, pp. 501-510, 1972.
- Ghuku S. and Saha K.N., A semi-analytical solution of statically indeterminate bar problem by using domain decomposition method, *Perspectives in Science*, <http://dx.doi.org/10.1016/j.pisc.2016.06.051>, 2016.

- Glushkov S.G., Stress determination in rotating disks having different elastic properties in two directions, Tr. Moskov, Stanko-Instrum. Inst. Sb. III, 1939.
- Grysa K and Kozlowski Z., One dimensional problems of temperature and heat flux determination at the surfaces of a thermoelastic slab: Part I The analytical solutions, Nuclear Engineering and Design, Vol. 74, pp. 1-14, 1982.
- Gupta V.K., Singh S.B., Chandrawat H.N. and Ray S., Creep behaviour of a rotating functionally graded composite disc operating under thermal gradient, Metallurgical and Materials Transactions A, Vol. 35, 1381-1391, 2004b.
- Gupta V.K., Singh S.B., Chandrawat H.N. and Ray S., Modelling of creep behaviour of a rotating disc in the presence of both composition and thermal gradients, Transactions of the ASME, Journal of Engineering Materials and Technology, Vol. 127, pp. 97-105, 2005.
- Gupta V.K., Singh S.B., Chandrawat H.N. and Ray S., Steady state creep and material parameters in a rotating disc of Al-SiC<sub>p</sub> composite, European Journal of Mechanics A/Solids, Vol. 23, pp. 335-344, 2004a.
- Güven U., Elastic-plastic stress distribution in rotating hyperbolic disk with rigid inclusion, International Journal of Mechanical Sciences, Vol. 40, pp. 97-109, 1998.
- Güven U., On the applicability of Tresca's yield condition to the linear hardening rotating solid disk of variable thickness, Zeitschrift für Angewandte Mathematik und Mechanik, Vol. 75, pp. 397-398, 1995a.
- Güven U., Parmaksizoglu C. and Altay O., Elastic-plastic rotating annular disk with rigid casing, Zeitschrift für Angewandte Mathematik und Mechanik, Vol. 79, pp. 499-503, 1999.
- Güven U., The fully plastic rotating disk of variable thickness, Zeitschrift für Angewandte Mathematik und Mechanik, Vol. 74, pp. 61-65, 1994.
- Güven U., The fully plastic rotating disk with rigid inclusion, Zeitschrift für Angewandte Mathematik und Mechanik, Vol. 77, pp. 714-716, 1997.
- Güven U., Tresca's yield condition and the linear hardening rotating solid disk of variable thickness, Zeitschrift für Angewandte Mathematik und Mechanik, Vol. 75, pp. 805-806, 1995b.
- Haslinger J., Repin S. and Sysala S., A reliable incremental method of computing the limit load in deformation plasticity based on compliance: Continuous and discrete setting, Journal of Computational and Applied Mathematics, Vol. 303, pp. 156-170, 2016.

## *Bibliography*

- Hassani A., Hojjati M.H., Farrahi G. and Alashti R.A., Semi-exact elastic solutions for thermo-mechanical analysis of functionally graded rotating disks, *Composite Structures*, Vol. 93, pp. 3239-3251, 2011.
- Hassani A., Hojjati M.H., Farrahi G. and Alashti R.A., Semi-exact solution for thermo-mechanical analysis of functionally graded elastic-strain hardening rotating disks, *Communications in Nonlinear Science and Numerical Simulation*, Vol. 17, pp. 3747-3762, 2012.
- Hencky H., Zur theorie plastischer deformation und der hierdurchin material hervorgerufene Nachspannen, *Zeitschrift für angewandte Mathematik und Mechanik*, Vol. 4, pp. 323-334, 1924.
- Hill R., *The Mathematical Theory of Plasticity*, Oxford University Press, Oxford, 1950.
- Hojjati M.H. and Hassani A., Theoretical and numerical analyses of rotating discs of non-uniform thickness and density, *International Journal of Pressure Vessels and Piping*, Vol. 85, pp. 694-700, 2008.
- Hojjati M.H. and Jafari S., Semi-exact solution of elastic non-uniform thickness and density rotating disks by homotopy perturbation and Adomian's decomposition method Part I: elastic solution, *International Journal of Pressure Vessels and Piping*, Vol. 85, pp. 871-878, 2008.
- Hojjati M.H. and Jafari S., Semi-exact solution of non-uniform thickness and density rotating disk, Part II: Elastic strain hardening solution, *International Journal of Pressure Vessels and Piping*, Vol. 86, pp. 307-318, 2009.
- Hojjati M.H. and Jafari S., Variational iteration solution of elastic non uniform thickness and density rotating disks, *Far East Journal of Applied Mathematics*, Vol. 29, pp. 185-200, 2007.
- Hojjati M.H., Hassani A., Mahdavi E., Alashti R.E. and Farrahi G., Thermo-mechanical analysis of rotating disks with non-uniform thickness and material properties, *International Journal of Pressure Vessels and Piping*, Vol. 98, pp. 95-101, 2012.
- Holms A.G. and Jenkins J.E., Effect of strength and ductility on burst characteristics of rotating disks, *NACA TN-1667*, 1948.

- Holms A.G., Jenkins J.E. and Repko A.J., Influence of tensile strength and ductility on strengths of rotating disks in presence of material and fabrication defects of several types, NACA TN-2397, 1951.
- Horgan C.O. and Baxter S.C., Effects of curvilinear anisotropy on radially symmetric stresses in anisotropic linearly elastic solids, *Journal of Elasticity*, Vol. 42, pp. 31-48, 1996.
- Horgan C.O. and Chan A.M., Torsion of Functionally Graded Isotropic Linearly Elastic Bars, *Journal of Elasticity*, Vol. 52, pp. 181-199, 1999.
- Horgan C.O., On the torsion of functionally graded anisotropic linearly elastic bars, *IMA Journal of Applied Mathematics*, Vol. 72, pp. 556-562, 2007.
- Huang H., Chen B. and Qiang H., Investigation on buckling behaviours of elastoplastic functionally graded cylindrical shells subjected to torsional loads, *Composite Structures*, Vol. 118, pp. 234-240, 2014.
- Jabbari M., Sohrabpour S. and Eslami M.R., Mechanical and thermal stresses in a functionally graded hollow cylinder due to radially symmetric loads, *International Journal of Pressure Vessels and Piping*, Vol. 79, pp. 493-497, 2002.
- Jafari S., The Karush-Kuhn-Tucker optimality conditions in minimum weight design of elastic rotating disks with variable thickness and density, *International Journal of Industrial Engineering Computations*, Vol. 2, pp. 765-774, 2011.
- Jahed H. and Dubey R.N., An Axisymmetric method of elastic-plastic analysis capable of predicting residual stress field, *Transactions of the ASME, Journal of Pressure Vessel Technology*, Vol. 119, pp. 264-273, 1997.
- Jahed H. and Sherkatti S., Thermoplastic analysis of inhomogeneous rotating disk with variable thickness, *Proceedings of EMAS Conference of Fatigue*, Cambridge, England, 2000.
- Jahed H. and Shirazi R., Loading and unloading behaviour of a thermoplastic disc, *International Journal of Pressure Vessels and Piping*, Vol. 78, pp. 637-645, 2001.
- Jahed H., Farshi B. and Bidabadi J., Minimum weight design of inhomogeneous rotating discs, *International Journal of pressure Vessels and piping*, Vol. 82, pp. 35-41, 2005.
- Jahromi B.H., Hashemi H.N. and Vaziri A., Elasto-Plastic Stresses in a Functionally Graded Rotating Disk, *Journal of Engineering Materials and Technology*, Vol. 134, pp. 021004 (1-11), 2012.

## *Bibliography*

- Jain R., Ramachandra K. and Simha K.R.Y., Rotating anisotropic disks of uniform strength, *International Journal of Mechanical Sciences*, Vol. 41, pp. 639-648, 1999.
- Jeong W. and Chung K., Stress analysis of rotating annular hyperbolic discs obeying a pressure-dependent yield criterion, *Structural Engineering and Mechanics*, vol. 58, pp. 689-705, 2016.
- Jeong W. and Pirumov A., Effect of plastic anisotropy of the distribution of stress and strain in rotating elastic/plastic discs, *The World Congress on Advances in Structural Engineering and Mechanics*, Ilsan (Seoul), Korea, 28<sup>th</sup> August-1<sup>st</sup> September, 2017.
- Johnson W. and Mellor P.B., *Engineering plasticity*, Van Nostrand, Princeton, London, 1962.
- Kachanov L.M., *Foundations of the theory of plasticity*, North-Holland Publication Co., Amsterdam, 1971.
- Kadkhodayan M. and Golmakani M.E., Non-linear bending analysis of shear deformable functionally graded rotating disk, *International Journal of Non-linear Mechanics*, Vol. 58, pp. 41-56, 2014.
- Kalali A.T., Moud S.H. and Hassani B., Elasto-plastic stress analysis in rotating disks and pressure vessels made of functionally graded materials, *Latin American Journal of Solids and Structures*, Vol. 13, pp. 819-834, 2016.
- Kamal S.M., Dixit U.S., Roy A., Liu Q. and Silberschmidt V.V., Comparison of plane-stress, generalized-plane-strain and 3D FEM elastic-plastic analyses of thick-walled cylinders subjected to radial thermal gradient, *International Journal of Mechanical Sciences*, Vol. (131-132), pp. 744-752, 2017.
- Katsikadelis J.T. and Sapountzakis E.J., Torsion of composite bars by boundary element method, *Journal of Engineering Mechanics*, Vol. 111, pp. 1197-1210, 1985.
- Katsikadelis J.T. and Tsiatas G.C., Saint-Venant Torsion of Non-homogeneous Anisotropic Bars, *Journal of Applied and Computational Mechanics*, Vol. 2, pp. 42-53, 2016.
- Khalili A. and Peddieson J., Evaluation of elastic compensation using elastic/plastic rotating circular disk problems, *Mechanics Research Communications*, Vol. 55, pp. 89-94, 2014.
- Khanna K., Gupta V.K. and Nigam S.P., Creep analysis of a variable thickness rotating FGM disc using Tresca criterion, *Defence Science Journal*, Vol. 65, pp. 163-170, 2015.

- Khorsand M. and Tang Y., Design functionally graded rotating disks under thermoelastic loads: Weight optimization, *International Journal of Pressure Vessels and Piping*, Vol. 161, pp. 33-40, 2018.
- Kim Y.J., Oh C.K., Myung M.S. and Park J.M., Fully plastic analyses for notched bars and plates using finite element limit analysis, *Engineering Fracture Mechanics*, Vol. 73, pp. 1849-1864, 2006.
- Kolodziej J.A. and Gorzelanczyk P., Application of method of fundamental solutions for elastoplastic torsion of prismatic rods, *Engineering Analysis with Boundary Elements*, Vol. 36, pp. 81-86, 2012.
- Kordkheili S.A.H. and Naghdabadi R., Thermo-elastic analysis of a functionally graded rotating disk, *Composite Structures*, Vol. 79, pp. 508-516, 2007.
- Kothari S. and Mukhopadhyaya S., Study of a problem of functionally graded hollow disk under different thermoelasticity theories-An analysis of phase-lag effects, *Computers & Mathematics with Applications*, Vol. 66, pp. 1306-1321, 2013.
- Kursuna A., Topcu M. and Tetik T., Stress analysis of functionally graded disc under thermal and mechanical loads, *Procedia Engineering*, Vol. 10, pp. 2949-2954, 2011.
- Lal R.K., Dwivedi J.P. and Singh V.P., Springback analysis of hollow rectangular bar of linear work-hardening material, *Emerging Materials Research*, Vol. 6, pp. 404-412, 2017.
- Laszlo F., Rotating disks in region of permanent deformation, *NACA TM 1192*, 1948.
- Leopold W.R., Centrifugal and thermal stresses in rotating disks, *Transactions of the ASME, Journal of Applied Mechanics*, Vol. 18, pp. 322-326, 1948.
- Leu S.Y. and Chien L.C., Thermoelastic analysis of functionally graded rotating disks with variable thickness involving non-uniform heat source, *Journal of Thermal Stresses*, Vol. 38, pp. 415-426, 2015.
- Liew K.M., Kitipornachi S., Zhang X.Z. and Lim C.W., Analysis of the thermal stress behaviour of functionally graded hollow circular cylinders, *International Journal of Solids and Structures*, Vol. 40, pp. 2355-2380, 2003.
- Loghman A., Arani A.G., Shajari A.R. and Amir S., Time-dependent thermoelastic creep analysis of rotating disk made of Al-SiC composite, *Archive of Applied Mechanics*, Vol. 81, pp. 1853-1864, 2011.

## *Bibliography*

- Lomakin E., Alexandrov S. and Jeng Y.R., Stress and strain fields in rotating elastic/plastic annular disks, *Archive of Applied Mechanics*, Vol. 86, pp. 235-244, 2016.
- Ma B.M., A further creep analysis for rotating solid disks of variable thickness, *Journal of The Franklin Institute*, Vol. 269, pp. 408-419, 1960.
- Ma B.M., Creep analysis of rotating solid disks with variable thickness and temperature, *Journal of The Franklin Institute*, Vol. 271, pp. 40-55, 1961.
- Ma B.M., Creep analysis of rotating solid disks, *Journal of The Franklin Institute*, Vol. 267, pp. 149-165, 1959.
- Ma G., Hao H. and Miyamoto Y., Limit angular velocity of rotating disc with unified yield criterion, *International Journal of Mechanical Sciences*, Vol. 43, pp. 1137-1153, 2001.
- Ma G.W. and Shao Z.S., Thermo-mechanical stresses in functionally graded circular hollow cylinder with linearly increasing boundary temperature, *Composite Structures*, Vol. 83, pp. 259-265, 2008.
- Ma L.S. and Lee D.W., Exact solutions for nonlinear static responses of a shear deformable FGM beam under an in-plane thermal loading, *European Journal of Mechanics A/Solids*, Vol. 31, pp. 13-20, 2012.
- Mack W., Rotating elastic-plastic tube with free ends, *International Journal of Solids and Structures*, Vol. 27, pp. 1461-1476, 1991a.
- Mack W., The rotating elastic-plastic solid shaft with free ends, *Technische Mechanik*, Vol. 12, pp. 119-124, 1991b.
- Mahdavi E., Ghasemi A. and Alashti R.A., Elastic-plastic analysis of functionally graded rotating disks with variable thickness and temperature-dependent material properties under mechanical loading and unloading, *Aerospace Science and Technology*, Vol. 59, pp. 57-68, 2016.
- Mahmoudi T., Parvizi A., Poursaeidi E. and Rahi A., Thermo-mechanical analysis of functionally graded wheel-mounted brake disk, *Journal of Mechanical Science and Technology*, Vol. 29, pp. 4197-4204, 2015.
- Mangal S.K., Kapoor N. and Singh T., Steady-state creep analysis of functionally graded rotating cylinder, *International Journal for Experimental Mechanics*, Vol. 49, pp. 457-466, 2013.



- Manson S.S., Analysis of rotating discs of arbitrary contour and radial temperature distribution in the region of plastic deformation, Proceedings of the First U.S. National Congress of Applied Mechanics, Vol. 1, pp. 569-577, 1951.
- Manson S.S., Direct method of design and stress analysis of rotating disks with temperature gradient, NACA Report 952, 1950.
- Manson S.S., The determination of elastic stresses in gas-turbine disks, NACA TN-1279, 1947.
- Martinez I., Thermal Effects on Materials, (Online article, 2016), <http://webservice.dmt.upm.es/~isidoro/ot1/Thermal%20effects%20on%20materials.pdf>
- Martynovich B.T. and Martynovich T.L., Use of Integral Equations in the Solution of Problems of Torsion of Rectilinear-Anisotropic Rods, *Izvestiya Akademii Nauk Mekhanika Tverdogo Tela*, Vol. 19, pp. 112-118, 1984.
- Mazarei Z. and Nejad M.Z., Thermo-elasto-plastic analysis of thick-walled spherical pressure vessels made of functionally graded materials, *International Journal of Applied Mechanics*, Vol. 8, pp. 1650054 (1-25), 2016.
- Maziere M., Besson J., Forest S., Tanguy B., Chalons H. and Vogel F., Overspeed burst of elastoviscoplastic rotating disks: Part II-Burst of a superalloy turbine disk, *European Journal of Mechanics A/Solids*, Vol. 28, pp. 428-432, 2009.
- Mellor P.B. and Percy M.J., Tensile Instability of hollow rotating discs of uniform thickness, Aeronautical Research Council current paper no. 692, 1963.
- Mendelson A. and Manson S.S., Practical solution of plastic deformation problems in elastic plastic range, NACA Technical Report TN-4088, 1957.
- Mendelson A., *Plasticity: theory and application*, Macmillan, 1968.
- Millenson M.B. and Manson S.S., Determination of stresses in gas-turbine disks subjected to plastic flow and creep, NACA 906, 1948.
- Miyamoto Y., Kaysser W.A., Rabin B.H., Kawasaki A. and Ford R.G., *Functionally graded materials: design, processing and application*, Kluwer Academic Publishers, London, 1999.
- Mohan S.C. and Maiti D.K., Structural optimization of rotating disk using response surface equation and genetic algorithm, *International Journal for Computational Methods in Engineering Science and Mechanics*, Vol. 14, pp. 124-132, 2013.

## *Bibliography*

- Mukhtar F.M. and Al-Gahtani H.J., Application of radial basis functions to the problem of elasto-plastic torsion of prismatic bars, *Applied Mathematical Modelling*, Vol. 40, pp. 436-450, 2016.
- Murthy D.N.S. and Sherbourne A.N., Elastic stresses in anisotropic disks of variable thickness, *International Journal of Mechanical Sciences*, Vol. 12, pp. 627-640, 1970.
- Nakamura T., Wang T. and Sampath S., Determination of properties of graded materials by inverse analysis and instrumented indentation, *Acta Materialia*, Vol. 48, pp. 4293-4306, 2000.
- Nayebi A., Tirmomenin A. and Damadam M., Elasto-plastic analysis of a functionally graded rotating disk under cyclic thermo-mechanical loadings considering continuum damage mechanics, *International Journal of Applied Mechanics*, vol. 7, Article ID 1550026, 2015.
- Nejad M.Z. and Fatehi P., Exact elasto-plastic analysis of rotating thick-walled cylindrical pressure vessels made of functionally graded materials, *International Journal of Engineering Science*, Vol. 86, pp. 26-43, 2015.
- Nejad M.Z. and Rahimi G.H., Deformations and stresses in rotating FGM pressurized thick hollow cylinder under thermal load, *Scientific Research and Essays*, Vol. 4, pp. 131-140, 2009.
- Nejad M.Z., Jabbari M. and Ghannad M., A semi-analytical solution for elastic analysis of rotating thick cylindrical shells with variable thickness using disk form multilayers, Hindawi Publishing Corporation, *The Scientific World Journal*, Article ID 932743, pp. 1-10, 2014.
- Nejad M.Z., Jabbari M. and Ghannad M., Elastic analysis of axially functionally graded rotating thick cylinder with variable thickness under non-uniform arbitrarily pressure loading, *International Journal of Engineering Science*, Vol. 89, pp. 86-99, 2015.
- Nejad M.Z., Rastgoo A. and Hadi A., Exact elasto-plastic analysis of rotating disks made of functionally graded materials, *International Journal of engineering Science*, Vol. 85, pp. 47-57, 2014.
- Nemirovskii Y.V. and Yankovskii A.P., Rational profiling of reinforced rotating disks, *Mechanics of Composite Materials*, Vol. 38, pp. 1-16, 2002.

- Nie G.J. and Batra R.C., Stress analysis and material tailoring in isotropic linear thermo-elastic incompressible functionally graded rotating disks of variable thickness, *Composite Structures*, Vol. 92, pp. 720-729, 2010.
- Niknam H., Fallah A. and Aghdam M.M., Nonlinear bending of functionally graded tapered beams subjected to thermal and mechanical loading, *International Journal of Non-linear Mechanics*, Vol. 65, pp. 141-147, 2014.
- Noda N., Thermal stress in materials with temperature-dependent properties, *Applied Mechanics Reviews*, Vol. 44, pp. 383-397, 1991.
- Obata Y. and Noda N., Steady thermal stresses in a hollow circular cylinder and a hollow sphere of a functionally gradient material, *Journal of Thermal Stresses*, Vol. 17, pp. 471-487, 1994.
- Orcan Y. and Eraslan A.N., Elastic-plastic stresses in linearly hardening rotating solid disks of variable thickness, *Mechanics Research Communications*, Vol. 29, pp. 269-281, 2002.
- Outinen J. and Makelainen P., Mechanical properties of structural steel at elevated temperatures and after cooling down, *Second International Workshop (Structures in Fire)*, Christchurch, 2002.
- Owen D.R.J. and Hinton E., *Finite Elements in Plasticity: Theory and Practice*, Pineridge Press Limited, U.K, 1980.
- Parmaksizoglu C. and Guven U., Stresses in rotating non-homogeneous disks with different compressive and tensile moduli, *Journal of Istanbul Technical University*, Vol. 46, pp. 58-62, 1988.
- Paul A. and Das D., Non-linear thermal post-buckling analysis of FGM Timoshenko beam under non-uniform temperature rise across, *Engineering Science and Technology, an International Journal*, Vol. 19, pp. 1608-1625, 2016.
- Peng X.L. and Li X.F., Elastic analysis of rotating functionally graded polar orthotropic disks, *International Journal of Mechanical Sciences*, Vol. 60, pp. 84-91, 2012.
- Peng X.L. and Li X.F., Thermal stress in rotating functionally graded hollow circular disks, *Composite Structures*, Vol. 92, pp. 1896-1904, 2010.
- Percy M.J., Ball K. and Mellor P.B., An experimental study of the burst strength of rotating disks, *International Journal of Mechanical Sciences*, Vol. 16, pp. 809-812, 1974.

## *Bibliography*

- Pirumov A., Alexandrov S. and Jeng Y.R., Enlargement of a circular hole in a disc of plastically compressible material, *Acta Mechanica*, Vol. 224, pp. 2965-2976, 2013.
- Pitakthapanaphong S. and Busso E.P., Self-consistent elastoplastic stress solutions for functionally graded material systems subjected to thermal transients, *Journal of the Mechanics and physics of Solids*, Vol. 50, pp. 695-716, 2002.
- Rattan M., Kaushik A., Chamoli N. and Bose T., Steady state creep behaviour of thermally graded isotropic rotating disc of composite taking into account the thermal residual stress, *European Journal of Mechanics A/Solids*, Vol. 60, pp. 315–326, 2016.
- Raveendra S.T. and Banerjee P.K., Analysis of rotating solids with cracks by the boundary element method, *International Journal of Solids and Structures*, Vol. 28, pp. 1155-1170, 1991.
- Reddy J.N., *An Introduction to Nonlinear Finite Element Analysis*, Oxford University Press, Oxford, 2005.
- Reddy J.N., Analysis of functionally graded plates, *International Journal for Numerical Methods in Engineering*, Vol. 47, pp. 663-684, 2000.
- Reddy J.N., Wang C.M. and Kitipornchi S., Axisymmetric bending of functionally graded circular and annular plates, *European Journal of Mechanics A/Solids*, Vol. 18, pp. 185-199, 1999.
- Reddy T.Y. and Srinath H., Elastic stresses in a rotating anisotropic annular disk of variable thickness and variable density, *International Journal of Mechanical Sciences*, Vol. 16, pp. 85-89, 1974.
- Rees D.A., Elastic–plastic stresses in rotating disks by von Mises and Tresca, *Zeitschrift für Angewandte Mathematik und Mechanik*, Vol. 79, pp. 281-288, 1999.
- Robinson E.L., Bursting of steam turbine disk wheels, *Transactions of the ASME*, Vol. 66, pp. 373-380, 1944.
- Sapountzakis E.J. and Tsipiras V.J., Nonlinear inelastic uniform torsion of composite bars by BEM, *Computers and Structures*, Vol. 87, pp. 151-166, 2009.
- Savi M.A. and Pacheco P.M.C.L., Chaos and unpredictability in the vibration of an elasto-plastic beam, *Journal of the Brazilian Society of Mechanical Sciences*, Vol. 23, pp. 253-267, 2001.
- Sayman O., Thermal stress analysis in an aluminum metal-matrix orthotropic disc, *Journal of Reinforced Plastics and Composites*, Vol. 23, pp. 1473-1479, 2004.

- Sayman O., Yanginci S. and Sayer M., Thermoelastic-plastic stress analysis in a thermoplastic composite disc, *Journal of Reinforced Plastics and Composites*, Vol. 24, pp. 21-33, 2005.
- Seif M., Main J., Weigand J., Mcallister T.P. and Luecke W., Finite element modelling of structural steel component failure at elevated temperatures, *Structure*, Vol. 6, pp. 134-145, 2016.
- Seireg A. and Surana K.S., Optimum design of rotating disks, *Transactions of the ASME, Journal of Engineering for Industry*, Vol. 92, pp. 1-10, 1970.
- Sen F. And Sayer M., Elasto-plastic thermal stress analysis in a thermoplastic composite disc under uniform temperature using FEM, *Mathematical and Computational Applications*, Vol. 11, pp. 31-39, 2006.
- Shabana Y.M., Noda N. and Tohgo K., Elasto-plastic thermal stresses in functionally graded materials considering microstructure effects, *Proceedings of the 7th Cairo University International MDP Conference on Current Advances in Mechanical Design and Production*, Cairo, Egypt, pp. 223-231, 2000.
- Shahzamanian M.M., Sahari B.B., Bayat M., Mustapha F. and Ismarrubie Z.N., Elastic contact analysis of functionally graded brake disks subjected to thermal and mechanical loads, *International Journal for Computational Methods in Engineering Science and Mechanics*, Vol. 14, pp. 10-23, 2013.
- Shanbhag M.R., Stress analysis of rotating disk with fem-emphasis on stresses at contours of dissimilar holes at the rim, *Computers and Structures*, Vol. 18, pp. 603-608, 1984.
- Shao Z.S., Mechanical and thermal stresses of a functionally graded circular hollow cylinder with finite length, *International Journal of Pressure Vessels and Piping*, Vol. 82, pp. 155-163, 2005.
- Sharma S. and Yadav S., Thermo elastic-plastic analysis of rotating functionally graded stainless steel composite cylinder under internal and external pressure using finite difference method, *Advances in Materials Science and Engineering*, Hindawi Publishing Corporation, Article ID 810508, 2013.
- Shen H.S., Xiang Y. and Fan Y., Nonlinear vibration of functionally graded graphene-reinforced composite laminated cylindrical shells in thermal environments, *Composite Structures*, Vol. 182, pp. 447-456, 2017.

## *Bibliography*

- Sherbourne A.N. and Murthy D.N.S., Stresses in discs with variable profile, *International Journal of Mechanical Sciences*, Vol. 16, pp. 449-459, 1974.
- Singh S.B. and Ray S., Modelling the anisotropy and creep in orthotropic aluminium-silicon carbide composite rotating disc, *Mechanics of Materials*, Vol. 34, pp. 363-372, 2002.
- Singh S.B. and Ray S., Steady-state creep behaviour in an isotropic functionally graded material rotating disc of Al-SiC composite, *Metallurgical and Materials Transactions A*, Vol. 32, pp. 1679-1685, 2001.
- Skidmore W.E., Bursting tests of rotating disks typical of small gas turbine wheel design, *Proceedings of the Society for Experimental Stress Analysis*, Vol. 8, pp. 29-48, 1951.
- Srinath L.S., *Advanced Mechanics of Solids*, Tata McGraw Hill, 2003.
- Sterner S.C., Saigal S., Kistler W. and Dietrich D.E., A unified numerical approach for the analysis of rotating disks using turbine rotors, *International Journal of Solids and Structures*, Vol. 31, pp. 269-277, 1994.
- Suresh S. and Mortensen A., *Fundamentals of functionally graded materials*, IOM Communications Limited, London, UK, 1998.
- Taamneh Y., Thermal analysis of gas turbine disk integrated with rotating heat pipes, *Case Studies in Thermal Engineering*, Vol. 10, pp. 335-342, 2017.
- Tahani M., Nosier A. and Zebarjad S.M., Deformation and stress analysis of circumferentially fiber-reinforced composite disks, Vol. 42, pp. 2741-2754, 2005.
- Tamura I., Tomota Y. and Ozawa H., Strength and ductility of Fe-Ni-C alloys composed of austenite and martensite with various strength, *Proceeding of the Third International Conference on Strength of Metals and Alloys*, Cambridge Institute of Metals, vol. 1, pp. 611-615, 1973.
- Tang S., Elastic stresses in rotating anisotropic disks, *International Journal of Mechanical Sciences*, Vol. 11, pp. 509-517, 1969.
- Tanigawa Y., Some basic thermoelastic problems for non homogeneous structural materials, *Applied Mechanics Reviews*, Vol. 48, pp. 287-300, 1995.
- Tayyar G.T., A new approach for elasto-plastic finite strain analysis of cantilever beams subjected to uniform bending moment, *Sadhana-Academy Proceedings in Engineering Sciences*, Vol. 41, pp. 451-458, 2016.

- Thompson A.S., Stresses in rotating discs at high temperature, Transactions of the ASME, Journal of Applied Mechanics, Vol.13, pp. A45-A52, 1946.
- Timoshenko S. and Goodier J.N., Theory of elasticity, McGraw-Hill, 1970.
- Timoshenko S., Strength of Materials: Part I Elementary Theory and Problems, D. Van Nostrand Company, Inc., New York, NY, 1930.
- Toussi H.E. and Farimani M.R., Elasto-plastic deformation analysis of rotating disc beyond its limit speed, International Journal of Pressure Vessels and Piping, Vol. 89, pp. 170-177, 2012.
- Tsiatas G.C. and Babouskos N.G., Elastic-plastic analysis of functionally graded bars under torsional loading, Composite Structures, Vol. 176, pp. 254-267, 2017.
- Turkylmazoglu M., Analytic approximate solutions of rotating disk boundary layer flow subject to a uniform suction or injection, International Journal of Mechanical Sciences, Vol. 52, pp. 1735-1744, 2010.
- Tutuncu N. and Temel B., A novel approach to stress analysis of pressurized FGM cylinders, disks and spheres, Composite Structures, Vol. 91, pp. 385-390, 2009.
- Tutuncu N., Effect of anisotropy on stresses in rotating disks, International Journal of Mechanical Sciences, Vol. 37, pp. 873-881, 1995.
- Vaz-Romero A., Rotbaum Y., Rodriguez-Martinez J.A. and Rittel A., Necking evolution in dynamically stretched bars: New experimental and computational insights, Journal of the Mechanics and Physics of Solids, Vol. 91, pp. 216-239, 2016.
- Vivio F. and Vullo V., Elastic stress analysis of rotating converging conical disks subjected to thermal load and having variable density along the radius, International Journal of Solids and Structures, Vol. 44, pp. 7767-7784, 2007.
- Vullo V. and Vivio F., Elastic stress analysis of non-linear variable thickness rotating disks subjected to thermal load and having variable density along the radius, International Journal of Solids and Structures, Vol. 45, pp. 5337-5355, 2008.
- Wahl A.M., Shankey G.O., Manjoine M.J. and Shoemaker E., Creep tests of rotating disks at elevated temperature and comparison with theory, Transactions of the ASME, Journal of Applied Mechanics, Vol. 21, pp. 225-235, 1954.
- Waldren N.E., Percy M.J. and Mellor P.B., Burst strength of rotating disks, Proceedings of the Institution of Mechanical Engineers, Vol. 180, pp. 111-130, 1965.

## *Bibliography*

- Wattanasakulpong N., Prusty B.G. and Kelly D.W., Thermal buckling and elastic vibration of third-order shear deformable functionally graded beams, *International Journal of Mechanical Sciences*, Vol. 53, pp. 734–743, 2011.
- Wilterdink P.I., Holms A.G. and Manson S.S., A theoretical and experimental investigation of the influence of temperature gradients on the deformation and burst speeds of rotating disks, NACA TN-2803, 1952.
- Wu M.H. Lee, Analysis of plane-stress problems with axial symmetry in strain hardening range, NACA TN 2217, 1950.
- Wu M.H. Lee, General plastic behaviour and approximate solutions of rotating disk in strain-hardening range, NACA TN 2367, 1951.
- Xin L., Dui G., Yang S. and Liu Y., Elastic-plastic analysis for functionally graded thick-walled tube subjected to internal pressure, *Advances in Applied Mathematics and Mechanics*, Vol. 8, pp. 331-352, 2016.
- Yamanoushi M., Koizumi M., Hirai T. and Shiota I., *Proceedings of the First International Symposium on Functionally Gradient Materials*, Japan, 1990.
- Yankelevsky D.Z., Elastic-plastic behaviour of a shallow two bar truss, *International Journal of Mechanical Sciences*, Vol. 41, pp. 663-675, 1999.
- Yeh K.Y. and Han R.P.S., Analysis of high-speed rotating disks with variable thickness and inhomogeneity, *Transactions of the ASME, Journal of Applied Mechanics*, Vol. 61, pp. 186-191, 1994.
- You L.H. and Zhang J.J., Elastic-plastic stresses in a rotating solid disk, *International Journal of Mechanical Sciences*, Vol. 41, pp. 269-282, 1999.
- You L.H., Long S.Y. and Zhang J.J., Perturbation solution of rotating solid disks with nonlinear strain hardening, *Mechanics Research Communications*, Vol. 24, pp. 649-658, 1997.
- You L.H., Tang Y.Y., Zhang J.J. and Zheng C.Y., Numerical analysis of elastic-plastic rotating disks with arbitrary variable thickness and density, *International Journal of Solids and Structures*, Vol. 37, pp. 7809-7820, 2000.
- Yu M.H., Twin shear stress yield criterion, *International Journal of Mechanical Sciences*, Vol. 25, pp. 71-74, 1983.



- Zarandi S.B., Wang Y.C. and Novozhilova O.V., Plastic behaviour of circular discs with temperature-dependent properties containing an elastic inclusion, *Structural Engineering and Mechanics*, Vol. 58, pp. 731-743, 2016.
- Zenkour A.M., Stress distribution in rotating composite structures of functionally graded solid disks, *Journal of Materials Processing Technology*, Vol. 209, pp. 3511-3517, 2009.
- Zhang L.W. and Liew M., Postbuckling analysis of axially compressed functionally graded carbon nanotube resting on Pasternak foundations by utilizing an element-free approach, *Composite Structures*, Vol. 138, pp. 40-51, 2016.
- Zheng Y., Bahaloo H., Mousanezhad D., Mahdi E., Vaziri A. and Nayeb-Hashemi H., Stress analysis in functionally graded rotating disks with non-uniform thickness and variable angular velocity, *International Journal of Mechanical Sciences*, vol. 119, pp. 283-293, 2016.
- Zhou F. and Ogawa A, Elastic solutions for a solid rotating disk with cubic anisotropy, *Transactions of the ASME, Journal of Applied Mechanics*, Vol. 69, pp. 81-83, 2002.